Research on Engineering Structures Materials

P-ISSN: 2148-9807 E-ISSN: 2149-4088 www.jresm.org

Volume 8

Issue 1

February 2022

Research Group

The International Journal of **Research on Engineering Structures and Materials (RESM)** is a peer-reviewed open access journal (p-ISSN: 2148-9807; o-ISSN: 2149-4088) published by MIM Research Group. It is published in February, June, September, and December.

The main objective of RESM is to provide an International academic platform for researchers to share scientific results related to all aspects of mechanical, civil and material engineering areas.

RESM aims the publication of original research articles, reviews, short communications technical reports, and letters to the editor on the latest developments in the related fields.

All expenditures for the publication of the manuscripts are most kindly reimbursed by *MIM Research Group*. Thus, authors do not need to pay for publishing their studies in the journal.

The scope of the journal covers (but not limited to) behavior of structures, machines and mechanical systems, vibration, impact loadings and structural dynamics, mechanics of materials (elasticity, plasticity, fracture mechanics), material science (structure and properties of concrete, metals, ceramics, composites, plastics, wood, etc.,), nano-materials performances of new and existing buildings and other structural systems, design of buildings and other structural systems, seismic behavior of buildings and other structural systems, repair and strengthening of structural systems, case studies and failure of structural systems, safety and reliability in structural and material engineering, use of new and innovative materials and techniques in energy systems and mechanical aspects of biological systems (biomechanics and biomimetics).

The topics covered in JRESM include:

- Structural Engineering
- Mechanical Engineering
- Material Engineering
- Earthquake Engineering
- Nano-technology
- Energy Systems
- Biomechanics and Biomimetics

Abstracting and Indexing
Please visit http://www.jresm.org for more information.

Graphics and Design

Yunus Demirtaş ydemirtas@jresm.net

RESEARCH on ENGINEERING STRUCTURES & MATERIALS

Research Group

Advisory Board Members

Advisory Board Members

Emre Esener	Bilecik Seyh Edebali University	Turkey
S. Ali Faghidian	Islamic Azad University	Iran
Abdullah Fettahoglu	Usak University	Turkey
Berker Fıçıcılar	Ondokuz Mayıs University	Turkey
Saeid Foroughi	Konya Technical University	Turkey
Chithambar Ganesh	Kalasalingam University	India
Mehmet Cemal Genes	Eastern Mediterranean University	North Cyprus
Can Gonenli	Ege University	Ege University
Orhan Gülcan	General Electric Aviation	USA
Ersin Asım Güven	Kocaeli University	Turkey
Kadir Gunaydın	GE Aviation	Turkey
Marijana Hadzima-Nyarko	University of Osijek	Croatia
Dulce Franco Henriques	Instituto Politécnico de Lisboa	Portugal
Qing Hong	Midwestern University	USA
Manuel Horta	Universidade do Porto	Portugal
Halit Levent Hosgun	Bursa Technical University	Bursa Technical University
Bulent Imamoglu	Gedik University	Turkey
Ercan Isik	Bitlis Eren University	Turkey
Khairul Nizar Ismail	Universiti Malaysia Perlis	Malaysia
Sahar Ismail	Saint Joseph University of Beirut	Beirut
Berrin Ikizler	Ege University	Turkey
Atike İnce Yardımcı	Usak University	Turkey
Liyana Jamaludin	Universiti Malaysia Perlis	Malaysia
Saifulnizan Jamian	Universiti Tun Hussein Onn Malaysia	Malaysia
Md. Salim Kaiser	Bangladesh University of Engineering and Technology	Bangladesh
Sreevani Kannan	Chennai Institute of Technology	India
Gökhan Kaplan	Atatürk University	Turkey

Advisory Board Members

Altug Karabey	Yuzuncu Yil University	Turkey
Abdulhalim Karasin	Dicle University	Turkey
Mehmet Kaya	Yozgat Bozok University	Turkey
Dogan Kaya	Cukurova University	Turkey
Deniz Kaya	Dokuz Eylul University	Turkey
Jibran Khaliq	Northumbria University	United Kingdom
Kadir Kılınç	Kırklareli University	Turkey
Abiodun Kilani	Federal University Oye Ekiti	Nigeria
Sedat Kömürcü	Istanbul Technical University	Turkey
A. Suresh	Kalasalingam Academy of Research and Education	India
Salmabanu Luhar	Universiti Malaysia Perlis	Malaysia
Lomesh Mahajan	Dr. Babasaheb Ambedkar Technological University	India
Waqas Ahmed Mahar	University of Liege	Belgium
Yelda Mert	Iskenderun Technical University	Turkey
Seyede Mahdieh Miralami	University of Rahman	Iran
Jinxu Mo	Yangtze University	China
Nebab Mokhtar	Hassiba Benbouali Universyt of Chlef	Algeria
Nahida Nazim Musayeva	Azerbaijan National Academy of Sciences	Azerbaijan
Elango Natarajan	UCSI University	Malaysia
Muhammed Yasin Naz	Universiti Teknologi Petronas	Malaysia
Samson Olalekan Odeyemi	Kwara State University	Nigeria
Osama Mohamed Omar	Beirut Arab University	Lebanon
Mehmet Orhan	Pamukkale University	Turkey
Hayri Baytan Ozmen	Usak University	Turkey
Zehra Özçelik	Ege University	Turkey
Alp Özdemir	Eskisehir Technical University	Turkey
Yasin Onuralp Özkılıç	Necmettin Erbakan University	Turkey

Advisory Board Members

In This Issue

Research on Engineering Structures & Materials
MIM Reseach Group Publications
P-ISSN: 2148-9807
E-ISSN: 2149-4088
http://www.jresm.org

ABSTRACTING / INDEXING

The international journal of Research on Engineering Structures and Materials (RESM) is currently Absracted/Indexed by Asos Indeks, CiteFactor, Cosmos, CrossRef, Directory of Research Journal Indexing, Engineering Journals (ProQuest), EZB Electronic Journal Library, Global Impact Factor, Google Scholar, International Institute of Organized Research (I2OR), International Scientific Indexing (ISI), Materials Science & Engineering Database (ProQuest), Open Academic Journals Index, Publication Forum, Research BibleScientific Indexing Service, Root Indexing, Scopus, Ulakbim TR Index (Tubitak), Universal Impact Factor and under evaluation by many other respected indexes.

Check web site for current indexing info, www.jresm.org

Research on Engineering Structures & Materials
journal homepage: http://www.jresm.org
Research Group

Research Article

Tensile and flexural properties of MWCNT-COOH and hBN integrated polyamide 66/short glass fiber composites

Özgür Demircan*[1, 2], Naser Rezaei Ansaroudi[1], Fatma Burcu Uzunoğlu[2]

[1]*Department of Metallurgical and Material Engineering, Ondokuz Mayıs University, Samsun, Turkey*
[2]*Department of Nanoscience and Nanotechnology, Ondokuz Mayıs University, Samsun, Turkey*

Article Info

Article history:
Received 22 Aug 2021
Revised 7 Oct 2021
Accepted 10 Oct 2021

Keywords:

Composite material; Polymer nanocomposite; Polyamide 66; Glass fiber; Carbon nanotube; Hexagonal Boron Nitride; Nanofillers; Plastic injection molding

Abstract

In this study, the effect of hexagonal boron nitride (hBN) and modified (carboxylic acid functionalized) multi-walled carbon nanotubes (MWCNTs-COOH) on tensile and flexural behaviour of 30% short glass fiber reinforced Polyamide 66 (PA 66/30SGF) is investigated. Initially, MWCNTs-COOH, hBN and MWCNTs-COOH/hBN are mechanically mixed with PA 66/30SGF granules in ethanol and stirred via a magnetic stirrer for one hour. After ethanol evaporates, MWCNTs-COOH, hBN and MWCNTs-COOH/hBN integrated granules are conditioned in an oven and the obtained granules are transferred to the plastic injection moulding machine for the fabrication process of specimens. Thus five types of specimens are produced; and their mechanical behaviors are examined by Instron 5982 test machine. The test results show that elastic modulus and flexural properties of PA 66/30SGF are improved with the addition of MWCNTs-COOH, hBN and MWCNTs-COOH+hBN.

1. Introduction

Plastic materials have been widely used in medical, biomedical, military, aerospace, structural applications and so forth [1, 2]. In the last years, production of plastics globally almost reached up to 370 million tonnes [2]. However, among all plastics, thermoplastics are the most preferred given that they account for virtually 80% of the plastics used throughout the world [3]. Thermoplastics owe this popularity to their advantageous properties such as high strength, easy processibility, and reasonable production cost and lightweight. Yet, despite these advantages, some thermoplastics such as PA 66 might suffer from micro-cracking during use or production [4]. In order to prevent such mechanical problems, thermoplastics could be improved by micro-scale or nano-scale reinforcing fillers. The mixtures of polymers with inorganic or organic fillers that have certain geometries (fibers, flakes, spheres, and particulates) are known as polymer composites and if these fillers are of nano-scale dimensions, the materials are known as polymer nanocomposites [5].

In polymer matrix composites, short glass fiber (SGF) has been frequently used as reinforcing filler due to its relatively low cost and superior mechanical properties [6]. Additionally, nano-scale materials provide considerable enhancement in mechanical properties of the polymers. However, in fabrication process of polymer matrix composites or nanocomposites, achieving the uniform dispersion of the fillers in the polymer could

*Corresponding author: ozgur.demircan@omu.edu.tr
[a] orcid.org/0000-0001-8235-3966 ; [b] orcid.org/0000-0001-9933-9706; [c] orcid.org/0000-0002-4197-785X
DOI: http://dx.doi.org/10.17515/resm2021.334me0822

even be a lot challenging due to the fact that some nano-scale fillers tend to form bundles or agglomerates in the polymer matrix [7].

Polyamide 66 (PA 66), also known as Nylon 66, is a semi-crystalline commercial thermoplastic mostly used as engineering resin in high-performance applications where good mechanical, chemical and thermal properties are required [8, 9]. With the addition of various fillers or nano-fillers, such as glass fibers, carbon fibers, carbon nanotubes, nano clays, mechanical properties of PA 66 could be altered. Among a variety of fillers, glass fibers are extensively preferred owing to their ability of increasing the stiffness and heat resistance of the composite as well as their relatively low processing costs [10]. Addition of glass fibers into PA 66 matrix up to a certain ratio leads to a large amount of improvement in the mechanical properties [11-18].

For the last a few decades, various nanomaterials, such as single-walled or multi-walled carbon nanotubes, nanoclays, boron nitride nanoparticles and so forth, have become commercially available. A number of studies revealed that multi-walled carbon nanotubes could be ideal candidates for polymer reinforcement owing to their high tensile strength, which is 11-63 GPa [19], and Young's modulus reaching up to 1 TPa [19, 20].

Regarding CNT/polyamide composites, a number of investigations have been carried out so far [21-35] and majority of them state that CNTs are able to enhance the mechanical performance of polymeric composite systems. Miyagawa et al. [36] and Coleman et al. [37] produced overall reviews on the mechanical reinforcement of polymers by the use of CNTs. And some studies focusing on CNT-polymer matrix interaction and crack behaviour of CNTs/polymer composites are also available in literature [38-42]. Mechanical and morphological investigations demonstrated that CNTs prevent crack opening and propagation by stretching across the cracks during the fracture and hence improves the mechanical performance. Ajayan et al. [43] and Liu et al. [44] obtained the SEM images indicating the bridging phenomenon of CNTs in polymeric matrices. Zhang et al. [45] investigated the mechanical properties of MWCNT/Polyamide 6 composite prepared by simple melt-compounding and revealed that the tensile strength and the elastic modulus of the composite increase by nearly 120% and 115%, respectively, with the addition of 1 wt.% MWNTs content. This significant enhancement in mechanical performance was attributed to uniform dispersion of MWNTs in the polymer matrix and the strong interaction between MWNTs' surface and polymeric matrix. Similarly, Ferreira et al. [46] explored that the presence of 1 wt.% pristine-CNT in PA 6 matrix increases the elastic modulus by 43% and the tensile strength by 33%.

A vast majority of the studies on polymeric nanocomposites point out that mechanical behaviour of the CNT/polymer composites are highly dependent on the dispersion, distribution and alignment of CNTs throughout the matrix and the interfacial interaction between CNT and polymer [22, 32, 47-50].

Despite the high reinforcing potential of CNTs, it is extremely difficult to have them well-dispersed in the polymer due to their agglomeration tendency caused by their long length and high polarizability as well as the van der Waals forces between their surfaces [51, 52]. Agglomerated CNTs may cause stress concentrations and act like defects, which brings about reduction in mechanical performance. One of the most effective ways to avoid CNT agglomeration and achieve efficient load transfer between matrix and CNT network is functionalization [22, 30, 37, 51]. Chopra et al. [53] carried out a study on functionalized-MWCNTs/PA 6 composites and reported that the inclusion of functionalized-MWCNTs (MWCNTs-COOH) increases the tensile strength of Polyamide 6 by almost 12%. The authors explained this improvement by efficient interaction between well-dispersed MWCNTs and Polyamide 6 matrix. The study of Chen et al. [27] on the properties of PA 66/MWCNTs-COOH fibers showed that tensile strength of PA 66 fibers improves by 24%,

when 1 wt.% MWNTs-COOH is incorporated. This effect was attributed to the homogeneous dispersion of MWNTs in PA 66 matrix.

In recent years, thanks to the developments in nanoscience and nanotechnology, new nanomaterials have been introduced to the market and one of the most prominent of them is hexagonal boron nitride (hBN) [54], which is a 2D crystal material composed of equal boron and nitrogen atoms in a honeycomb arrangement [55-57]. Due to its structural similarity to graphene and novel properties such as excellent thermal stability, chemical inertness and high strength, hBN has become the subject of many studies to date [57-59]; and it is considered to be a potential reinforcement for polymer matrix composites. Mortazavi and Cuniberti [60] calculated the elastic modulus and tensile strength of pristine hBN films as 800-850 GPa and 150±15 GPa, respectively. Similar results regarding the mechanical properties of hBN were also presented by several authors in literature [61-64]. In addition, Joy et al. [65] provided an overall review on boron nitride based polymer nanocomposites.

Nanofillers such as nanoparticles and nanoplatelets could alter the direction of crack propagation and thereby stop the crack propagation and crack pinning along the original direction [66], which improves the mechanical performance of the composite system. According to the computational study of Spanos and Anifantis [62], even small volume fractions of boron nitride nano sheet (BNNS) can significantly contribute to the reinforcement of matrix material. The authors pointed out that sufficient interface, matrix stiffness and BNNS size and volume fraction are the critical parameters determining the elastic mechanical properties of BNNS-based nanocomposites. Similiarly, the study of Muralidhara et al. [67] revealed that presence of hBN results in increment in mechanical properties of CF filled epoxy. Moreover, Randhawa and Patel [68] reported that tensile strength and modulus of PA 6 increased by 15.2% and 64.5%, respectively, after the addition of 8 wt.% hBN.

Despite the large number of research on polymer nanocomposites in literature, to the best of our knowledge, merely a few of them discuss the mechanical performance of the composites filled with binary or ternary hybrid reinforcements. Thus, this paper aims to present the tensile and flexural properties of the nanocomposites consisting of PA 66 matrix and glass fiber+MWCNTs-COOH+hBN hybrid fillers. The results obtained in this study are expected to make a contribution to the relevant fields of science and technology in designing high-performance nanocomposites.

2. Experimental

2.1. Composite Constituents

Neat PA 66 and 30 wt.% short fiber reinforced PA 66 (PA 66/30SGF) granules used as matrix materials were purchased from Mat Polymer, Istanbul/Turkey. MWCNTs-COOH with a mass purity of more than 95%, 2.00 wt.% COOH-content, outer diameter from 10 to 20 nm, interior diameter from 5 to 10 nm, length from 10 to 30 μm, were purchased from Ege Nanotek Kimya Sanayi, Izmir/Turkey. hBN with size of 300-400 nm were supplied by the National Boron Research Institute (BOREN), Ankara/Turkey.

2.2. Fabrication Method

Specimen preparation process of hBN integrated PA 66/30SGF hybrid composites are demonstrated in Figure 1 (a) to (g). MWCNTs-COOH and/or hBN integrated composite specimens were also prepared through the same method and instruments. The list of the produced specimens and the labels assigned to them are shown in Table 1.

Table 1. List of the composite specimens

Labels	Specimens
C1	Neat PA 66
C2	PA 66/30SGF
C3	0.4 wt.% MWCNT-COOH integrated PA 66/30SGF
C4	0.4 wt.% hBN integrated PA 66/30SGF
C5	0.2 wt.% MWCNT-COOH + 0.2 wt.% hBN integrated PA 66/30SGF

Firstly, C2 granules were mixed with MWCNTs-COOH and hBN in different beakers and stirred in ethanol for one hour by means of a hot plate magnetic stirrer. After ethanol vaporized, 0.4 wt.% MWCNTs-COOH integrated C2 and 0.4 wt.% hBN integrated C2 granules were obtained. By following the same steps, 0.2 wt.% MWCNTs-COOH + 0.2 wt.% hBN integrated C2 granules were produced. These three types of granules, as well as C1 and C2 granules, were conditioned in an oven at 100 °C for 2 hours and transferred to the plastic injection moulding machine for the production of specimens. During this process, the granules fed to the funnel of the machine proceeded towards the nozzle passing through three hot zones, in which the temperature was approximately 285 °C, via a rotating screw. Owing to this high-temperature and the rotation of the screw in the hot zones, MWCNTs-COOH and hBNs efficiently mixed in C2 matrix.

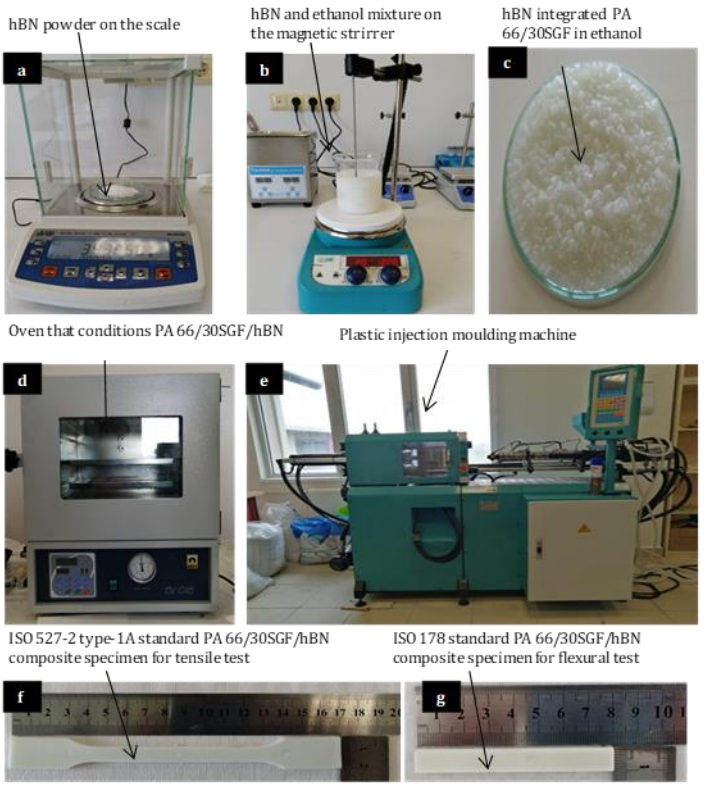

Fig. 1 Preparation process of PA 66/30SGF/hBN composite specimens

2.3. Characterization

During the plastic injection moulding process, five types of composite specimens in accordance with ISO 527-2 type-1A and ISO 178 standards were produced. Tensile and flexural properties of the specimens were analysed using Instron 5982 100 KN (USA) test machine at room temperature with a crosshead speed of 5mm/min. Scanning electron microscopy (SEM) images were obtained in a JSM-7001 F analytical field-emission SEM (Japan). Chemical structures of the specimens were analysed by Perkin Elmer Spectrum Two Fourier transform infrared spectrometer.

3. Results and Discussion

3.1. Surface Characteristics of the Fractured Composite Specimens

Figure 2 (a) to (c) represents the SEM images of the surface morphology of the fractured C3 specimen. Agglomerated MWCNT-COOH can be clearly seen in Figure 2 (b) and (c). When used as reinforcement material, CNTs stretch or bridge across the cracks and absorb the fracture energy; thus, they prevent crack opening and propagation during the fracture. This stretching behaviour of CNTs was monitored in some studies [44, 69, 70]. Moreover, in the hybrid reinforced composite systems where CNTs and fibers are used together as filler material, CNTs can create an interconnecting effect between the fiber and matrix, which leads to improvement in mechanical properties.

Figure 2 (b) demonstrates that MWCNTs-COOH are strongly embedded within C1 matrix, which is the evidence of strong interfacial adhesion between MWCNTs-COOH and the matrix. However, entangled MWCNTs-COOH or agglomerates were also observed in Figure 2 (c). They limit the mobility of PA 66 chains and hence decrease the crystallinity and confinement effect deployed by the MWCNTs-COOH [71, 72]. Despite the presence of embedded MWCNTs-COOH, agglomerated MWCNTs-COOH may cause stress concentrations and act as defects; which may lead to deterioration in mechanical properties.

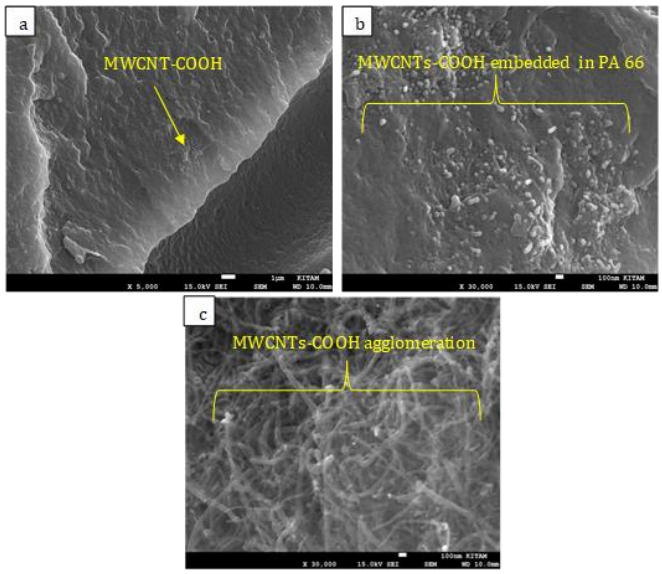

Fig. 2 SEM images of (a) fractured C3; (b) MWCNTs-COOH embedded in C1 matrix; (c) MWCNTs-COOH agglomeration

SEM images of surface morphology of fractured C4 are shown in Figure 3 (a) to (d). There is a certain amount of hBN to absorb the fracture energy and stop the crack propagation and crack pinning [60]. However, as indicated in Figure 3 (d), agglomerated hBN particles may act as defects and thereby contribute to the occurrence of microcracks within the composite system.

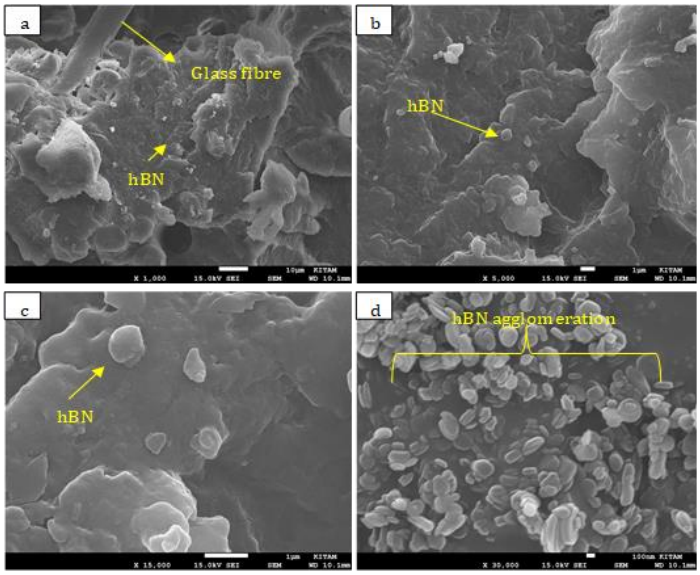

Fig. 3 SEM images of (a) fractured C4; (b) and (c) individual hBN particles; (d) hBN agglomeration

Figure 4 (a) to (c) represent the SEM images of surface morphology of fractured C5 specimen. Agglomerated hBN particles were observed, as shown in Figure 4 (a). Figure 4 (b) and Figure (c) show that MWCNTs-COOH are strongly embedded in PA 66, which indicates that an sufficient surface interaction between MWCNTs-COOH and the PA 66 matrix is achieved. However, Figure 4 (c) demonstrates a few MWCNTs-COOH pull-out probably due to the fracture or poor interfacial interaction between MWCNTs-COOH and PA 66. When the fracture ends, CNTs somewhat close and loosen getting a worm-like form, as shown by yellow arrow in Figure 4 (c). This worm-like form is due to the relaxation or uneven crack propagation [40]. On the other hand, no direct interaction between MWCNT-COOH and hBN was observed.

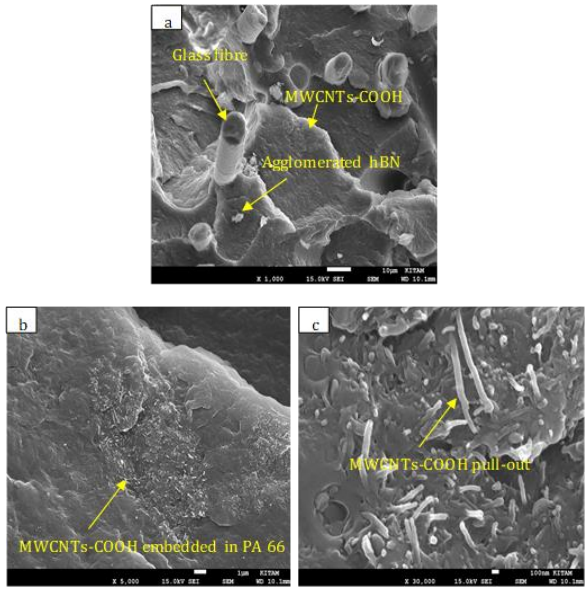

Fig. 4 SEM images of (a) fractured C5; (b) MWCNTs-COOH embedded in PA 66; (c) MWCNTs-COOH pull-out

3.2. Chemical Analysis

Understanding the chemical structure of the components in a material is quite useful so as to achieve good mechanical properties by controlling the process parameters. From Fourier Transform Infrared (FTIR) spectra of the injection-moulded composite specimens, shown in Figure 5, it can be seen that the signature regions do not exhibit a significant difference by the addition of micro- and nano-scale fillers. In neat PA 66, the absorption band at 3267 cm−1 is correlated to the stretching vibrations of N-H group. The absorption bands at 2912 cm−1, 2843 cm−1 and 1192 cm−1 stem from the symmetric and asymmetric C–H stretching vibrations and C–H twisting. The peaks appearing at 1636 cm−1 and 1545 cm−1 are assigned to the stretching vibration of the C=O group of the amide I and the N–H bending and C– N stretching vibration of amide II, respectively. The peak at 1283 cm−1 is associated with C–N–H coupling vibration of amide III. The presence of glass fibers does not bring about a significant change in the molecular structure of PA 66, which could be due to the lack of chemical interaction between glass fibers and PA 66 matrix [63].

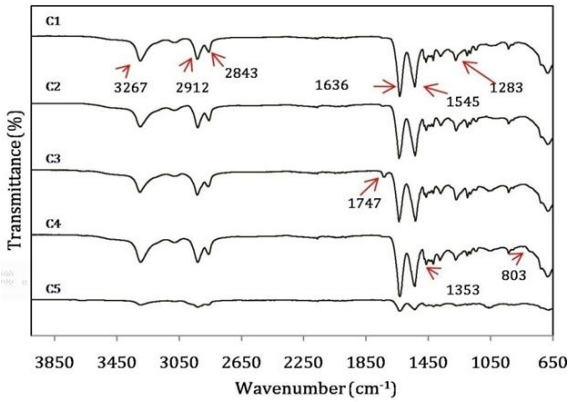

Fig. 5 FTIR spectra of the specimens

In Figure 5 (c), the absorption band at 1747 cm−1 results from C=O symmetric stretching of carboxyl, which confirms the presence of MWCNT-COOH. Similar observations were also made by Al-Hobaib et al. [64] and Chen et al. [26]. And also, considering the observations made by B. Zhang et al. [65], characteristic peaks of hBN at 1353 cm−1 and 803 cm−1 shown in Figure 5 (d) can be correlated to in-plane B-N stretching and out-of-plane B-N bending vibrations of hBN, respectively. The appearance of the characteristic peaks of carboxyl group of MWCNT-COOH and hBN indicates that no chemical reaction occurred during the melting and mixing step of plastic injection process. Therefore, physical interactions alone are likely to be responsible for any change in the mechanical properties of the composite system. Yet, considering the study by Demircan et al. [66], due to the high-temperature (nearly 285°C) in the hot zones of the plastic injection machine chemical interaction at some level might have occurred.

3.3 Tensile Test Results

Load-displacement curves and the tensile-fractured specimens are represented in Figure 6 (a) and (b) respectively. As shown in Figure 6 (c), C2 exhibits the highest tensile strength (87.05 MPa) whereas C5 exhibits the highest elastic modulus (5.17 GPa). The graphs demonstrate that the inclusion of glass fibers improves the tensile strength and elastic modulus of C1. This result is in accordance with the results of relevant studies in literature [10-12, 15, 17]. However, the addition of 0.4 wt.% MWCNTs-COOH into C2 leads to reduction by 28% in tensile strength while increasing the elastic modulus by 14.7%. This failure can be explained by the agglomeration of MWCNTs-COOH in the matrix. Similarly, presence of 0.4 wt.% hBN in C2 increases the elastic modulus by nearly 11.2% and reduces the tensile strength by 20.6%. The findings of some relevant studies in literature support these results [69, 77-80].

Considering the number of similar investigations in literature, it can be claimed that mechanical performance of hybrid composites incorporating ternary fillers has not been fully revealed yet. However, the present study revealed that the addition of MWCNTs-COOH and hBN together increases the elastic modulus of C2 by 15.4% and decreases the tensile strength of it by 13.33%. It is obvious that C3 exhibits better tensile performance over C4. Moreover, the addition of MWCNTs-COOH and hBN together further improves the tensile properties, which indicates that these two nanomaterials are compatible with each other in a ternary-filler polymeric composite system.

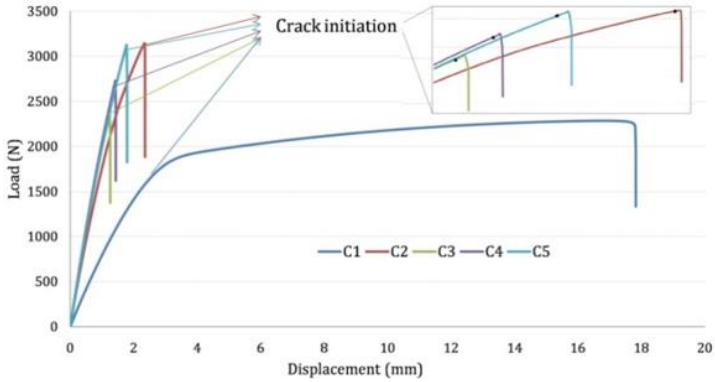

(a)

(b)

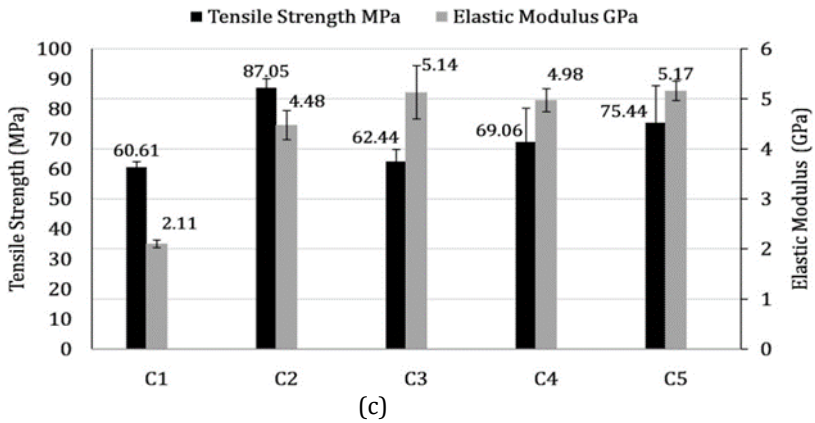

(c)

Fig. 6 (a) Load-displacement curves of the specimens after tensile tests; (b) Tensile-fractured specimens; (c) Tensile properties of the specimens

3.4 Flexural Test Results

Figure 7 (a) and (b) represent the load-displacement curves after 3-point flexural tests and the fractured specimens, respectively. According to the results, shown in Figure (c), C5 exhibits the highest flexural strength (170.48 MPa) and flexural modulus (3.89 GPa) whereas C1 exhibits the lowest flexural strength (65.33 MPa) and flexural modulus (1.07 GPa). It is clear that the presence of short glass fibers enhances the flexural performance of C1. As aforementioned, this improvement can be attributed to the good mechanical properties of glass fibers as well as their homogeneous distribution in the matrix. With the addition of 0.4 wt.% MWCNTs-COOH, flexural strength and flexural modulus of C2 increase by nearly 7% and 13%, respectively. This positive effect can be explained by the fact that

CNTs prevent crack opening and propagation by bridging across the cracks during the fracture. Moreover, they cause an interlocking effect between fibers and matrix and thereby improve the flexural and tensile properties of the composite system.

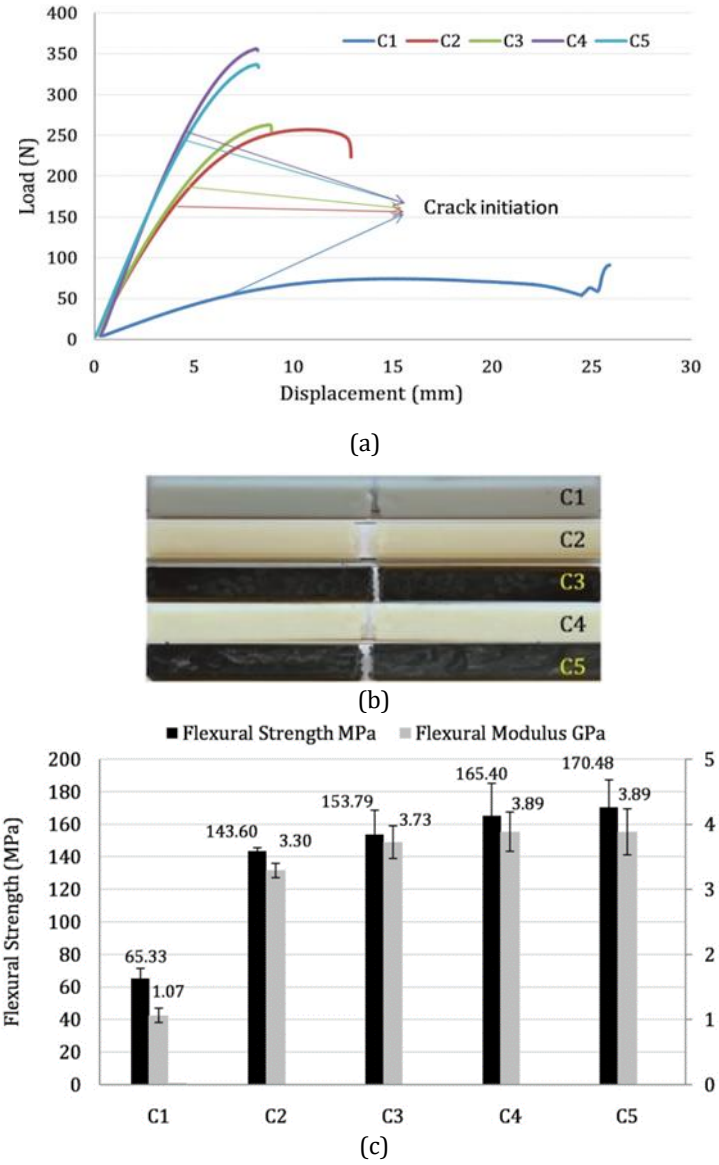

Fig. 7 (a) Load-displacement curves of the specimens after three-point flexural tests; (b) Flexural-fractured specimens; (c) Flexural properties of the specimens

In the present study, 0.4 wt.% hBN integration results in better flexural performance over that with 0.4 wt.% MWCNTs-COOH whereas the composite with 0.2 wt.% MWCNTs-COOH + 0.2 wt.% hBN fillers exhibits the best flexural performance. Since good filler-matrix facial interaction allows the fillers to absorb the fracture energy and thus contributes to the enhancement in mechanical properties, the improvement in flexural properties can be attributed to the good surface interaction between the fillers and the PA

66 matrix. Similar results were obtained and discussed in a number of studies in literature [80, 88].

Figure 8 (a) to (d) represents the optical micrographs of fractured specimens after 3-point flexural tests. Failure modes of the specimens were mainly matrix cracks along the direction of tension. Longer cracks were observed in fractured C2.

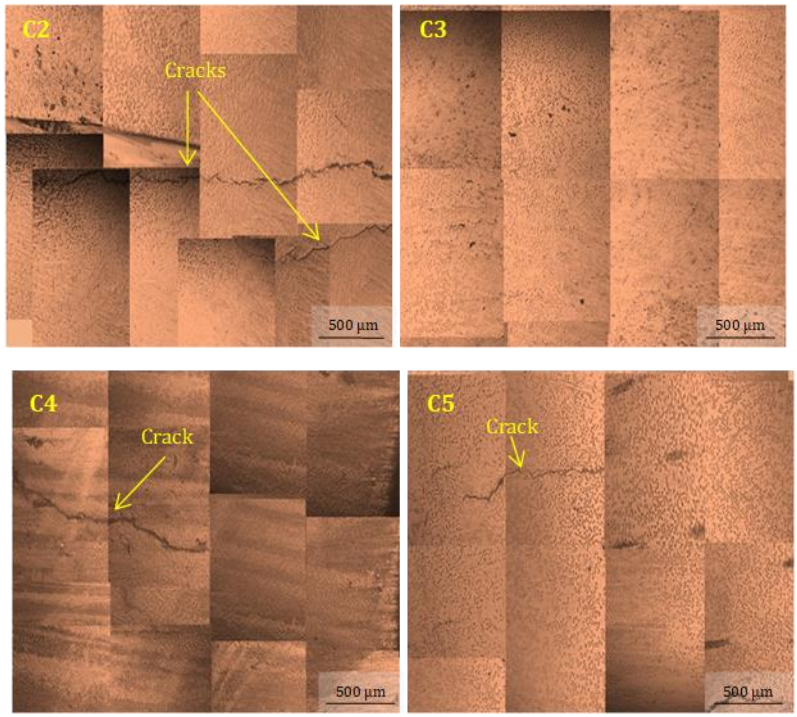

Fig. 8 Optical micrographs of fractured C2, C3, C4 and C5

5. Conclusions

In this study, mechanical properties of MWCNT-COOH and/or hBN integrated PA 66/30SGF composites were investigated. Mechanical analyses showed that the presence of short glass fibers positively influences the tensile and flexural performance of PA 66. This behavior can be explained by good mechanical properties of glass fibers and their sufficient facial interaction with the matrix surface.

The obtained test results demonstrated that the highest tensile strength and elastic modulus were exhibited by PA 66/30SGF and MWCNTs-COOH+hBN integrated PA 66/30SGF composite specimens, respectively. However, it was observed that the addition of MWCNTs-COOH and hBN leads to deterioration in the tensile strength. Since the desired reinforcement highly depends on the uniform stress transfer between the filler and matrix, we can conclude that the external stress applied to the specimens incorporating MWCNTs-COOH was not well distributed along the matrix due to the presence of agglomerates; consequently, the tensile strength decreased.

On the other hand, addition of MWCNTs-COOH and hBN enhanced the flexural properties of PA 66/30SGF composites. Having tubular form, MWCNTs are able to stretch across the cracks absorbing the fracture energy and hence prevent crack opening and propagation.

Besides this bridging phenomenon, MWCNTs can cause interlocking effect between the fiber and matrix and prevent glass fibers from slipping, which improve the mechanical performance of the composite system. hBN particles, on the other hand, can stop crack propagation and crack pinning by changing the direction of crack propagation and hence make a contribution to the mechanical properties. The specimens with 0.4 wt.% hBN exhibit higher mechanical performance than that with 0.4 wt.% MWCNTs-COOH, which might be due to their mechanical and geometrical or morphological differences as well as the difference in their agglomeration tendency. The highest flexural values were found in specimens where MWCNTs-COOH and hBN were integrated together; therefore, we can conclude that the hybrid reinforcement mechanism worked efficiently and that MWCNT-COOH and hBN are compatible with each other. The shorter cracks in MWCNT-COOH and hBN filled PA 66/SGF observed by optical microscopy confirm this conclusion.

FTIR spectra of the specimens confirmed the molecular structure of PA 66 as well as the presence of MWCNT-COOH and hBN in the system. It was also observed that glass fibers do not bring about a drastic change in the chemical structure of PA 66. Although a chemical interaction due to the high temperature applied in the specimen production process might have occurred, since no significant chemical bond was detected, the increase in mechanical properties are dominantly due to the physical interactions.

Considering the increments in elastic modulus, flexural modulus and flexural strength of the specimens, MWCNT and hBN integrated PA 66/glass fiber composites are expected to be quite promising for future applications in which high mechanical performance is required.

Acknowledgement

The authors acknowledge that the fund of this study has been provided by Research fund of Ondokuz Mayıs University Project No: PYO.MUH.1901.18.008.

References

[1] Ching YC, Chuah CH, Ching KY, Abdullah LC, Rahman A. Applications of thermoplastic-based blends. Recent Developments in Polymer Macro, Micro and Nano Blends2017. p. 111-29. https://doi.org/10.1016/B978-0-08-100408-1.00005-4

[2] Europe P. Plastics-the Facts 2020 An analysis of European plastics production, demand and waste data Brussels: Plastics Europe; 2020 [Available from: https://www.plasticseurope.org.

[3] Dynisco. Understanding Plastics and Polymers - The Different Types of Plastic: AZoM; 2019 [Available from: https://www.azom.com/article.aspx?ArticleID=17477 .]

[4] Awaja F, Zhang S, Tripathi M, Nikiforov A, Pugno N. Cracks, microcracks and fracture in polymer structures: Formation, detection, autonomic repair. Progress in Materials Science. 2016;83:536-73. https://doi.org/10.1016/j.pmatsci.2016.07.007

[5] Xanthos M. Polymers and Polymer Composites. Functional Fillers for Plastics. Second ed. 2010. p. 1-18. https://doi.org/10.1002/9783527629848.ch1

[6] Hamerton I. Book Review: Functional Fillers for Plastics. By Marino Xanthos (Ed.). Advanced Materials, 2006;18:248-. https://doi.org/10.1002/adma.200500797

[7] Rangari V. Polymer Nanocomposite Materials for Structural Applications. Advances in Nanocomposites - Synthesis, Characterization and Industrial Applications2011. https://doi.org/10.5772/15615

[8] Chow WS, Mohd Ishak ZA. Polyamide blend-based nanocomposites: A review. Express Polymer Letters. 2015;9(3):211-32. https://doi.org/10.3144/expresspolymlett.2015.22

[9] Gilbert M. Chapter 18 - Aliphatic Polyamides. In: Gilbert M, editor. Brydson's Plastics Materials (Eighth Edition): Butterworth-Heinemann; 2017. p. 487-511. https://doi.org/10.1016/B978-0-323-35824-8.00018-9
[10] Zhou Y, Mallick PK. A non-linear damage model for the tensile behavior of an injection molded short E-glass fiber reinforced polyamide-6,6. Materials Science and Engineering: A. 2005;393(1):303-9. https://doi.org/10.1016/j.msea.2004.10.038
[11] Javangula S, Ghorashi B, Draucker CC. Mixing of glass fibers with nylon 6,6. Journal of Materials Science. 1999;34(20):5143-51. https://doi.org/10.1023/A:1004777520458
[12] Srivastava VK, Lal S. Mechanical properties of E-glass fiber reinforced nylon 6/6 resin composites. Journal of Materials Science. 1991;26(24):6693-8. https://doi.org/10.1007/BF0240266
[13] Kagan V, McPherson R, Chung J. An Advanced High Modulus (HMG) Short Glass-Fiber Reinforced Nylon 6: Part I - Role and Kinetic of FiberGlass Reinforcements. Journal of Reinforced Plastics and Composites. 2003; 22:1035-44. https://doi.org/10.1177/0731684403023285
[14] Çuvalci H, Erbay K, İpek H. Investigation of the Effect of Glass Fiber Content on the Mechanical Properties of Cast Polyamide. Arabian Journal for Science and Engineering. 2014;39(12):9049-56. https://doi.org/10.1007/s13369-014-1409-8
[15] Lingesh BV, Rudresh BM, Ravikumar BN. Effect of Short Glass Fibers on Mechanical Properties of Polyamide66 and Polypropylene (PA66/PP) Thermoplastic Blend Composites. Procedia Materials Science. 2014;5:1231-40. https://doi.org/10.1016/j.mspro.2014.07.434
[16] Kim J-W, Kim H-S, Lee D-G. Tensile Strength of Glass Fiber-Reinforced Plastic by Fiber Orientation and Fiber Content Variations. International Journal of Modern Physics: Conference Series. 2012;06:640-5. https://doi.org/10.1142/S201019451200390X
[17] Autay R, Mars J, Fakhreddine D. Mechanical and tribological study of short glass fiber-reinforced PA 66. Polymers and Polymer Composites. 2019;27. https://doi.org/10.1177/0967391119853956
[18] Nuruzzaman DM, Iqbal AKMA, Oumer AN, Ismail NM, Basri S. Experimental investigation on the mechanical properties of glass fiber reinforced nylon. IOP Conference Series: Materials Science and Engineering. 2016;114. https://doi.org/10.1088/1757-899X/114/1/012118
[19] Yu MF, Lourie O, Dyer MJ, Moloni K, Kelly TF, Ruoff RS. Strength and breaking mechanism of multiwalled carbon nanotubes under tensile load. Science. 2000;287(5453):637-40. https://doi.org/10.1126/science.287.5453.637
[20] Salvetat J-P, Briggs G, Bonard J-M, Bacsa R, Kulik A, Stöckli T, et al. Elastic and Shear Moduli of Single-Walled Carbon Nanotube Ropes. Physical Review Letters. 1999;82(5):944-7. https://doi.org/10.1103/PhysRevLett.82.944
[21] Arash B, Wang Q, Varadan VK. Mechanical properties of carbon nanotube/polymer composites. Sci Rep. 2014;4:6479. https://doi.org/10.1038/srep06479
[22] Sahoo NG, Rana S, Cho JW, Li L, Chan SH. Polymer nanocomposites based on functionalized carbon nanotubes. Progress in Polymer Science. 2010;35(7):837-67. https://doi.org/10.1016/j.progpolymsci.2010.03.002
[23] Tarfaoui M, Lafdi K, El Moumen A. Mechanical properties of carbon nanotubes based polymer composites. Composites Part B: Engineering. 2016;103:113-21. https://doi.org/10.1016/j.compositesb.2016.08.016
[24] Moniruzzaman M, Chattopadhyay J, Billups WE, Winey KI. Tuning the mechanical properties of SWNT/nylon 6,10 composites with flexible spacers at the interface. Nano Lett. 2007;7(5):1178-85. https://doi.org/10.1021/nl062868e
[25] Coleman JN, Khan U, Blau WJ, Gun'ko YK. Small but strong: A review of the mechanical properties of carbon nanotube-polymer composites. Carbon. 2006;44(9):1624-52. https://doi.org/10.1016/j.carbon.2006.02.038

[26]Jin F-L, Park S-J. A review of the preparation and properties of carbon nanotubes-reinforced polymer compositess. Carbon letters. 2011;12(2):57-69. https://doi.org/10.5714/CL.2011.12.2.057
[27]Chen T, Liu H, Wang X, Zhang H, Zhang X. Properties and Fabrication of PA66/Surface-Modified Multi-Walled Nanotubes Composite Fibers by Ball Milling and Melt-Spinning. Polymers (Basel). 2018;10(5). https://doi.org/10.3390/polym10050547
[28]Hassani AJ, Mohd Ishak ZA, Mohamed AR. Preparation and characterization of polyamide 6 nanocomposites using MWCNTs based on bimetallic Co-Mo/MgO catalyst. Express Polymer Letters. 2014;8(3):177-86. https://doi.org/10.3144/expresspolymlett.2014.21
[29]Zhang J, Gao X, Zhang X, Liu H, Zhang H, Zhang X. Polyamide 66 and amino-functionalized multi-walled carbon nanotube composites and their melt-spun fibers. Journal of Materials Science. 2019;54(16):11056-68. https://doi.org/10.1007/s10853-019-03619-0
[30]Spitalsky Z, Tasis D, Papagelis K, Galiotis C. Carbon nanotube-polymer composites: Chemistry, processing, mechanical and electrical properties. Progress in Polymer Science. 2010;35(3):357-401. https://doi.org/10.1016/j.progpolymsci.2009.09.003
[31]Khan W, Sharma R, Saini P. Carbon Nanotube-Based Polymer Composites: Synthesis, Properties and Applications. Carbon Nanotubes - Current Progress of their Polymer Composites2016. https://doi.org/10.5772/62497
[32]Zabegaeva ON, Sapozhnikov DA, Buzin MI, Krestinin AV, Kotelnikov VA, Baiminov BA, et al. Nylon-6 and single-walled carbon nanotubes polyamide composites. High Performance Polymers. 2016;29(4):411-21. https://doi.org/10.1177/0954008316645848
[33]Song Y, Zheng N, Dong X, Gao J. Flexible Carboxylated CNT/PA66 Nanofibrous Mat Interleaved Carbon Fiber/Epoxy Laminates with Improved Interlaminar Fracture Toughness and Flexural Properties. Industrial & Engineering Chemistry Research. 2020;59(3):1151-8. https://doi.org/10.1021/acs.iecr.9b05854
[34]Kumar A, Sharma K, Dixit AR. A review on the mechanical properties of polymer composites reinforced by carbon nanotubes and graphene. Carbon Letters. 2021;31(2):149-65. https://doi.org/10.1007/s42823-020-00161-x
[35]Kang S, Kim J, Park JH, Jung I, Park M. Multiwalled carbon nanotube pretreatment to enhance tensile properties, process stability, and filler dispersion of polyamide 66 nanocomposites. Composites Part B: Engineering. 2020;198:108204. https://doi.org/10.1016/j.compositesb.2020.108204
[36]Miyagawa H, Misra M, Mohanty AK. Mechanical properties of carbon nanotubes and their polymer nanocomposites. J Nanosci Nanotechnol. 2005;5(10):1593-615. https://doi.org/10.1166/jnn.2005.181
[37]Coleman JN, Khan U, Gun'ko YK. Mechanical Reinforcement of Polymers Using Carbon Nanotubes. Advanced Materials. 2006;18(6):689-706. https://doi.org/10.1002/adma.200501851
[38]Gorga RE, Lau KKS, Gleason KK, Cohen RE. The importance of interfacial design at the carbon nanotube/polymer composite interface. Journal of Applied Polymer Science. 2006;102(2):1413-8. https://doi.org/10.1002/app.24272
[39]Gupta AK, Harsha SP. Effect of crack and determination of fracture energy of carbon nanotube-reinforced polymer composites. Proceedings of the Institution of Mechanical Engineers, Part N: Journal of Nanoengineering and Nanosystems. 2014;229(3):110-6. https://doi.org/10.1177/1740349914531758
[40]Shindo Y, Kuronuma Y, Takeda T, Narita F, Fu S-Y. Electrical resistance change and crack behavior in carbon nanotube/polymer composites under tensile loading. Composites Part B: Engineering. 2012;43(1):39-43. https://doi.org/10.1016/j.compositesb.2011.04.028

[41]Kuronuma Y, Shindo Y, Takeda T, Narita F. Crack growth characteristics of carbon nanotube-based polymer composites subjected to cyclic loading. Engineering Fracture Mechanics. 2011;78(17):3102-10. https://doi.org/10.1016/j.engfracmech.2011.09.006
[42]Kuronuma Y, Shindo Y, Takeda T, Narita F. Fracture behaviour of cracked carbon nanotube-based polymer composites: Experiments and finite element simulations. Fatigue & Fracture of Engineering Materials & Structures. 2010;33(2):87-93. https://doi.org/10.1111/j.1460-2695.2009.01419.x
[43]Ajayan PM, Schadler L, Giannaris C, Rubio A. Single-walled carbon nanotube-polymer COMPOSITES: Strength and weakness. Advanced Materials. 2000;12:750-+. https://doi.org/10.1002/(SICI)1521-4095(200005)12:10<750::AID-ADMA750>3.0.CO;2-6
[44]Liu T, Phang IY, Shen L, Chow SY, Zhang W-D. Morphology and mechanical properties of multiwalled carbon nanotubes reinforced nylon-6 composites. Macromolecules. 2004;37(19):7214-22. https://doi.org/10.1021/ma049132t
[45]Zhang W, Shen L, Phang I, Liu T. Carbon Nanotubes Reinforced Nylon6 Composite Prepared by Simple Melt-Compounding. Macromolecules. 2004;37:256-9. https://doi.org/10.1021/ma035594f
[46]Ferreira T, Paiva MC, Pontes AJ. Dispersion of carbon nanotubes in polyamide 6 for microinjection moulding. Journal of Polymer Research. 2013;20(11). https://doi.org/10.1007/s10965-013-0301-7
[47]Jogi BF, Sawant M, Kulkarni M, Brahmankar PK. Dispersion and Performance Properties of Carbon Nanotubes (CNTs) Based Polymer Composites: A Review. Journal of Encapsulation and Adsorption Sciences. 2012;02(04):69-78. https://doi.org/10.4236/jeas.2012.24010
[48]Pötschke P, Bhattacharyya AR, Janke A, Pegel S, Leonhardt A, Täschner C, et al. Melt Mixing as Method to Disperse Carbon Nanotubes into Thermoplastic Polymers. Fullerenes, Nanotubes and Carbon Nanostructures. 2005;13(sup1):211-24. https://doi.org/10.1081/FST-200039267
[49]Kim SW, Kim T, Kim YS, Choi HS, Lim HJ, Yang SJ, et al. Surface modifications for the effective dispersion of carbon nanotubes in solvents and polymers. Carbon. 2012;50(1):3-33. https://doi.org/10.1016/j.carbon.2011.08.011
[50]Wise KE, Park C, Siochi EJ, Harrison JS. Stable dispersion of single wall carbon nanotubes in polyimide: the role of noncovalent interactions. Chemical Physics Letters. 2004;391(4-6):207-11. https://doi.org/10.1016/j.cplett.2004.04.096
[51]Ma P-C, Siddiqui NA, Marom G, Kim J-K. Dispersion and functionalization of carbon nanotubes for polymer-based nanocomposites: A review. Composites Part A: Applied Science and Manufacturing. 2010;41(10):1345-67. https://doi.org/10.1016/j.compositesa.2010.07.003
[52]Banerjee J, Dutta K. Melt-mixed carbon nanotubes/polymer nanocomposites. Polymer Composites. 2019;40(12):4473-88. https://doi.org/10.1002/pc.25334
[53]Chopra S, Deshmukh KA, Deshmukh AD, Peshwe DR. Functionalization and Melt-compounding of MWCNTs in PA-6 for Tribological Applications. IOP Conference Series: Materials Science and Engineering. 2018;346. https://doi.org/10.1088/1757-899X/346/1/012005
[54]Raman C, Meneghetti P. Boron nitride finds new applications in thermoplastic compounds. Plastics, Additives and Compounding. 2008;10:26-31. https://doi.org/10.1016/S1464-391X(08)70092-8
[55]Zhang Z, Liu Y, Yang Y, Yakobson BI. Growth Mechanism and Morphology of Hexagonal Boron Nitride. Nano Lett. 2016;16(2):1398-403. https://doi.org/10.1021/acs.nanolett.5b04874

[56]Nag A, Raidongia K, Hembram KPSS, Datta R, Waghmare UV, Rao CNR. Graphene Analogues of BN: Novel Synthesis and Properties. ACS Nano. 2010;4(3):1539-44. https://doi.org/10.1021/nn9018762
[57]Golberg D, Bando Y, Terao T, Mitome M, Tang C, Zhi C. Boron Nitride Nanotubes and Nanosheets. ACS nano. 2010;4:2979-93. https://doi.org/10.1021/nn1006495
[58]Peng Q, Ji W, De S. Mechanical properties of the hexagonal boron nitride monolayer: Ab initio study. Computational Materials Science. 2012;56:11-7. https://doi.org/10.1016/j.commatsci.2011.12.029
[59]Rasul MG, Kiziltas A, Arfaei B, Shahbazian-Yassar R. 2D boron nitride nanosheets for polymer composite materials. npj 2D Materials and Applications. 2021;5(1):56. https://doi.org/10.1038/s41699-021-00231-2
[60]Mortazavi B, Cuniberti G. Mechanical properties of polycrystalline boron-nitride nanosheets. RSC Adv. 2014;4(37):19137-43. https://doi.org/10.1039/C4RA01103A
[61]Li N, Ding N, Qu S, Liu L, Guo W, Wu C-ML. Mechanical properties and failure behavior of hexagonal boron nitride sheets with nano-cracks. Computational Materials Science. 2017;140:356-66. https://doi.org/10.1016/j.commatsci.2017.09.011
[62]Spanos KN, Anifantis NK. Mechanical characterization of hexagonal boron nitride nanocomposites: A multiscale finite element prediction. Journal of Composite Materials. 2017;52(16):2229-41. https://doi.org/10.1177/0021998317740942
[63]Qi-lin X, Zhen-huan L, Xiao-geng T. The defect-induced fracture behaviors of hexagonal boron-nitride monolayer nanosheets under uniaxial tension. Journal of Physics D: Applied Physics. 2015;48(37). https://doi.org/10.1088/0022-3727/48/37/375502
[64]Zhao S, Xue J. Mechanical properties of hybrid graphene and hexagonal boron nitride sheets as revealed by molecular dynamic simulations. Journal of Physics D: Applied Physics. 2013;46(13). https://doi.org/10.1088/0022-3727/46/13/135303
[65]Joy J, George E, Haritha P, Thomas S, Anas S. An overview of boron nitride based polymer nanocomposites. Journal of Polymer Science. 2020;58(22):3115-41. https://doi.org/10.1002/pol.20200507
[66]Sun L, Gibson RF, Gordaninejad F, Suhr J. Energy absorption capability of nanocomposites: A review. Composites Science and Technology. 2009;69(14):2392-409. https://doi.org/10.1016/j.compscitech.2009.06.020
[67]Muralidhara B, Babu SPK, Suresha B. Studies on mechanical, thermal and tribological properties of carbon fiber-reinforced boron nitride-filled epoxy composites. High Performance Polymers. 2020;32(9):1061-81. https://doi.org/10.1177/0954008320929396
[68]Randhawa KS, Patel AD. Enhancing tribo-mechanical properties and thermal stability of nylon 6 by hexagonal boron nitride fillers. e-Polymers. 2020;20(1):733-45. https://doi.org/10.1515/epoly-2020-0069
[69]Puch F, Hopmann C. Morphology and tensile properties of unreinforced and short carbon fiber reinforced Nylon 6/multiwalled carbon nanotube-composites. Polymer. 2014;55(13):3015-25. https://doi.org/10.1016/j.polymer.2014.04.052
[70]Qian D, Dickey EC, Andrews R, Rantell T. Load transfer and deformation mechanisms in carbon nanotube-polystyrene composites. Applied Physics Letters. 2000;76(20):2868-70. https://doi.org/10.1063/1.126500
[71]Chen J-y, Mao X-p, Wang G-w. Mechanical Properties of MWCNTs/PA66 Composites under Impact Loading. DEStech Transactions on Engineering and Technology Research. 2017. https://doi.org/10.12783/dtetr/ameme2016/577
[72]Reza Sanei SH, Drozynski H, Hetrick D, editors. Effect of Strain Rate on Tensile Properties of Injection Molded Multiwall Carbon Nanotube Reinforced PA 6/6 Nanocomposites. ASME 2020 International Mechanical Engineering Congress and Exposition; 2020. V003T03A015. https://doi.org/10.1115/IMECE2020-23049
[73]Lakkur Munirajappa M, Harijan Basavaraju R. Microstructural characterization of short glass fiber and PAN based carbon fiber reinforced nylon 6 polymer composites.

Polymer Engineering & Science. 2018;58(8):1428-37. https://doi.org/10.1002/pen.24737
[74]Al-Hobaib AS, Al-Sheetan KM, Shaik MR, Al-Suhybani MS. Modification of thin-film polyamide membrane with multi-walled carbon nanotubes by interfacial polymerization. Applied Water Science. 2017;7(8):4341-50. https://doi.org/10.1007/s13201-017-0578-5
[75]Zhang B, Wu Q, Yu H, Bulin C, Sun H, Li R, et al. High-Efficient Liquid Exfoliation of Boron Nitride Nanosheets Using Aqueous Solution of Alkanolamine. Nanoscale Research Letters. 2017;12(1):596. https://doi.org/10.1186/s11671-017-2366-4
[76]Demircan O, Al-darkazali A, Inanc I, Eskizeybek V. Investigation of the effect of CNTs on the mechanical properties of LPET/glass fiber thermoplastic composites. Journal of Thermoplastic Composite Materials. 2019;33:089270571983310. https://doi.org/10.1177/0892705719833105
[77]Mahmood N, Islam M, Hameed A, Saeed S, Khan AN. Polyamide-6-based composites reinforced with pristine or functionalized multi-walled carbon nanotubes produced using melt extrusion technique. Journal of Composite Materials. 2013;48(10):1197-207. https://doi.org/10.1177/0021998313484779
[78]Meng H, Sui GX, Fang PF, Yang R. Effects of acid- and diamine-modified MWNTs on the mechanical properties and crystallization behavior of polyamide 6. Polymer. 2008;49(2):610-20. https://doi.org/10.1016/j.polymer.2007.12.001
[79]Chan KW, Wong HM, Yeung KWK, Tjong SC. Polypropylene Biocomposites with Boron Nitride and Nanohydroxyapatite Reinforcements. Materials (Basel). 2015;8(3):992-1008. https://doi.org/10.3390/ma8030992
[80]Ayrilmis N, Dundar T, Kaymakci A, Ozdemir F, Kwon JH. Mechanical and thermal properties of wood-plastic composites reinforced with hexagonal boron nitride. Polymer Composites. 2014;35(1):194-200. https://doi.org/10.1002/pc.22650
[81]Goriparthi BK, Naveen PNE, Ravi Sankar H, Ghosh S. Effect of functionalization and concentration of carbon nanotubes on mechanical, wear and fatigue behaviours of polyoxymethylene/carbon nanotube nanocomposites. Bulletin of Materials Science. 2019;42(3). https://doi.org/10.1007/s12034-019-1746-z
[82]Nguyen-Tran HD, Hoang VT, Do VT, Chun DM, Yum YJ. Effect of Multiwalled Carbon Nanotubes on the Mechanical Properties of Carbon Fiber-Reinforced Polyamide-6/Polypropylene Composites for Lightweight Automotive Parts. Materials (Basel). 2018;11(3). https://doi.org/10.3390/ma11030429
[83]Mathur RB, Pande S, Singh BP, Dhami TL. Electrical and mechanical properties of multi-walled carbon nanotubes reinforced PMMA and PS composites. Polymer Composites. 2008;29(7):717-27. https://doi.org/10.1002/pc.20449
[84]Panchagnula KK, Kuppan P. Improvement in the mechanical properties of neat GFRPs with multi-walled CNTs. Journal of Materials Research and Technology. 2019;8(1):366-76. https://doi.org/10.1016/j.jmrt.2018.02.009
[85]Prolongo SG, Gude MR, Ureña A. Improving the flexural and thermomechanical properties of amino-functionalized carbon nanotube/epoxy composites by using a pre-curing treatment. Composites Science and Technology. 2011;71(5):765-71. https://doi.org/10.1016/j.compscitech.2011.01.028
[86]Salmoria GV, Paggi RA, Lago A, Beal VE. Microstructural and mechanical characterization of PA12/MWCNTs nanocomposite manufactured by selective laser sintering. Polymer Testing. 2011;30(6):611-5. https://doi.org/10.1016/j.polymertesting.2011.04.007
[87]Koilraj TT, Kalaichelvan K. Experimental Study on Mechanical Properties of PA66 Blended with MWNTs. Applied Mechanics and Materials. 2015;766-767:383-8. https://doi.org/10.4028/www.scientific.net/AMM.766-767.383

[88]Zhou W, Zuo J, Zhang X, Zhou A. Thermal, electrical, and mechanical properties of hexagonal boron nitride-reinforced epoxy composites. Journal of Composite Materials. 2013;48(20):2517-26. https://doi.org/10.1177/0021998313499953

Research on Engineering Structures & Materials
journal homepage: http://www.jresm.org
Research Group

Research Article

Mechanical and durability characterization of hybrid fibre reinforced green geopolymer concrete

Kadarkarai Arunkumar[*1,a], Muthiah Muthukannan[1,b], Arunachalam Sureshkumar[1,c], Arunasankar Chithambarganesh[2,d], Rangaswamy Kanniga Devi R[3,e]

[1] *Department of Civil Engineering, Kalasalingam Academy of Research and Education, India.*
[2] *Department of Civil Engineering, Sree Vidya Nikethan Engineering College, Tirupati, India.*
[3] *Department of Computer Science and Engineering, Kalasalingam Academy of Research and Education, India.*

Article Info

Article history:
Received 16 Apr 2021
Revised 06 Oct 2021
Accepted 03 Nov 2021

Keywords:

Green Geopolymer Concrete;
Wood Waste Ash;
Water Absorption;
Electrical Resistivity;
Waste Utilization

Abstract

Finding a suitable waste utilization approach to produce a cleaner environment is the most crucial aspect globally. Geopolymer is the most promising alternate for cement and source for major waste utilization. Disposal of waste rubber tires is a challenging task for the cleaner environment. Hence, abundant wastes, which create environmental pollution, such as wood waste ash and waste rubber, are used to invent the green geopolymer concrete in this research. The geopolymer is uncomfortable with carrying impact energy, ductility, and energy absorption. Fibre addition could enhance the above properties. Waste wood ash is replaced by 30 percent with fly ash. This research assesses the individual effect of adding polypropylene and rubber fibre by 0, 0.5%, 1%, 1.5%, and 2% of volume fractions. In addition, the effects of fibre hybridization on the mechanical and durability characteristics of green geopolymer concrete have also been analyzed. The study finds the maximum performance in mechanical and durability behaviors with the mix having 0.5% PP and 0.5% rubber. The microstructure characteristics are also assessed using SEM for understanding the phase development in green geopolymer concrete. The research hypothesis proves that an intellectual approach is made to utilize the waste materials such as rubber and waste wood ash in the invention of green geopolymer concrete, which can help to eliminate the environmental impact and can act as a sustainable concrete.

1. Introduction

An amorphous form of polymer (i.e., Geopolymer) was made in nature by dissolving silica and alumina from raw materials such as fly ash, metakaolin, and slag with extremely concentrated alkaline hydroxide and silicate solution [1]. Most of the researchers used fly ash as the binder for the production of geopolymer concrete [2–10]. Fly ash-based geopolymer concrete requires heat curing of 60^0C for 24hrs and needs a high alkaline solution to achieve the characteristic strength [11,12]. The molarity of NaOH played a vital role in the enhancement of GPC strength. The geopolymerization was formed easily with the molarity up to 12, whereas it was disrupted with the increased molarity beyond 12M. The geopolymer concrete with up to 12M promoted silica and alumina dissolution from raw materials [13]. The strength reduction was noted with the molarity exceeds 12M [8]. According to the fly ash production and use in 2017, while production fell to 169.25Mt, use increased to 107.10Mt. The demand for fly ash in forthcoming years was enlarged to high [14]. Hence, the researchers needed to find the alternate raw material to reduce the

*Corresponding author: arunapcivil@gmail.com
[a] orcid.org/0000-0002-5745-6864; [b] orcid.org/0000-0003-1912-3513; [c] orcid.org/0000-0001-9406-2576; [d] orcid.org/0000-0001-5004-4587; [e] orcid.org/0000-0001-6288-5607
DOI: http://dx.doi.org/10.17515/resm2021.280ma1604

amount of fly ash utilization in geopolymer concrete. GGBS (Ground Granulated Blast furnace Slag), which has high calcium, was used as alternate source material for fly ash [15]. In GGBS, the high calcium was the threat that could take the alkaline compounds for producing the geopolymer reaction at earlier ages [16]. The formation of the geopolymeric reaction enhanced the strength at an early age. However, the silica and alumina were left unreacted with the disruption of calcium [17,18]. The reaction of silica and alumina with an alkaline solution was also a vital chemical formation in the geopolymer formation [19]. If the reaction was not formed properly, the alkali-silica expansion was formed on the prolonged ages. Therefore, the raw material with less calcium which requires a lower alkaline activator might be the solution. Moreover, the raw material with inbuilt alkaline compounds (K_2O) [20] was also suggested to substitute the fly ash.

The wood waste ash with inbuilt potassium composition was used as a binder material in conventional concrete, enhancing strength slightly [21]. Waste woods procured from timber industries are used to fuel food production in roadside hotels [21]. The wastes were burnt in the boiler but not limiting the temperature and resulted in the production of flyable ash [22]. The ash derived from the available local hotels was thrown into landfills, polluting the environment equally to global warming [23]. The chemical composition of wood ash was analyzed and showed the presence of potassium oxide in the inside matrix of wood ash [24]. Biomass Wood Ash was used to produce the geopolymer concrete, and it was limited to 10 percent due to the uncertainty of later age geopolymer reaction [25]. High Calcium wood ash was used as an aluminosilicate source material to produce geopolymer concrete, resulting in reduced strength in later ages due to high calcium [26]. When partially substituted, the waste wood ash with less calcium could be a promising binder material [27]. Hence, the waste wood ash procured from nearby hotels with less calcium was partially substituted for fly ash in this research to invent green geopolymer concrete.

Geopolymer concrete was weak in brittle, ductile, impact energy and energy absorption. The major solution invented for improving the above-mentioned properties of geopolymer was the incorporation of fibres within the specified limit. Incorporation of any type fibres had its capability of enhancing the properties. However, there was a specified limit of 2% of volume fraction for the incorporation of any type fibre. The most used type of low modulus fibre was polypropylene fibre which helped to enhance the bonding effect and first crack load. Due to its surface texture and bonding capacity, polypropylene fibre was chosen [28]. The flexural strength and toughness were increased with the addition of polypropylene fibre, and also it limits the deformation due to shrinkage. Meanwhile, the incorporation of polypropylene enhanced the impact strength of geopolymer concrete by 6.25 percent [29,30]. Ductility was increased, and the degree of compression was reduced by incorporating polypropylene [31]. Moreover, polypropylene fibre was specialized in limiting crack formation and propagation [32]. Enhancement in resisting the crack formation was observed with the 0.5 percent PP fibre addition [33]. However, the enhancement in the crack resistance and mechanical properties of GPC by incorporating polypropylene fibre was not efficient in using the GPC in heavy-loaded structural elements. Hence, hybridization of two or more different types of fibres could be adopted to improve the impact and energy absorption of GPC. This study aimed to choose one of the low modulus fibre which could enhance the GPC performances to use it in heavy loaded members.

Dumping waste rubber tires led to the formation of bacteria and fungus [34]. The burning of waste rubber tires produced some toxic gases, which led to death [35]. In the meantime, the burning of rubber tires releases an eminent amount of carbon di-oxides [36], and some developing countries banned it. Hence, disposal of that waste rubber tire was a challenging task for the cleaner environment. Awareness on utilizing waste rubber tires in concrete

composites was increased, and it was used as a filler material and coarse aggregate [37]. Crumped rubber was replaced by 15percent with fine aggregate, which enhanced better performance; however, it reduces the compressive strength [36]. The strength reduction was due to the high amount of replacement of rubber tires. Hence, the addition of rubber as fibre instead of replacement, can be appropriate in the effective utilization of waste rubber [38]. The mechanical and durability properties were enhanced with the incorporation of rubber fibre [39]. Meanwhile, the increased amount of rubber fibre decreased the compressive strength of GPC, and enhancement in energy absorption was observed with the rubber addition [40,41]. The impact strength of GPC was also enhanced with the incorporation of rubber fibre, which can retain the plastic state [42]. The incorporation of rubber fibre was limited to a smaller volume fraction, which could also increase the mechanical properties of GPC [43]. There was a research gap on utilizing the rubber as a fibre with a smaller volume fraction in this study. Further, a combination of both PP and rubber fibre could allow enhancing the properties of GPC in all aspects to use in heavy-loaded structural elements [44].

In the author's previous study [45], the ratio of aluminosilicate binder materials, molarity optimization, and alkaline activators to binder ratio optimization was done. Hence the effect of individual fire addition on the mechanical properties of green geopolymer concrete was studied in this research. In addition, the effects of the hybridization of polypropylene and rubber fibre on the mechanical characteristics of green geopolymer concrete were investigated. Further, microstructural characterization analysis of hybrid fibre reinforced green geopolymer concrete was assessed by SEM.

2. Material Properties

In this research, Fly Ash (FA) derived from the thermal power plant station situated in Neyveli, was used as the raw binder [45]. Energy Dispersive X-Ray analysis was performed to find the chemical compounds present in the fly ash, as shown in figure 1, and also to define the class of fly ash type [46]. Standard ASTM procedures were followed to find the physical characters of FA [47]. The substitute raw material for FA was waste wood ash collected from the nearby hotels [48]. Figure 2 illustrates the Energy Dispersive X-Ray analysis performed to find the chemical compounds present in the waste wood ash and define the calcium present in the low calcium waste wood ash (LCWA) [26]. The composition of LCWA was found in EDX, which has 14.5% of K2O, which could help to reduce the requirement of alkaline solution [20] [24]. The required physical properties of constituent materials are illustrated in Table 1.

Table 1. Physical characteristics of the constituents

Properties / Constituents	Consistency	Initial Setting Time	Final Setting Time	Fineness Modulus	Specific Gravity
Fly ash	38%	18.00	36.00	6%	2.3
Waste Wood ash	58%	2.30	3.00	9%	1.7
Fine Aggregate	-	-	-	2.91	2.62
Coarse Aggregate	-	-	-	7.6	2.42
NaOH	-	-	-	-	1.61
Na_2SiO_3	-	-	-	-	1.47

In this research, fine aggregate and coarse aggregate [49] were also used, and their properties were tabulated in Table 1. The optimal size of FA and CA used in this study was

1.18mm and 10mm. Further polypropylene fibre and waste tire rubber fibre of length 20mm was added individually by 0%, 0.5%, 1%, 1.5% and 2% of volume fraction [50]. Hybridization of polypropylene and rubber fibre was also done by varying 0, 0.25, 0.5, 0.75, and 1% volume fraction. Table 2 lists the chemical compounds present in the FA and LCWA.

Table 2. Chemical composition of fly ash and LCWA [48]

Chemical compound	% by Mass	
	LCWA	FA
Al_2O_3	0.6	17.4
SiO_2	8.01	23.6
K_2O	14.49	0.9
CaO	3.61	1.8
Fe_2O_3	-	1.99
MgO	3.02	60
Gd	0.51	-
P_2O_5	3.06	-
TiO_2	-	0.99
MnO	-	-
C	10.22	2.99

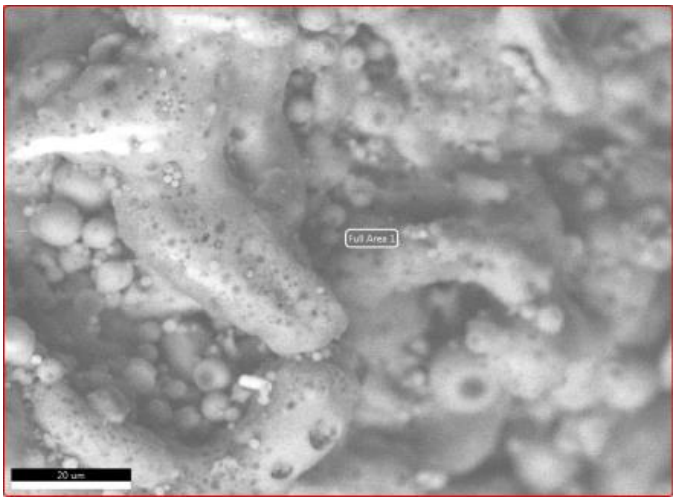

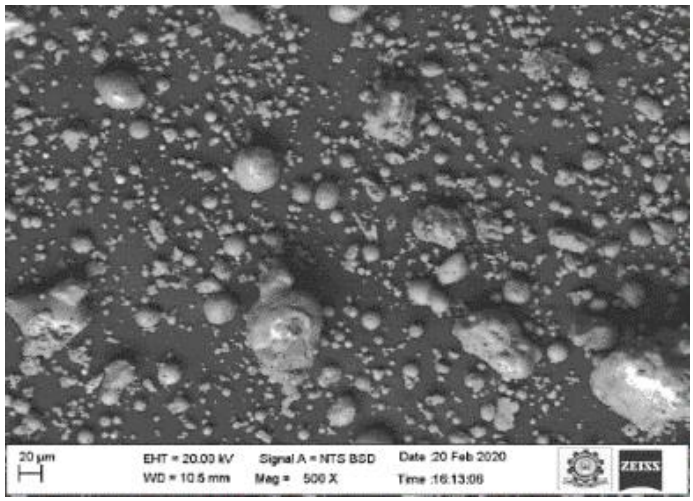

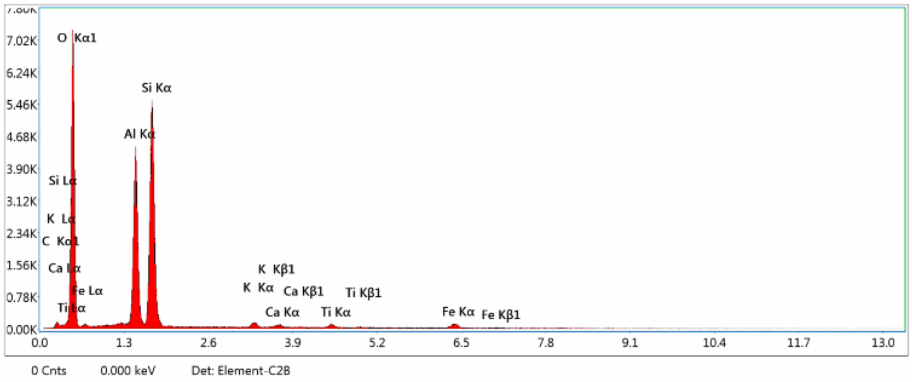

Fig. 1 Microstructure analysis of FA through SEM and EDX

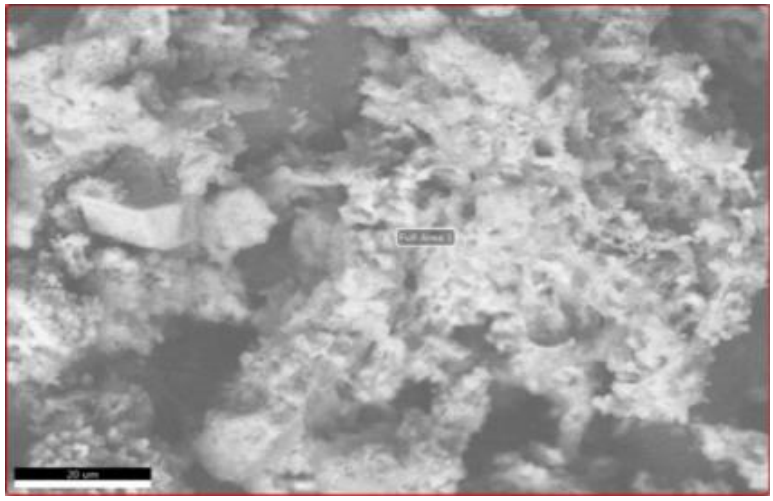

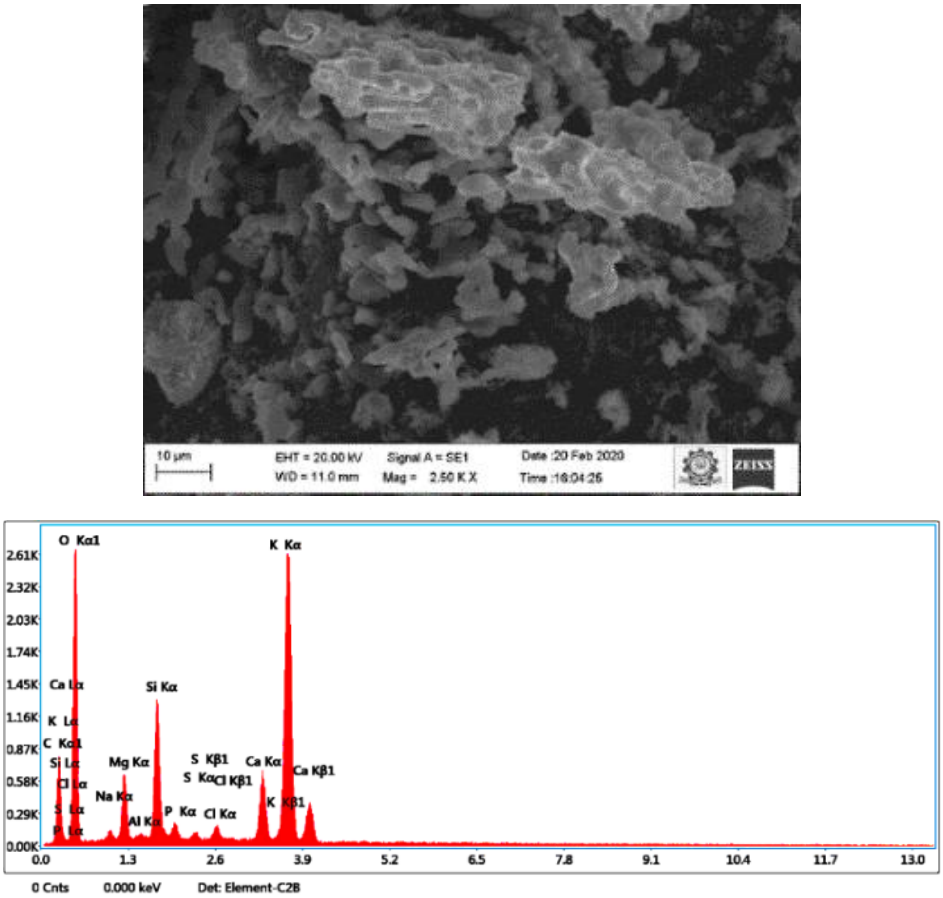

Fig. 2 Microstructure analysis of LCWA through SEM and EDX

3. Mix Proportion

In this research, the mix proportion for low calcium green geopolymer concrete was designed by the Indian standard modified guidelines for geopolymer concrete mix design [51]. The design mix was calculated as 1:1.05:1.57 with an activator to binder ratio of 0.61 [48]. The individual fibres such as polypropylene and rubber fibres were added by 0%, 0.5%, 1%, 1.5% and 2% of volume fraction [50]. The quantity of materials as per the mix design of individual fibre addition was tabulated in Table 3. This study found the influence of individual fibre on the mechanical characteristics of low calcium green geopolymer concrete. Table 3 shows the references of different mix id.

Further, the combination of rubber and polypropylene fibre was carried out by varying the percentage of both fibre at a variation of 0%, 0.25%, 0.5%, 0.75%, and 1% of volume fraction. Table 4 illustrates the quantity of material required for the hybridization of rubber and polypropylene fibre.

Table 3. Material quantity required for different fibre addition

Mix id (kg/m³)	GC	Polypropylene fibre			
		0.5PFRG	1.0PFRG	1.5PFRG	2.0PFRG
FA	385	385	385	385	385
LCWA	96	96	96	96	96
NaOH	110	110	110	110	110
Na_2SiO_3	276	276	276	276	276
Sand	667	667	667	667	667
CA	994	994	994	994	994
Fibre	0	2.41	4.82	7.22	9.63

Table 4. (Con.) Material quantity required for different fibre addition

Mix id (kg/m³)	GC	Rubber Fibre			
		0.5RFRG	1.0RFRG	1.5RFRG	2.0RFRG
FA	385	385	385	385	385
LCWA	96	96	96	96	96
NaOH	110	110	110	110	110
Na_2SiO_3	276	276	276	276	276
Sand	667	667	667	667	667
CA	994	994	994	994	994
Fibre	0	2.41	4.82	7.22	9.63

Table 5. Material quantity required for hybridization of fibre

Mix id	PP Fibre (kg/m³)	Rubber Fibre (kg/m³)	Fly ash (kg/m³)	LCWA (kg/m³)	NaOH (kg/m³)	Na_2SiO_3 (kg/m³)	Sand (kg/m³)	CA (kg/m³)
GC	0	0	385	96.3	110.2	275.59	666.58	993.7
0P/1.0R HFRG	0	4.82	385	96.3	110.2	275.59	666.58	993.7
0.25P/0.75R HFRG	1.21	3.61	385	96.3	110.2	275.59	666.58	993.7
0.5P/0.5R HFRG	2.41	2.41	385	96.3	110.2	275.59	666.58	993.7
0.75P/0.25R HFRG	3.61	1.21	385	96.3	110.2	275.59	666.58	993.7
1.0P/0R HFRG	4.82	0	385	96.3	110.2	275.59	666.58	993.7

4. Experimental Program

4.1 Mechanical Characterization

In accordance with ASTM C109 [52], ASTM- C215 [53], ASTM-C293 [54] standards, the compressive strength, tensile strength, and flexural strength of the mix was determined by

testing the standard specimens in the Universal Testing Machine. The standard specimens for compressive strength testing were taken as 100mm x 100mm x 100 mm size cubes, and for computing tensile strength, 100mm x 200mm size cylinder was cast. 500mm x 100mm x 100mm size prism was casted for the computation of flexural strength. The specimens were cured at ambient temperature till the occurrence of testing ages of 3, 7 and 28 days. In this study, the effect of both rubber and polypropylene fibre on the compressive, flexural and split tensile strengths of low calcium based GPC was carried out at the required ages. Average of three specimens test results were taken as strength parameters for all ages of curing. The failure of specimens was shown in figure 3.

4.2 Durability Characterization

The water absorption of concrete specimens was a simple way of assessing the potential of concrete in durability aspects. In compliance with ASTM C 642 [55], the water absorption test was performed. For 24hrs, oven-dried specimens were soaked in water. Percentage growth in weight as water absorption was noted. According to time, the measurement of capillary water suction in a uniform direction was sorptivity. According to ASTM C267 [56], the resistance to acidic conditions was assessed. 3% sulfuric acid solution was used for submerging the specimens to find the reaction against the acidic environment. Initial specimen weights were determined.

Fig. 3 Failure of specimens

Mass loss, the residual strength of compression, and physical conditions of the tested specimen were noted after 30 days. Based on the procedure given in ASTM C1760[57], the electrical resistivity of the specimen was derived. While considering the determination of durability in terms of electrical resilience, this electrical conductivity method was easy and fast. The test was performed by measuring the variable voltage at the ends of the specimen using DC power. The current was measured for the average current for each applied voltage. Calculation of resistivity was done by using q = RA/L where R = V/I, L = In between distance of electrodes and A was c/s area of the specimen.

5. Result and Discussion

5.1 Mechanical Characterization

5.1.1 Effect of Polypropylene Fibre

The influence of polypropylene fibre incorporation on the mechanical characters of low calcium green geopolymer concrete is shown in figure 4 (a-c). The various proportion of polypropylene fibre incorporation was 0, 0.5, 1, 1.5, 2% of volume fraction and their effects on low calcium green geopolymer concrete were assessed. Table 5 represents the test results.

The specified limit of fibre incorporation was up to 2% of volume fraction due to augmentation of fibre in one place and reduced workability [50,58]. From the test result, at all ages of concrete, there was an enhancement in all strength noted with the 1% of PP fibre [59]. The strength parameters were started to decrease with the fibre addition exceeds 1% due to the augmentation of fibres in one place [31]. While comparing the testing ages, the specimens tested after 3 days of ambient curing was achieved the highest percentage of strength gaining than the control mix [60].

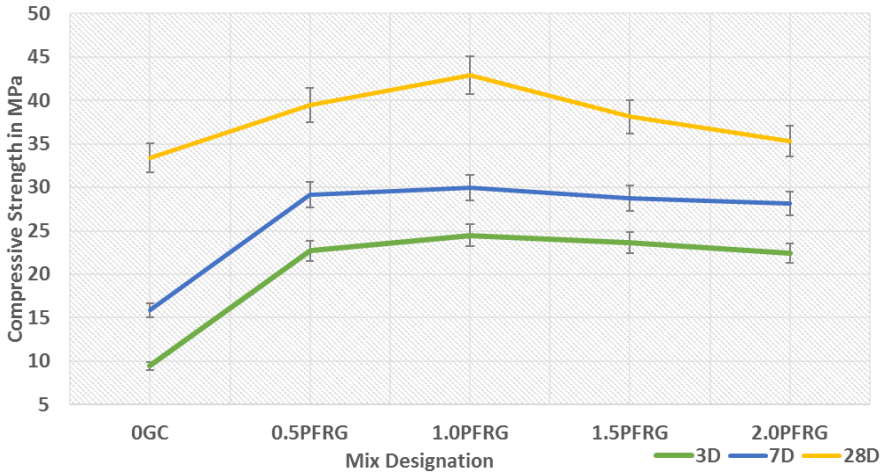

Fig. 4 a Influence of PP fibre in compressive strength

Table 6. Results of each mix

Mix ID	Compressive Strength (MPa)			Tensile Strength (MPa)		
	28D	7D	3D	28D	7D	3D
0GC (Control Mix)	15.9	33.4	9.45	2.4	2.8	3.3
0.5PFRG	39.5	29.1	22.7	3.5	2.9	2.5
1.0PFRG	42.9	30	24.5	3.7	3.1	2.7
1.5PFRG	38.1	28.8	23.6	3.4	3	2.5
2.0PFRG	35.3	28.1	22.4	3.4	2.9	2.5
0.5RFRG	35.9	29.3	22.4	3.4	3	2.5
1.0RFRG	36.5	29.8	23.6	3.7	3.1	2.7
1.5RFRG	36.1	29	23.1	3.5	3	2.6
2.0RFRG	35.8	27.6	22.1	3.3	2.9	2.4
0P/1.0R HyFRG	36.5	29.8	23.6	3.5	3.1	2.7
0.25P/0.75R HyFRG	37.5	30.2	24.1	3.7	3.3	2.8
0.5P/0.5R HyFRG	43.9	32.5	25.3	3.9	3.4	3
0.75P/0.25R HyFRG	38.6	31.7	24.9	3.7	3.2	2.7
1.0P/0R HyFRG	35.9	30	24.5	3.7	3.1	2.7

Table 7. (Con.) Results of each mix

Mix ID	Flexural Strength (MPa)		
	28D	7D	3D
0GC (Control Mix)	4.3	3.8	3.3
0.5PFRG	4.5	4.1	3.4
1.0PFRG	4.8	4.3	3.6
1.5PFRG	4.4	4	3.5
2.0PFRG	4.3	3.9	3.3
0.5RFRG	4.3	4	3.3
1.0RFRG	4.4	4.2	3.4
1.5RFRG	4.3	4	3.4
2.0RFRG	4.3	3.9	3.3
0P/1.0R HyFRG	4.3	3.8	3.3
0.25P/0.75R HyFRG	4.3	3.9	3.3
0.5P/0.5R HyFRG	4.4	4	3.4
0.75P/0.25R HyFRG	4.8	4.1	3.5
1.0P/0R HyFRG	4.4	4	3.4

The percentage of strength gaining of the specimens was noticed a gradual increment up to 1 % PP fibre, then a sudden drop down in strength was noticed in the mix with 1.5% PP fibre. While at the age of 28 days showed an increment in strength compared to the control mixture [33]. Compared to other curing ages, the increment rate was less. The maximum increment rate in compressive strength of 61.4% was observed with 1% PP fibre [61]. In the meantime, the fibre addition of 1% enhanced the compressive strength in 3, 7, and 28 days by 61.4%, 47%, 22.2%, respectively [29].

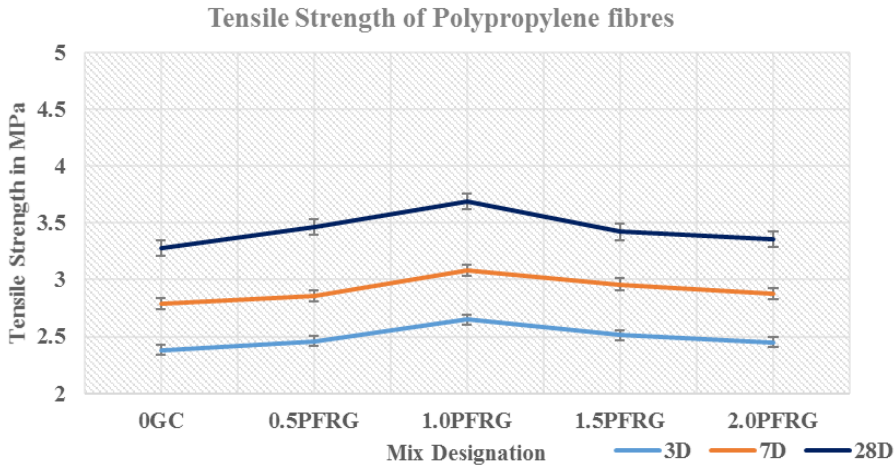

Fig. 4 b Influence of PP fibre in tensile strength

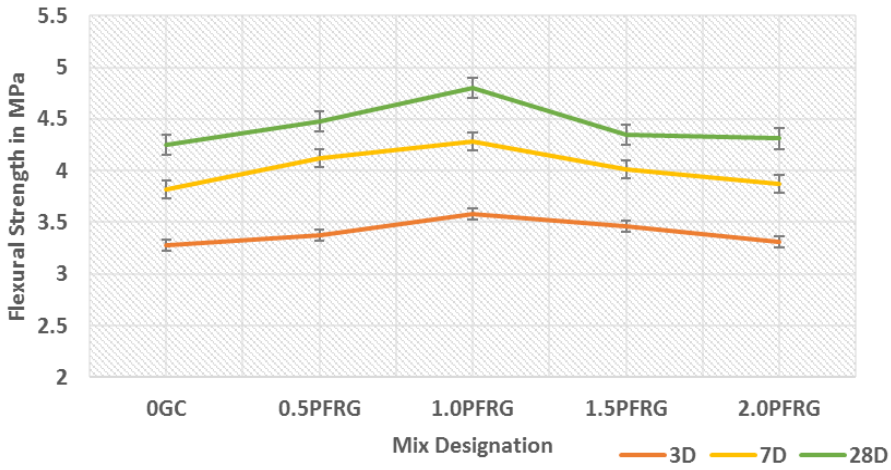

Fig. 4 c Influence of PP fibre in flexural strength

Meanwhile, the GPC incorporated with 0.5% polypropylene and 1% polypropylene achieved the maximum rate of increment in 28days tensile strength of 5.2% and 15.7%, compared to the control mixture [62]. The GPC mix incorporated with 1% polypropylene enhanced the tensile strength in 3, 7 and 28 days by 10.2%, 9.4% and 15.7% [50]. The findings showed that incorporation of polypropylene fibre up to 1 % achieved the maximum rate of increment compared to other mixes. Hence, the polypropylene fibre improved the tensile and flexural strength of GPC [28]. The GPC incorporated with 0.5% polypropylene and 1% polypropylene achieved the maximum rate of increment in 28days flexural strength of 5.13% and 11.4% compared to the control mixture [50]. On the other hand, The GPC mix incorporated with 1% polypropylene enhanced the flexural strength in 3, 7, and 28 days by 8.38%, 10.75%, and 11.46% [44]. incorporation of polypropylene fibre up to 1 % achieved the maximum rate of increment compared to other mixes. [32].

5.1.2 Effect of Rubber Fibre

The influence of various percentages of rubber fibre addition on the mechanical characters of low calcium GPC was illustrated in figure 5 (a-c). In the previous studies, the rubber was replaced with fine aggregate at various percentages [42], and rubber replacement up to 5 percent achieved equal performance related to the control specimen [39]. The studies stated that the addition of rubber in smaller volume fractions could help in improving mechanical performance. The rubber was incorporated with smaller volume fractions such as 0.5%, 1%, 1.5%, and 2% in this research. The 1% rubber fibre addition enhanced the compressive, flexural, and tensile strengths by 8.5%, 3.19%, and 11.83% [48]. The rate of increment in compressive strength at all curing ages was gradual with 1% rubber, compared to the control mixture [35]. The strength character was reduced with increasing the rubber fibre addition above 1% due to the unstiffened matrix developed by the augmentation of fibres [63]. The rate of increment in early age compressive strength was higher than the other ages [24]. The maximum increment rate in compressive strength of 59.89% was observed with 1% rubber fibre [36].

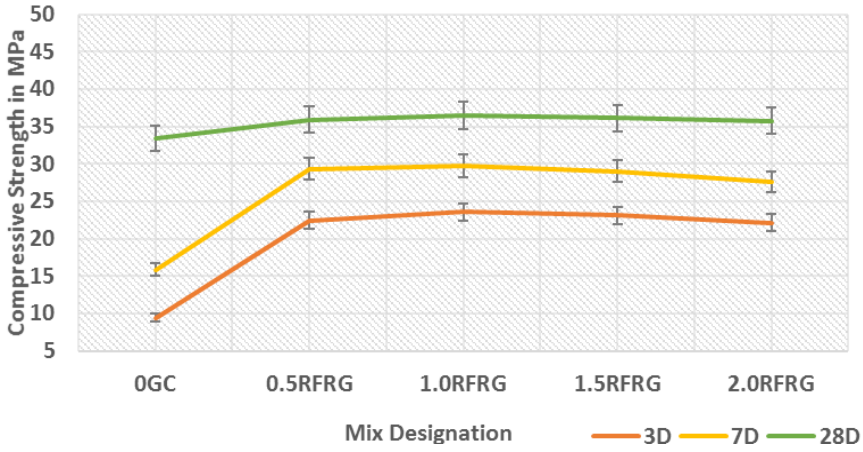

Fig. 5 a Influence of rubber fibre in compressive strength

In the meantime, the rubber fibre addition of 1% enhanced the compressive strength in 3, 7, and 28 days by 59.89%, 46.66%, 8.65%, respectively [48]. However, the addition of PP fibre enhanced the compressive strength than the rubber fibre addition due to the lower degree of compressibility of rubber fibre [64].

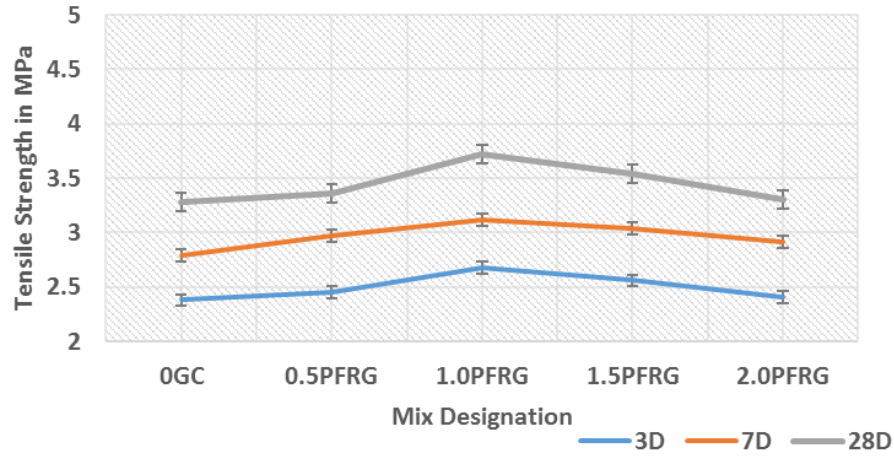

Fig. 5 b Influence of rubber fibre in Split Tensile Strength

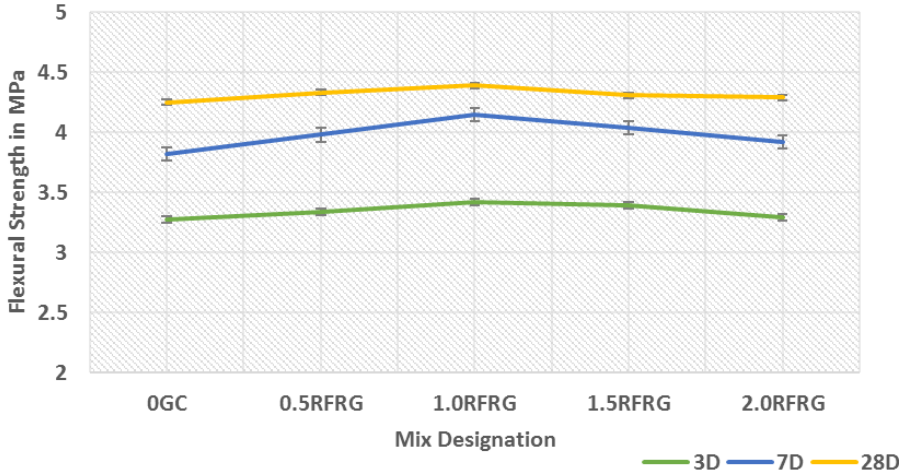

Fig. 5 c Influence of rubber fibre in flexural strength

The maximum rate of increment in 28 days tensile strength of 2.38% and 11.83% was attained by adding 0.5% rubber and 1.0% rubber fibre, and the rate of increment of each mix was illustrated in figure 5 b [48]. The GPC mix incorporated with 1% rubber enhanced the tensile strength in 3, 7, and 28 days by 11.19%, 10.58%, and 11.83% [42]. [50]. The findings showed that incorporating rubber fibre up to 1 % achieved the maximum increment rate compared to other mixes. Hence, the rubber fibre improved the tensile and flexural strength of GPC [37,42].

The GPC incorporated with 0.5% rubber and 1% rubber achieved the maximum rate of increment in 28days flexural strength of 1.85% and 3.19% compared to the control mixture [39,65]. On the other hand, The GPC mix incorporated with 1% rubber enhanced the tensile strength in 3, 7, and 28 days by 4.09%, 7.95%, and 3.19% [48]. The incorporation of rubber fibre up to 1 % achieved the maximum rate of increment compared to other mixes. [66,67].

5.1.3 Effect of Hybridization of Polypropylene and Rubber Fibre

The research found that the optimum percentage of individual fibre addition on the geopolymer concrete was 1% for both polypropylene and rubber fibre [44]. In addition, mechanical characteristics of hybrid fibre reinforced green geopolymer concrete due to the various percentage of hybridization of polypropylene and rubber were assessed [62]. The results are illustrated in figure 6 (a-c).

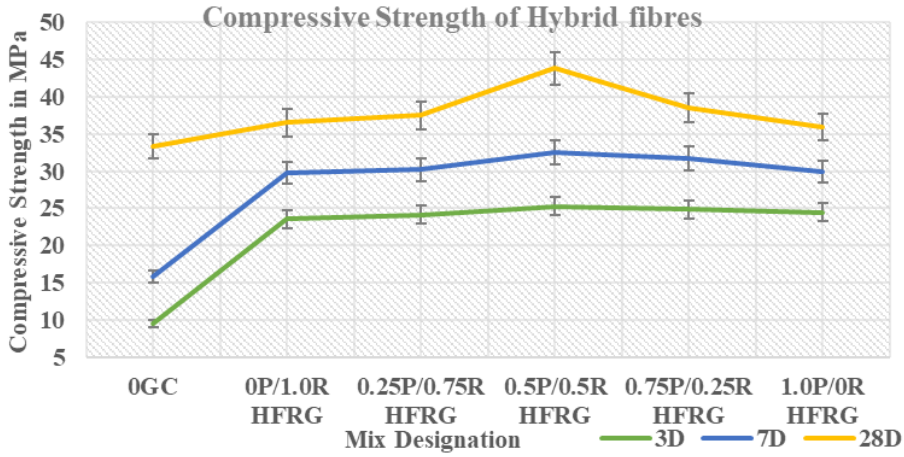

Fig. 6 (a) Influence of hybrid fibre in compressive strength

The maximum increment rate in all strength parameters was noticed with the mix having 0.5% rubber and 0.5% polypropylene [44]. The rate of increment in early compressive strength of the optimum mix (0.5P/0.5R HyFRG) was higher than the other curing ages. Meanwhile, the optimum mix attained the maximum compressive strength and high rate of increment at 28 days [17]. The optimum mix increment rate in 3, 7, and 28 days of compressive strength was enhanced by 62.6%, 51.2%, and 23.9% than the other mixes [32]. The findings explored a decrease in strength when the rubber fibre addition exceeds 0.5% [62]. In the meantime, compressive strength was enhanced with the addition of polypropylene fibre [50]. The GPC with 1% polypropylene fibre attained higher compressive strength than the mix with 1% rubber fibre [68].

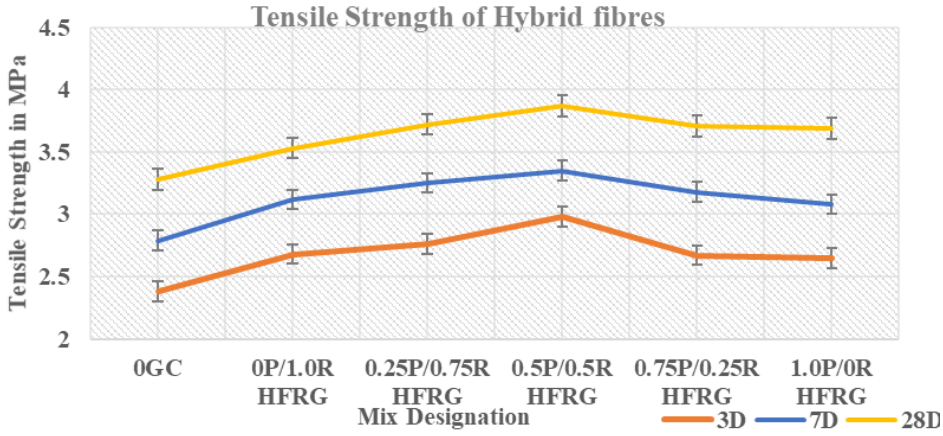

Fig. 6 (b) Influence of hybrid fibre in split tensile strength

The maximum rate of increment in 3, 7, and 28 days tensile strength of 20.1%, 16.7%, and 15.2% were attained by the optimum mix (0.5P/0.5R HyFRG), and the rate of increment of each mix was illustrated in figure 6 b [66]. The enhancement in tensile strength was higher with the rubber fibre addition than the polypropylene fibre addition [39]. The maximum rate of increment in early age tensile strength was higher than the other curing ages [33].

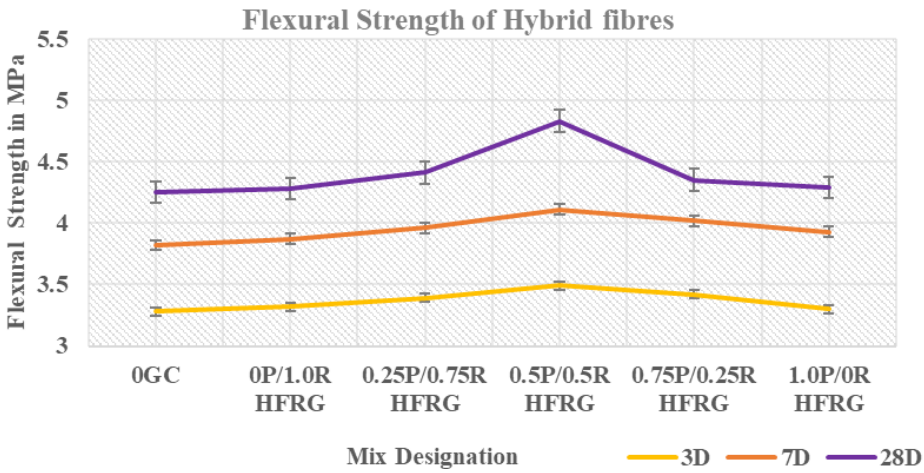

Fig. 6 (c) Influence of hybrid fibre in flexural strength

The maximum rate of increment in flexural strength was achieved with the optimum mix (0.5P/0.5R HyFRG). In the increase of flexural strength, the percentage increment was much higher than that of tensile strength. The maximum strength was achieved by adding 0.5% polypropylene fibers and 0.5% rubbers [44]. The maximum rate of increment in 3, 7, and 28 days of tensile strength of 6%, 7.1%, and 12.0% were attained by the optimum mix (0.5P/0.5R HyFRG), and the rate of increment of each mix was illustrated in figure 6 c [33]. The enhancement in flexural strength was noticed with the increasing the rubber fibre.

5.2 Durability Characteristics

5.2.1 Water Absorption

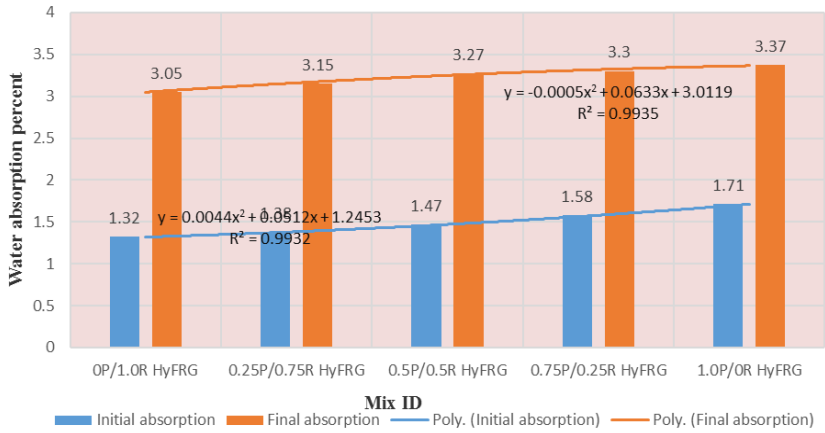

Fig. 7 Initial and final water absorption capacity of each specimen

The water absorption capacity of each specimen was evaluated by comparing the wet weight to the oven-dried weight. For the initial capacity to absorb water, the specimen was weighed 60 minutes after immersion, and the final capability for water absorption was quantified 24 hours later [66]. The chart in Figure 7 depicts the absorption capacities of

each specimen. Initial and final water absorption was lower for the control mix (0GC). The control mix absorbed water at 1.32 and 3.05 at the start and end. The 1P/0R HyFRG mixture absorbed 3.66 percent of the total water [20]. The optimal 0.5P/0.5R HyFRG mix observed 3.27 closer to the control mix. The percentage of hybrid fibre added increased the capacity of the geopolymer concrete to absorb water. Incorporating hybrid fibre may allow for greater water absorption than the control mix. The greater water absorption was because of the large surface area and porous medium of the mix, which allows it to absorb more water [69]. However, the mix with 0.5 percent PP+0.5R absorbs less water than the mix with 100% PP and can be used for efficient hybridization [70]. Relation between the replacement percentage of hybridization(x) to the water absorption of each mix(y) obtained from regression analysis was y=-0.0005x2+0.0633x+3.0119, R^2 = 0.9935 [71].

5.2.2 Electrical Resistivity

Each specimen's electrical resistivity was measured in K-Ohm-cm [69] per ASTM C1760 [57] standards. The electrical resistivity of various mixtures is shown in Figure 8. Adding PP and rubber fibres reduced the electrical resistivity of GPC beyond the optimum limit. The optimum 0.5PP/0.5R HyFRG mix had the highest electrical resistivity of 440 compared to other mixes [72]. The control mix had 375K-Ohm-cm resistivity. The 0.5PP+0.5R hybridization displayed superior resistivity to the control sample. The super resistivity was due to rubber fibre with a greater surface area and higher specific electrical resistance [73]. The relation between the hybridization of fibre (x) to the electrical resistivity of each specimen was obtained by regression analysis. The relation is y=--13.214x^2+78.786x+311, R^2 = 0.9142 [27].

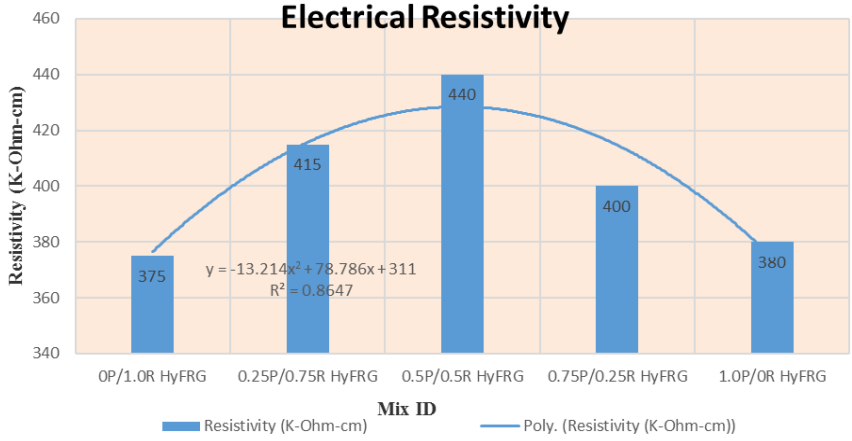

Fig. 8 Electrical resistivity of LCGPC mixes

5.2.3 Acid Attack Resistance

Figure 9 shows the resistance to sulphuric acid attack for each mix, and Figure 10 shows the percent weight loss and percent compressive strength loss for each mix. The sample weight was determined and compared to the starting weight of oven-dried samples after immersion in sulfuric acid for 1 day [69]. Its compressive strength was also measured. The findings showed that the addition of 0,5PP+0,5R in the acidic medium was most responsive [74]. The increase in the replacement percentage of GPC fibre increased the mass loss percentage [20]. With a mix of 1 percent PP fibre, maximum losses were observed in 6.39

percent. The 1% rubber fibre mix lost 4.28 percent weight. Thus, rubber fibre may be able to withstand acidic environmental conditions. The regression analysis was performed for the % loss in weight of each mix under the sulphuric acid environment. The relation between hybridization of fibre (x) to the percentage loss in mass of the specimen(y) was determined as $y = -0.0025x^2 + 0.2565x + 3.9504$, $R^2 = 0.9882$. The value of R2 closer to 1 showed that there is a good correlation of results.

Fig. 9 Specimens after exposure to the acidic environment

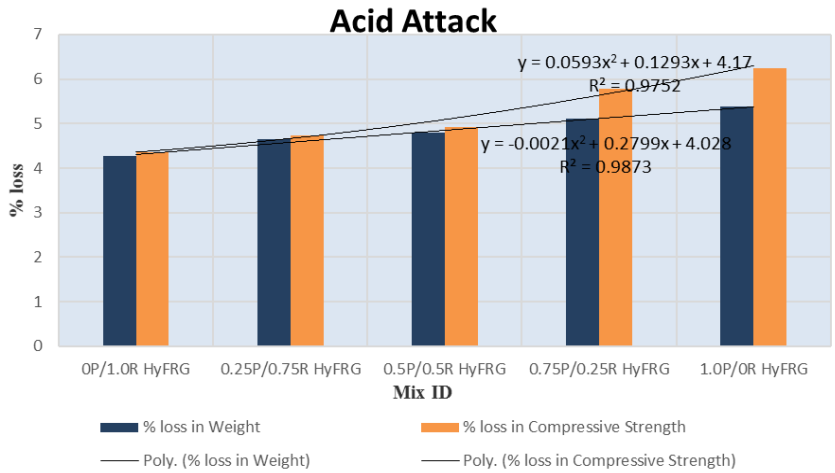

Fig. 10 Percentage loss in mass and compressive strength of LCGPC mixes due to acid attack

In the meantime, for each specimen, there was a percent loss in compression strength. Control specimens were sufficiently capable of resisting the reaction in acidic environments [66]. After being attacked by sulphuric acid, the specimens suffered a 4.28-4.79 percent reduction in compressive strength. The loss of compressive strength, when exposed to acidic conditions, has increased due to the addition of PP fibre [75]. However, adding PP at a concentration of 0.5 percent resulted in a loss of compressive strength comparable to that of the control mixture [22]. It demonstrates that the rubber fibre has enhanced compressive strength performance and resistant to compression strength loss in acidic conditions. The relation between hybridization of fibre (x) to the percentage loss in compressive strength(y) was determined as $y = 0.0339x^2 + 0.1442x + 4.0967$, $R^2 = 0.9944$. The value of R2 closer to 1 showed that there is a good correlation of results.

5.3 Microstructural Characterization

5.3.1 Scanning Electron Microscope

HyFRG-specimens were analyzed microstructurally with the aid of a scanning electron microscope (SEM) and shown in Fig 11. (a-f). Figure 10 shows the pores bridging of PP fibre (a-c). The PP fibre micrograph shows a heterogeneous and cracked matrix with a nonremoved solvent after being cured. These findings indicate a greater linkage among reacted and unreacted microspheres [68]. On the other hand, the particle pore bridging determines the results. The 0.5P/0.5R HyFRG mix has good porosity and microcracks, but the early strength production is limited. Replacing LCWWA results in a better geopolymerization and microstructure reaction [11].

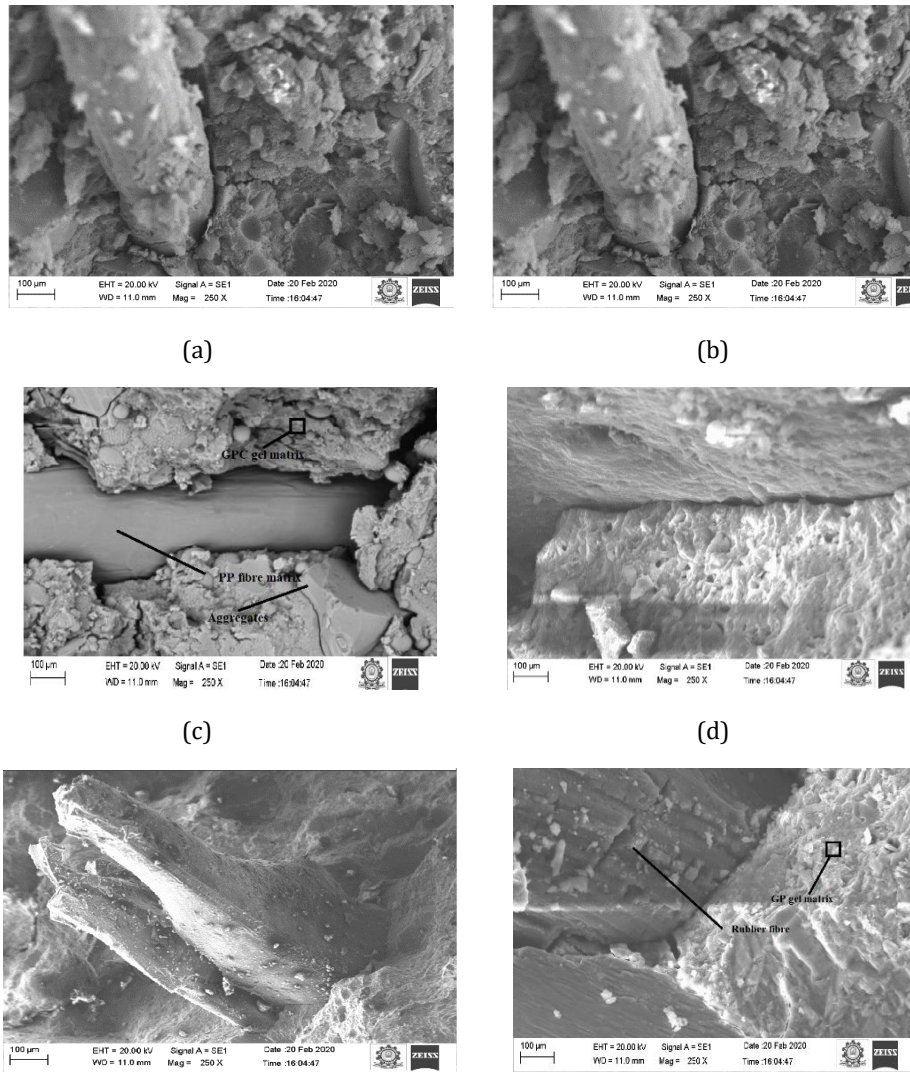

Fig. 11 Microstructure Analysis of HyFRG Mixes (a-c) PP fibre (e-f) Rubber Fibre

The ITZ zone of the geopolymer matrix and rubber fibre presence was established in Figure 10 (d-f). More homogeneous and dense gel matrices were observed when the optimum mix of 0.25P/0.75R HyFRG was used compared to a PP fibre-containing mixture [76]. The pore bridging impact among both fibres was enhanced by adding a small number of fibres to the mixture.

6. Conclusion

In this research, an intellectual approach for the utilization of wastes in the invention of green geopolymer concrete was made for a clean and sustainable environment. Influences on the mechanical characters of the green geopolymer concrete by rubber and polypropylene fibre have been studied. In addition, the mechanical and durability characteristics of green geopolymer concrete were characterized by the effects of the hybridization of polypropylene and rubber fiber. In contrast to the control mixture, the addition of PP up to 1% exhibited an increasing trend in all mechanical strengths at all curing periods. While increasing the addition of fibre over 1% resulted in decreasing all strength parameters. In the age of 28days curing period, the mix with 1% PP attained a maximum increase in compressive, flexural, and tensile strength as 61.4%, 47.0%, and 22.2%, respectively. The mix with 0.5%PP and 1%PP showed the maximum percentage of increase as 5.13% and 11.4% compared to the control mixture cured for 28 days. On the other hand, up to 1% rubber addition enlarged the highest strengths in all mechanical characterizations. Compared with the control mixture, the compressive strength, tensile strength, and flexural strength were increased by 8.65%, 11.83%, and 3.19%, respectively. Meanwhile, rubber addition over 1% results in decreasing the strength attainment. While hybridization of fibres, the compressive, tensile, and flexural strength of mix with 0.5% of PP fibre and 0.5% of rubber fibre had increased by 23.9%, 15.2%, and 12% at the age of 28 days compared to other mixes with and without fibres. The mix with 0.5P+0.5R performed better in water absorption, electrical resistivity, and acidic environmental exposure in the durability characteristics. The optimum mix of 0.5P/0.5R HyFRG was observed water absorption of 3.27, which was nearer to the control mix. The optimum mix 0.5PP/0.5R HyFRG observed the electrical resistivity of 440, which was the maximum resistance value compared to other mixes. Also, the mix 0.5P/0.5R HyFRG showed the most reactive and retained its compressive strength in the acidic environment. In the microstructure of the optimum mix 0.5P/0.5R HyFRG showed increased homogeneity and density of gel matrices. The bore bridging effect of both the fibres was enhanced with the limited addition of fibres. The replacement of LCWWA leads to improving the geopolymerization reaction and also the microstructure. Hence, the research hypothesis was proven that waste materials like rubber tire fibre and wood ash could be effectively utilized to produce green geopolymer concrete, and it paved the way for a clean and sustainable environment.

7. Future Study

In the future study, the study will be extended by investigating low calcium fibre reinforced Ferro-geopolymer concrete paver block. The optimization of size, shape, and surface texture of the paver block will be studied in detail.

Acknowledgement

The authors acknowledge that this study does not have any funding information.

References

[1] Davidovits J. Geopolymer chemistry and properties. Proceedings of the 1st International Conference on Geopolymer'88 1988;88:25-48.

[2] Rangan B V. Fly Ash-Based Geopolymer Concrete (Column). Engineering Faculty Curtin University of Technology Perth, Australia 2008:3124-30. https://doi.org/10.1201/9781420007657.ch26

[3] Hardjito D, Wallah SE, Sumajouw DMJ, Rangan BV. On the development of fly ash-based geopolymer concrete. ACI Materials Journal 2004;101:467-72. https://doi.org/10.14359/13485

[4] Mishra A, Choudhary D, Jain N, Kumar M, Sharda N, Dutt D. Effect of concentration of alkaline liquid and curing time on strength and water absorption of geopolymer concrete. ARPN Journal of Engineering and Applied Sciences 2008;3:14-8.

[5] Thakur RN, Ghosh S. Effect of mix composition on compressive strength and microstructure of fly ash based geopolymer composites. Journal of Engineering and Applied Sciences 2009;4:68-74.

[6] Reddy BSK. Strength and workability of low lime fly-ash based geopolymer concrete. Indian Journal of Science and Technology 2010;3:1188-9. https://doi.org/10.17485/ijst/2010/v3i12.11

[7] Sarker PK, Haque R, Ramgolam K V. Fracture behaviour of heat cured fly ash based geopolymer concrete. Materials & Design 2013;44:580-6. https://doi.org/10.1016/j.matdes.2012.08.005

[8] Hamidi RM, Man Z, Azizli KA. Concentration of NaOH and the Effect on the Properties of Fly Ash Based Geopolymer. Procedia Engineering 2016;148:189-93. https://doi.org/10.1016/j.proeng.2016.06.568

[9] Shadnia R, Zhang L. Experimental Study of Geopolymer Synthesized with Class F Fly Ash and Low-Calcium Slag. Journal of Materials in Civil Engineering 2017;29:04017195. https://doi.org/10.1061/(ASCE)MT.1943-5533.0002065

[10] Luo Z, Li W, Wang K, Castel A, Shah SP. Comparison on the properties of ITZs in fly ash-based geopolymer and Portland cement concretes with equivalent flowability. Cement and Concrete Research 2021;143:106392. https://doi.org/10.1016/j.cemconres.2021.106392

[11] Huseien GF, Ismail M, Khalid NHA, Hussin MW, Mirza J. Compressive strength and microstructure of assorted wastes incorporated geopolymer mortars: Effect of solution molarity. Alexandria Engineering Journal 2018;57:3375-86. https://doi.org/10.1016/j.aej.2018.07.011

[12] Wasim M, Ngo TD, Law D. A state-of-the-art review on the durability of geopolymer concrete for sustainable structures and infrastructure. Construction and Building Materials 2021;291:123381. https://doi.org/10.1016/j.conbuildmat.2021.123381

[13] Nuaklong P, Wongsa A, Sata V, Boonserm K, Sanjayan J, Chindaprasirt P. Properties of high-calcium and low-calcium fly ash combination geopolymer mortar containing recycled aggregate. Heliyon 2019;5. https://doi.org/10.1016/j.heliyon.2019.e02513

[14] Yadav, Virendra Fulekar M. THE CURRENT SCENARIO OF THERMAL POWER PLANTS AND FLY ASH : International Journal of Advance Engineering and Research. International Journal of Advance Engineering and Research Development 2018;5:768-77.

[15] Mehta A, Siddique R. Sustainable geopolymer concrete using ground granulated blast furnace slag and rice husk ash: Strength and permeability properties. Journal of Cleaner Production 2018;205:49-57. https://doi.org/10.1016/j.jclepro.2018.08.313

[16] Suresh Kumar A, Muthukannan M, Sri Krishna I. Optimisation of bio medical waste ash in GGBS based of geopolymer concrete. IOP Conference Series: Materials Science and Engineering 2020;872:012163. https://doi.org/10.1088/1757-899X/872/1/012163

[17] Chithambar GA, Muthukannan M. Investigation on the glass fiber reinforced geopolymer concrete made of M-sand. Journal of Materials and Engineering Structures 2019;6:501-12.
[18] Arunachalam SK, Muthiah M, Rangaswamy KD, Kadarkarai A, Arunasankar CG. Improving the structural performance of reinforced geopolymer concrete incorporated with hazardous heavy metal waste ash. World Journal of Engineering 2021;ahead-of-p. https://doi.org/10.1108/WJE-01-2021-0055
[19] Suresh Kumar A, Muthukannan M, Kanniga Devi R, Arunkumar K, Chithambar Ganesh A. Reduction of hazardous incinerated bio-medical waste ash and its environmental strain by utilizing in green concrete. Water Science and Technology 2021. https://doi.org/10.2166/wst.2021.239
[20] Ban CC, Ken PW, Ramli M. Mechanical and Durability Performance of Novel Self-activating Geopolymer Mortars. Procedia Engineering 2017;171:564-71. https://doi.org/10.1016/j.proeng.2017.01.374
[21] Cheah CB, Ramli M. The implementation of wood waste ash as a partial cement replacement material in the production of structural grade concrete and mortar: An overview. Resources, Conservation and Recycling 2011;55:669-85. https://doi.org/10.1016/j.resconrec.2011.02.002
[22] Cheah CB, Part WK, Ramli M. The hybridizations of coal fly ash and wood ash for the fabrication of low alkalinity geopolymer load bearing block cured at ambient temperature. Construction and Building Materials 2015;88:41-55. https://doi.org/10.1016/j.conbuildmat.2015.04.020
[23] Cheah CB, Ramli M. Load capacity and crack development characteristics of HCWA-DSF high strength mortar ferrocement panels in flexure. Construction and Building Materials 2012;36:348-57. https://doi.org/10.1016/j.conbuildmat.2012.05.034
[24] Arunkumar K, Muthukannan M, Kumar AS, Ganesh AC, Devi RK. Cleaner Environment Approach by the Utilization of Low Calcium Wood Ash in Geopolymer Concrete. Applied Science and Engineering Progress 2021:1-13. https://doi.org/10.14416/j.asep.2021.06.005
[25] Abdulkareem OA, Ramli M, Matthews JC. Production of geopolymer mortar system containing high calcium biomass wood ash as a partial substitution to fly ash: An early age evaluation. Composites Part B: Engineering 2019;174:106941. https://doi.org/10.1016/j.compositesb.2019.106941
[26] Cheah CB, Samsudin MH, Ramli M, Part WK, Tan LE. The use of high calcium wood ash in the preparation of Ground Granulated Blast Furnace Slag and Pulverized Fly Ash geopolymers: A complete microstructural and mechanical characterization. Journal of Cleaner Production 2017;156:114-23. https://doi.org/10.1016/j.jclepro.2017.04.026
[27] Arunkumar K, Muthukannan M, Sureshkumar K, Chithambar Ganesh A, Kanniga Devi R. Mathematical Formulation for Prediction of Structural Performance of Green Geopolymer Concrete Beams and Columns. Turkish Journal of Computer and Mathematics Education 2021;12:3806-15.
[28] Koenig A, Wuestemann A, Gatti F, Rossi L, Fuchs F, Fessel D, et al. Flexural behaviour of steel and macro-PP fibre reinforced concretes based on alkali-activated binders. Construction and Building Materials 2019;211:583-93. https://doi.org/10.1016/j.conbuildmat.2019.03.227
[29] Zhang Z, Yao X, Zhu H, Hua S, Chen Y. Preparation and mechanical properties of polypropylene fiber reinforced calcined kaolin-fly ash based geopolymer. Journal of Central South University of Technology 2009;16:49-52. https://doi.org/10.1007/s11771-009-0008-4
[30] Farhan KZ, Johari MAM, Demirboğa R. Impact of fiber reinforcements on properties of geopolymer composites: A review. Journal of Building Engineering 2021;44:102628. https://doi.org/10.1016/j.jobe.2021.102628

[31] Reed M, Lokuge W, Karunasena W. Fibre-reinforced geopolymer concrete with ambient curing for in situ applications. Journal of Materials Science 2014;49:4297-304. https://doi.org/10.1007/s10853-014-8125-3
[32] Zabihi SM, Tavakoli H, Mohseni E. Engineering and Microstructural Properties of Fiber-Reinforced Rice Husk-Ash Based Geopolymer Concrete. Journal of Materials in Civil Engineering 2018;30:04018183. https://doi.org/10.1061/(asce)mt.1943-5533.0002379. https://doi.org/10.1061/(ASCE)MT.1943-5533.0002379
[33] Ganesh C, Sivasubramanaian J, Seshamahalingam MS, Millar J, Kumar VJ. Investigation on the Performance of Hybrid Fiber Reinforced Geopolymer Concrete Made of M-Sand under Heat Curing. Materials Science Forum 2021;1019:73-81. https://doi.org/10.4028/www.scientific.net/MSF.1019.73
[34] Saloni, Parveen, Pham TM, Lim YY, Malekzadeh M. Effect of pre-treatment methods of crumb rubber on strength, permeability and acid attack resistance of rubberised geopolymer concrete. Journal of Building Engineering 2021;41. https://doi.org/10.1016/j.jobe.2021.102448
[35] Jalal M, Nassir N, Jalal H. Waste tire rubber and pozzolans in concrete: A trade-off between cleaner production and mechanical properties in a greener concrete. Journal of Cleaner Production 2019;238. https://doi.org/10.1016/j.jclepro.2019.117882
[36] Gupta T, Siddique S, Sharma RK, Chaudhary S. Effect of elevated temperature and cooling regimes on mechanical and durability properties of concrete containing waste rubber fiber. Construction and Building Materials 2017;137:35-45. https://doi.org/10.1016/j.conbuildmat.2017.01.065
[37] Arunkumar K, Muthukannan M, Kumar AS, Ganesh AC, Devi RK, Muthiah M, et al. Invention of sustainable geopolymer concrete made with low calcium waste wood ash. World Journal of Engineering 2021. https://doi.org/10.1108/WJE-03-2021-0162
[38] Charkhtab Moghaddam S, Madandoust R, Jamshidi M, Nikbin IM. Mechanical properties of fly ash-based geopolymer concrete with crumb rubber and steel fiber under ambient and sulfuric acid conditions. Construction and Building Materials 2021;281:122571. https://doi.org/10.1016/j.conbuildmat.2021.122571
[39] Gupta T, Chaudhary S, Sharma RK. Mechanical and durability properties of waste rubber fi ber concrete with and without silica fume. Journal of Cleaner Production 2016;112:702-11. https://doi.org/10.1016/j.jclepro.2015.07.081
[40] Shaikh FUA, Luhar S, Arel HŞ, Luhar I. Performance evaluation of Ultrahigh performance fibre reinforced concrete - A review. Construction and Building Materials 2020;232:117152. https://doi.org/10.1016/j.conbuildmat.2019.117152
[41] Luhar S, Luhar I. Potential application of E-wastes in construction industry: A review. Construction and Building Materials 2019;203:222-40. https://doi.org/10.1016/j.conbuildmat.2019.01.080
[42] Luhar S, Chaudhary S, Luhar I. Development of rubberized geopolymer concrete : Strength and durability studies. Construction and Building Materials 2019;204:740-53. https://doi.org/10.1016/j.conbuildmat.2019.01.185
[43] Luhar S, Cheng TW, Luhar I. Incorporation of natural waste from agricultural and aquacultural farming as supplementary materials with green concrete: A review. Composites Part B: Engineering 2019;175:107076. https://doi.org/10.1016/j.compositesb.2019.107076
[44] Chithambar Ganesh A, Muthukannan M. Experimental Study on the Behaviour of Hybrid Fiber Reinforced Geopolymer Concrete under Ambient Curing Condition. IOP Conference Series: Materials Science and Engineering 2019;561:012014. https://doi.org/10.1088/1757-899X/561/1/012014
[45] Zakka WP, Abdul Shukor Lim NH, Chau Khun M. A scientometric review of geopolymer concrete. Journal of Cleaner Production 2021;280:124353. https://doi.org/10.1016/j.jclepro.2020.124353

[46] ASTM C618. Standard Specification for Coal Fly Ash and Raw or Calcined Natural Pozzolan for Use. Annual Book of ASTM Standards 2010:3-6.
[47] Malkawi AB, Nuruddin MF, Fauzi A, Almattarneh H, Mohammed BS. Effects of Alkaline Solution on Properties of the HCFA Geopolymer Mortars. Procedia Engineering 2016;148:710-7. https://doi.org/10.1016/j.proeng.2016.06.581
[48] Arunkumar., Muthukannan M, Suresh kumar A, Chithambar Ganesh A. Mitigation of waste rubber tire and waste wood ash by the production of rubberized low calcium waste wood ash based geopolymer concrete and influence of waste rubber fibre in setting properties and mechanical behavior. Environmental Research 2021;194:110661. https://doi.org/10.1016/j.envres.2020.110661
[49] (BIS) B of IS. IS 383: 1970 Specification for Coarse and Fine Aggregates From Natural Sources for Concrete. Indian Standards 1970:1-24.
[50] Arunkumar K, Muthukannan M, Dinesh Babu A, Hariharan AL, Muthuramalingam T. Effect on addition of Polypropylene fibers in wood ash-fly ash based geopolymer concrete. IOP Conference Series: Materials Science and Engineering 2020;872:012162. https://doi.org/10.1088/1757-899X/872/1/012162
[51] Anuradha R. Modified Guidelines for Geopolymer Concrete Mix Design using Indian Standard. Asian Journal of Civil Engineering (Uilding and Housing) 2011;13:357-68.
[52] ASTM C109/C109M-02. Standard Test Method for Compressive Strength of Hydraulic Cement Mortars. Annual Book of ASTM Standards 2002;04:1-6.
[53] ASTM C215. Standard Test Method for Fundamental Transverse, Longitudinal, and Torsional Resonant Frequencies of Concrete Specimens, C 215. Annual Book of ASTM Standards, American Society for Testing and Materials 1991:1-7.
[54] ASTM-C293. C293 - 15 Flexural Strength of Concrete (Using Simple Beam With Center-Point Loading). ASTM International 2015:1-3.
[55] ASTM- C642. Standard test methods for Density, Absorption, and Voids in Hardened Concrete 1. Test 2005:1-3.
[56] ASTM-C267. Standard Test Methods for Chemical Resistance of Mortars , Grouts , and Monolithic. Current 1998;04:1-6.
[57] ASTM-C1760. ASTM Standard C1760 - Standard Test Method for Bulk Electrical Conductivity of Hardened Concrete. ASTM International 2012;i:1-5. https://doi.org/10.1520/C1760-12.2
[58] Özkılıç YO, Aksoylu C, Arslan MH. Experimental and numerical investigations of steel fiber reinforced concrete dapped-end purlins. Journal of Building Engineering 2021;36:102119. https://doi.org/10.1016/j.jobe.2020.102119
[59] Ganesh AC, Muthukannan M. Development of high performance sustainable optimized fiber reinforced geopolymer concrete and prediction of compressive strength. Journal of Cleaner Production 2021;282:124543. https://doi.org/10.1016/j.jclepro.2020.124543
[60] Wang Y, Zheng T, Zheng X, Liu Y, Darkwa J, Zhou G. Thermo-mechanical and moisture absorption properties of fly ash-based lightweight geopolymer concrete reinforced by polypropylene fibers. Construction and Building Materials 2020;251:118960. https://doi.org/10.1016/j.conbuildmat.2020.118960
[61] Al-mashhadani MM, Canpolat O, Aygörmez Y, Uysal M, Erdem S. Mechanical and microstructural characterization of fiber reinforced fly ash based geopolymer composites. Construction and Building Materials 2018;167:505-13. https://doi.org/10.1016/j.conbuildmat.2018.02.061
[62] Chithambar Ganesh A, Muthukannan M, Dhivya M, Sangeetha CB, Daffodile SP. Structural performance of hybrid fiber geopolymer concrete beams. IOP Conference Series: Materials Science and Engineering 2020;872:012155. https://doi.org/10.1088/1757-899X/872/1/012155

[63] Mhaya AM, Baghban MH, Faridmehr I, Huseien GF, Abidin ARZ, Ismail M. Performance evaluation of modified rubberized concrete exposed to aggressive environments. Materials 2021;14. https://doi.org/10.3390/ma14081900
[64] Gupta T, Sharma RK, Chaudhary S. Impact resistance of concrete containing waste rubber fiber and silica fume Trilok. International Journal of Impact Engineering
[65] Rahman SK, Al-Ameri R. A newly developed self-compacting geopolymer concrete under ambient condition. Construction and Building Materials 2021;267:121822. https://doi.org/10.1016/j.conbuildmat.2020.121822
[66] Chithambar Ganesh A. Experimental Study on the Behaviour of Hybrid Fiber Reinforced Geopolymer Concrete Made of M Sand. Kalasaliingam Academy of Research and Education, 2020. https://doi.org/10.1088/1757-899X/561/1/012014
[67] Singh K. Experimental study on metakolin and baggashe ash based geopolymer concrete. Mater. Today Proc., vol. 37, Elsevier Ltd; 2020, p. 3289-95. https://doi.org/10.1016/j.matpr.2020.09.116
[68] Jiang X, Zhang Y, Xiao R, Polaczyk P, Zhang M, Hu W, et al. A comparative study on geopolymers synthesized by different classes of fly ash after exposure to elevated temperatures. Journal of Cleaner Production 2020;270:122500. https://doi.org/10.1016/j.jclepro.2020.122500
[69] Salahuddin H, Qureshi LA, Nawaz A, Raza SS. Effect of recycled fine aggregates on performance of Reactive Powder Concrete. Construction and Building Materials 2020;243:118223. https://doi.org/10.1016/j.conbuildmat.2020.118223
[70] Hassan A, Arif M, Shariq M. Use of geopolymer concrete for a cleaner and sustainable environment - A review of mechanical properties and microstructure. Journal of Cleaner Production 2019;223:704-28. https://doi.org/10.1016/j.jclepro.2019.03.051
[71] A SK, Muthukannan M, K AK, A CG, R KD. Mathematical Prediction on the strength and behaviour of structural member by incorporating Incinerated Bio-Medical Waste Ash in Ground Granulated Blast Furnace Slag based Geopolymer Concrete. Turkish Journal of Computer and Mathematics Education 2021;12:4070-9.
[72] Kabir SMA, Alengaram UJ, Jumaat MZ, Yusoff S, Sharmin A, Bashar II. Performance evaluation and some durability characteristics of environmental friendly palm oil clinker based geopolymer concrete. Journal of Cleaner Production 2017;161:477-92. https://doi.org/10.1016/j.jclepro.2017.05.002
[73] Zhang P, Wang K, Li Q, Wang J, Ling Y. Fabrication and engineering properties of concretes based on geopolymers/alkali-activated binders - A review. Journal of Cleaner Production 2020;258:120896. https://doi.org/10.1016/j.jclepro.2020.120896
[74] Zhang P, Gao Z, Wang J, Guo J, Hu S, Ling Y. Properties of fresh and hardened fly ash/slag based geopolymer concrete: A review. Journal of Cleaner Production 2020;270:122389. https://doi.org/10.1016/j.jclepro.2020.122389
[75] Hwang C-L, Huynh T-P, Guo X, Shi H, Lin M, Dong W, et al. Effect of alkali-activator and rice husk ash content on strength development of fly ash and residual rice husk ash-based geopolymers. Construction and Building Materials 2015;101:1-9. https://doi.org/10.1016/j.conbuildmat.2015.10.025
[76] Sivasakthi M, Jeyalakshmi R, Rajamane NP. Fly ash geopolymer mortar: Impact of the substitution of river sand by copper slag as a fine aggregate on its thermal resistance properties. Journal of Cleaner Production 2021;279:123766. https://doi.org/10.1016/j.jclepro.2020.123766

Research on Engineering Structures & Materials
journal homepage: http://www.jresm.org
Research Group

Research Article

Analysis of effect of variation of Honeycomb core cell size and sandwich panel width on the stiffness of a sandwich structure

Anil Kumar*[1,a], Surjit Angra[2,b], Arindam Kumar Chanda[1,c]

[1]*Department of Mechanical and Automation Engineering, G.B.P.E.C., New Delhi, India*
[2]*Department of Mechanical Engineering, N.I.T., Kurukshetra, India*

Article Info

Article history:
Received 6 June 2021
Revised 12 Sep 2021
Accepted 16 Sep 2021

Keywords:

Kevlar® Honeycomb core;
Stiffness of Sandwich Panel;
Finite Element Method;
Core Cell Size:
3PBT

Abstract

A sandwich structure consists of three main parts i.e. the facing skins, the core and the adhesive. It acts in a way similar to that of the I- Beam. In this research, a sandwich structure has been designed with a regular hexagon honey-comb core made up of Kevlar® and face sheet of carbon fiber. The design has been modelled and the model has also been validated with the experimental and analytical method. Six different configurations of sandwich structures have been proposed. Out of these six, three configurations have the varying cell size i.e. 3.2 mm, 4 mm and 4.8 mm and the other three configurations have the varying panel width i.e. 40 mm, 45 mm and 50 mm keeping rest of the design parameters unchanged. Using ANSYS, analysis has been performed for all these six configurations and equivalent stiffness has been calculated. It has been observed that the honeycomb core cell size does not have a significant effect on the stiffness properties of a composite sandwich panel. The analysis also reveals that with the increased panel width the stiffness of composite panel increases significantly.

1. Introduction

A composite is a combination of two or more materials, where each material retains its unique characteristics and contributes its own structural properties, enabling the newer material to have better properties in many aspects. The composites have many desirable properties as compared to the other conventional materials such as light weight, higher stiffness, resistance to heat and corrosion, lower cost and easy availability. The composites structures are the most valuable products for the future of space and automobile industries as they have higher strength with the lowest weight. [1]

There are three main classifications of composites materials i.e. particle-reinforced, fiber-reinforced and structural composites.

A fibre-reinforced polymer composite material can provide considerable high tensile strength but they lack in bending strength. The bending strength of a fibre-reinforced polymer composite can be enhanced by increasing the thickness of the composite. But increasing the thickness of composite may lead to higher cost and considerable time consumption. One more side effect of fabrication of thicker composite materials is the possibility of generation of exothermic reactions leading to the detrimental effects on different chemical and physical properties of the fabricated materials. So to avoid these limitations related with higher thickness of the composite materials, a unique type of reinforcement is needed to increase the bending load bearing capacity of composite materials. The composites having this type of reinforcement are called as Composite sandwich structures.

*Corresponding author: anilapmae@gmail.com
[a] orcid.org/0000-0001-8264-0586; [b] orcid.org/0000-0002-4863-7815; [c] orcid.org/0000-0002-5689-3149
DOI: http://dx.doi.org/10.17515/resm2021.308me0606

Composite sandwich structures and different core dimensions are shown in Figure 1. A composite can be produced by inserting a low density, lightweight and thick core between two strong, stiff and thin facesheets. To join these different layers of facesheets with core, an adhesive material has to be used. Due to the insertion of a thick core, the overall thickness of the composite structure increases which ultimately leads to an increased bending load bearing capacity of the composite sandwich structure.

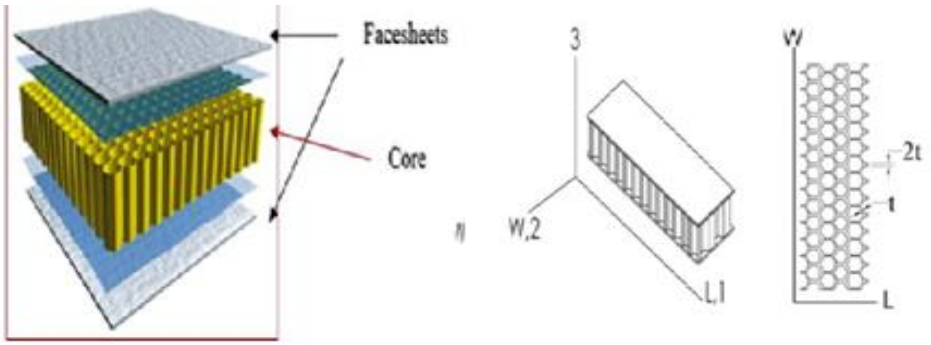

Fig. 1. Composite sandwich structure and core directions

The three basic elements of a composite sandwich structure can be described as –

Face Sheet - It will be responsible for bearing the bending stress of the sandwich structure. Carbon, Glass and Basalt Fibers are most widely used as Facesheet materials for fabrication of composite sandwich structures [15]. Kumar et al. [12] observed that the stiffness of sandwich structure initially increases at a faster rate and then reduces and tends to become constant with increasing thickness of face sheet.

Core - Mainly four types of cores are used in sandwich structures i.e. Corrugated, Honeycomb, Balsa wood and Foams. Most required property of a core of a composite sandwich structure is "the low density" to reduce the sandwich weight. Vamja et al. [2] describes that the sandwich panels having hexagonal core leads to a weight savings of approximately 39% as compared to other sandwich panels. The density, shear modulus, shear strength etc. are the most important properties of a core. J. S. Kumar et al. [3] observed that cell size along with core height was the most influencing structural parameters and the cell wall thickness was the least influencing one. Kumar et al. [6] in his study on sandwich structure observed that the tensile and flexural strength of the composite sandwich increases with increases of the height of the core. Arbaoui et al. [8] observed that the stiffness of the sandwich structures increase with core thickness. Thomas et al. [9] observed that Honeycomb core performance was dependant on geometrical parameters like cell size, node length, cell wall thickness and cell configuration. Rao et al. [10] in their research observed that the core height is not very effective parameter on the crushing behavior of sandwich structure having honeycomb core. But the wall thickness of a core cell is a pretty important parameter for the crushing strength of the sandwich panels. Akiwate et al. [11] made **e**xperimental investigation of bending behavior of aluminum alloy honeycomb sandwich structure using four point bending tests. They studied the Effects of the variation in honeycomb core height and honeycomb sandwich panel skin. Mohammed et al. [13] made experimental and numerical Study of bending behavior for honeycomb sandwich panel with different core configurations. Their results show that the square honeycomb's core shape bears the highest load from the other core shapes and the hexagonal have the lowest value and this value increased by increasing the facing thickness. Wahl et al. [17] observed that the

stresses are highest at a core orientation between the L or X and W or Y -direction and the weakest angle is 62° and the L-direction is the strongest direction. Lister [18] also observed that Core ribbon orientation has an important role in a sandwich beam's bending behavior. Kiran et al. [21] described that core cell size and core sheet thickness has negligible effect i.e. they contribute only 4% towards the stiffness per unit weight as compared to other design factors.

Core is always supposed to bear the shear and the core shear strains produce deformations and core shear stresses. For this reason, always such a core has been chosen which would not fail under the applied transverse load and whose shear modulus is high enough to give the required shear stiffness. The core shear stresses in composite sandwich can be found using straight forward formulas loaded by transverse forces. Zhang et al. [22] explain that the out of plane shear strength and stiffness of honeycombs are independent of core cell size ultimately they have very little effect on the stiffness of the composite sandwich panel. Prakash et al. [7] found that for the given core density the core shear modulus of the Fiber Reinforced Plastic (FRP) honeycomb core is far higher than that of Polyurethane (PUR) foam, but the shear strength of the FRP sandwich panels is only a little bit higher than PUR foam sandwich panel.

Honeycomb core can be made of metallic or non-metallic materials such as aluminium, impregnated glass or Aramid fibre mats, such as Nomex. Uddin et al. [14] found that an Aramid honeycomb sandwich structure with carbon Prepreg system can be used as primary structures in aircraft, in wind turbine, automotive etc. Liu et al. [19] observed that due to the different manufacturing methods the different honeycombs have different in and out-of-plane properties. But, Nomex honeycomb core is weak in, out-of-plane direction.

Adhesive - The purpose of an adhesive in a composite sandwich structure is to provide a good bond between the materials components. Epoxy Resins are most widely used adhesive as they are low temperature curing materials, normally between 20 to 90 °C. The biggest advantage of use of epoxy is that due to the absence of solvents, epoxies can be used with almost every type of core material. Epoxies are available in almost every form such as paste, films, powder, or as solid adhesives. The shear strength of most of the epoxies are about 20-25 MPa. Also other adhesives are available such as Modified Epoxies**,** Phenolics and Polyurethanes and Polyester and Vinyl ester Resin etc. [6]

Rupani et al. [4] supported modelling of sandwich structure as equivalent homogeneous structure leading to best results. They observed that core gives high compressive strength in Z direction whereas face sheet gives shear strength in Z and Y direction. Altan et al. [5] successfully determined the reliability of the individual in-plane and out-of-plane effective elastic constants of honeycomb cores. Ijaz et al. [16] observed that the modified 'Gibson and Ashbey model' is the best analytical model to determine the orthotropic properties of a honeycomb core. Gibson and Ashbey initially determine the formulae for detection of nine orthotropic properties for honeycomb materials with constant wall thickness followed by the number of revisions by 'Zhang and Ashbey' to include the double wall thickness for the out of plane values. [22]

Hussain et al. [24] observed that the "Three point bending test (3PBT)" can be performed using numerical analysis and its result can be verified using the experimental setup. The FEA is the best option for testing of different sandwich structures.

Form the literature review; it has been observed that the performance of a composite sandwich panel depends on the different design factors such as material, thickness, orientation of factsheet and core, core cell size, use of adhesive, panel shape etc. Double-wall thickness regular hexagon honeycomb type cores are the extensively used cores

because of its low density and relatively higher shear properties. Aluminium, Steel and Nomex have been widely used materials for making honeycomb cores. The finite element Analysis (FEA) is the most widely used and accepted simulation method to predict the physical behaviour of systems and structures. For FEA the core can be converted onto an equivalent solid. But to develop an equivalent solid of a honeycomb core, the elastic orthotropic properties have to be calculated.

The most of the research has been done on determining the effects on various mechanical properties of sandwich structure due to variation only in the Sandwich's core height, core materials and core cell wall thickness [6, 7]. So the objective of this research is to find out the effect of two other design factors i.e. varying 'Honeycomb Core Cell Size & Panel Width' on Stiffness of a composite sandwich structure.

In this research, for numerical modelling of a sandwich structure, a sandwich structure, having Carbon fiber reinforced face sheet and a non-metallic material (Kevlar® Honeycomb) will be modelled. Gibson and Ashbey model formulae for honeycomb core will be employed to determine the equivalent orthotropic properties of Kevlar® Honeycomb core so that the honeycomb core can be converted into an equivalent solid. 3PBT will be performed on sandwich panel using Ansys as per C393 ASTM standard and ultimate load, deformation and the equivalent stiffness will be calculated. Then for experimental results, a composite sandwich will be fabricated and a 3PBT also will also be performed on it. The stiffness value obtained from numerical and experimental model will then be compared and if the values from different analyses will be successfully match then the model will be assumed as valid and will be recommended for numerical modelling of other similar sandwich panels. Then the three panels with different Core cell size and three panels with different Panel Width, with all others parameters remaining constant, will be designed and tested as per ASTM C393 standard [20] using ANSYS. After finding the values of equivalent stiffness for different configurations, an analysis of the effect of varying Honeycomb Core cell Size and Panel Width on the equivalent stiffness of sandwich panels will be made.

2. Material and Methods

2.1 Materials for different elements of a Sandwich Panel

The Carbon Fiber Reinforced Plastic, Regular Hexagon Kevlar Honeycomb and Epoxy have been used as the Face sheet, Core and Adhesive material respectively for design and fabrication of the sandwich structure. These different materials have been chosen as they are responsible for providing the different properties to the final Sandwich Structure. The different characteristics of face sheet, core and adhesive materials are as under-

Face Sheet Material (Carbon fiber)

Carbon fibers have elastic constants almost equivalent to steel, so they act as best material for face sheet manufacturing. They are resistant to moisture and chemicals and low in weight resulting in, reduced overall weight of the panel [15]. The different properties of Carbon Fiber Reinforced Plastic are shown in Table 1.

Table 1. Properties of Epoxy Carbon Woven (230 GPa) [6]

Property	Value
Young's Modulus (X- Direction)	61340 MPa
Young's Modulus (Y- Direction)	61340 MPa
Young's Modulus (Z- Direction)	6900 MPa
Poission's Ratio XY	0.04
Poission's Ratio YZ	0.3
Poission's Ratio XZ	0.3
Shear Modulus XY	195000 MPa
Shear Modulus YZ	2700 MPa
Shear Modulus XZ	2700 MPa

Core Material (Kevlar Honeycomb core)

It is made up of Aramid fibers which are arranged in the form of Para-Aramid fibers. Kevlar is about five times lighter than steel in terms of the same tensile strength. PK2 (Plascore) [23] has been used here as core material and the different in and out plane properties of the core has been shown below in Table 2.

Table 2. In and Out plane properties of the core [22]

S.N.	Property	Cell Size 3.2 mm	Cell Size 4.0 mm	Cell Size 4.8 mm
1	E_x (MPa)	0.287	0.25	0.142
2	E_y (MPa)	0.287	0.25	0.142
3	V_{xy}	0.999	0.999	0.999
4	G_{xy} (MPa)	0.013	0.009	0.006
5	E_z (MPa)	480.48	450	420.42
6	V_{xz} and V_{yz}	0	0	0
7	G_{xz} (MPa)	70	65	60
8	G_{yz} (MPa)	110	100	100

Adhesive (Epoxy Resin)

Epoxy Resins are low temperature curing materials, available in almost every form such as paste, films, powder or as solid adhesives and mostly have the shear strength of about 20-25 MPa.

2.2 Design Parameters

For designing the sandwich panels, four different design parameters i.e. Core Cell Size, Face Sheet Thickness, Core Height and Panel Shape have been selected.

To analyze the effect of variation of core cell size on stiffness property of a sandwich structure, three different sandwich Structures having three different core cell sizes i.e. 3.2 mm, 4 mm and 4.8 mm have been chosen. The other three design parameters i.e. Face Sheet Thickness, Core Height and Panel Shape for all the three sandwich structures have been kept same having the values .8 mm, 12.7mm and 45x200 mm^2 respectively.

To analyze the effect of variation of panel width on stiffness of a sandwich structure, three more sandwich structures having three different panel widths i.e. 40 mm, 45 mm and 50 mm have been chosen. The other three design parameters i.e. Core cell size, Face sheet thickness and Core height for the three sandwich structures have been kept same having

the values 3.2 mm, .8 mm and 12.7 mm respectively. The Figure 2 shows an equivalent composite sandwich structure having b, c, t and d as width, core thickness, face sheet thickness and overall thickness of composite respectively with a panel size of 45x200 mm^2.

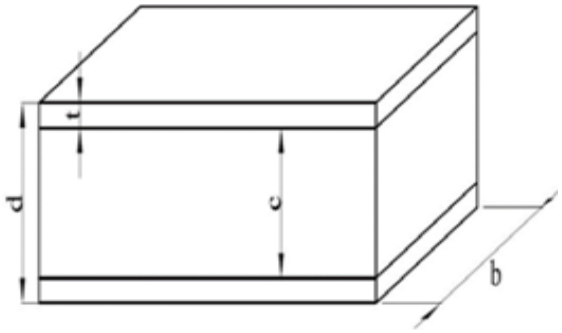

Fig. 2. Equivalent Composite Sandwich structure

2.3 Modelling and FEA of Sandwich Panel

Modelling is done in the Ansys. The Face sheets are modelled orthotopically in the Ansys composite prep-post while the homogenised core is modelled in Design modeller available in Ansys. The homogenised core is modelled by replacing honeycomb cells with a solid core that acts as a honeycomb itself in a macroscopic view as shown in Figure 3(a, b). The solid core is given the same orthotropic properties as the honeycomb core. The main advantage of this method is that the number of elements in solid core is highly reduced than the actual honeycomb geometry. Hence this method is computationally cheap. The homogenized core is meshed using SOLID 186 elements while face sheet is meshed using SHELL 181 elements.

Bonded contact is assigned such that face sheet have 'contact body' and core have 'target body' setting. Default 'program controlled' was used to set up the formulation of contact, hence it considers the FEA approach as penalty method.

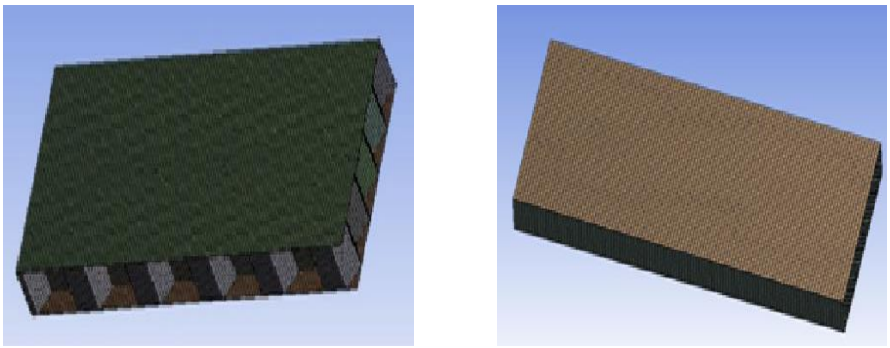

(a) (b)

Fig. 3. Sandwich model (a) honeycomb core (b) equivalent solid core

The Finite Element Analysis is the best and much powerful numerical techniques to solve the complex physical phenomenon regulated by the differential equations. Lots of practical engineering problems can be analyzed by the Finite Element Analysis. Out of the above mentioned 6 sandwich configurations, a sandwich panel having core cell size 3.2 mm, face sheet thickness .8 mm, core height 12.7mm and panel shape of 45x200 mm^2 has been randomly selected for Finite Element and Experimental Analysis, so that the model can be validated.

2.4 Fabrication of sandwich panel

The process of fabrication of sandwich structure having Honeycomb Core and Carbon fiber has been completed using the "Vacuum Assisted Hand Layup Method". Initially a surface has been prepared and a mold has been set with double side tape. Than wax coating has been applied on the working area for easy removal of sandwich plate after fabrication. After 10 minutes of application of wax, epoxy resin has been applied on the surface and then a carbon fiber of required specification has been placed on it and again epoxy has been applied on it. Then honeycomb core has been placed on the carbon fabric layer and again epoxy resin has been properly applied on it followed by placing of carbon fabric on the top of honeycomb core. Then the structure has been covered with a blue perforated film followed by peel ply. Then the entire set up has been covered with breather fabric so that the vacuum process can be easily performed. After fixing of breather fabric layer vacuum bag is connected and close the all sides carefully. After that a vacuum pump has been switched on so that air can be sucked from the bag as shown in Figure 4. Utmost care has to be taken during this process as leakage in the system and possibility of air bubble can lead to defects in the sandwich structure layer bonding.

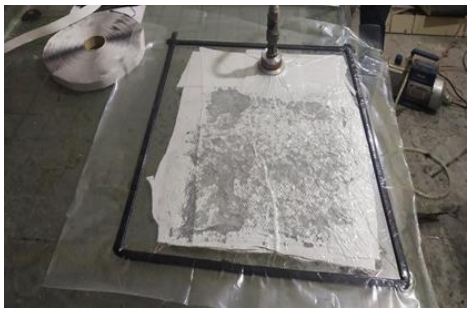

Fig. 4. Final set up for sandwich structure

Then this set up has been left for about a day for curing and then the sandwich has been brought out followed by cleaning of the edges of the sandwich panel with carbide tip/grit. Figure 5 shown below gives the view of a finally fabricated sandwich structure having Kevlar as a honeycomb core.

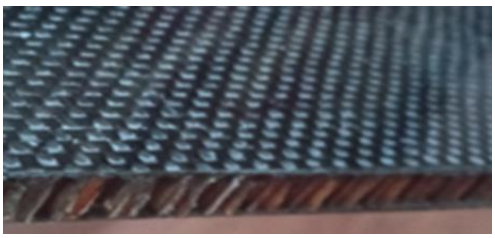

Fig. 5. Final sandwich structure

The Three Points Bend Test has been performed on two sandwich panels as per ASTM C393 standard and the values of critical load and deflection has been calculated for both of these specimens. The testing setup on universal testing machine has been shown in Figure 6.

Fig. 6. Three-point bend testing set up for sandwich pane

4. Results and Discussion

4.1 FEA of Sandwich Panel

After defining the material properties and modelling of the sandwich panel, the panel is imported in the static structure module of Ansys. A load is applied until the failure of the panel according to the standards of ASTM C-393. The sandwich will fail due to shear crimping which arrives due to weak core material as compared to the face sheets and when the shear stress due to load in the homogenized core reaches the shear strength in the X direction. This load is called the Ultimate load.

Ultimate Force calculated by FEA for sandwich panel using Ansys as per ASTM C 393 standard has been shown in Figure 7 and it has been observed that the Ultimate Load achieved for this sandwich panel is 1949.5 N.

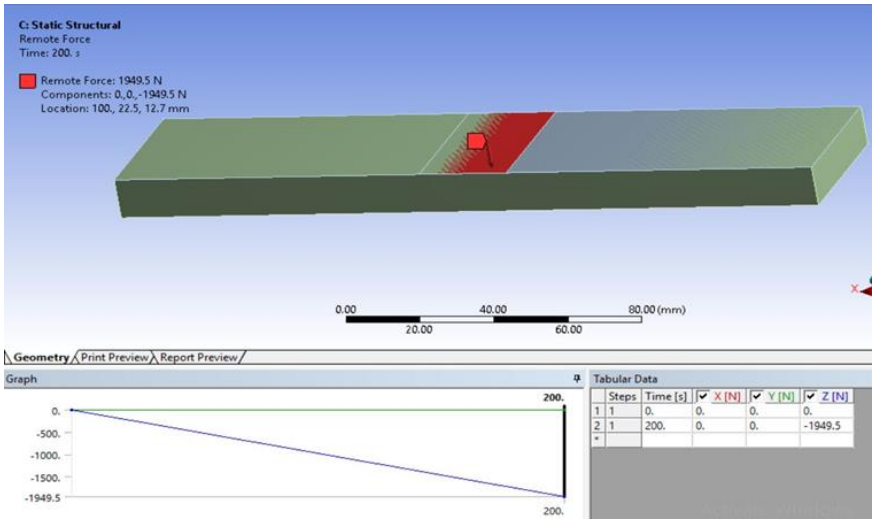

Fig. 7. Ultimate load using FEA

Figure 8 shown below determines the deformation of composite sandwich panel using Ansys as per ASTM C 393 standard. The Deflection found at Ultimate load is 2.017 mm.

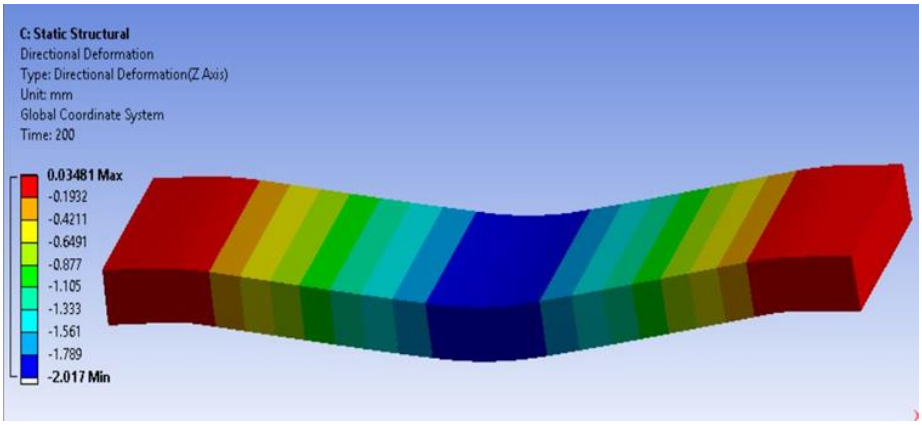

Fig. 8. Deformation at ultimate load using FEA

For Pre-buckling stage i.e., from starting of application of load to the ultimate load condition, the sandwich panel gives a linear elastic deformation and the ratio of ultimate load to deflection gives the stiffnessof the sandwich panel.

Ultimately, the Stiffness of panel= Load/deflection= 1949.5/2.017= 966.53 N/mm.

4.2 Experimental Analysis of Sandwich Panel

3PBT have been performed on two samples of sandwich panel as per ASTM C393 standard. Figure 9 (a) shows the condition of a test specimen during the 3PBT whereas the Figure 9(b) shows the condition of two test specimens after 3PBT. The values of critical load, deflection and stiffness have been calculated for two samples as shown in Table 3. It has been observed that the sandwich panel failed due to shear crimping which arrived due to weak core material.

(a) (b)

Fig. 9. Test specimens (a) under 3PBT (b) after 3PBT

Table 3. Load, Deflection and stiffness of Test Samples

Critical Load, Pc [N]	Avg. Critical load [N]	Deformation [mm]	Average Deformation [mm]	Stiffness [N/mm]
1703	1719.5	1.680	1.696	1013.85
1736		1.713		

4.3 Validation of Finite Element Model

To check the validity of the generated model, the values of stiffness obtained from 2 types of analyses has been compared as shown in the Table 4-

Table 4. Comparison of results of FE and Experimental analyses

FEA Results Stiffness (N/mm)	Experimental Results Stiffness (N/mm)	% Error
966.53	1013.85	4.66%

Table 4 shows that the difference between the results of Numerical and Experimental methods is below 5%. This shows that the two types of analysis are in good agreement with each other and the Model generated is valid and hence this model can be utilized for analysis of similar type of composite sandwich structures.

4.4 FEA of all six Sandwich Structures

FEA of all sandwich panels have been done using same model with different design parameters mentioned above and the results obtained are under in Table 5.

Table 5. Stiffness of panels for varying cell size and panel width

Confi. No.	Design Factor	Value	Ultimate Load (N)	Deformation (mm)	Stiffness (N/mm)
1	Core Cell Size (mm)	3.2	1949.5	2.016	967.01
2		4	1932	1.99	970.85
3		4.8	1928	2.0	964
4	Panel Width (mm)	40	1741.5	1.86	936.29
5		45	1949.5	2.016	967.01
6		50	2181	1.62	1346.29

Table 5 shows the different values of ultimate load, deformation and ultimately the stiffness of these sandwich structures. The stiffness for three sandwich panels having cell sizes as 3.2 mm, 4mm and 4.8 mm are 967.01, 970.85 and 964 N/mm respectively and it is evident from the Table 5 that honeycomb core cell size does not have a significant effect on the stiffness properties of a composite sandwich panel. This is in accordance with the analytical results made by Gibson and Ashbey [1] that, the stiffness in mainly a factor dependent on the properties of the facesheet and the thickness of the core of sandwich panel.

Also three different panel widths i.e. 40 mm, 45 mm and 50 mm have been chosen for 3 different sandwich structures and FEA for these sandwich panels have been done. The stiffness for three sandwich panels having panel widths of 40 mm, 45 mm and 50 mm are 936.29, 9670.01 and 1346.29 N/mm respectively. It is clear from the Table 5 that with the increased panel width the stiffness of composite panel increases significantly.

5. Conclusions

This research is aimed to analysis the effect of variation of core cell size and panel width on stiffness property of sandwich panels, for which six different configurations of sandwich structures have been proposed, three configurations have the varying cell size i.e. 3.2 mm, 4 mm and 4.8 mm and the other three configurations have the varying panel width i.e. 40 mm, 45 mm and 50 mm keeping rest of the design parameters unchanged. Then FEA in ANSYS has been performed for all these six configurations and stiffness has been calculated for each panel. From the analysis of the stiffness values based on different criteria-

- It has been observed that honeycomb core cell size doesn't have a significant effect on the stiffness properties of a composite sandwich panel. This is in accordance with the observations made by Kiran et al [21] and Zhang and Ashbey [22] that the core cell size of a honeycomb core has negligible effect on the stiffness property of a composite sandwich panel.
- Also it has been found that with increased panel width the stiffness of composite panel increases significantly.

Acknowledgement

The authors acknowledge the support of Mechanical Engineering Department of G. B. Pant Government Engineering College, New Delhi, India for allowing them to use the labs for the experimental work for this research work.

References

[1] Gibson J, Ashby A. Cellular Solids: Structure and Properties, Cambridge University Press, 2001.
[2] Vamja DG, Tejani GG. Experimental Test on Sandwich Panel Composite Material, International Journal of Innovative Research in Science, Engineering and Technology, 2013;2(7):3047-3054.
[3] Kumar JS, Kalaichelvan K. Taguchi-Grey Multi-Response Optimization on Structural Parameters of Honeycomb Core Sandwich Structure for Low Velocity Impact Test. Silicon, 2017; 10(3): 879-889. https://doi.org/10.1007/s12633-016-9544-3
[4] Rupani SV, Jani SS, Acharya GD. Design, Modelling and Manufacturing aspects of Honeycomb Sandwich Structures, International Journal of Scientific Development and Research, 2017; 2(4):526-532.
[5] Çınar O, Erdal M, Kayran A. Accurate Equivalent Models of Sandwich Laminates with Honeycomb Core and Composite Face Sheets via Optimization Involving Modal Behavior, Journal of Sandwich Structures & Materials, 2017;19(2):139-166. https://doi.org/10.1177/1099636215613934
[6] Kumar A, Angra S, Chanda AK. Analysis of the effects of varying core thicknesses of Kevlar Honeycomb sandwich structures under different regimes of testing, Materials Today: Proceedings, 2020; 21:1615-1623. https://doi.org/10.1016/j.matpr.2019.11.242
[7] Prakash MDAA, Guptha VLJ, Sharma R S, Mohan B. Influence of Cell Size on the Core Shear Properties of FRP Honeycomb Sandwich Panels, Materials and Manufacturing Processes, 2011; 27(2): 169-176. https://doi.org/10.1080/10426914.2011.560227
[8] Arbaoui J, Schmitt Y, Royer F. Effect of core thickness and intermediate layers on mechanical properties of polypropylene honeycomb multi-layer sandwich structures. Archives of metallurgy and material, 2014; 59(1): 11-16. https://doi.org/10.2478/amm-2014-0002
[9] Thomas T, Tiwari G. Crushing behavior of honeycomb structure: a review, International Journal of Crashworthiness, 2019: 1-25.

[10] Rao KK, Rao KJ, Sarwade AG, Chandra MS. Strength Analysis on Honeycomb Sandwich Panels of different Materials, International Journal of Engineering Research and Applications, 2012; 2(3): 365-374.
[11] Akiwate SB, Shinde VD. Experimental Investigation of Bending behaviour of Aluminum Alloy Honeycomb Sandwich Structure using Four Point Bending Tests, International Journal for Innovative Research in Science & Technology, 2017; 4(1):97-101.
[12] Kumar A, Chanda AK, Angra S. Analysis of effects of varying face sheet thickness on different properties of composite sandwich Structure, Materials Today: Proceedings,2021;38(1): 116-121. https://doi.org/10.1016/j.matpr.2020.06.114
[13] Mohammed DF, Ameen HA, Mashloosh KM. Experimental and Numerical Study of Bending Behavior for Honeycomb Sandwich Panel with Different Core Configurations, The Iraqi Journal for Mechanical And Material Engineering, 2016; 16(4):315-328.
[14] Uddin M, Gandy HTN, Rahman MM. Adhesiveless honeycomb sandwich structures of prepreg carbon fiber composites for primary structural applications, Advanced Composites and Hybrid Materials,2019; 2(2): 339-350. https://doi.org/10.1007/s42114-019-00096-6
[15] Ashraf W, Ishak MR, Zuhri MYM, Yidris N, Yaacob AMB, Asyraf MRM. "Investigation of different facesheet materials on compression properties of honeycomb sandwich composite." In Seminar Enau Kebangsaan, 129-132. 2019.
[16] Ijaz H, Asad M, Memon A, Ahmed K B, Abbasi H, Laghari A N. Strain Energy Based Homogenization Method to Find The Equivalent Orthotropic Properties of Sandwich Structures. Sindh Univ. Res. Jour. (Sci. Ser.), 2014; 46(1): 93-98.
[17] Laurent W, Stefan M, Daniele W, Arno Z, Patrick F. Shear stresses in honeycomb sandwich plates: Analytical solution, finite element method and experimental verification, Journal of Sandwich Structures and Materials.2012; 14:449-468. https://doi.org/10.1177/1099636212444655
[18] Lister J. [2014]. Study the effects of core orientation and different face thicknesses on mechanical behavior of honeycomb sandwich structures under three point bending. [Thesis, Masters of Science in Aerospace Engineering, The Faculty of California Polytechnic State University, San Luis Obispo].
[19] Liu LL, Wang H, Guan ZW. Numerical models with layered elements for Nomex honeycomb core under flat wise compression", 20th International Conference on Composite Materials, Copenhagen, 19-24th July 2015.
[20] ASTM C393 / C393M-20, Standard Test Method for Core Shear Properties of Sandwich Constructions by Beam Flexure, ASTM International, West Conshohocken, PA, 2020, www.astm.org.
[21] Kiran S, Balasundar MP, Gopinath IK, Raghu T. Parametric study on factors influencing the stiffness of honeycomb sandwich panels using impulse excitation technique. Journal of Sandwich Structures & Materials, 2019; 21(1):115-134. https://doi.org/10.1177/1099636216686649
[22] Zhang J, Ashby MF. The Out-of-Plane Properties of honeycombs, International journal of Mechanical science, 1992; 34(5):475-489. https://doi.org/10.1016/0020-7403(92)90013-7
[23] https://www.plascore.com/download/datasheets/honeycomb_data_sheets/PLA_PK2_2019.pdf . (Accessed 2019 Jan. 20)
[24] Hussain M, Khan R, Abbas N. Experimental and computational studies on honeycomb sandwich structures under static and fatigue bending load. Journal of King Saudi University, 2019, 31:222-229. https://doi.org/10.1016/j.jksus.2018.05.012

Research on Engineering Structures & Materials
journal homepage: http://www.jresm.org
MIM Research Group

Review Article

Recent developments in vibrothermography

Orhan Gülcan

General Electric Aviation, Gebze, Kocaeli, Turkey

Article Info

Article history:
Received 22 Aug 2021
Revised 25 Oct 2021
Accepted 26 Oct 2021

Keywords:
Vibrothermography;
Ultrasound excitation;
Non-destructive testing;
Infra-red

Abstract

Due to the sensitivity of fluorescent penetrant inspection to surface roughness of the inspected material, researchers have been investigating alternative inspection methods. Vibrothermography is one of the contactless non-destructive testing methods in which vibration pulses with high frequencies (typically 20-40 kHz) are used in a part for a short period of time to produce thermal gradient at the defect. In this technique, thermographic or infra-red cameras are used for radiation detection due to thermal gradient in the range of 0.9-14 μm electromagnetic spectrum. This paper focuses on the recent developments in vibrothermography. It covers basics, history, equipments used, types, materials, probability of detection, principle of heat generation mechanism and factors that affect detectability in vibrothermography.

1. Introduction

Inspection is one of the main steps in quality control of manufactured parts. Although there are different inspection methods used in different industries, liquid / fluorescent penetrant inspection (FPI) method has found wide industrial application. The main disadvantage of FPI is its need for a very smooth examination surface. Therefore, surface roughness of the examined parts should be lowered by machining, polishing or similar techniques before FPI [1]. Due to this disadvantage, researchers have investigated different alternatives for FPI. One of the alternatives for FPI is infra-red (IR) thermography which is less affected by surface roughness [2]. IR thermography depends on thermal properties of the material and thermal gradients occurred in the inspected part rather than material geometrical parameters which makes it a good inspection alternative to FPI [3].

When an object is heated, it radiates electromagnetic energy. This energy depends on object's temperature. When temperature sensors are used, these sensors collect the energy and make a relation between the intensity of the gathered radiation and object's temperature [4]. Temperature distribution of the surface exposed to a thermal gradient can be recorded by an IR camera [5]. If a material with a crack in the surface and/or sub surface is heated, the thermal gradient over the crack will be different from the surrounding area. This thermal gradient difference can be used to detect and quantify the related crack [6]. Based on this philosophy, IR thermography is a contactless non-destructive testing method for determining the temperature response of a material by converting the radiation that is given off by the surface as it is heated up into an electrical signal through the use of specialized sensors that convert infrared radiation into electrical signals [7].

In electromagnetic spectrum, the infrared spectrum covers 0.74-1000 μm wavelength range. The most widely used wavelength ranges in infrared thermography applications are near IR (NIR) (0.74–1 μm), short-wave IR (SWIR) (1–3 μm), mid-wave IR (MWIR) (3–5

Corresponding author: orhan.gulcan@ge.com
http://orcid.org/0000-0002-6688-2662
DOI: http://dx.doi.org/10.17515/resm2021.333me0822

μm) and long-wave IR (LWIR) (8–14 μm). MWIR and LWIR are widely used for detection of sub-surface defects in non-destructive testing applications [8].

The basis of IR thermography is thermal rays whose existence was believed to be proposed by Titus Lucretius Carus (99-55 BCE), but the first person officially discovered the IR radiation in 19th century is Sir William Herschel who first called it "invisible light" and later "infrared" [9]. Then in 20th century, German physicist Max Planck (Planck's law) precisely described blackbody radiation. Later, Albert Einstein suggested that photons with separate energies are the basis of an electromagnetic wave, such as light [10]. In 1947, transistor was discovered and after this discovery, the first cryogenic cooled IR detectors emerged. In 1965, first commercial IR cameras were discovered to detect scene images which used a single detector mounted to an optical-mechanical scanning mechanism. From 1970s to 1990s, different IR cameras with more and more resolution have started to be seen commercially (nowadays largest arrays are 2048 × 2048) [11]. Due to the unavailability of IR cameras with high temperature resolution until 1990s, pioneering works lacked continuity but with the development of affordable IR cameras with high temperature resolutions (between 20 to 30 mK range) in the late of twentieth century, IR thermography started to be used widely in different industries [12].

IR thermography needs an external stimulation to produce thermal gradient in the material. This stimulation can be heat lamps, eddy current or mechanical excitation. Based on stimulation types, IR thermography can be categorized mainly as lock-in thermography, pulsed thermography, eddy current thermography and vibrothermography (Fig. 1) [13].

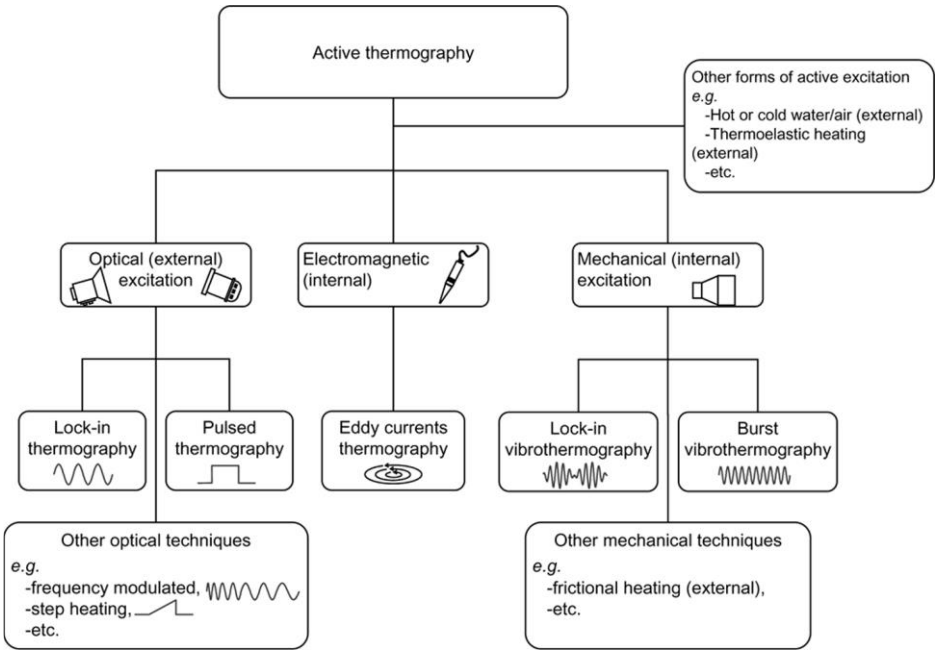

Fig. 1 Active thermography methods [13]

2. Basics and History of Vibrothermography

Vibrothermography is a type of IR thermography methods in which ultrasound excitations are used to produce thermal gradient in the material (Fig. 2) [14]. Thermosonics, ultrasonic infrared thermography, sonic IR, acoustic thermography, vibro IR, elastic-wave-

activated thermography or thermal vibration method are some of the similar names given to vibrothermography in scientific literature [15]. Vibrothermography is based on the idea of applying a vibration pulse with a high frequency of typically 20-40 kHz to a material for a very limited time of less than one second and with the help of produced thermal gradient at the crack/defect area, using an IR camera to produce images of changes in heating and cooling process [16]. In general, vibrothermography has mainly three main steps; vibration, heat generation and heat detection. First of all, vibration pulse must be applied to the part with the help of a vibration source to interact with any existing defects in inspected specimen. Next, thermal gradient is generated at the defect area due to different mechanisms. Then, this thermal gradient will radiate away from the defect region via conduction and be detected by an IR camera [17].

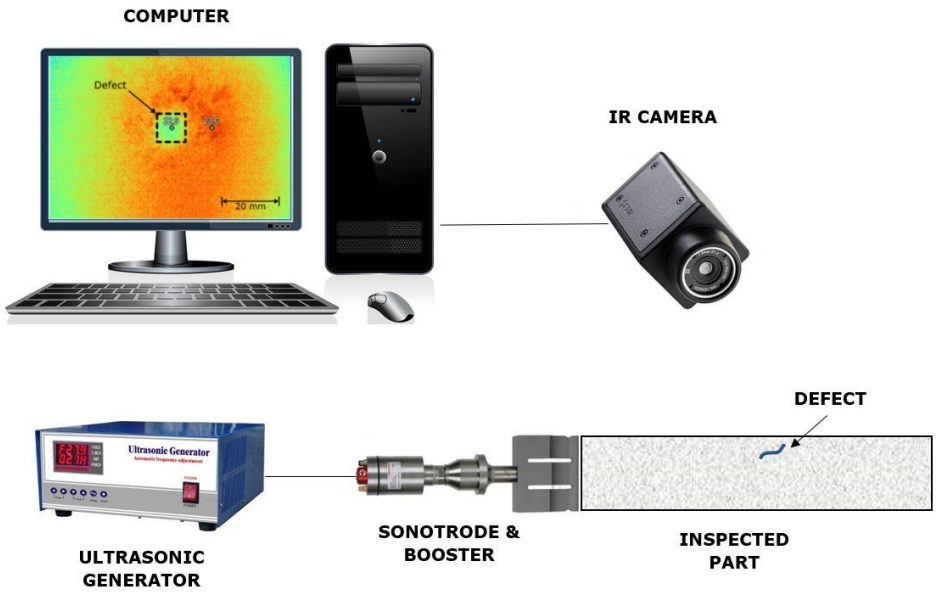

Fig. 2 Vibrothermography with ultrasonic thermal excitation

When a surface and /or a subsurface crack are excited by a nearly 20 kHz vibration pulse, it becomes a thermal source, because of frictional dissipation at the surfaces of the crack [18]. Thomas stated that this thermal source reveals a crack's presence on a time scale much less than a second. He also suggested that only the crack (not saw-cut) heats up significantly in the presence of the vibration excitation [19]. On the contrary to IR thermography, where very narrow cracks may not be detected due to low thermal gradient they produce when subjected to heat, vibrothermography is based on the idea of relative motion of crack faces when sample is excited with ultrasounds. This relative motion produces heat which spreads out in the material and finally reaches surface of the inspected part. IR camera detects this surface temperature elevation revealing the presence of the crack [20]. As Renshaw et al. stated, since frictional rubbing, one of the heat generation mechanisms in vibrothermography, is not affected by crack openings for an effective inspection, vibrothermography has greater reliability with detection of tighter cracks than other non-destructive testing methods [21].

In 1970's Henneke et al. used vibrothermography in composite materials and observed and measured large temperature variations around delaminations. He attributed this thermal gradient to generated heat at delaminations and low thermal conductivities of

polymer-based materials [22]. This was the first usage of vibrothermography in scientific literature, but the details of mechanics of vibrothermography was given by Reifsnider et al. in 1980 [23]. In 1981, Mignogna et al. used vibrothermography technique to detect cracks in steel, brass, copper and aluminum parts. They concluded that if there were no large defects in the material, heat was observed to flow uniformly through the material, but if there were natural and artificial defects, such as grain boundaries, fatigue cracks and saw cuts, then heat gradient was observed at the sites of these defect regions [24]. Lock-in vibrothermography where response of a material was analyzed with respect to the modulation frequency was proposed in 90s [25]. Then later, in 21st century, ultrasound burst phase thermography [26] and ultrasound frequency modulated thermography [27] were proposed.

Being a very effective technique with simple and robust test setup and short measurement time, vibrothermography requires only simple image processing which makes it easy to implement in various applications [28]. It finds its usage in different industries and applications as non-destructive defect detection; aircraft structure wings, automobile engines, biomedical devices etc. [29]. Zweschper et al. stated that vibrothermography can detect areas of cracks in rows of rivets, hidden corrosion, disbonds, delaminations and impacts in aerospace structures [30]. DiMambro et al. used vibrothermography and detected several cracks in a Boeing 767-wheel half, bolt, brake key and brake manifold and in second and fourth stage turbine blades from a Pratt and Whitney JT-8D aircraft engine [31]. Zalameda et al. used vibrothermography method in helicopter blades and their study successfully revealed core damages in sandwich honeycomb structures [32]. Guo and Ruhge used vibrothermography in service-retired gas turbine blades to inspect low-cycle fatigue cracks. They stated that vibrothermography favors FPI and visual non-destructive testing in terms of defect detection [33]. Szwedo et al. applied vibrothermography to fuselage panels and mating parts of a jet fighter aircraft successfully [34]. Apart from aviation industry, vibrothermography has been applied to bonded joints in modern automobiles to detect defects including entrapped air, kissing bonds, poor adhesion and non-cured or missing adhesive [35], to historical and archaeological discoveries for surface crack and defect detection [36] and to sports equipment for detection of mechanical performance of tennis racket strings [37, 38].

3. Vibrothermography Equipments

Generally, a vibrothermography set up consists of a transducer system, specimen, IR camera and in some cases vibrometer. A transducer system or vibration source consists of a piezoelectric transducer, a sonotrode which conveys the signal to the inspected part and a booster, which changes the signal [39]. To prevent hammering action on the surface of inspected part and harmonic generation, contact between transducer and inspected part should be maintained. For that purpose, sometimes a pneumatic cylinder can be used to press transducer against the inspected part. Holding the specimen in place especially during vibration excitation and inspection is very important in vibrothermography since it is an ultrasound process. For that purpose, clamps can be used. Between clamps and the specimen, rubber mounts can be placed to reduce the vibration effect of the mounting on specimen [17]. When excitation is applied to the specimen, the defected area will behave differently than the surrounding area which will be detected and visualized by vibrometer. IR or thermographic cameras are used for radiation detection in the range of 0.9-14 μm electromagnetic spectrum [40].

In most of the cases, a coupling media is strongly recommended to be inserted between the transducer and the sample to reduce the risk of specimen damaging, to place the specimen correctly, to increase quality of ultrasound transmission and to reduce the possibility of unwanted heat creation in the vicinity of excitation point [13]. In scientific

literature, different coupling medias such as moisten fabric, aluminum or water-based gels have been used [15]. Zweschper et al. suggested using thin aluminum plate [41], Renshaw et al. used a business card or piece of cardstock [17], and Guo and Vavilov used 0.16 mm-thick piece of plastic as coupling media [42].

4. Types of Vibrothermography

Depending on oscillating amplitude and excitation frequency, vibrothermography can be classified as ultrasonic ultrasonic burst phase thermography, lock-in thermography and ultrasonic sweep or ultrasonic frequency modulated thermography [43, 44]. In ultrasonic lock-in thermography, a frequency of a few tens of millihertz is used to excite the part and produce a phase and an amplitude image [45]. On the other hand, in ultrasonic burst phase thermography, a single vibration pulse with a frequency of 20-40 kHz is used to heat the defect locally in a very short period of time [46]. When there is a subsurface defect in the specimen, defect surfaces will move relative to each other giving rise to a heat increase in this area which then be monitored by IR cameras [47]. Ultrasonic sweep or ultrasonic frequency modulated thermography is based on determining the thermal gradient change with respect to ultrasonic excitation at various frequencies in the range of typically 15 - 25 kHz and at constant vibration amplitudes [48, 49].

5. Vibrothermography Advantages and Disadvantages

All IR thermography methods are based on producing thermal gradient in the material and are constrained thermal diffusion rate within specimen. Apart from other IR thermography techniques where the heat has to travel from the surface to the defect area and return to the surface again, in vibrothermography, heat has to travel from the defect area to the surface only which make vibrothermography a very fast method [50]. Ibarra-Castanedo et al. compared different types of IR thermography techniques and stated that vibrothermography is capable of determining deeper damages than other techniques because in this technique, thermal waves have to travel shorter distances due to internal heat generation [51]. Surface-breaking and subsurface cracks with any orientation with respect to the surface of the part can be seen without the necessity for applying paint, or other emissivity-modifying coatings in vibrothermography [52]. Bolu et al. applied vibrothermography to defected and undefected turbine blades and stated that no apparent change in the resonance behavior of blades was observed which showed vibrothermography as a safe NDT method for turbine blades [53].

The general advantages of vibrothermography can be listed as follows [54, 17]:

- It can detect surface and sub-surface defects over a large area in a few seconds;
- It is a simple inspection method where the inspected parts often do not need cleaning;
- The probability of defect detection is high;
- It is sensitive to material thermal properties differences rather than material geometrical properties differences (scratches, high surface roughness, etc.) which is a real problem in most of other non-destructive inspection methods.

Despite these advantages, the widespread application of vibrothermography has been limited so far due to repeatability issue. Renshaw et al. stated that some permanent microscopic changes including fretting, plastic deformation, oxidation, adhesive wear and phase transformations can occur within the material in vibrothermography which causes the problem of lack of repeatability and suggested using minimum vibrational stresses [55]. The need for contact between the sample and the transducer is one of the most important challenge in vibrothermography. Since this contact is mostly made manually, the produced vibration spectrum is variable from contact to contact [56].

6. Materials and Probability of Detection

Vibrothermography can used in different industries and applications for defects detection in different materials. In aerospace applications, vibrothermography has been used in different parts made of CFRP, C/C-SiC and different metals [57]. Rantala et al. applied vibrothermography for defect detection in polymer and composite specimens. The results showed that material discontinuities, such as small cracks, voids and impact damages can be easily detected by using this technique [44]. Vibrothermography was successfully applied to Glass Reinforced Fiber Metal Laminates (GLARE) for detection of artificial defects [41].

Inspection capability or probability of detection of any non-destructive testing is very important for suitable selection of the method for the target material. The cracks in rigid and heavy metal structures are more difficult to detect due to their greater mass and stiffness, [58]. Favro et al. employed high frequency excited vibrothermography for detection of small fatigue cracks (about 0.7 mm in length) in aluminum and delaminations between plies in CFRP composite specimens [16]. Vertical fatigue cracks in aluminum alloy specimens, with 2 mm, 3 mm and 4 mm crack depths and with crack lengths of approximately 1.5 mm were successfully detected via vibrothermography [18]. Solodov et al. stated that aluminum aviation components can be inspected via vibrothermography with 11.6 kHz excitation frequency [59].

Mabrouki et al. stated that vibrothermography has capable of detecting surface cracks as short as 0.1 mm in steel plates [60]. Weekes et al. applied vibrothermography on airplasma sprayed CoNiCrAlY coated Inconel parts and concluded that cracks buried beneath a metallic coating remain detectable by vibrothermography, although they are less easily detected [61]. DiMambro et al. performed vibrothermography on 144 Ti64 specimens and 92 Inconel 718 specimens. These specimens had known fatigue cracks (0.016-0.182 inches lengths for Ti64 and 0.022-0.422 inches lengths for Inconel 718). They stated that for crack sizes 0.04 inches and more, vibrothermography came out to have higher probability of defect detection than FPI inspection [62]. Vibrothermography can be applied to detect as small as 20-micron long cracks in titanium fatigue samples [63].

Han et al. used vibrothermography for crack detection in a complex-shaped massive aircraft engine disk. They detected very small cracks (20 μm) in this study [64]. Almond et al. used laser spot thermography, eddy current thermography and vibrothermography for crack detection in metal parts. They stated that they detected corrosive cracks with 8 mm lengths and opening less than 1 μm in a last-stage steam turbine blade with vibrothermography technique [65]. Studies conducted by Montanini et al. revealed that 3.5 mm depth discontinuities below the surface can be detected with vibrothermography [46].

7. Principle of Heat Generation in Vibrothermography

As stated before, vibrothermography relies on heat generation in cracks due to excitation of the material with vibration pulse. Generally, three mechanism have been proposed for heat generation in cracks: frictional rubbing of crack surfaces / faces, plastic deformations due to propagation of cracks and viscoelasticity / material damping [66]. Many researchers simply labeled heat generation in vibrothermography as friction induced, but other researchers suggested that thermo-plastic heat generation or thermoelasticity, viscoelasticity and anelasticity, or a combination of these mechanisms are the sources of crack heating [67]. For instance, Montanini et al. stated that for flat-bottomed hole defects, viscoelasticity is the primary heat source, on the other hand the combination of viscoelasticity and friction is the primary heat source for elamination and cracks [68]. Vavilov et al. stated that friction between defect surfaces or plastic deformation are the main source of defect detection in composites [9]. Bai et al. stated that crack frictions and

viscoelasticity are main contributions to the heat generation in vibrothermography [69]. The study conducted by Schiefelbein suggests that friction or adhesion are the main cause of heat generation in vibrothermography rather than plastic flow, linear absorption or thermoelasticity [67].

For frictional heating in crack faces, three relative motion modes were proposed in the literature (Fig. 3). It was suggested that the anti-plane shear mode (mode III, rubbing mode) and the tensile mode (mode I, clapping) might be the two modes responsible for the heat generation at the crack faces. It was also noted that the in-plane shear mode (mode II, rubbing) has very little contribution to the heat generation at the crack faces due to its significantly smaller relative magnitude when compared to the other modes [70].

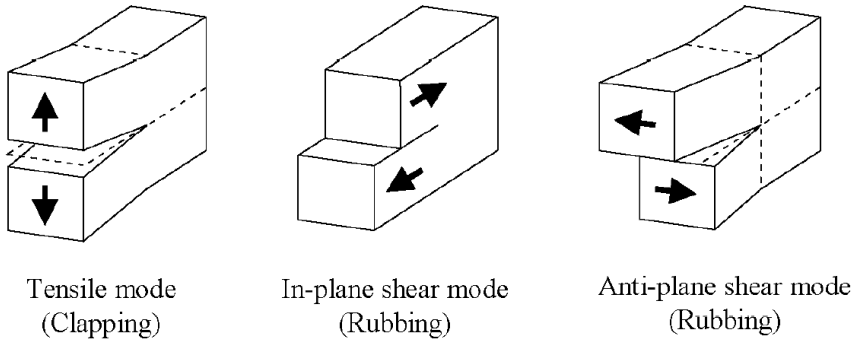

Fig. 3 Possible crack vibrational modes I to III (from left to III) [70].

In vibrothermography, if the parts go compression loading, the heating effect in crack closure tends to decrease due to limited friction between contacting faces [71]. On the other hand, Renshaw et al. have shown that under tensile loading of titanium, heat generation due to crack moves to the crack-tips without a heat generation in the central region. This is due to the fact that, under tensile loading, no relative movement toward the crack-tips and away from the crack-tips are observed. On the other hand, heat is generated due to the relative movement of contacting faces between these two regions [21]. The same conclusion was proposed by Weekes et al. when inspection of austenitic nickel super-alloy samples with vibrothermography [72].

Since determination of heat generation mechanism in vibrothermography is rather complex, artificial defects can be used to investigate the heat generation mechanism. Renshaw et al. used viscous material-filled synthetic defects in vibrothermography for heat generation. They stated that when the specimens were excited with resonant modes, honey filled drilled holes generated heat very efficiently when the beam vibrated in resonant modes [73].

8. Factors That Affect Vibrothermography Performance

Table 1 shows vibrothermography measurements for different materials and technical details of these experimental studies performed in literature. There are several factors that affect defect detection in vibrothermography: excitation frequency, crack size, loading mode, dynamic stress, crack closure etc.

Excitation frequency and amplitude of the vibration are two key parameters in successful detection of cracks in vibrothermography. For efficient crack detection, sufficient amplitude vibrations should be used. On the other hand, when high amplitude vibrations are used, specimen may be damaged [74]. Experimental studies have shown that metal

parts depend highly on frequency when inspected [75]. Holland et al. showed that when frequency is increased, heat generation also increases in fatigue cracks detection [76]. On the other hand, Qingju et all. stated that the higher frequency results in noisier phase image. Therefore, it is hard and sometimes impossible to detect defects for larger frequencies [77]. Song and Han studied the effect of frequency on crack detectability in vibrothermography. They used three different frequency (20, 30 and 40 kHz) on Al bars. They concluded that when frequency is increased, acoustic energy and detectability of cracks decrease [78].

Due to convenience and commercial availability, fixed frequency excitation is commonly used in most of the studies. However, it has been demonstrated that each defect has a particular resonant frequency, referred to as the local defect resonance (LDR), at which its response will be maximized. For instance in a study conducted for defect detection in 28 x 13 cm graphite epoxy beam, it was revealed that two artificial and embedded defects of 10 x 7 mm and 7 x 7 mm sizes can be seen only between 13.5 and 15.0 kHz excitation frequencies [79]. For overcoming this problem, one promising approach is finding LDR values of defects via FEM analysis and stimulating the material with these values or using multi-frequency excitation [80]. By using this method, different defects with different sizes can be detected by changing the vibration at related LDR frequency [81-83]. For distinguishing damaged regions from surroundings, multi-frequency excitation is a very useful method which enables that the resulting heat generation covers the whole length of the material [84, 85]. There are two advantages of multi-frequency excitation; first, reducing the number of excitation locations needed to form a complete picture of the defects present within a material; and second, reducing the number of blind zones that cannot be detected with single frequency implementation [86].

There are two other factors which affect crack detectability in vibrothermography: the crack closure amount and closure stresses distribution between crack faces [21]. If the crack surfaces are too close, then the relative motion between crack faces will be limited and heat generation at defects will not be enough for detection by IR camera [17].

Low surface emissivity is also a very important thermal property which can reduce the detectability of cracks in vibrothermography [17].

Type of mounting, excitation point location, pressure applied against mounting faces, and quality of coupling quality are main factors which are responsible for proper crack detection in vibrothermography [42]. For sample mounting methods, Xu et al. conducted vibrothermography experiments on a thin aluminum beam where three cracks were located in different locations. They suggested that for these types of thin specimens, double fixed ends configuration is the best way for detecting of cracks [87]. For holding pressure, Min et al. concluded that when engagement force increases, the temperature rise also increases [88]. For the location of the excitation point, Liu et al. stated that this location should be closer to the defects which are located at greater depth from the surface [89]. For coupling media, Song et al. compared duct tape and leather tape and stated that the duct tape is better than leather tape [78]. Bolu et al. performed vibrothermography inspection on high strength Nickel alloy turbine blades and stated that a general increase in the temperature rise can be seen with an increase in the horn static force, vibration amplitude and excitation time. Also, they tried gaffer tape, Silicone tape, electrical tape, paper and duct tape as coupling material and concluded that maximum temperature rise was seen with electrical tape, followed by gaffer tape [90].

Power, excitation duration and distance between sample and the horn also affect detectability of cracks in vibrothermography. Sathish et al. stated that when excitation power was increased from 500 to 1000 W, the highest temperature that the specimen gained also increased if distance between sample and the horn and excitation time were

fixed. When excitation duration was increased from 250 ms to 1000 ms, then the highest temperature that the specimen gained also increased if power and distance were fixed. If distance between sample and the horn increased, change in maximum temperature decreased exponentially power and excitation duration were fixed. They suggested that larger distance between horn and sample, longer excitation time and minimum excitation power should be used in applications [91].

Table 1. Vibrothermography measurements for different materials and technical details

Material	IR Camera	Vibrometer	Excitation Frequency	Excitation Power	Excitation Time	Reference
CFRP	InSb Flir Phoenix	-	20 kHz	-	-	[15]
AISI 304	Cedip Titanium 560 M	Polytec PSV-400-H4	15.5-19.5 kHz	350 W	20 s	[16]
Graphite cast iron	Titanium 560 M, Flir Systems	PSV-400-H4, Polytec GmbH	15-25 kHz	0-2.2 kW		[46]
AISI 304	Cedip Titanium 560 M	Polytec PSV-400-H4	15-25 kHz	0-2.2 kW	20 s	[47]
S355 steel	Flir Phoenix	-	15-25 kHz	-	-	[48]
Ti64 and Inconel 718	Phoenix-MWIR 9803	-	40 kHz	-	800 ms	[62]
Austenitic nickel super-alloy	Merlin Indigo	-	40 kHz	400 W	-	[72]
Aluminum	-	OFV 511	20, 30, 40 kHz	750, 800, 1000 W	-	[78]
GFRC	InfraTec VarioCam hr	Polytec PSV-400	0-1600 Hz	-	5 min	[84]
Aluminum	FLIR E60	-	40.7 kHz	-	1-2 s	[87]
C45 ferritic steel	FLIR T640	-	0.4 Hz	-	5 s	[88]

Table 2. (Con.) Vibrothermography measurements for different materials and technical details

Material	IR Camera	Vibrometer	Excitation Frequency	Excitation Power	Excitation Time	Reference
CFRP	Flir Phoenix	-	15-25 kHz	-	10 s	[89]
Ti-6 Al-4V	Merlin Mid-IR, Indigo Inc.	Polytec -PSV-400, OFV-5000	20 kHz	1000 W	250-1000 ms	[91]

Nickel based superalloy	Cedip Jade	-	20 kHz	400 W	0.5 s	[92]
Inconel 100	Indigo Merlin-Mid	Polytec PI, sensor head: OFV 353, controller: OFV 3001	20 kHz	2000 W	-	[93]
CFRP	Indigo Merlin MWIR	-	40 kHz	1 W	0-30 s	[94]
Tungsten carbide	InSb Phoenix Indigo	-	15-25 kHz	-	0.8 ms	[95]
Nickel based superalloy and mild steel	Cedip Jade	-	40 kHz	400 W	0.4-0.6 s	[96]
2024-T3 Aluminum	FLIR ThermaCAM SC 3000	-	10 Hz - 20kHz	-	-	[97]
Metal	CEDIP/FLIR Silver 420M	-	35 kHz	.2-2 kW	50-3000 ms	[98]
Aramid composite	FLIR SC 7600	-	35 kHz	80-130 W	5 s	[99]
CFRP	IRCAM Equus 327	Polytec PSV 300	0-100 kHz	-	30 s	[100]
CFRP	InSb Phoenix Indigo	-	20 kHz	-	5 s	[101]
GFRC	InfraTec VarioCam hr	Polytec PSV-400	0-1250 Hz	-	5 min	[102]
CFRP	FLIR A6750sc	Polytec PSV-500-3D XTRA	1-250 kHz	-	0-50 s	[103]
CFRP	FLIR A6750sc	Polytec PSV-500-3D XTRA	1-250 kHz	-	50 s	[104]
VHB3914 and VHB3095	FLIR SC6000	-	12-30 kHz	-	-	[105]

9. Conclusions

The main aim of this study is to give researchers recent developments and state of the art in vibrothermography. Some of the main conclusions can be given as follows:

- A coupling media between sample and transducer is strongly recommended to be used in vibrothermography testing. Thin plastic tape, gaffer tape, silicone tape, electrical tape, paper and duct tape can be used as coupling media;
- Heat generation is attributed to frictional rubbing of crack faces, plastic deformations due to crack propagation and viscoelasticity / material damping but as stated in most of the studies, frictional heating is the most dominant factor in heat generation in vibrothermography;
- Using single frequency excitations could result in blind zones where defects cannot be detected. Multifrequency excitation is a good alternative to solve this problem

where part is excited with different LDRs so that various damage features can be detected;

- A crack with 0.7 mm length in aluminum plates, 0.1 mm length in steel plates, 1 mm length in Ti64 and Inconel 718 plates can be successfully detected by vibrothermography;
- In vibrothermography, amplitude vibrations should not be high to prevent the specimen from damage. It should not be very low either for proper defect detection;
- The material being detected need to have high surface emissivity for proper defect detection.
- For proper defect detection in vibrothermography, the specimen needs to be fixed with double fixed ends configuration and pressed with high engagement force and excitation point should be closer to the defects;
- Larger distance between horn and sample, longer excitation time and minimum excitation power should be used in vibrothermography applications;
- Vibrothermography is less sensitive to surface roughness than other non-destructive inspection methods. Complex shapes produced by Additive Manufacturing (AM) is, in one aspect, an advantage for this technology, but in terms of inspection, it is a challenge. High surface roughness of AMed parts is one of the biggest problems in the inspection of these parts. Vibrothermography seems to be a good alternative to conventional methods in the inspection of AM parts and it could eliminate the necessity of post processing of AMed parts. But to the best of author's knowledge, there is no data yet on background response of rough as-built surfaces and the challenge of inspecting internal features with no line of sight in AM parts.

Acknowledgement

The authors acknowledge that this study is funded by Technological and Scientific Council of Turkey (TUBITAK) Technology and Innovation Support Program, grant number 5158001.

References

[1] Lu QY, Wong CH. Applications of non-destructive testing techniques for post process control of additively manufactured parts. Virtual and Physical Prototyping, 2017; 12: 301-321. https://doi.org/10.1080/17452759.2017.1357319

[2] Montinaro N, Cerniglia D, Pitarresi G. Defect detection in additively manufactured titanium prothesis by flying laser scanning thermography. Procedia Structural Integrity, 2018; 12: 165-172. https://doi.org/10.1016/j.prostr.2018.11.098

[3] Ibarra-Castanedo C, Maldague X. Pulsed phase thermography reviewed. Quantitative InfraRed Thermography Journal, 2004; 1 (1): 47-70. https://doi.org/10.3166/qirt.1.47-70

[4] Moylan S, Whitenton E, Lane B, Slotwinski J. Infrared thermography for laser-based powder bed fusion additive manufacturing processes. AIP Conference Proceedings, 2014; 1581: 1191-1196. https://doi.org/10.1063/1.4864956

[5] Carvalho MS, Martins AP, Santos TG. Simulation and validation of thermography inspection for components produced by additive manufacturing. Applied Thermal Engineering, 2019; 159: 113872. https://doi.org/10.1016/j.applthermaleng.2019.113872

[6] Ciampa F, Mahmoodi P, Pinto F, Meo M. Recent advances in active infrared thermography for non-destructive testing of aerospace components. Sensors, 2018; 18: 609. https://doi.org/10.3390/s18020609

[7] Raplee JB. (2017). Monitoring the metal additive manufacturing process through thermographic data analysis. Master's Dissertation, University of Tennessee, USA.
[8] Akhloufi MA, Guyon Y, Castanedo C-I, Bendada A. Three-dimensional thermography for nondestructive testing and evaluation. Quantitative InfraRed Thermography Journal, 2016; 14 (1): 79-106. https://doi.org/10.1080/17686733.2016.1229245
[9] Vavilov V. Thermal NDT: historical milestones, state-of-the-art and trends. Quantitative InfraRed Thermography Journal, 2014; 11 (1): 66-83. https://doi.org/10.1080/17686733.2014.897016
[10] Meola C, Boccardi S, Carlomagno GM. Infrared thermography in the evaluation of aerospace composite materials, Woodhead Publishing, Sawston, United Kingdom, 2015.
[11] Khodayar F, Sojasi S, Maldague X. Infrared thermography and NDT: 2050 horizon. Quantitative InfraRed Thermography Journal, 2016; 13 (2): 210-231. https://doi.org/10.1080/17686733.2016.1200265
[12] Mendioroz A, Celorrio R, Salazar A. Ultrasound excited thermography: an efficient tool for the characterization of vertical cracks. Measurement Science and Technology, 2017; 28 (11): 112001. https://doi.org/10.1088/1361-6501/aa825a
[13] Ibarra-Castanedo C, Piau JM, Guilbert S, Avdelidis NP, Genest M, Bendada A, Maldague XPV. Comparative study of active thermography techniques for the nondestructive evaluation of honeycomb structures. Research in Nondestructive Evaluation, 2009; 20 (1):1-31. https://doi.org/10.1080/09349840802366617
[14] Swiderski W, Hlosta P. Pulsed eddy current thermography for defects detection in joints of metal sheets. 11th European Conference on Non-Destructive Testing (ECNDT 2014), Prague, Czech Republic, 6-10 October, 2014.
[15] Deane S, Avdelidis NP, Ibarra-Castanedo C, Zhang H, Nezhad HY, Williamson AA, Mackley T, Davis MJ, Maldague X, Tsourdos A. Application of NDT thermographic imaging of aerospace structures. Infrared Physics and Technology, 2019; 97: 456-466. https://doi.org/10.1016/j.infrared.2019.02.002
[16] Favro LD, Han X, Ouyang Z, Sun G, Sui H, Thomas RL. Infrared imaging of defects heated by a sonic pulse. Review of Scientific Instruments, 2000; 71 (6): 2418-2421. https://doi.org/10.1063/1.1150630
[17] Renshaw JB. (2009). The mechanics of defect detection in vibrothermography. PhD Dissertation, Iowa State University, Iowa, USA.
[18] Ouyang Z, Favro LD, Thomas RL, Han X. Theoretical modeling of thermosonic imaging of cracks. AIP Conference Proceedings, 2002; 615: 577-581. https://doi.org/10.1063/1.1472850
[19] Thomas RL. Thermal NDE techniques-from photoacoustics to thermosonics. AIP Conference Proceedings, 2002; 615: 3-13. https://doi.org/10.1063/1.1472775
[20] Cavallone C, Colom M, Mendioroz A, Salazar A, Palumbo D, Galietti U. Sizing the length of surface breaking cracks using vibrothermography. NDT&E International, 2020; 112: 102250. https://doi.org/10.1016/j.ndteint.2020.102250
[21] Renshaw J, Holland SD, Thompson RB, Uhl C. The effect of crack closure on heat generation in vibrothermography. AIP Conference Proceedings, 2009; 1096 (1): 473-480. https://doi.org/10.1063/1.3114289
[22] Henneke EG, Reifsnider KL, Stinchcomb WW. Vibrothermography: investigation, development, and application of a new nondestructive evaluation technique. U.S. Army Research Office Final Report DAAG29-82-K-0180, p. 22, 1986.
[23] Reifsnider KL, Henneke EG, Stinchcomb WW. The mechanics of vibrothermography. In Mechanics of Nondestructive Testing, Springer, Boston, USA, 1980. https://doi.org/10.1007/978-1-4684-3857-4_12
[24] Mignogna RB, Green Jr RE, Duke Jr JC, Henneke II Reifsnider KL. Thermographic investigation of high-power ultrasonic heating in materials. Ultrasonics, 1981; 19 (4): 159-163. https://doi.org/10.1016/0041-624X(81)90095-0

[25] Rantala J, Wu D, Busse G. Amplitude-modulated lock-in vibrothermography for NDE of polymers and composites. Research in Nondestructive Evaluation, 1996; 7: 215-228. https://doi.org/10.1080/09349849609409580
[26] Dillenz A, Zweschper T, Busse G. Burst phase-angle thermography with elastic waves. Thermosense XXIV, SPIE, Orlando, FL, USA, 2002. https://doi.org/10.1117/12.459609
[27] Zweschper T, Dillenz A, Riegert G, Scherling D, Busse G. Ultrasound excited thermography using frequency modulated elastic waves. Insight - Non-Destructive Testing and Condition Monitoring, 2003; 45: 178-182. https://doi.org/10.1784/insi.45.3.178.53162
[28] Roemer J, Uhl T, Pieczonka Ł. Laser spot thermography for crack detection in aluminum structures. 7th International Symposium on NDT in Aerospace, Bremen, Germany, 6-18 November, 2015.
[29] Suratkar A, Sajjadi AY, Mitra K. Non-destructive evaluation (NDE) of composites for marine structures: detecting flaws using infrared thermography (IRT). In Non-Destructive Evaluation (NDE) of Polymer Matrix Composites, Woodhead Publishing Series in Composites Science and Engineering, Sawston, United Kingdom, 2013. https://doi.org/10.1533/9780857093554.4.649
[30] Zweschper T, Dillenz A, Busse G. Inspection of aerospace structures with ultrasound lock-in-thermography. 15th World Conference on Nondestructive Testing, Roma, Italy, 2000.
[31] DiMambro J, Ashbaugh DM, Han X, Favro LD, Lu J, Zeng Z, Li W, Newaz GM, Thomas RL. The potential of sonic ir to inspect aircraft components traditionally inspected with fluorescent penetrant and or magnetic particle inspection. AIP Conference Proceedings, 2006; 820: 536-543. https://doi.org/10.1063/1.2184574
[32] Zalameda JN, Winfree WP, Yost WT. Air coupled acoustic thermography (ACAT) inspection technique. AIP Conference Proceedings, 2008; 975: 467-474. https://doi.org/10.1063/1.2902697
[33] Guo Y, Ruhge FR. Comparison of detection capability for acoustic thermography, visual inspection and fluorescent penetrant inspection on gas turbine components. AIP Conference Proceedings, 2009; 1096: 1848-1854. https://doi.org/10.1063/1.3114183
[34] Szwedo M, Pieczonka L, Uhl T. Vibrothermographic testing of structures. Key Engineering Materials, 2012; 518: 418-427. https://doi.org/10.4028/www.scientific.net/KEM.518.418
[35] Zweschper T, Riegert G, Dillenz A, Busse G. Ultrasound burst phase thermography (UBP) for applications in the automotive industry. AIP Conference Proceedings, 2003; 657: 531-536. https://doi.org/10.1063/1.1570182
[36] Capua C, Morello R, Jablonski I. Active and eddy current pulsed thermography to detect surface crack and defect in historical and archaeological discoveries. Measurement, 2018; 116: 676-684. https://doi.org/10.1016/j.measurement.2017.10.035
[37] Luong MP. Non-destructive testing of sports equipment: the use of infrared thermography. In Materials in Sports Equipment Volume 2, Woodhead Publishing, Sawston, United Kingdom, 2007. https://doi.org/10.1201/9781439824108.ch2
[38] Quesada JIP, Carpes FP. Application of infrared thermography in the assessment of sport equipment. In Materials in Sports Equipment (Second Edition), Woodhead Publishing Series in Composites Science and Engineering, Sawston, United Kingdom, 2019.
[39] Umar MZ, Vavilov V, Abdullah H, Ariffin AK. Ultrasonic infrared thermography in non-destructive testing: a review. Russian Journal of Nondestructive Testing, 2016; 52 (4): 212-219. https://doi.org/10.1134/S1061830916040082
[40] Abdelhafiz A. Thermal3DImage, Survey Review, 2013; 45 (328): 35-43. https://doi.org/10.1179/1752270612Y.0000000002

[41] Zweschper T, Riegert G, Dillenz A, Busse G. Ultrasound excited thermography - advances due to frequency modulated elastic waves. Quantitative InfraRed Thermography Journal, 2005; 2 (1): 65-76. https://doi.org/10.3166/qirt.2.65-76
[42] Guo X, Vavilov V. Crack detection in aluminum parts by using ultrasound-excited infrared thermography. Infrared Physics & Technology, 2013; 61: 149-156. https://doi.org/10.1016/j.infrared.2013.08.003
[43] Dillenz A, Busse G, Wu D. Ultrasound lock-in thermography: feasibilities and limitations. Diagnostic Imaging Technologies and Industrial Applications, 1999; 3827: 10-15. https://doi.org/10.1117/12.361008
[44] Rantala J, Wu D, Salerno A, Busse G. Lock-in thermography with mechanical loss angle heating at ultrasonic frequencies. Proceedings of the third quantitative infrared thermography conference, Pisa, Italy, 1996. https://doi.org/10.21611/qirt.1996.064
[45] Salerno A, Dillenz A, Wu D, Rantala J, Busse G. Progress in ultrasound lockin thermography. Proceedings of the 4th quantitative infrared thermography conference, 1998. https://doi.org/10.21611/qirt.1998.024
[46] Montanini R, Freni F, Rossi GL. Quantitative evaluation of hidden defects in cast iron components using ultrasound activated lock-in vibrothermography. Review of Scientific Instruments, 2012; 83: 094902. https://doi.org/10.1063/1.4750977
[47] Montanini R, Freni F. Correlation between vibrational mode shapes and viscoelastic heat generation in vibrothermography. NDT&E International, 2013; 58: 43-48. https://doi.org/10.1016/j.ndteint.2013.04.007
[48] Plum R, Ummenhofer T. Ultrasound excited thermography of thickwalled steel load bearing members. Quantitative InfraRed Thermography Journal, 2009; 6 (1): 79-100. https://doi.org/10.3166/qirt.6.79-100
[49] Yang R, He Y. Optically and non-optically excited thermography for composites: A review. Infrared Physics & Technology, 2016; 75: 26-50. https://doi.org/10.1016/j.infrared.2015.12.026
[50] Barden TJ, Almond DP, Cawley P, Morbidini M. Advances in thermosonics for detecting impact damage in CFRP composites. AIP Conference Proceedings, 2006; 820: 550- 557. https://doi.org/10.1063/1.2184576
[51] Ibarra-Castanedo C, Genest M, Guibert S, Guibert S, Piau J-M, Maldague XPV, Bendada A. Inspection of aerospace materials by pulsed thermography, lock-in thermography and vibrothermography: a comparativestudy. Proceedings of SPIE-the international society for optical engineering, Orlando, FL, USA, 9 April, 2007. https://doi.org/10.1117/12.720097
[52] Favro LD, Han X, Li L, Ouyang Z, Sun G, Thomas RL, Richards A. Thermosonic imaging for NDE. AIP Conference Proceedings, 2001; 557: 478-482. https://doi.org/10.1063/1.1373796
[53] Bolu G, Gachagan A, Pierce G, Harvey G, Choong L. Monitoring crack propagation in turbine blades caused by thermosonics. AIP Conference Proceedings, 2010; 1211: 1654-1661. https://doi.org/10.1063/1.3362267
[54] Zweschper T, Dillenz A, Riegert G, Busse G. Ultrasound thermography in NDE: principle and applications. Acoustical Imaging, 2004; 27: 113-120. https://doi.org/10.1007/978-1-4020-2402-3_15
[55] Renshaw J, Holland SD, Thompson RB, Anderegg J. Vibration-induced tribological damage to fracture surfaces via vibrothermography. International Journal of Fatigue, 2011; 33: 849-857. https://doi.org/10.1016/j.ijfatigue.2011.01.005
[56] Wilson J, Tian GY, Abidin IZ, Yang S, Almond D. Modelling and evaluation of eddy current stimulated thermography. Nondestructive Testing and Evaluation, 2010; 25 (3): 205-218. https://doi.org/10.1080/10589750903242533
[57] Zweschper T, Dillenz A, Busse G. Ultrasound lockin thermography - an NDT method for the inspection of aerospace structures. Proceedings of the 5th Quantitative InfraRed Thermography Conference, 2000. https://doi.org/10.21611/qirt.2000.046

[58] Guo X. An analytical model and parametric analysis of ultrasound-excited infrared thermography. Quantitative InfraRed Thermography Journal, 2015; 12 (2):137-148. https://doi.org/10.1080/17686733.2015.1039291
[59] Solodov I, Rahammer M, Derusova D, Busse G. Highly-efficient and noncontact vibro-thermography via local defect resonance. Quantitative InfraRed Thermography Journal, 2015; 12 (1): 98-111. https://doi.org/10.1080/17686733.2015.1026018
[60] Mabrouki F, Thomas M, Genest M, Fahr A. Frictional heating model for efficient use of vibrothermography. NDT&E International, 2009; 42: 345-352. https://doi.org/10.1016/j.ndteint.2009.01.012
[61] Weekes B, Cawley P, Almond DP. The effects of crack opening and coatings on the detection capability of thermosonics. AIP Conference Proceedings, 2011; 1335: 399-406. https://doi.org/10.1063/1.3591880
[62] DiMambro J, Ashbaugh DM, Nelson CL, Spencer FW. Sonic infrared (IR) imaging and fluorescent penetrant inspection probability of detection (POD) comparison. AIP Conference Proceedings, 2007; 894: 463-470. https://doi.org/10.1063/1.2718008
[63] Han X, Favro LD, Ouyang Z, Thomas RL. Recent developments in thermosonic crack detection. AIP Conference Proceedings, 2002; 615: 552-557. https://doi.org/10.1063/1.1472846
[64] Han X, Zeng Z, Li W, Islam S, Lu J, Loggins V, Yitamben E, Favro LD, Newaz G, Thomas RL. Acoustic chaos for enhanced detectability of cracks by sonic infrared imaging. Journal of Applied Physics, 2004; 95 (7): 3792-3797. https://doi.org/10.1063/1.1652243
[65] Almond DP, Weekes B, Li T, Pickering SG, Kostson E, Wilson J, Tian GY, Dixon S, Burrows S. Thermographic techniques for the detection of cracks in metallic components. Insight - Non-Destructive Testing and Condition Monitoring, 2011; 53 (11): 614-620. https://doi.org/10.1784/insi.2011.53.11.614
[66] Renshaw J, Chen JC, Holland SD, Thompson RB. The sources of heat generation in vibrothermography. NDT&E International, 2011; 44: 736-739. https://doi.org/10.1016/j.ndteint.2011.07.012
[67] Schiefelbein B. (2017). A crack closure model and its application to vibrothermography nondestructive evaluation. Graduate Theses and Dissertations, Iowa State University, Ames, Iowa, USA.
[68] Montanini R, Freni F. Investigation of heat generation sources in sonic infrared thermography using laser doppler vibrometry. 11th International Conference on Quantitative InfraRed Thermography, Naples, Italy, 11-14 June, 2012. https://doi.org/10.21611/qirt.2012.177
[69] Bai G, Lamboul B, Roche J, Baste S. Investigation of multiple cracking in glass/epoxy 2D woven composites by vibrothermography. Quantitative InfraRed Thermography Journal, 2016; 13 (1): 35-49. https://doi.org/10.1080/17686733.2015.1079013
[70] Hassan W, Homma C, Wen Z, Vensel F, Hogan B. Detection of tight fatigue cracks at the root of dampers in fan blades using sonic ir inspection: a feasibility demonstration. AIP Conference Proceedings, 2007; 894: 455-462. https://doi.org/10.1063/1.2718007
[71] Lu J, Han X, Newaz G, Favro LD, Thomas RL. Study of the effect of crack closure in Sonic Infrared Imaging. Nondestructive Testing and Evaluation, 2007; 22 (2-3): 127-135. https://doi.org/10.1080/10589750701448175
[72] Weekes B, Cawley P, Almond DP, Li T. The effect of crack opening on thermosonics and laserspot thermography. AIP Conference Proceedings, 2010; 1211: 490-497. https://doi.org/10.1063/1.3362434
[73] Renshaw J, Holland SD, Barnard DJ. Viscous material-filled synthetic defects for vibrothermography. NDT&E International, 2009; 42: 753-756. https://doi.org/10.1016/j.ndteint.2009.07.003
[74] Vaddi JS. (2011). Transducer characterization for Vibrothermography. Graduate Theses and Dissertations, Iowa State University, Ames, Iowa, USA.

[75] Gleiter A, Spiessberger C, Busse G. Improved ultrasound activated thermography using frequency analysis. Quantitative InfraRed Thermography Journal, 2007; 4 (2): 155-164. https://doi.org/10.3166/qirt.4.155-164
[76] Holland SD, Uhl C, Renshaw J. Toward a viable strategy for estimating vibrothermographic probability of detection. Proceedings of the Review of Progress in Quantitative Nondestructive Evaluation, Ames, IA, USA, 20-25 July, 2008. https://doi.org/10.1063/1.2902701
[77] Qingju T, Junyan L, Yang W, Hui L. Subsurface interfacial defects of metal materials testing using ultrasound infrared lock-in thermography. Procedia Engineering, 2011; 16: 499-505. https://doi.org/10.1016/j.proeng.2011.08.1116
[78] Song Y, Han X. Effect of driving frequency on non-linear coupling between ultrasound transducer and target under inspection in Sonic Infrared Imaging. Infrared Physics & Technology, 2014; 66: 43-48. https://doi.org/10.1016/j.infrared.2014.05.009
[79] Hiremath SR, Mahapatra DR, Srinivasan S. Detection of crack in metal plate by thermo sonic wave based detection using FEM. JEST-M Journal, 2012; 1: 12-18.
[80] Solodov I, Busse G. Resonance ultrasonic thermography: highly efficient contact and air-coupled remote modes. Applied Physics Letters, 2013; 102 (6): 061905. https://doi.org/10.1063/1.4792236
[81] Fierro GPM, Calla' D, Ginzburg D, Ciampa F, Meo M. Nonlinear ultrasonic stimulated thermography for damage assessment in isotropic fatigued structures. Journal of Sound and Vibration, 2017; 404: 102-115. https://doi.org/10.1016/j.jsv.2017.05.041
[82] Dyrwal A, Meo M, Ciampa F. Nonlinear air-coupled thermosonics for fatigue micro-damage detection and localization. NDT E International, 2018; 97: 59-67. https://doi.org/10.1016/j.ndteint.2018.03.012
[83] Derusova DA, Vavilov VP, Guo X, Druzhinin NV. Comparing the efficiency of ultrasonic infrared thermography under high-power and resonant stimulation of impact damage in a CFRP composite. Russian Journal of Nondestructive Testing, 2018; 54: 356-362. https://doi.org/10.1134/S1061830918050030
[84] Katunin A, Wronkowicz-Katunin A, Wachla D. Impact damage assessment in polymer matrix composites using self-heating based vibrothermography. Composite Structures, 2019; 214: 214-226. https://doi.org/10.1016/j.compstruct.2019.02.003
[85] Katunin AA. Concept of thermographic method for non-destructive testing of polymeric composite structures using self-heating effect. Sensors, 2018; 18 (1): 74. https://doi.org/10.3390/s18010074
[86] Willey CL, Xiang D, Long M. A novel thermosonic imaging system for non-destructive testing. AIP Conference Proceedings, 2017; 1806, 070006. https://doi.org/10.1063/1.4974621
[87] Xu C, Xie J, Zhang W, Kong Q, Chen G, Song G. Experimental investigation on the detection of multiple surface cracks using vibrothermography with a low-power piezoceramic actuator. Sensors, 2017; 17: 2705. https://doi.org/10.3390/s17122705
[88] Min Q, Zhu J, Feng F, Xu C, Sun J. Study on optimization method of test conditions for fatigue crack detection using lock-in vibrothermography. Infrared Physics & Technology, 2017; 83: 17-23. https://doi.org/10.1016/j.infrared.2017.04.002
[89] Liu B, Zhang H, Fernandes H, Maldague X. Experimental evaluation of pulsed thermography, lock-in thermography and vibrothermography on foreign object defect (FOD) in CFRP. Sensors, 2016; 16: 743. https://doi.org/10.3390/s16050743
[90] Bolu G, Gachagan A, Pierce G, Harvey G. Reliable crack detection in turbine blades using thermosonics: an empirical study. AIP Conference Proceedings, 2010; 1211: 474-481. https://doi.org/10.1063/1.3362431
[91] Sathish S, Welter JT, Jata KV, Schehl N, Boehnlein T. Development of nondestructive non-contact acousto-thermal evaluation technique for damage detection in materials. Review of Scientific Instruments, 2012; 83: 095103. https://doi.org/10.1063/1.4749245

[92] Barden TJ, Almond DP, Morbidini M, Duffour P, Cawley P. A quantitative investigation of thermosonics. Quantitative InfraRed Thermography, 2004. https://doi.org/10.21611/qirt.2004.058
[93] Mayton D, Spencer F, Alvarez C. Characterizing the effects of sonic IR variables on turbine disk inspection using a design of experiments approach. AIP Conference Proceedings, 2005; 760: 642-649. https://doi.org/10.1063/1.1916736
[94] Barden TJ, Almond DP, Pickering SG, Morbidini M, Cawley P. Detection of impact damage in CFRP composites by thermosonics. Nondestructive Testing and Evaluation, 2007; 22 (2-3): 71-82. https://doi.org/10.1080/10589750701447540
[95] Piau J, Bendada A, Maldague X, Legoux J. Nondestructive testing of open microscopic cracks in plasma-sprayed-coatings using ultrasound excited vibrothermography. Nondestructive Testing and Evaluation, 2008; 23 (2): 109-120. https://doi.org/10.1080/10589750701775817
[96] Morbidini M, Cawley P. A calibration procedure for sonic infrared nondestructive evaluation. Journal of Applied Physics, 2009; 106: 023504. https://doi.org/10.1063/1.3169518
[97] Mabrouki F, Thomas M, Genest M, Fahr A. Numerical modeling of vibrothermography based on plastic deformation. NDT&E International, 2010; 43: 476-483. https://doi.org/10.1016/j.ndteint.2010.05.002
[98] Szwedo M, Pieczonka L, Uhl T. Application of vibrothermography in nondestructive testing of structures. 6th European Workshop on Structural Health Monitoring (EWSHM 2012), Dresden, Germany, July 3-6, 2012.
[99] Swiderski W, Pracht M. Ultrasonic IR thermography detection of defects in multi-layered aramid composites. 19th World Conference on Non-Destructive Testing (WCNDT 2016), Munich, Germany, 13-17 June, 2016. https://doi.org/10.1117/12.2277110
[100] Rahammer M, Kreutzbruck M. Fourier-transform vibrothermography with frequency sweep excitation utilizing local defect resonances. NDT&E International, 2017; 86: 83-88. https://doi.org/10.1016/j.ndteint.2016.11.012
[101] Zhang H, Avdelidis NP, Osman A, Ibarra-Castanedo C, Sfarra S, Fernandes H, Matikas TE, Maldague XPV. Enhanced infrared image processing for impacted carbon/glass fiber-reinforced composite evaluation. Sensors, 2018; 18: 45. https://doi.org/10.3390/s18010045
[102] Katunin A, Wachla D. Analysis of defect detectability in polymeric composites using self-heating based vibrothermography. Composite Structures, 2018; 201: 760-765. https://doi.org/10.1016/j.compstruct.2018.06.105
[103] Segers J, Hedayatrasa S, Verboven E, Poelman G, Paepegem WV, Kersemans M. In-plane local defect resonances for efficient vibrothermography of impacted carbon fiber-reinforced polymers (CFRP). NDT and E International, 2019; 102: 218-225. https://doi.org/10.1016/j.ndteint.2018.12.005
[104] Hedayatrasa S, Segers J, Poelman G, Verboven E, Paepegem WV, Kersemans M. Vibrothermographic spectroscopy with thermal latency compensation for effective identification of local defect resonance frequencies of a CFRP with BVID. NDT&E International, 2020; 109: 102179. https://doi.org/10.1016/j.ndteint.2019.102179
[105] Vaddi JS, Holland SD, Kessler MR. Loss modulus measurement of a viscoelastic polymer at acoustic and ultrasonic frequencies using vibrothermography. Measurement, 2021; 168: 108311. https://doi.org/10.1016/j.measurement.2020.108311

Research on Engineering Structures & Materials
journal homepage: http://www.jresm.org
Research Group

Research Article

Analytical evaluation of plasticity models for anisotropic materials with experimental validation

Emre Esener*[a], Aysema Ünlü[b]

Department of Mechanical Engineering, Bilecik Seyh Edebali University, Bilecik, Turkey

Article Info

Article history:
Received 26 Oct 2021
Revised 11 Dec 2021
Accepted 17 Dec 2021

Keywords:

Plasticity modeling;
Anisotropy;
Aluminum alloy;
TBF1050

Abstract

The plastic behavior of a material can be represented by plasticity models. The ability of plasticity models to represent material behavior depends on their mathematical form, the assumptions they hold, and the sensitivity of the input parameters. Plasticity models are of great importance, especially in finite element analysis. While the mathematical forms of plasticity models are implemented in finite element analysis software, some coding-related inaccuracies may occur. Therefore, the capacity of the plasticity model to represent the plastic behavior of the material can be revealed more accurately by examining it analytically. After this verification, the choice of the plasticity model to be used in the finite element analysis can be realized with more accuracy and less time loss. In this direction, in this study, the capacity of plasticity models, which are frequently used today, to model the plastic behavior of anisotropic materials was evaluated. For this purpose, Hill48, Barlat89, Hu2003 and Poly6 plasticity models were analyzed analytically and TBF1050 3rd generation advanced high strength steel and 5XXX series aluminum alloy were used as materials. The predictive capacities of the plasticity models were evaluated with the yield locus and angular variations of anisotropy coefficient and yield stress ratios. As a result, it has been revealed that polynomial-based models can model the plasticity behavior of the material more accurately for both material groups.

1. Introduction

In order to model the plastic deformations that occur in the material in plastic forming methods, the determination of material models that describe the elastic and plastic behavior of the material is very critical in terms of method engineering. In this context, it is equally important to accurately determine the necessary material parameters for material models. Plastic behavior is a more complex concept than elastic behavior of materials. In the elastic part, there is a linear relationship between strains and stresses by means of Hooke's law. In general, plastic strains are not defined by stresses alone. Plastic strains depend on the entire loading history and how the stress state is reached [1]. During a plastic forming process, the materials exhibit non-linear behavior due to hardening. In order to model the plastic behavior of a material under general stress condition, a yield criterion describing the relationship between stress components at the time of yielding, a yield rule describing the relationship between stress and strain ratio components, and a hardening rule describing the evolution of the initial yield stress during the deformation process is needed. The yield criteria (plasticity models) which describe the plastic behavior of materials determined by mathematical models. Yield criteria contain a margin of error due to their constructs, containing assumptions, or number of input parameters. This margin of error in the yield criteria, greatly affects the prediction accuracy of material

*Corresponding author: emre.esener@bilecik.edu.tr
[a] orcid.org/0000-0001-5854-4834; [b] orcid.org/0000-0002-4288-6212
DOI: http://dx.doi.org/10.17515/resm2021.356me1026

behavior. Predictions performed in this way show low accuracy and have time-consuming steps. In industrial applications engineers generally uses well-known plasticity models to describe the plastic behavior of materials. These models show significantly poor performance, especially on new generation materials. For this reason, engineers in the industry, generally analyze the material behavior by using different plasticity models based on the trial-and-error method. This procedure continues until a plasticity model predicts the material behavior within the expected tolerance of the product. The analyzes of material behavior performed in this way are time-consuming and this causes major problems especially for mass production. The choice of yield criterion is of great importance at this point. Simple experimental verifications are made in order to give the effective result of the selected yield criterion. Among the mechanical tests, tensile test, fatigue test, shear test, and hydraulic bulge test are the most frequently used tests for experimental verification. If the yield criteria are validated by experimental data, the above-mentioned time and cost loss will be less in the design stage of the process.

There are many yield criteria in the literature [2-7]. These criteria, which define the material behavior, contain various assumptions according to the material and hardening conditions. Models can be divided into two categories according to the isotropic and anisotropic behavior assumptions of the material. Isotropy is a concept related to uniformity and states that the properties of the material will not change with different crystallographic orientations, that is, they will be independent of the direction. The concept of anisotropy, on the other hand, states that the mechanical properties may change depending on the direction due to the crystal structure of the material or the characteristics of the rolling process. The direction-dependent change in plastic behavior with anisotropy is expressed by the term called Lankford parameter or anisotropy coefficient [8]. This parameter can be determined by a uniaxial tensile test. Anisotropy values are usually determined by displacement measurements taken after 20% elongation from the tensile test. In the literature, it is generally performed for three different directions (rolling direction, diagonal direction, transverse direction) [9-11].

With the help of the yield criteria, yield loci of materials are obtained and the behavior of the material under loading conditions is determined with these surfaces. Yield loci should be closed, convex and smooth. Stresses within the surface line cause elastic deformation, while stresses above the surface line cause plastic deformation. Stresses outside the locus have no physical meaning. While the horizontal axis represents the rolling direction, the vertical axis represents the 90º direction (transverse) to the rolling direction. With the help of yield criteria, directional yield stress ratios and anisotropy coefficients can also be predicted. Sensitivity of the yield criterion prediction can be validated by experimental data. Analytical verification of plasticity models before finite element analysis prevents time loss in process design. Otherwise, a finite element analysis should be performed at each trial stage in order to determine the plasticity model that yields sensitive results. While obtaining the yield loci of a model takes a short time, a complex form of non-linear finite element analysis takes hours. As explained above, in the finite element analysis step of production methods, it is very important to determine the yield criterion that makes an accurate and precise prediction.

Material grade can affect the plasticity model predictions since the material behavior varies with the material grade. For the automotive industry, materials with low thickness, high strength, good formability, shock absorbing ability, collision resistance and low cost are of great importance to ensure safety without sacrificing lightness [12]. In this context, Advanced High Strength Steels (AHSS) are used in the automotive industry. New generation AHSSs are handled in three generations according to their technological developments [12]. Third generation AHSSs were produced due to the strength capabilities of the first-generation steels were limited and the second-generation steels

were expensive hence they contained high-cost alloying elements [13]. These steels are materials with high formability and high strength and at the same time produced with lower costs. Today, third generation AHSSs are increasingly being incorporated into automotive production to increase vehicle fuel efficiency and crash resistance [14]. In this context, three steel classes called TBF (TRIP Aided Bainitic Ferrite) steels, QP (Quenching & Partitioning) steels and Nano steels have been developed as the third generation AHSSs [15]. Among the third generation improved high strength steels, TBF steels stand out due to their properties such as high ductility, formability, toughness, fatigue strength and delayed fracture strength.

Aluminum alloys, on the other hand, are industrial materials that are widely used in applications that require advanced technology. Here, automobiles, aircraft and ship industries are the most important areas of use. Aluminum and its alloys are generally called light alloys and their strength is increased by adding different alloying elements to the base material (aluminum), which is ductile and has high corrosion resistance. Unlike iron-based materials, they contain small amounts of alloying elements. The main alloying element of aluminum 5XXX alloys is magnesium [16]. They are known for their general strength, corrosion resistance and weldability. The tensile strength increases with increasing magnesium ratio [17]. These series alloys are mostly used in marine transportation vehicles and automotive industry.

The aim of the study is to analyze the analytical models of yield criteria based on their predictive performance of the plastic behavior of the anisotropic materials. In this direction, analytical performance evaluations of yield criteria for steel and non-ferrous materials actively used in the automotive industry were performed and the evaluations were confirmed by mechanical tests.

2. Materials and Method

In this study, cold-rolled Aluminum 5XXX alloy and cold-rolled TBF1050 steel with gauge thickness values as 1.5 mm and 1.2 mm, respectively are used. TBF (TRIP-assisted baintic-ferritic) steels are in use as 3rd generation of advanced high strength steels (AHSS). In this study, TBF-grades with a minimum tensile strength of 1050 MPa is used. The high strength of these steel stems from a fine-grained martensitic or bainitic matrix while an increased fraction of retained austenitic inclusions utilize the TRIP effect which leads to enhanced elongations [18-19]. TBF1050 steel used in this study is not subjected any heating stage. In the aluminum alloy that is used in this study, the main alloying element is magnesium and strain hardening grade of aluminum alloy is H1.

2.1. Material Testing

In the first stage of the study, uniaxial tensile tests were performed to obtain the verification parameters. Tensile tests were performed in ASTM-E8 standard [20] and with 3 repetitions. Uniaxial tensile tests were carried out on the 300 kN capacity Zwick/Roell Z300E testing machine and the dimensional changes in length and width of the specimens were measured with extensometers. Anisotropy coefficients and yield stress ratios were obtained as a result of the tests with a strain rate of 0.0067 1/s performed in 7 directions (0^o, 15^o, 30^o, 45^o, 60^o, 75^o, 90^o).

In the second step of the study, hydraulic bulge tests were performed to obtain biaxial anisotropy coefficient and biaxial yield stress ratios. Hydraulic bulge tests were carried out in 3 repetitions on a 600 kN capacity Zwick/Roell BUP600 test device using 200x200 mm square specimens. In hydraulic bulge tests, strain values were obtained using the GOM Argus system with the Digital Image Correlation (DIC) method by non-contact cameras. In these tests, biaxial yield stresses were obtained by using linear fit region to stress-strain

curve of the materials in addition biaxial anisotropy coefficients were calculated with the ratio of the strains. Strain values are obtained by DIC method.

The visuals of the mechanical tests are given in Fig. 1. Anisotropy coefficients and yield stress ratios obtained from the mechanical tests are shown in Table 1.

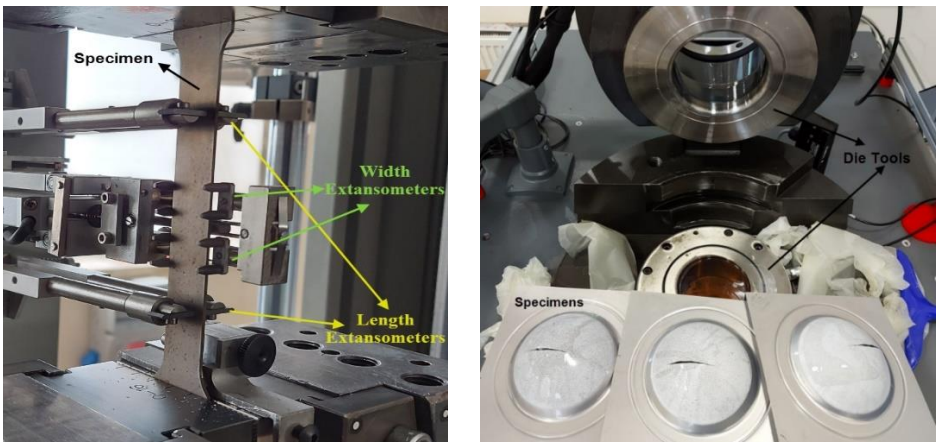

(a) (b)

Fig. 1 Mechanical test systems (a) Uniaxial tensile test (b) Hydrolic bulge test

As it can be seen from the Fig. 1. Uniaxial tensile tests were performed with length and width extensometers. The elongation in the length of the test sample and the contraction in the width of the test sample are measured with these extensometers. The changes by means of the material gauge thickness are obtained by the volume constancy. Anisotropy coefficients (r) are calculated by using ratio of the strain values as given in the Eq. (1).

$$r = \frac{\varepsilon_w}{\varepsilon_t} \tag{1}$$

where, ε_w is the width strain and ε_t is the thickness strain.

Table 1. Material validation parameters obtained with mechanical tests

Material		Angle (°)							Biaxial
		0	15	30	45	60	75	90	
TBF1050	Anisotropy coefficent	0.95	0.93	1.08	1.06	0.99	1.04	1.10	0.98
	Yield stress ratio	1	1.03	1.04	1.04	1.04	1.03	1.05	0.97
AA5XXX	Anisotropy coefficent	0.80	0.74	0.71	0.71	0.75	0.80	0.81	1.01
	Yield stress ratio	1	0.99	0.99	0.99	0.99	1.01	0.99	1.11

2.2. Plasticity Models

In this study, Hill48, Barlat89, Hu2003 and 6th order polynomial based (Poly6) plasticity models were used to model the plastic behavior of anisotropic materials. In this part of the study, the analytical expressions of the plasticity models are explained. The first yield

criterion for anisotropic materials was presented by R. Hill in 1948 [21] and this quadratic criterion is given in the Eq. (2).

$$2f = F\left(\sigma_{yy} - \sigma_{zz}\right)^2 + G(\sigma_{zz} - \sigma_{xx})^2 + H\left(\sigma_{xx} - \sigma_{yy}\right)^2 + 2L{\tau_{yz}}^2 + 2M{\tau_{zx}}^2 + 2N{\tau_{xy}}^2 = 1 \quad (2)$$

In the equation above, F, G, H, L, M and N are the material parameters to be calibrated. For plane stress condition, this criterion can be expresses as,

$$22f = (G + H)\sigma_{sx}^2 - 2H\sigma_{xx}\sigma_{yy} + (F + H)\sigma_{yy}^2 + 2N\sigma_{xy}^2 = 1 \quad (3)$$

These parameters were determined based on Lankford's coefficients using Eqs. (4)-(7) This situation is named as "Hill48-r based" within the scope of the study.

$$F = \frac{r_0}{r_{90}(1+r_0)} \quad (4)$$

$$G = \frac{1}{1 + r_0} \quad (5)$$

$$H = \frac{r_0}{1+r_0} \quad (6)$$

$$N = \frac{(r_0 + r_{90})(1 + 2r_{45})}{2r_{90}(1 + r_0)} \quad (7)$$

Here, r_0, r_{45} and r_{90} represent the anisotropy coefficients in the rolling direction, 45 degrees to the rolling direction and 90 degrees to the rolling direction, respectively. Due to the simple r-based approach of the Hill48 criterion in defining the anisotropies of materials, it offers a great advantage to the users, and this advantage makes this criterion still one of the most frequently used criteria today [22-24]. F, G, H and N coefficients can also be calculated on the basis of stress in the Hill48 yield criterion. This situation is named as "Hill48-Stress (S) based" within the scope of the study. Stress-based expressions of these parameters are given in Eqs. (8)-(11).

$$F = \frac{1}{2}\left(\left(\frac{\sigma_0}{\sigma_{90}}\right)^2 - 1 + \left(\frac{\sigma_0}{\sigma_b}\right)^2\right) \quad (8)$$

$$G = \frac{1}{2}\left(1 - \left(\frac{\sigma_0}{\sigma_{90}}\right)^2 + \left(\frac{\sigma_0}{\sigma_b}\right)^2\right) \quad (9)$$

$$H = \frac{1}{2}\left(1 + \left(\frac{\sigma_0}{\sigma_{90}}\right)^2 - \left(\frac{\sigma_0}{\sigma_b}\right)^2\right) \quad (10)$$

$$N = \frac{1}{2}\left(\left(\frac{2\sigma_0}{\sigma_{45}}\right)^2 - \left(\frac{\sigma_0}{\sigma_b}\right)^2\right) \quad (11)$$

where σ_b represents the biaxial yield stress.

In 1989, Barlat and Lian presented a criterion for materials with planar anisotropy under plane stress conditions [25]. This criteron allows the use of the Lankford parameters for the definition of the anisotropy. Barlat89 criterion can be written as Eq. (12).

$$f = a|k_1 + k_2|^M + a|k_1 - k_2|^M + c|2k_2|^M = 2\sigma_e^M \quad (12)$$

Here "M" exponent depends on the crystal structure of materials. For face centered cubic (FCC) materials M = 8 is recommended and for body centered cubic (BCC) materials M = 6 may be used [26]. k_1 and k_2 coefficients can be written as Eq. (13) and (14).

$$k_1 = \frac{\sigma_{11} + h\sigma_{22}}{2} \quad (13)$$

$$k_2 = \left[\left(\frac{\sigma_{11}-h\sigma_{22}}{2}\right)^2 + p^2\sigma_{12}^2\right]^{1/2} \quad (14)$$

a, c, and h represent material constants are obtained through r_0, r_{45}, and r_{90}. These parameters can be written as Eqs. (15-17).

$$a = 2 - 2\sqrt{\left(\frac{r_0}{1+r_0}\right)\left(\frac{r_{90}}{1+r_{90}}\right)} \quad (15)$$

$$c = 2 - a \quad (16)$$

$$h = \sqrt{\left(\frac{r_0}{1+r_0}\right)\left(\frac{1+r_{90}}{r_{90}}\right)} \quad (17)$$

"p" parameter can be found by optimization. Barlat89 model is one of the most used models in finite element analyses since the model has a simple construction and needs a few numbers of material parameters [27-29].

Hu, developed the Hill48 criterion in 2003 and proposed a new plasticity model [30]. The Hu-2003 criterion can be written in the general form as in Eq. (18).

$$f(\overline{\sigma}) = \frac{1}{\sigma_0^4}\sigma_1^4 - \frac{4r_0}{(1+r_0)\sigma_0^4}\sigma_1^3\sigma_2 + \left(\frac{1}{\sigma_b^4} - \frac{1}{\sigma_0^4} - \frac{1}{\sigma_{90}^4} + \frac{4r_0}{(1+r_0)\sigma_0^4} + \frac{4r_{90}}{(1+r_{90})\sigma_{90}^4}\right)\sigma_1^2\sigma_2^2 - \frac{4r_{90}}{(1+r_{90})\sigma_{90}^4}\sigma_1\sigma_2^3 + \frac{1}{\sigma_{90}^4}\sigma_2^4 + \left(\frac{16}{(1+r_{45})\sigma_{45}^4} - \frac{2}{\sigma_b^4}\right)(\sigma_1^2 + \sigma_2^2 - \sigma_1\sigma_2)\sigma_{12}^2 + \left(\frac{1}{\sigma_b^4} + \frac{16r_{45}}{(1+r_{45})\sigma_{45}^4}\right)\sigma_{12}^4 = 1 \quad (18)$$

According to this criterion, it has the ability to model the plastic behavior of the material with a total number of 7 parameters: anisotropy coefficients in the rolling direction, 45 degrees to the rolling direction and 90 degrees to the rolling direction, yield stresses in the same directions and hydraulic bulge test yield stress.

The sixth-order homogeneous polynomial yield criterion (Poly6) was developed by Soare in order to describe anisotropic behavior of materials [31]. Poly6 criterion could be used for not only plane stress but also 3D stress state. Besides, the derivatives of polynomial functions could easily be computed and this provides convenience for implementation of the material model into finite element (FE) codes. The model has 16 material coefficients for plane stress state and it can be expressed as follows:

$$f = a_1{\sigma_x}^6 + a_2{\sigma_x}^5\sigma_y + a_3{\sigma_x}^4{\sigma_y}^2 + a_4{\sigma_x}^3{\sigma_y}^3 + a_5{\sigma_x}^2{\sigma_y}^4 + a_6\sigma_x{\sigma_y}^5 + a_7{\sigma_y}^6 + \left(a_8{\sigma_x}^4 + a_9{\sigma_x}^3\sigma_y + a_{10}{\sigma_x}^2{\sigma_y}^2 + a_{11}\sigma_x{\sigma_y}^3 + a_{12}{\sigma_y}^4\right){\sigma_{xy}}^2 + \left(a_{13}{\sigma_x}^2 + a_{14}\sigma_x\sigma_y + a_{15}{\sigma_y}^2\right){\sigma_{xy}}^4 + a_{16}{\sigma_{xy}}^6 \quad (19)$$

Qui et.al. [32] developed an analytical determination of anisotropic parameters for Poly6 yield criterion. The parameters of Poly6 yield criterion are expressed with the r-values and yield stresses without any optimization method. According to their study a_1-a_7 parameters can be calculated analytically using the Eqs. (20)-(26).

$$a_1 = 1 \quad (20)$$

$$a_7 = \left(\frac{\sigma_0}{\sigma_{90}}\right)^6 \quad (21)$$

$$a_2 = -6\frac{r_0}{r_0+1} \quad (22)$$

$$a_6 = -6\frac{r_{90}}{r_{90}+1}a_7 \tag{23}$$

$$a_5 = \frac{3}{2}\frac{r_b-1}{r_b+1}\left(\frac{\sigma_0}{\sigma_b}\right)^6 + \frac{1}{4}\left[\left(\frac{\sigma_0}{\sigma_b}\right)^6 + \left(\frac{\sigma_0}{\sigma_\tau}\right)^6\right] - [(a_6 + 2a_7) - (a_1 + a_2)] \tag{24}$$

$$a_3 = \frac{1}{2}\left[\left(\frac{\sigma_0}{\sigma_b}\right)^6 + \left(\frac{\sigma_0}{\sigma_\tau}\right)^6\right] - (a_1 + a_5 + a_7) \tag{25}$$

$$a_4 = \left(\frac{\sigma_0}{\sigma_b}\right)^6 - (a_1 + a_2 + a_3 + a_5 + a_6 + a_7) \tag{26}$$

In Ref. [32] σ_τ is calculated from the analytical Poly4 [31] and given in Eq. (27).

$$\frac{\sigma_0}{\sigma_\tau} = \left\{\left(\frac{\sigma_0}{\sigma_b}\right)^4 + 8\left[\frac{r_0}{r_0+1} + \frac{r_{90}}{r_{90}+1}\left(\frac{\sigma_0}{\sigma_{90}}\right)^4\right]\right\}^{1/4} \tag{27}$$

Then a_{16} coefficient is expressed as Eq. (28)

$$a_{16} = \left\{16[1 - (r_{45}+1)^{-1}]\left(\frac{\sigma_0}{\sigma_{45}}\right)^4 + \left(\frac{\sigma_0}{\sigma_b}\right)^4\right\}^{3/2} \tag{28}$$

Other eight parameters (a_8 - a_{15}) is determined from the uniaxial tension test.

$$Y_1(\theta)a_8 + Y_2(\theta)a_9 + Y_3(\theta)a_{10} + Y_4(\theta)a_{11} + Y_5(\theta)a_{12} + Y_6(\theta)a_{13} + Y_7(\theta)a_{14} + Y_8(\theta)a_{15} = \Gamma_y(\theta) \tag{29}$$

where

$$Y_1(\theta) = cos^{10}\theta\, sin^2\theta \tag{30}$$

$$Y_2(\theta) = cos^8\theta\, sin^4\theta \tag{31}$$

$$Y_3(\theta) = cos^6\theta\, sin^6\theta \tag{32}$$

$$Y_4(\theta) = cos^4\theta\, sin^8\theta \tag{33}$$

$$Y_5(\theta) = cos^2\theta\, sin^{10}\theta \tag{34}$$

$$Y_6(\theta) = cos^8\theta\, sin^4\theta \tag{35}$$

$$Y_7(\theta) = cos^6\theta\, sin^6\theta \tag{36}$$

$$Y_8(\theta) = cos^4\theta\, sin^8\theta \tag{37}$$

$$\Gamma_y(\theta) = \left(\frac{\sigma_0}{\sigma_\theta}\right)^6 - z_y(\theta) - cos^6\theta\, sin^6\theta\, a_{16} \tag{38}$$

$$z_y(\theta) = a_1\, cos^{12}\theta + a_2\, cos^{10}\theta\, sin^2\theta + a_3\, cos^8\theta\, sin^4\theta + a_4\, cos^6\theta\, sin^6\theta + a_5\, cos^4\theta\, sin^8\theta + a_6\, cos^2\theta\, sin^{10}\theta + a_7\, sin^{12}\theta \tag{39}$$

Based on the definition of rθ Eq. (40) can be written.

$$R_1(\theta)a_8 + R_2(\theta)a_9 + R_3(\theta)a_{10} + R_4(\theta)a_{11} + R_5(\theta)a_{12} + R_6(\theta)a_{13} + R_7(\theta)a_{14} + R_8(\theta)a_{15} = \Gamma_r(\theta) \tag{40}$$

where,

$$R_1(\theta) = \left[r_p(\theta)cos^2\theta - 4\right]cos^8\theta\, sin^2\theta \tag{41}$$

$$R_2(\theta) = \left[r_p(\theta)cos^2\theta\, sin^2\theta - (1 + 2\, sin^2\theta)\right]cos^6\theta\, sin^2\theta \tag{42}$$

$$R_3(\theta) = \left[r_p(\theta)cos^2\,\theta\,sin^2\,\theta - 2\right] cos^4\,\theta\,sin^4\,\theta \tag{43}$$

$$R_4(\theta) = \left[r_p(\theta)cos^2\,\theta\,sin^2\,\theta - (1 + 2\,cos^2\,\theta)\right] cos^2\,\theta\,sin^6\,\theta \tag{44}$$

$$R_5(\theta) = \left[r_p(\theta)sin^2\,\theta - 4\right] cos^2\,\theta\,sin^8\,\theta \tag{45}$$

$$R_6(\theta) = \left[r_p(\theta)cos^2\,\theta - 2\right] cos^6\,\theta\,sin^4\,\theta \tag{46}$$

$$R_7(\theta) = \left[r_p(\theta)cos^2\,\theta\,sin^2\,\theta - 1\right] cos^4\,\theta\,sin^4\,\theta \tag{47}$$

$$R_8(\theta) = \left[r_p(\theta)sin^2\,\theta - 2\right] cos^4\,\theta\,sin^6\,\theta \tag{48}$$

$$\Gamma_r(\theta) = z_r(\theta) - z_y(\theta)r_p(\theta) - r_p(\theta)cos^6\,\theta\,sin^6\,\theta\,a_{16} \tag{49}$$

$$r_p(\theta) = \frac{6}{r_\theta + 1} \tag{50}$$

$$\begin{aligned} z_r(\theta) = {} & (6a_1 + a_2)cos^{10}\,\theta + (5a_2 + 2a_3)cos^8\,\theta\,sin^2\,\theta + \\ & (4a_3 + 3a_4)cos^6\,\theta\,sin^4\,\theta + (3a_4 + 4a_5)cos^4\,\theta\,sin^6\,\theta + \\ & (2a_5 + 5a_6)cos^2\,\theta\,sin^8\,\theta + (a_6 + 6a_7)\,sin^{10}\,\theta \end{aligned} \tag{51}$$

As Eqs. (29) and (40) are the linear equations of a_8-a_{15}, the parameters can be analytically solved with eight equations. If five r-values and three uniaxial tension yield stresses are used, the expressions of a_8-a_{15} can be calculated as Eq. (52) and this situation is named as "r-based Poly6" in this study. If three r-values and five UT (uniaxial tension) yield stresses are used the expressions of a_8-a_{15} can be calculated as Eq. (53) and this situation is named as "Stress(S)-based Poly6" in this study.

$$\begin{bmatrix} a_8 \\ a_9 \\ a_{10} \\ a_{11} \\ a_{12} \\ a_{13} \\ a_{14} \\ a_{15} \end{bmatrix} = \begin{bmatrix} R_1(\theta_1) & R_2(\theta_1) & R_3(\theta_1) & R_4(\theta_1) & R_5(\theta_1) & R_6(\theta_1) & R_7(\theta_1) & R_8(\theta_1) \\ R_1(\theta_2) & R_2(\theta_2) & R_3(\theta_2) & R_4(\theta_2) & R_5(\theta_2) & R_6(\theta_2) & R_7(\theta_2) & R_8(\theta_2) \\ R_1(\theta_3) & R_2(\theta_3) & R_3(\theta_3) & R_4(\theta_3) & R_5(\theta_3) & R_6(\theta_3) & R_7(\theta_3) & R_8(\theta_3) \\ R_1(\theta_4) & R_2(\theta_4) & R_3(\theta_4) & R_4(\theta_4) & R_5(\theta_4) & R_6(\theta_4) & R_7(\theta_4) & R_8(\theta_4) \\ R_1(\theta_5) & R_2(\theta_5) & R_3(\theta_5) & R_4(\theta_5) & R_5(\theta_5) & R_6(\theta_5) & R_7(\theta_5) & R_8(\theta_5) \\ Y_1(\theta_6) & Y_2(\theta_6) & Y_3(\theta_6) & Y_4(\theta_6) & Y_5(\theta_6) & Y_6(\theta_6) & Y_7(\theta_6) & Y_8(\theta_6) \\ Y_1(\theta_7) & Y_2(\theta_7) & Y_3(\theta_7) & Y_4(\theta_7) & Y_5(\theta_7) & Y_6(\theta_7) & Y_7(\theta_7) & Y_8(\theta_7) \\ Y_1(\theta_8) & Y_2(\theta_8) & Y_3(\theta_8) & Y_4(\theta_8) & Y_5(\theta_8) & Y_6(\theta_8) & Y_7(\theta_8) & Y_8(\theta_8) \end{bmatrix}^{-1} \begin{bmatrix} \Gamma_r(\theta_1) \\ \Gamma_r(\theta_2) \\ \Gamma_r(\theta_3) \\ \Gamma_r(\theta_4) \\ \Gamma_r(\theta_5) \\ \Gamma_y(\theta_6) \\ \Gamma_y(\theta_7) \\ \Gamma_y(\theta_8) \end{bmatrix} \tag{52}$$

$$\begin{bmatrix} a_8 \\ a_9 \\ a_{10} \\ a_{11} \\ a_{12} \\ a_{13} \\ a_{14} \\ a_{15} \end{bmatrix} = \begin{bmatrix} R_1(\theta_1) & R_2(\theta_1) & R_3(\theta_1) & R_4(\theta_1) & R_5(\theta_1) & R_6(\theta_1) & R_7(\theta_1) & R_8(\theta_1) \\ R_1(\theta_2) & R_2(\theta_2) & R_3(\theta_2) & R_4(\theta_2) & R_5(\theta_2) & R_6(\theta_2) & R_7(\theta_2) & R_8(\theta_2) \\ R_1(\theta_3) & R_2(\theta_3) & R_3(\theta_3) & R_4(\theta_3) & R_5(\theta_3) & R_6(\theta_3) & R_7(\theta_3) & R_8(\theta_3) \\ Y_1(\theta_4) & Y_2(\theta_4) & Y_3(\theta_4) & Y_4(\theta_4) & Y_5(\theta_4) & Y_6(\theta_4) & Y_7(\theta_4) & Y_8(\theta_4) \\ Y_1(\theta_5) & Y_2(\theta_5) & Y_3(\theta_5) & Y_4(\theta_5) & Y_5(\theta_5) & Y_6(\theta_5) & Y_7(\theta_5) & Y_8(\theta_5) \\ Y_1(\theta_6) & Y_2(\theta_6) & Y_3(\theta_6) & Y_4(\theta_6) & Y_5(\theta_6) & Y_6(\theta_6) & Y_7(\theta_6) & Y_8(\theta_6) \\ Y_1(\theta_7) & Y_2(\theta_7) & Y_3(\theta_7) & Y_4(\theta_7) & Y_5(\theta_7) & Y_6(\theta_7) & Y_7(\theta_7) & Y_8(\theta_7) \\ Y_1(\theta_8) & Y_2(\theta_8) & Y_3(\theta_8) & Y_4(\theta_8) & Y_5(\theta_8) & Y_6(\theta_8) & Y_7(\theta_8) & Y_8(\theta_8) \end{bmatrix}^{-1} \begin{bmatrix} \Gamma_r(\theta_1) \\ \Gamma_r(\theta_2) \\ \Gamma_r(\theta_3) \\ \Gamma_y(\theta_4) \\ \Gamma_y(\theta_5) \\ \Gamma_y(\theta_6) \\ \Gamma_y(\theta_7) \\ \Gamma_y(\theta_8) \end{bmatrix} \tag{53}$$

Using the analytical expressions of all plasticity models described above, the representativeness of the plasticity models for anisotropic materials was evaluated.

3. Results and Discussion

In this part of the study, the plasticity models described in Chapter 2 were analyzed analytically and converted to Matlab codes, and the directionality of anisotropy coefficients and yield stress ratios were estimated for TBF1050 and AA5XXX. The results obtained

were compared with the validation parameters obtained from mechanical tests. First, yield loci of the materials were analyzed, and the loci obtained by analytical expressions of plasticity models were compared for TBF1050 steel and AA5XXX alloy in Fig. 2 and Fig. 3, respectively.

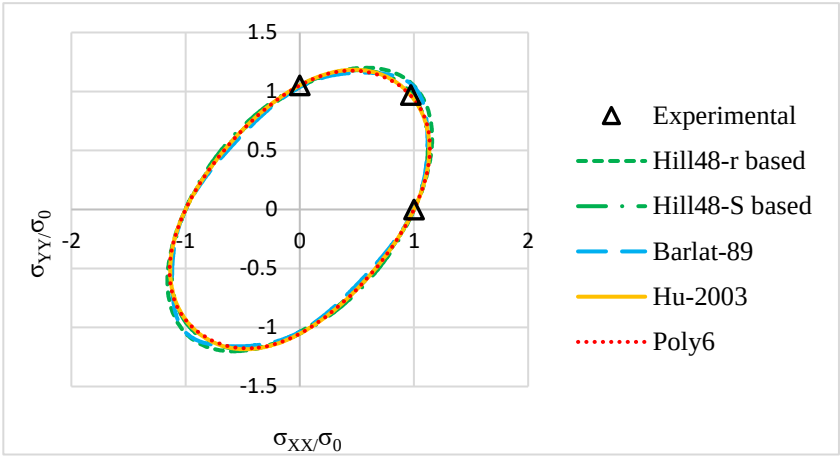

Fig. 2 Yield locus comparison for TBF1050 steel

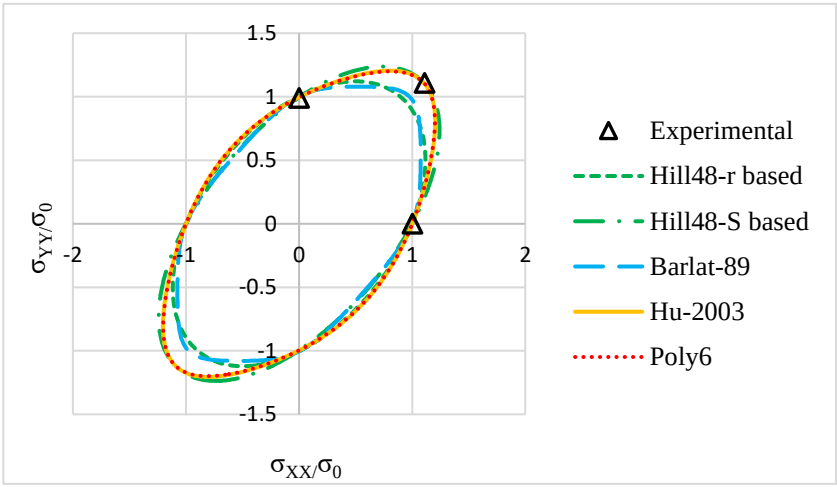

Fig. 3 Yield locus comparison for AA5XXX alloy

As it can be seen from the figures, the stress-based Hill48 model, Hu2003 model and Poly6 model for both materials represented the experimental data quite successfully and gave the most sensitive results in terms of yield loci. The Hill48-r based and Barlat89 models, on the other hand, gave close results to each other, but failed to represent the biaxial tensile behavior especially for aluminum alloy. These results shows that the stress-based of the plasticity models predicts the yield loci more accurately since the yield loci is a stress-based surface. Poly6 and Hu2003 models use the biaxial yield stress values as an input for this reason biaxial part of the yield loci can be predicted more accurately.

In the next step of the study, directional anisotropy coefficients and yield stress ratios predicted by the plasticity models were obtained. The prediction results were verified with experimental data and are shown in Figure 4-7. As can be seen from the figures, the Poly6

model for both materials gave results that are in good agreement with the experimental data. Here, the anisotropy coefficient-based version of the Poly6 model was able to model the directionality of the anisotropy coefficient values, while the stress-based version was able to model the angular variation of the yield stress ratio values exactly overlapping with the experimental data. Except for the Poly6 model, the most suitable results with the experimental data were obtained with the Hu2003 model. The Hu2003 model is in agreement with the experimental results for TBF1050 steel, except for the 30° prediction of the anisotropy coefficient and the 75° direction of the yield stress ratio estimation. However, for the AA5XXX alloy, except for the 0°, 45° and 90° directions, it predicts far from the experimental data. The stress-based version of the Hill48 model showed a successful performance in the yield stress ratio estimations of 0°, 45° and 90° directions for both materials, but showed a very poor estimation performance in the anisotropy coefficient predictions. Finally, Hill48 and Barlat89 models based on anisotropy coefficients, although giving consistent results with each other, were not successful in representing the directional material behavior, especially in terms of yield stress ratio.

These results shows that the Hill48 model (both r-based and S-based) can only predicts the rolling, diagonal, and transverse direction values since the Hill48 model use these values as input. In addition, this model shows a poor performance except these directions for both material. Barlat89 model has a similar approach with the Hill48-r based model. It can be seen from the results that the predictions of anisotropy coefficients and yield stress ratios are very similar with the Hill48-r based model. When it comes to Hu2003 model, this model can predict anisotropy coefficient directionality better than the stress ratio results since this model predominantly based on anisotropy coefficients. However, Poly6 plasticity model shows the best prediction performance for both anisotropy coefficients and stress ratio directionalities for all materials. This results shows that the increasing number of the coefficients of the plasticity models increases the prediction accuracy. Poly6 model has 16 coefficients for determining the material behavior at plane stress state. Stress based Poly6 model predicted the stress ratio values, and r-based Poly6 model predicted the anisotropy coefficients values for 7 directions with an accurate agreement with the experimental results.

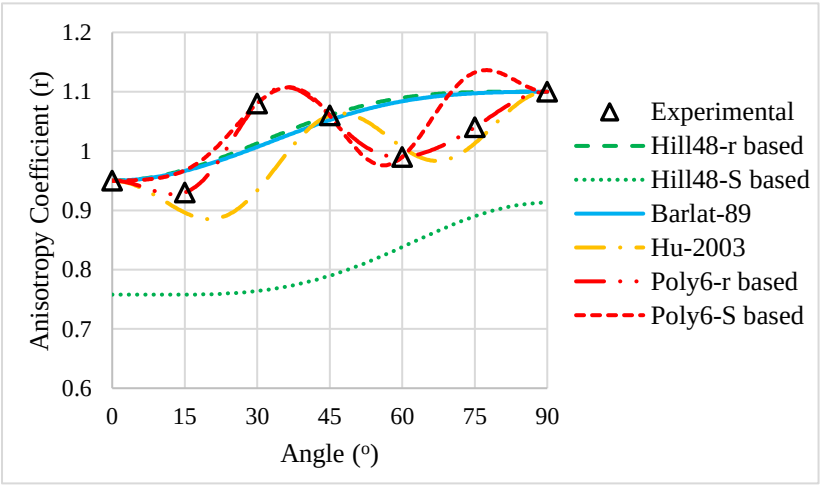

Fig. 4 Angular variation of anisotropy coefficients for TBF1050 steel

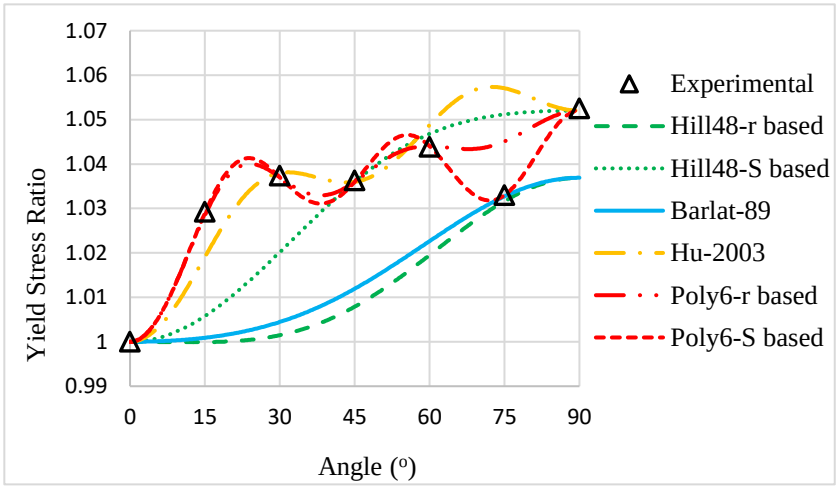

Fig. 5 Angular variation of yield stress ratios for TBF1050 steel

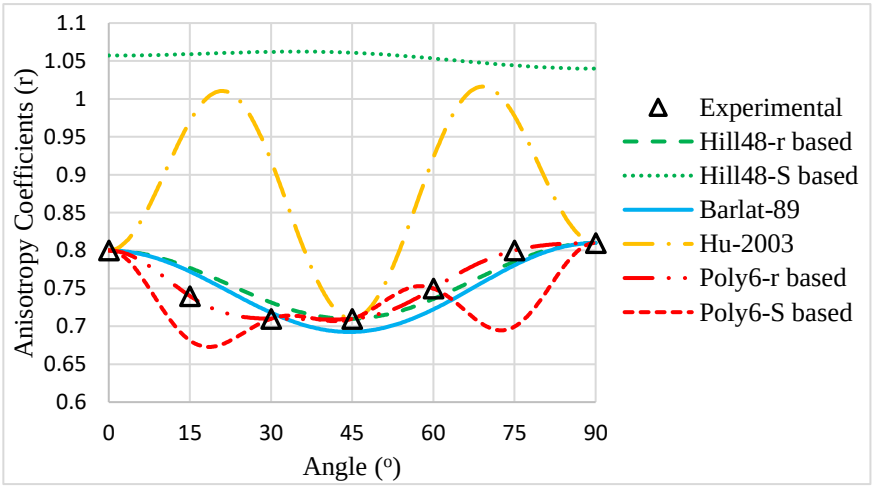

Fig. 6 Angular variation of anisotropy coefficients for AA5XXX alloy

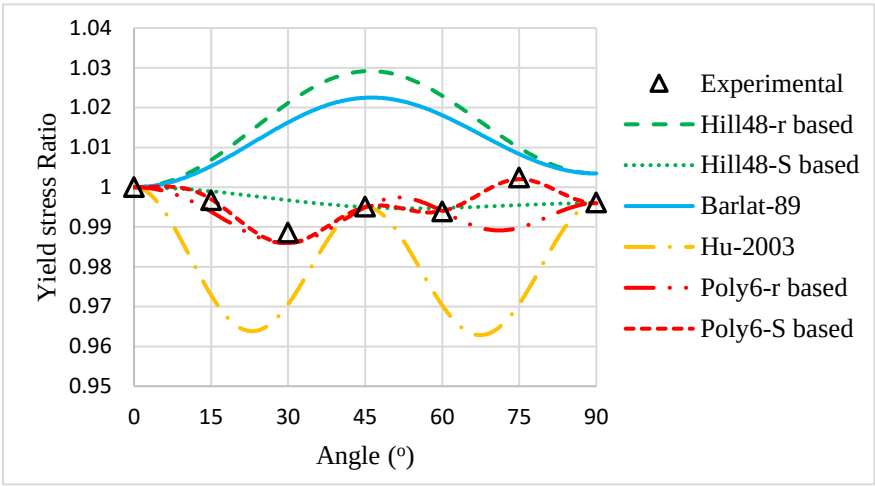

Fig. 7 Angular variation of yield stress ratios for AA5XXX alloy

4. Conclusions

The main purpose of the study is to model the plastic behavior of steel and non-ferrous materials by using analytical expressions of plasticity models that are frequently used today. For this purpose, the directional anisotropy coefficients and yield stress ratios of the materials were predicted by plasticity models and the prediction results were compared with the experimental data. Hill48, Barlat89, Hu2003 and Poly6 yield criteria were used as plasticity models. Among these models, Hill48 and Poly6 plasticity models were evaluated with two different versions as anisotropy coefficient-based and stress-based. Experimental data were obtained from uniaxial tensile tests performed in 7 directions (0º, 15º, 30º, 45º, 60º, 75º, 90º) and hydraulic bulge tests in order to validate the analytical models. In the study, TBF1050 steel, one of the 3rd generation advanced high strength steels, and 5XXX series aluminum alloy were used as non-ferrous material. As a result of the study, the following conclusions were reached:

- The stress-based Hill48 model, Hu2003 model and Poly6 model for both materials represented the experimental data quite successfully and performed the most sensitive results in terms of yield loci.
- The Hill48-r based and Barlat89 models presented similar behavior but failed to represent the biaxial tensile behavior especially for aluminum alloy by means of yield loci.
- The Poly6 model for both materials gave results that are in good agreement with the experimental data with the perspective of directional anisotropy coefficients and yield stress ratios.
- The anisotropy coefficient-based version of the Poly6 model was able to model the directionality of the anisotropy coefficient values, while the stress-based version was able to model the angular variation of the yield stress ratio values exactly overlapping with the experimental data.
- The Hu2003 model has an agreement with the experimental results for TBF1050 steel, except for the 30º prediction of the anisotropy coefficient and the 75º direction of the yield stress ratio estimation. However, for the AA5XXX alloy, except for the 0º, 45º and 90º directions, it predicts far from the experimental data.

- The stress-based version of the Hill48 model showed a successful performance in the yield stress ratio estimations of 0º, 45º and 90º directions for both materials, but showed a poor prediction performance in the anisotropy coefficient predictions.
- The Hill48 and the Barlat89 models based on anisotropy coefficients, although giving consistent results with each other, were not successful in representing the directional material behavior, especially in terms of yield stress ratio.

As can be seen, the most successful results were obtained with polynomial-based plasticity models. As a result of the study, it has been revealed that the plastic behavior of the materials can be modeled quite successfully with the uniaxial tensile test and hydraulic bulge test data. With an accurate finite element implementation, the plasticity models used analytically in this study can also be used in numerical studies, effectively.

Acknowledgement

This study was supported by Bilecik Seyh Edebali University Scientific Research Projects Commission (Project Number: 2020-01.BŞEÜ.03-05, 2021).

References

[1] Clausing DP. Effect of plastic strain state on ductility and toughness. International Journal of Fracture Mechanics, 1970; 6(1): 71-85. https://doi.org/10.1007/BF00183662

[2] Karafillis AP, Boyce MC. A general anisotropic yield criterion using bounds and a transformation weighting tensor. Journal of the Mechanics and Physics of Solids, 1993; 41(12): 1859-1886. https://doi.org/10.1016/0022-5096(93)90073-O

[3] Hill R. A user-friendly theory of orthotropic plasticity in sheet metals. International Journal of Mechanical Sciences, 1993; 35(1): 19-25. https://doi.org/10.1016/0020-7403(93)90061-X

[4] Yoshida F, Hamasaki H, Uemori T. A user-friendly 3D yield function to describe anisotropy of steel sheets. International Journal of Plasticity, 2013; 45: 119-139. https://doi.org/10.1016/j.ijplas.2013.01.010

[5] Barlat F, Brem JC, Yoon JW, et. al., Chung K, Dick RE, Lege DJ, Pourboghrat F, Choi SH, Chu E. Plane stress yield function for aluminum alloy sheets-part 1: theory. International Journal of Plasticity, 2003; 19(9): 1297-131. https://doi.org/10.1016/S0749-6419(02)00019-0

[6] Cazacu O, Plunkett B, Barlat F. Orthotropic yield criterion for hexagonal closed packed metals. International Journal of Plasticity, 2006; 22(7): 1171-1194. https://doi.org/10.1016/j.ijplas.2005.06.001

[7] Yoshida F, Uemori T. A model of large-strain cyclic plasticity describing the Bauschinger effect and workhardening stagnation. International journal of plasticity, 2002; 18(5-6): 661-686. https://doi.org/10.1016/S0749-6419(01)00050-X

[8] Banabic D, Bunge HJ, Pohlandt K, Tekkaya AE. Formability of Metallic Materials (Springer, Heidelberg, 2000). https://doi.org/10.1007/978-3-662-04013-3

[9] Wang L, Lee TC. The Effect of Yield Criteria on The Forming Limit Curve Prediction and The Deep Drawing Process Simulation. International Journal of Machine Tools & Manufacture, 2006; 46: 988-995. https://doi.org/10.1016/j.ijmachtools.2005.07.050

[10] Ozsoy M, Esener E, Ercan S, Fırat M. Springback predictions of a dual-phase steel considering elasticity evolution in stamping process. Arabian Journal for Science and Engineering, 2014; 39(4): 3199-3207. https://doi.org/10.1007/s13369-013-0910-9

[11] Banabic D. Sheet Metal Forming Processes-Constitutive Modelling and Numerical Simulation (Springer, NewYork, 2010) https://doi.org/10.1007/978-3-540-88113-1

[12] Cornette D, Cugy P, Hildenbrand A, et. al., Bouzekri M, Lovato G. Ultra high strength FeMn TWIP steels for automotive safety parts. Metallurgical Research & Technology, 2005; 102(12): 905-918. https://doi.org/10.1051/metal:2005151
[13] Billur E, Karabulut S, Yılmaz İÖ, et. al., Erzincanoğlu S, Çelik H, Altınok E, Başer T. Mechanical Properties of Trip Aided Bainitic Ferrite (TBF) Steels in Production and Service Conditions. Hittite Journal of Science and Engineering, 2018; 5(3): 231-237. https://doi.org/10.17350/HJSE19030000100
[14] Bhattacharya D, Cho L, Van der Aa E, et. al., Pichler A, Pottore N, Ghassemi-Armaki H, Findley KO, Speer JG. Influence of the Starting Microstructure of an Advanced High Strength Steel on the Characteristics of Zn-Assisted Liquid Metal Embrittlement. Materials Science &Engineering A, 2020; 804: 1-14. https://doi.org/10.1016/j.msea.2020.140391
[15] Galdos L, Argandoña ES de, Mendiguren J, et. al., Gil I, Ulibarri U, Mugarra E. Numerical simulation of U-Drawing test of Fortiform 1050 steel using different material models. Procedia Engineering, 2017; 207: 137-142. https://doi.org/10.1016/j.proeng.2017.10.751
[16] Tzeng YC, Chen RY, Lee SL. Nondestructive tests on the effect of Mg content on the corrosion and mechanical properties of 5000 series aluminum alloys. Materials Chemistry and Physics, 2021; 259: 124202. https://doi.org/10.1016/j.matchemphys.2020.124202
[17] Rana RS, Purohit R, Das S. Reviews on the influences of alloying elements on the microstructure and mechanical properties of aluminum alloys and aluminum alloy composites. International Journal of Scientific and research publications, 2012; 2(6): 1-7.
[18] Hausmann K, Krizan D, Pichler A, Werner E. TRIP-aided bainitic-ferritic sheet steel: A critical assessment of alloy design and heat treatment. Material Science and Technology (MS&T), 2013; 13: 209-218.
[19] Winkelhofer F, Hebesberger T, Krizan D, Avakemian A, Pichler A. Development of cold rolled TBF-steels with a tensile strength of 1180 MPa. voestalpine Stahl GmbH, White Paper.
[20] Standard, A.S.T.M. E8/E8M. Standard test methods for tension testing of metallic materials, 2011; 3: 66.
[21] Hill R. A theory of the yielding and plastic flow of anisotropic metals. Proceedings of the Royal Society of London. Series A. Mathematical and Physical Sciences, 1948; 193(1033): 281-297. https://doi.org/10.1098/rspa.1948.0045
[22] Wang L, Lee TC. The effect of yield criteria on the forming limit curve prediction and the deep drawing process simulation. International Journal of Machine Tools and Manufacture, 2006; 46(9): 988-995. https://doi.org/10.1016/j.ijmachtools.2005.07.050
[23] Lazarescu L, Ciobanu I, Nicodim IP, et. al., Comsa DS, Banabic D. Effect of the mechanical parameters used as input data in the yield criteria on the accuracy of the finite element simulation of sheet metal forming processes. In Key Engineering Materials, 2013; 554: 204-209. Trans Tech Publications Ltd. https://doi.org/10.4028/www.scientific.net/KEM.554-557.204
[24] Neto DM, Oliveira MC, Alves JL, Menezes LF. Influence of the plastic anisotropy modelling in the reverse deep drawing process simulation. Materials & Design, 2014; 60: 368-379. https://doi.org/10.1016/j.matdes.2014.04.008
[25] Barlat F, Lian K. Plastic behavior and stretchability of sheet metals. Part I: A yield function for orthotropic sheets under plane stress conditions. International journal of plasticity, 1989; 5(1): 51-66. https://doi.org/10.1016/0749-6419(89)90019-3
[26] Ls-Dyna Theoretical Manual. Livermore Software Technology Corporation, 1998.

[27] Liu H, Liu Y. Cross section deformation of heterogeneous rectangular welded tube in rotary draw bending considering different yield criteria. Journal of Manufacturing Processes, 2021; 61: 303-310. https://doi.org/10.1016/j.jmapro.2020.11.015
[28] Pandre S, Takalkar P, Morchhale A, et. al., Kotkunde N, Singh SK. Prediction capability of anisotropic yielding behaviour for DP590 steel at elevated temperatures. Advances in Materials and Processing Technologies, 2020; 6(2): 396-404. https://doi.org/10.1080/2374068X.2020.1728647
[29] Harpell ET, Worswick MJ, Finn M, et. al., Jain M, Martin P. Numerical prediction of the limiting draw ratio for aluminum alloy sheet. Journal of Materials Processing Technology, 2000; 100(1-3): 131-141. https://doi.org/10.1016/S0924-0136(99)00468-9
[30] Hu W. Characterized behaviors and corresponding yield criterion of anisotropic sheet metals. Materials Science and Engineering: A, 2003; 345(1-2): 139-144. https://doi.org/10.1016/S0921-5093(02)00453-7
[31] Soare S, Yoon JW, Cazacu O. On the use of homogeneous polynomials to develop anisotropic yield functions with applications to sheet forming. International Journal of Plasticity, 2008; 24(6): 915-944. https://doi.org/10.1016/j.ijplas.2007.07.016
[32] Hu Q, Yoon JW, Stoughton TB. Analytical determination of anisotropic parameters for Poly6 yield function. International Journal of Mechanical Sciences, 2021; 201: 106467. https://doi.org/10.1016/j.ijmecsci.2021.106467

Research on Engineering Structures & Materials
journal homepage: http://www.jresm.org
Research Group

Technical Note

Manufacturing brick using waste rocket propellant: thermal insulation improvement through eco-friendly disposal

Pravin Kumar Mehta[1], A Kumarswamy[2,a], V.K. Saraswat[3], Himanshu Shekhar [*1,b]

[1]*Defence Research and Development Organisation India, Pune, India*
[2]*Defence Institute of Advanced Technology, Pune, India*
[3]*NITI Aayog, New Delhi, India*

Article Info

Article history:
Received 15 Jun 2021
Revised 16 Aug 2021
Accepted 17 Aug 2021

Keywords:

Brick;
Composite Propellants;
Porous Materials;
Thermal Properties;
Building;
Temperature sweep

Abstract

Waste propellant impregnated fire clay brick is investigated for variation in thermal conductivity, thermal diffusivity and specific heat of sample, for different propellant percentage, temperature sweep and propellant percentage. Propellant quantities of 0.0%, 2.5%, 5.0% and 7.5% by weight is added to the green mix of brick and baking in horizontal and vertical direction is carried out for samples made to the size of diameter 12.6+0.1 mm and thickness 2-3 mm. Temperature sweep from 30oC to 100oC is carried out for characterization of brick for thermal diffusivity and specific heat, by using laser flash technique. Higher propellant impregnation by weight results in lowering of thermal diffusivity, enhanced specific heat and reduction in thermal conductivity. Vertical baking results in better thermal insulation properties than horizontal insulation for the same 7.5% propellant impregnated bricks. The thermal conductivity from an average value of 0.7 W/mK for reference brick is observed. 7.5% propellant impregnation by weight in brick may result in thermal conductivity of less than 0.5 W/mK during vertical baking. This substantial reduction definitely leads to an insulating solution to construction, with an eco-friendly disposal solution.

1. Introduction

Brick is an essential construction material for buildings and the thermal properties of brick can have far reaching consequences in terms of reduction in air-conditioning load, thermal insulation requirements and comfort conditions. The properties of Bricks can be altered by adding different additive, which is a better disposal action than dumping or open burning, in terms of environmental concerns. Many attempts are made to incorporate organic agro-waste and household throwaways [1-9], sludge [10-13] and others materials [14-16] as disposal means and also as reduction to the raw material for brick manufacture. into the With this in mind an attempt is made to understand the behaviour of non-homogenous porous brick samples for variation of their thermo-physical properties like thermal diffusivity and specific heat. In literature on Brick the specific heat is mentioned as around 850 J/kg.K and thermal conductivity is of the order of 0.7 W/mK [17]. Additionally, baking orientation and temperature sweeps are also introduced as viable parameters, affecting brick properties. The study illustrates utilization of waste propellant in brick manufacture to alter their thermo-physical properties, as a viable and feasible alternative from sustenance, disposal and environmental concerns.

*Corresponding author: himanshudrdo@rediffmail.com
[a] orcid.org/0000-0001-9101-638X; [b] orcid.org/0000-0002-9403-4070
DOI: http://dx.doi.org/10.17515/resm2021.313st0615tn

2. Thermo-Physical Characterization of Bricks

The main ingredient of reference brick is clay, which is hydrated alumina-silicate refractory material, suitable for withstanding high temperature. Many attempts are made to alter the thermal properties of bricks and in one such attempt, 9 types of clay were investigated from thermal insulation point of view to finalize the ingredient of brick [18]. It is worth mention that thermal insulation desire lower thermal conductivity of building materials and attention is focused on these aspects Thermo-physical Characterization of bricks, in open literature is limited to reporting values, due to addition of various percentages of additional combustible ingredients [19,20].

The attempt in this paper for inclusion of waste rocket propellants is towards utilization of waste materials and at the same time, deriving long term benefits of enhanced thermal insulation of buildings for reduction in heat loads on air-conditioning systems and protection against hot and cold climatic conditions with smaller wall thicknesses. The waste rocket propellants are generally disposed by open burning and its utilization in brick-manufacture is an eco-friendly disposal alternative. The waste propellant is obtained from one of the propellant processing facilities in India and the indicative composition is 65-68% oxidizer, 16-18% Aluminium powder and rest hydrocarbon binder cured by isocyanate curative using urethane formation reaction. As waste propellant is not central theme of the paper, the information is restricted. Additionally, the small percentage of aluminium powder (16-18 %) in composite propellant results in formation of alumina in finished brick. The formation of additional pores by addition of composite propellant and formation of alumina, both enhances insulation properties. The effect of pores orientation can pave way for better thermal insulation characteristics without any change in resources, materials, cost, process or time. It is only stacking of raw molded brick in the kiln, which is affected and enhanced properties can be incorporated in the brick. This requires higher value of thermal diffusivity and specific heat, both. However, the effects which are responsible for reduction in thermal diffusivity can in fact enhance specific heat. Under such circumstances of contradictory, complementary and competing nature of parameters, it is worth exploration to find an optimum percentage of propellant in brick for better results.

To explore this, at first 2.5% by weight waste rocket propellant is added in the Brick and various properties like water absorption, compressive strength, SEM and XRD are explored. As marginal changes are observed in these properties, thermal insulation properties are also explored for bricks impregnated with 2.5% propellant. In fact the processing of impregnated bricks with various particle sizes of rocket propellant waste is conducted. Larger size of propellants was resulting in breakage of Bricks. So size of propellant for addition to the green mix of brick is optimized to 300 micron for better and favorable results. Attempt is made to assess the efficacy of mixing and addition. After finding them favorable, propellant percentage is increased to 5.0% and 7.5% by weight in the brick formulation and thermal insulation properties are assessed for impregnated brick. For adding one more parameter, the baking of brick is conducted in two orientations and thermal conductivity is also assessed with temperature sweep spanning from 30oC to 100oC. This paper explores, effect of percentage addition of propellant, baking orientation, and temperature on thermal conductivity of rocket propellant impregnated bricks.

3. Materials and Method

Green mix of the Brick is prepared using waste powdered rocket propellants, in weight percentages of 2.5%, 5.0% and 7.5%. The samples are position in the oven for baking according to a pre-set temperature cycle with peak temperature exceeding 100oC in two orientations – flat surface and on edges. Um-impregnated sample is also kept for kilning as

reference sample. Normal cuboidal brick samples are prepared for water absorption, compressive strength testing (Figure 1). After baking, they are subjected to water absorption test by immersion in water for 24 hour after heating in oven at 110oC. Weight gain in water immersion is calculated in percentage to give percentage weight gain, indication water absorption capacity of brick. The compressive test is carried out on universal testing machine. Consistent, uniform mix is molded in the button sample, having dimension of 12.6+0.1 mm diameter and 2-3 mm thickness (Figure 1). After baking the obtained samples are subjected to thermo-physical characterization using laser flash method as per ASTM E 1461. Each test is conducted with minimum 5 samples and reported values are average of the 5 test results.

Fig. 1 Rocket Propellant Impregnated Brick Samples

The soil used in the manufacturing of bricks was taken from brick kilns, Nasik, India. The characterization of clay is given in this reference under soils developed on interfluves under sub-humid zone in Nasik [21]. The mix proportion of various materials in the bricks is soil ~ 60 %, flyash ~26%, HEP waste ~4 % and water ~10 %. The mix proportion of various materials in the bricks is soil ~ 60 %, flyash ~26%, waste propellant ~1.5 % and water ~10 %. Waste composite propellant, containing 65-80% Ammonium Perchlorate oxidizer (200-300 micron), 16-18% Aluminium powder (15-20 micron) and 14-20% Hydroxyl terminated polybutadiene (HTPB) as binder, is taken in powder form of 300 micron major dimension, for incorporation in the green mix of brick. The waste composite propellant has a density of 1750 kg/m3 and calorific value of 1200 cal/g. The propellant is added to the tune of 2.5%, 5.0% and 7.5% by weight in the raw material for brick, before baking the same.

Sigma blade mixer with single blade is used for homogeneous mixing of the propellant, soil and fly ash. The duration of mixing is 80 min and speed is 60 rpm. The mixing process was carried out initially with soil, flyash and water for 20 min and subsequently after weathering, waste propellant is added and mixing was carried out for 60 min. The soil dough with fly ash was blended with propellant dust (1.5 wt %) and distilled water (20 to 25 %) to obtain desired level of plasticity. Homogeneity of mix is ensured with the milling cycle to avoid localization of propellant dust powder. The achieved level of water plasticity obtained in this soil dough is in the range of 22 to 24 and the same is obtained through Atterberg plastic limit. The brick samples were oven dried for 48 h at 100˚C to remove excess moisture and avoid cracks during firing. The propellant composition decomposes at around 350 to 400 ˚C. The dried samples were then heated slowly in electric furnace at 1100-1150 ˚C and dwelled for 6 hours and cooled down to ambient temperature.

Thermal Characterization is based on laser pulse method. This technique is one of the most popular methods for the determination of thermal properties of materials because of ease to use at high temperatures, non-contact sensing, very fast measurement, absolute thermal diffusivity measurement etc. In this method, a pulsating flash/ laser energy is made incident onto one side of button shaped (12.5-12.7 mm diameter and 2-3 mm thickness) sample which is placed into the sample holder. Sample holder is kept inside the furnace. An IR detector / thermocouple detector is used at other side of the sample. An schematic of measurement set-up is shown as figure 2.

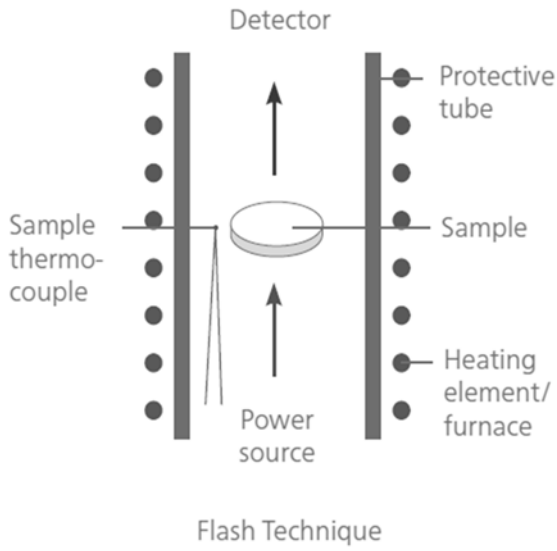

Fig. 2 Schematic of Laser Flash Method for Thermal Properties Assessment

This detector record the thermal disturbances/ temperature rise generated on other side of the sample, due to incident laser on first side. This signal is recorded with time. The signal received from the detector is further amplified, conditioned, denoised and further passed to data acquisition unit. For a given sample thickness (L in mm), the value of Thermal diffusivity is given by α=(1.38 L^2)/(π^2 t_(1/2)), where t1/2 is the time required for the back surface to reach half of the maximum temperature rise. After that heat loss, contact resistance, finite pulse width of laser flash and other corrections are applied. The calibration and validation of test equipment and method is carried out using standard Graphite coated VESPEL material which is Dow Corning make polyimide with good thermal stability. Specific heat is measured by comparison with standard. The equipment used in the study is Antemark Flashline 3000, which has provision to hold sample on a trolley. The trolley moves inside a furnace and required thermal flash is applied on one side of standard and test sample, simultaneously and measurements are made (Figure 3).

The main reason for concentrating on thermo-physical characterization is to observe the effect of incorporating composite propellant in bricks. During preliminary studies, it was observed that incorporation of composite propellant enhances porosity but water absorption, density and compressive strength is not affected significantly. So, in this study an effort is made to exhaustively study the thermo-physical properties for different percentages of composite propellant incorporation. Such thermo-physical characterization studies are used for polymeric, metallic and refractory materials, but are rarely reported for bricks. The reliability of measurement is stated to be around 0.01% and testing at least 5 samples of each type with consistent result is implemented. The values reported are average of these repeated test results.

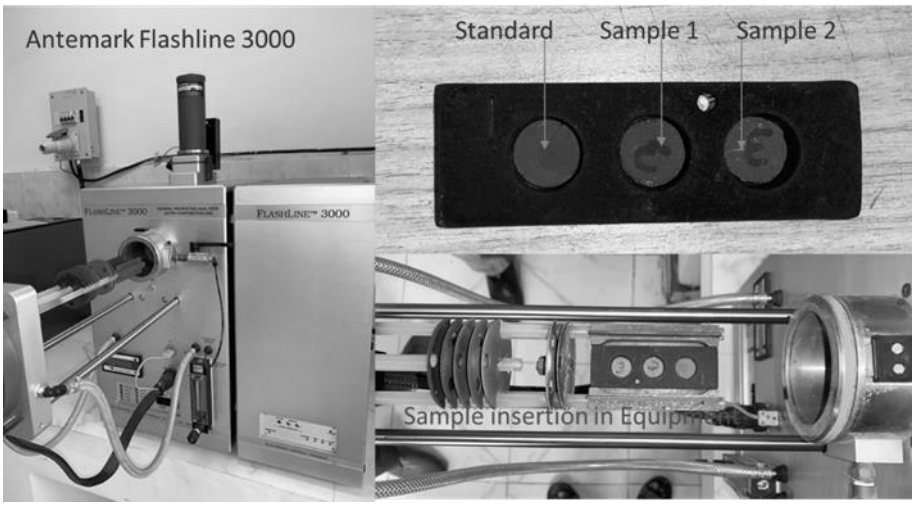

Fig. 3 Thermal Characterization Equipment and Samples

4. Results and Discussion

Initially, a feasibility study was undertaken to understand the effect of adding waste propellant in the manufacture of brick. Waste rocket propellant in range of 0.5% upto 4.0% by weight is added in brick formulation and initial studies were conducted. The variation of compressive strength, water absorption, XRD studies and SEM results were presented elsewhere [22]. Once results were found satisfactory, the study is extended to have thermo-physical characterization and understand the changes in thermal conductivity due to waste propellant addition and baking in different orientation. It is observed that propellant gets consumed during baking of bricks and combustion gases form micro-risers in the bricks. These micro-risers are elongated micro-pores, which are formed by moving upward combustion gases in the bricks. They are blind holes, but can impart directional effects to the thermal conductivity of bricks.

Addition of 2.5% waste rocket propellant in Brick formulation was analyzed first and properties are assessed with reference to the reference sample or non-impregnated brick. Scanning Electron Microscope (SEM) micrograph is used for understanding the variation in internal micro-structure due to impregnation of waste rocket propellant. Addition of waste propellant resulted in formation of micro-pores, as depicted in the Figure 4. Propellant definitely acts as pores-forming agent and the micro-structure in regions other than pores are dense. So, addition of waste rocket propellants has two effects – one is pores formation and local hardening of zones around pores.

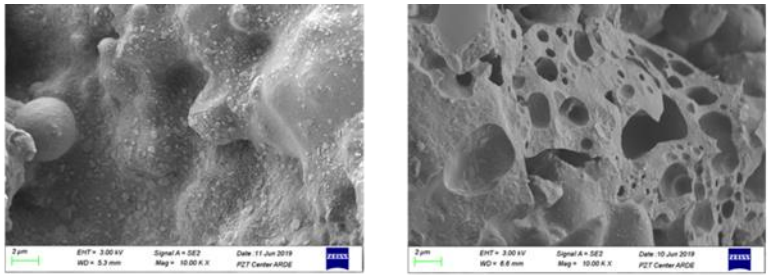

a. Reference Sample without propellant Impregnation

b. 2.5% by weight Propellant Impregnated Sample

Fig. 4 SEM Micrograph of Bricks

Percentage gain after immersion in water is carried out for 5 samples of each type and the average values are obtained. Reference sample gave a weight gain of 29±3 %, while the impregnated sample gave around 20±2 % weight gain. This clearly indicated that although samples might have become porous due to propellant addition, but the pores are not assessable to water. This may be attributed to local hardening around pores, which makes water ingress difficult and makes the pores impervious to water. In fact less water absorption is an advantage for the bricks. Compressive strength of the reference brick is found to be 4.25±0.5MPa, while that for impregnated brick is 4.0±0.5 MPa. Compressive strength is not adversely affected by propellant addition. The thermal conductivity increased from 0.72 W/mK at ambient condition to around 0.88 W/mK for the 2.5% by weight impregnated brick sample. Although much gain in thermal insulation properties were not ascertained but reduction in water absorption and marginally change in compressive strength, encouraged to impregnate higher weight percentage of waste propellant in brick and characterize for thermal properties. Additionally, effect of orienting brick sample horizontally (on flat surface) and vertically (on edges) is attempted to find any effect on the thermal properties. Temperature sweep from 30°C and 100°C is also carried out to get thermo-physical properties of Bricks in entire operational range.

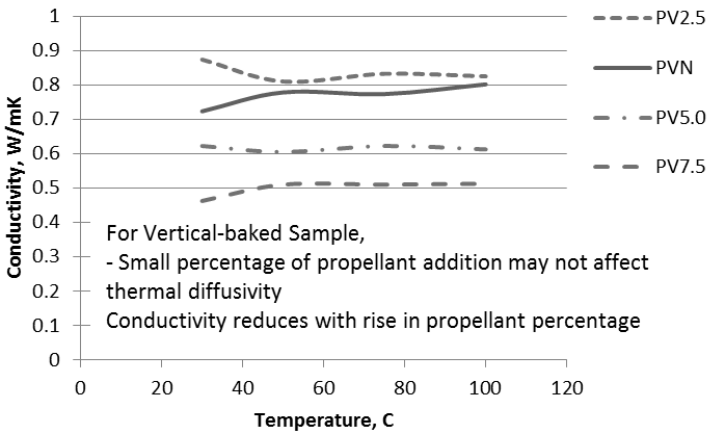

Fig. 5 Thermal Conductivity of Vertically Baked Impregnated Brick

For the vertically baked brick, temperature sweep data for different weight percentages of waste rocket propellant, in respect of thermal conductivity is presented in Figure 5. In the figure, the curves has followed a definite nomenclature. 'P' indicated propellant impregnation, 'V' indicates vertical curing, 'N' indicates reference non-impregnated sample and numerical values are indicating weight percentage of waste propellant. For examples PV2.5 indicates propellant impregnation, vertically cured, 2.5% waster rocket propellant impregnation. It is clear from the curve that over the specified temperature range, the value of thermal conductivity is more or less constant. At room temperature, reference have a thermal conductivity of 0.72 W/mK and the values for 2.5%, 5.0% and 7.5% propellant addition by weight changed the thermal conductivity at room temperature to around 0.89 W/mK, 0.61 W/mK and 0.48 W/mK, respectively. For 7.5%, waste propellant addition, the thermal conductivity at room temperature displayed reduction by 33.3% in numerical value. So, propellant addition improved thermal insulation properties of the brick. the same trend is present for all other temperature ranges also.

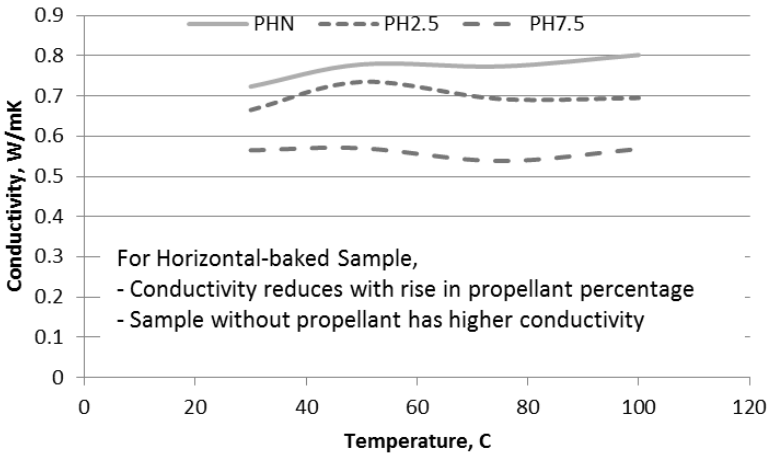

Fig. 6 Temperature Sweep For Thermal Conductivity of Horizontally Baked Impregnated Brick

The exercise is repeated for the horizontally baked sample too and the results are plotted as figure 6. In the figure the curve nomenclature has 'H' indicating horizontal baking condition of the samples. It is observed that for horizontal baking the reduction in thermal conductivity is visible even ay 2.5% waste propellant impregnation. At ambient condition, 0.0% (reference), 2.5% and 7.5% propellant impregnation gave thermal conductivity of 0.72 W/mK, 0.68 W/mK and 0.58 W/mK, respectively. The reduction at 7.5% waste propellant impregnation is around 19%. Although the reduction, in case of 7.5% propellant impregnation for thermal conductivity at room temperature is lower for horizontal baked sample than vertically baked sample, but the reduction even at 2.5% propellant impregnation is the advantage of horizontal baking.

Overall, if practical applications are also considered, it is clear that for vertically baked propellant impregnated brick sample, lower additives quantity lead to enhancement in thermal conductivity, thus defeating the main attempt of enhancing thermal insulation properties. Although such bricks with higher thermal conductivity may be suitable as lining for furnace and boilers. Higher propellant quantity in vertical baking of brick may result in reduction in thermal conductivity, but the structural integrity of bricks is compromised due to large amount of porosity and reduced compressive strength. Contrary

to this, horizontal baking results in reduction of thermal conductivity even for the small quantity of composite propellant as additives. So, for thermal insulation application, such bricks are practically useful.

5. Conclusion

Waste rocket propellant is added to brick to understand any change in water absorption, compressive strength or microstructure. Addition of waste rocket propellant in brick makes it porous but water absorption is reduced, due to local hardening around pores by heat generation from propellant during baking of bricks. Orientation, temperature and percentage propellant impregnation, all three affects the thermo-physical characterization of brick sample. The orientation of brick during baking orients pores created by rising combustion gases from combustion of propellants. Thermal conductivity for reference non-impregnated sample of brick is around 0.72 W/mK at ambient condition. For horizontal baking the value reduces to 0.48 W/mK for 7.5% propellant impregnated brick. However, for vertical baking, the value for 7.5% propellant impregnation is 0.58 W/mK. So, higher propellant impregnation and vertical orientation of baking is capable to give bricks with lower thermal conductivity, imparting higher thermal insulation properties. Horizontal baking with 2.5% waste propellant has thermal conductivity value of 0.67 W/m.K and this method of baking is suitable for smaller percentage of waste propellant addition, for enhanced thermal insulation capacity of bricks.

References

[1] Sutcu M, Akkurt S. The use of recycled paper processing residues in making porous brick with reduced thermal conductivity, J. Ceram. Inter. 35 (2009) 2625. https://doi.org/10.1016/j.ceramint.2009.02.027

[2] Sutcu M, Akkurt S, Bayram A, Uluca U. Production of anorthite refractory insulating firebrick from mixtures of clay and recycled paper waste with sawdust addition, J. Ceram. Inter. 38 (2012) 1033. https://doi.org/10.1016/j.ceramint.2011.08.027

[3] Janbuala S, Mana A, Pitak L. Effect of Rice Husk and Rice Husk Ash to Properties of Bricks, Procedia Engineering 32:1061-1067 · December 2012. https://doi.org/10.1016/j.proeng.2012.02.055

[4] Mohan NV, Satyanarayana PVV, Srinivasa Rao KS. Performance Of Rice Husk Ash Bricks, International Journal of Engineering Research and Applications (IJERA), Vol. 2, Issue 5, September- October 2012, pp.1906-1910.

[5] Arshad MS, Pawade PY. Reuse Of Natural Waste Material For Making Light Weight Bricks, International Journal Of Scientific & Technology Research, Volume 3, Issue 6, June 2014, 49-53.

[6] Akar C,Canbaz M. Effect of molasses as an admixture on concrete durability, Journal of Cleaner Production 112 · September 2015. https://doi.org/10.1016/j.jclepro.2015.09.081

[7] Bhide S, Darshane J, Shinde D, Dhokale S, Deshmukh P, Desai Y, Kodag P. Effect of Sugarcane Molasses on Compressive Strength and Workability of Fly Ash Mixed Concrete, IJSRSET, May-June 2017, Volume 3, Issue 3, Themed Section: Engineering and Technology, 607-612.

[8] Magudeaswaran P, Hilal AS. Development of Eco Brick and Concrete with the partially replacement of cow dung, International Journal of Science and Engineering Research (IJ0SER), Vol 6, Issue 5, May-2018, 3221-5687.

[9] Kavitha S, Dethan PD,Jyothi P, J A. Effect Of Cowdung And Coir In Strengthening Of Clay Bricks, International Research Journal of Engineering and Technology (IRJET), Volume: 05 Issue: 10 | Oct 2018, 1891-1894.

[10] Badr El-Din Hegazy E, FouadHanan A,Hassanain Ahmed M. Brick Manufacturing from Water Treatment Sludge and Rise Husk Ash, Australian Journal of Basic and Applied Sciences, vol. 6(3), pp. 453-461. 2012.
[11] Jahagirdar Shrikant S, Shrihari S, Manu B. Reuse of Textile Mill Sludge in Burnt Clay Bricks, International Journal of Advanced Technology in Civil Engineering, vol 2(1), pp. 96-99, 2013.
[12] Reddy Babu G, VenkataRamana N. Durability of Bricks Cast with Industrial Sludge, IOSR Journal of Machanical and Civil Engineering (IOSR-JMCE), vol. 6(4), pp. 43-46. 2013. https://doi.org/10.9790/1684-644346
[13] Elias ML,Cultrone G. On the Use of Sodium Chloride and Calcined Diatomite Sludge as Additives to Improve the Engineering Properties of Bricks Made with a Clay Earth from Jun (Granada, Spain), Minerals 2019, 9, 64. https://doi.org/10.3390/min9010064
[14] Baspinar MS, Demir I, Orhan M. Utilization potential of silica fume in fired clay bricks, Waste Management & Research, ISSN 0734-242X, 2010: 28: 149-157. https://doi.org/10.1177/0734242X09104385
[15] Koseoglu K, Polat M, Polat H. Encapsulating fly ash and acidic process waste water in brick structure, Journal of Hazardous Materials 176 (2010) 957-964. https://doi.org/10.1016/j.jhazmat.2009.11.133
[16] Kartini K, Norul Ernida ZA, Noor Fazilla B, Ahmad Farhan H. Development of Light Weight Sand Cement Brick using Quarry Dust, Rice Husk and Kenaf Powder for Sustainability, International Journal of Civil & Environmental Engineering IJCEE-IJENS, Dec 2012, Vol:12 No:06, 1-7.
[17] Wilson J. Thermal Properties of Building Materials, Posted on 01 Feb 2008 in Technical data column of site electronics-cooling.com/2008/02/thermal-properties-of building-materials/
[18] Al-Hadrani LM, Ahmed A. Assessment of Thermal Performance of Different Types of Masonary Brick Used in Saudi Arabia, Applied Thermal Engineering, 29(5-6), April 2009, 1123-1130. https://doi.org/10.1016/j.applthermaleng.2008.06.003
[19] Meukam P, Noumowé A, Jannot Y, Duval R. Thermophysical and mechanical characterization of stabilized clay bricks for building thermal insulation, Materials and Structures 36(7):453-460 · August 2003. https://doi.org/10.1007/BF02481525
[20] Vivancos JL, Soto J, Perez I, Ros-Lis J. A new model based on experimental results for the thermal characterization of bricks, Building and Environment 44(5):1047-1052 · May 2009. https://doi.org/10.1016/j.buildenv.2008.07.016
[21] Prasad J, Satyavathi PLA, Srivastava R, Nair KM. Characterisation and classification of soils of Nasik District, Maharashtra. Agropedology, 1995, 5, 25-28.
[22] Mehta PK, Kumaraswamy A, Saraswat VK, Kumar BP. Studies on High Energy Propellant Waste in the processing of Fired Clay Brick, Defence Science Journal, 70(6), Nov 2020, 596-602. https://doi.org/10.14429/dsj.70.15740

Research on Engineering Structures & Materials
journal homepage: http://www.jresm.org
Research Group

Research Article

Effect of elevated temperature on strength and durability properties of concrete using nano-silica and alccofine

Ashwini K.*[a], Srinivasa Rao P.[b]

Department of Civil Engineering, Jawaharlal Nehru Technological University Hyderabad, Hyderabad, Telangana, India.

Article Info

Article history:
Received 19 Apr 2021
Revised 01 Jul 2021
Accepted 09 Jul 2021

Keywords:

Concrete;
Alccofine;
Nano-silica;
Strength property;
Durability studies

Abstract

The strength and durability properties of concrete using nano-silica and alccofine after exposed to higher temperatures were investigated in this study. Concrete with 3% nano-silica and 15% alccofine were prepared and water cured for 28 days. In an electric boogie furnace, concrete specimens with and without nano-silica and alccofine were heated to 400°C and 800°C for 4 hours. The specimens then were allowed to cool until they reached room temperature. The compressive strength test was used to determine strength, whereas the water absorption, porosity, and rapid chloride permeability tests were conducted to check durability properties. SEM images were used to examine the microstructure of concrete specimens at elevated temperatures. According to the test results, the strength and durability properties of concrete using nano-silica and alccofine deteriorated at high temperatures. At room temperature, concretes containing alccofine and nano silica performed better than control mixes. A severe loss in strength and a significant increase in charge pass, water absorption and porosity were observed at 800°C for concrete using alccofine and nano silica. The microstructural analysis using scanning electron microscopy methods also reported that the porosity increased with increase in temperature.

1. Introduction

Fire remains one of the most serious potential hazards, as it affects the structural integrity of concrete structures. [1]. Fire has an adverse and unrecoverable effect on the physical, strength, and serviceability properties of concrete. As a result, it is critical to look into the efficiency of concrete that's been subjected to fire. It has been reported that the duration of exposure will have no or little impact on the concrete's compressive strength when subjected to fires up to 200°C [2-5]. Moreover, regardless of the exposure temperature, growing the exposure duration has been shown to have a negative impact on the residual capacity of concretes, particularly the strength properties [3]. Some supplementary cementitious materials from agricultural and industrial waste shows an unpredictable effect on performance of concrete under fire, and therefore been extensively studied by a number of researchers [6, 7]. Carbonates start to break down at 500-600°C, and are believed to trigger permanent destruction to concrete and they're a key component of the primary binder form of concrete [8]. In particular, temperature over 800°C, almost all contents of concrete degrade, resulting in considerable strength as well as weight loss since the thermal characteristics of aggregates and cement paste differ, this causes residual stress and cracking [9]. Poon et al. [10] compared the compressive strength and durability properties like rapid chloride diffusion, porosity & crack pattern of control mixes and high strength mixes for temperature up to 800°C and concluded that a significant loss in durability in terms of permeability occurred than the loss of compressive strength. As such, several advanced laboratory techniques, such as scanning electron microscopy analysis,

*Corresponding author: ashwini.kota@gmail.com
[a] https://orcid.org/0000-0003-2708-7911; [b] https://orcid.org/0000-0002-9020-5944
DOI: http://dx.doi.org/10.17515/resm2021.281st0419

energy dispersive spectrometer, and X-ray diffraction analysis, are used to reveal concrete degradation mechanisms after exposed to elevated temperatures [11]. Karahan [12] tested experimentally the transport properties after being exposed to elevated temperatures, of high-volume slag or fly ash added concretes and found that according to rapid chloride permeability (RCPT) test results, slag-based concrete binds more chlorine than fly ash-based concrete, and the behavior of slag-based concrete at elevated temperatures was superior to that of fly ash-based concrete. Demez et al. [13] assessed mechanical characteristics of high strength concrete (HSC) using pyrophyllite aggregate after exposed to elevated temperatures and concluded that the loss of compressive strength was much more pronounced in all concrete mixes subjected to temperatures above 600°C. Ercolani et al. [14] investigated the action of concrete when subjected to elevated temperatures and various cooling systems and found that if water is employed as a cooling medium, the rise in temperature affects physical as well as mechanical characteristics causing increase in degradation with development of cracks or microcracks. Mousavimehr et al. [15] stated that in addition to enhancing the mechanical as well as durability properties of rubberized concrete at elevated temperatures, the combined effect of metakaolin and silica fume can indeed create environmentally sustainable mixes by minimizing carbon footprint in comparison to a control mix. Because extreme heat can disintegrate the mechanical characteristics of concrete and potentially harm the entire structure, it's indeed critical to ascertain the impact of elevated temperatures upon on mechanical characteristics of high-performance concrete (HPC) [16]. With increasing elevated temperatures, HPC's thermal expansion dramatically increases. Therefore, from above studies it is self-evident that concrete's high-temperature characteristics are critical for simulating the fire behavior of concrete structures. It was discovered in a prior study that adding nano-silica and alccofine to concrete increased its strength properties [17]. Because nano-silica and alccofine aid in the development of high strength concrete, their use in concrete may expand. As a result, it is critical to determine if concrete manufactured from these ingredients is safe in the event of a fire or high temperatures.

Since no research has been done on the durability properties of concrete using nano-silica and alccofine after subjected to higher temperatures. Therefore, in this study an attempt has been made to evaluate the residual compressive strength and durability properties like water absorption and porosity, rapid chloride permeability and morphology of concrete mixes using alccofine and nano silica after exposure high temperatures. To relate the strength and durability properties of different concretes mixes at elevated temperatures, they must be prepared and evaluated under identical material and heating regimes.

2. Experimental Studies

2.1. Material Used

OPC of 53 grades confirming to IS 12269-1987 was used in this study with specific gravity 3.15. The physical properties of cement are given in Table 1.

Table 1. Physical properties of cement

Sr. no	Properties	Values	Requirements as per IS: 12269-1987
1.	Soundness (Le Chatelier method)	1.2	< 10mm
2.	Initial setting time	56 min	> 30min
3.	Final setting time	259 min	< 600 min
4.	Fineness	300 (m^2/kg)	> 225 m^2/kg
5.	Standard Consistency	32%	-

Alccofine (Al) which is an ultra-fine slag or ggbs having particle size 4-6μm and specific gravity 2.86. It was procured from local dealers. Nano silica (Ns) having size of 17nm and specific gravity 2.2-2.4 shown in Fig. 2 was used. The properties alccofine and Ns obtained from manufacturer are given below in Table 2. As a fine aggregate, locally accessible river sand with specific gravity 2.65 has been used and coarse aggregates with a size of 20 mm having specific gravity 2.79 were used. Conplast SP430DIS is a high range water reducer superplasticizer that is used to maintain the workability of concrete mix. The laboratory tap water was used.

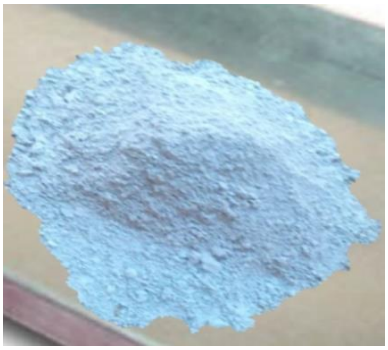

Fig. 1 Alccofine

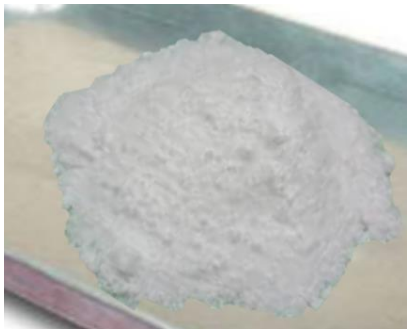

Fig. 2 Nano silica

Table 2. Chemical and physical properties of materials

Item	Calcium oxide	Silicon dioxide	Aluminum oxide	Ferric oxide	Magnesium oxide	Sulfur trioxide	Avg. particle size
Al	32.1-34.3	33-35	18.0-20.0	1.8-2	8.0-10.0	0.30-0.70	4-6μm
Ns	0.060	99.880	0.0050	0.0010	-	-	17nm

2.2. Mix Proportions

Three blends of different concrete M40, M50, and M60 were taken into account to research the characteristics of concrete using nano-silica and alccofine, and mix design has been carried for all concrete grades according the IS10262:2019 and IS 456:2005 with w/c ratios of 0.4, 0.36, and 0.3. Alccofine (15%) and nano silica (3%) were used to replace cement. The mix proportions of the concrete mixes are given in Table 3.

Table 3. Mix proportions and notations of different concrete mixes

Concrete grade	Additives	Notations	Water Kg/m^3	Cement Kg/m^3
M40	0	M4	160	400
	AL+ Ns	M4AlNs	160	328
M50	0	M5	159	440
	AL+ Ns	M5AlNs	159	360.8
M60	0	M6	158	527
	AL+ Ns	M6AlNs	158	400

Table 3 (Con.). Mix proportions and notations of different concrete mixes

Concrete grade	FA Kg/m^3	CA Kg/m^3	Al Kg/m^3	Ns Kg/m^3	w/c
M40	667	1248	-	-	0.4
	667	1248	60	12	0.4
M50	642	1243	-	-	0.36
	642	1243	66	13.2	0.36
M60	596	1218	-	-	0.3
	596	1218	79	15.8	0.3

Fig. 3 Electric bogie for heating specimens

Fig. 4 Rapid chloride permeability test apparatus

Fig. 5 Compression testing apparatus

2.3. Test Methods

Concrete samples of cubic size 150 mm & 100mm and disc sample of 100mm diameter and 50mm height size were casted and cured for 28 days in water. After curing the samples were dried and then placed in electronic bogie furnace shown in Fig. 3. The elevated temperature of 400 and 800 degree Celsius was maintained for 4hours duration. The fire duration of 4hrs is considered because as per National Building Code of India, desirable fire grading of columns and beams is 4 and 3 hrs. The samples were then cooled to room temperature by leaving them out in the open air. 150 mm samples were tested for compressive strength as per IS: 516 – 1959 [18].

Using the ASTM C 642-06 [19] procedure, 100 mm samples were used to determine water absorption and porosity. The ASTM C1202 [20] specification was used as a guide for the rapid chloride permeability assessment using a 50 mm disc samples. After completing the compressive strength test, the specimens were ground into fine powder for microstructural analysis using Scanning Electron Microscopy (SEM) test. Test apparatus for compressive strength test and rapid chloride permeability test shown in the Fig. 3 & 4. The results at room temperature (RT) were compared to those obtained at higher temperatures.

3. Result and Discussion

3.1. Compressive Strength

The Compressive strength results of concrete specimens subjected to elevated temperatures are depicted in the Fig. 6 as the average of the observations. It can be seen from the Fig. 6 that increasing the temperature decreases compressive strength. Compressive strength results of Al+Ns concrete mixes were between 66 to 83 Mpa at RT, 64.9 to 80 MPa at 400°C, and 29 to 41.3 MPa at 800°C, respectively, as shown in Fig. 6. And compressive strength results of control mixes were between 51.1 to 68.5 MPa, 57 to 67.4 MPa and 30.3 to 30.9 MPa at RT, 400°C, and 800°C, respectively. Compressive strength

decreased by 0.3 to 1.7% at 400°C, 40 to 48% at 800°C for control mixes, and 1.5 to 3.3% at 400°C, 50 to 56% at 800°C for Al+Ns mixes.

The percentage decrease in compressive strength was greater for Al+Ns concrete mixes M4AlNs, M5AlNs, & M6AlNs compared to control mixes M4, M5 & M6 because of degradation of calcium silicate hydrates [1]. Despite the fact that Al+Ns mixes had higher compressive strength than control mixes at 400°C, the percentage decrease in compressive strength was significantly higher for Al+Ns mixes. Fig. 13 shows that the compressive strength decreases as the porosity increases. Therefore, increase in porosity with temperature is one of reason for decrease in compressive strength at higher temperatures. Cross sections of concrete samples at different temperatures are shown in Fig. 7, 8 & 9. The color of hardened concrete changed after exposed to higher temperatures. Cracks appeared in the aggregate & paste's interfacial transition zone (ITZ), as well as within the aggregate at 800°C from Fig. 9 which is another reason for reduced compressive strength. Because the interfacial transition zone (ITZ) is the weakest connection between cement paste and aggregate, it can enhance crack propagation. As a result, increasing temperature raises internal stresses, which accelerates material cracking, multiplies defects, and thereby lowers strength [21, 22].

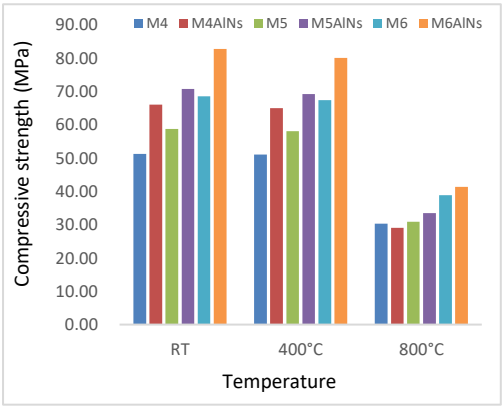

Fig. 6 Compressive strength values at elevated temperatures

Fig. 7 Cross section of a hardened concrete at room temperature.

Fig. 8 Cross section of a hardened concrete at 400°C.

Fig. 9 Cross section of a hardened concrete at 800°C.

3.2. Water Absorption and Porosity

Water absorption and porosity values of concrete with and without Al and Ns were calculated using test procedure given in ASTM C642 for all the concrete grades. The water absorption of concrete specimens subjected to elevated temperatures are depicted in the Fig. 10 as the average of the observations.

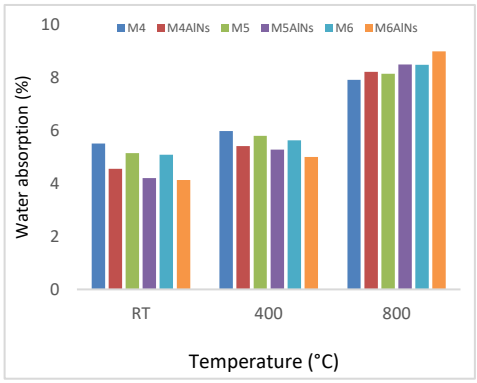

Fig. 10 Water absorption values at elevated temperatures

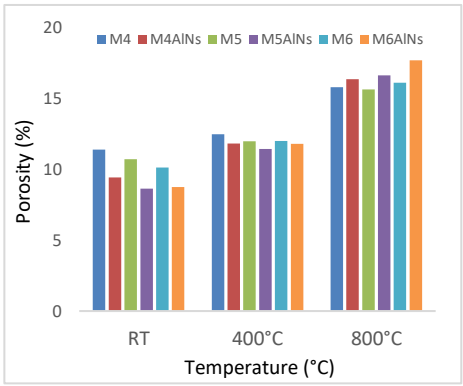

Fig. 11 Porosity values at elevated temperatures

It can be seen from the Fig. 10 that increasing the temperature increases water absorption due to internal cracking. The three major reasons of such an internal cracking could be the breakdown of crystalline calcium hydrate particles, development of steam pressure, and degradation of C-S-H [7].

Concrete with a water absorption value of less than 5% is considered to be of high quality [23]. Water absorption of Al+Ns concrete mixes ranged from 4.1 to 4.6 %, 5.4 to 5.8 %, and 8.2 to 9% at RT, 400°C, and 800°C, respectively, as shown in Fig. 10. And water absorption of control mixes ranged from 5 to 5.5 %, 5.6 to 6%, and 7.8 to 8.5 % at RT, 400°C, and 800°C, respectively. At RT, concretes mixes containing Al+Ns showed less than 5% water absorption. At 400°C and 800°C, all the concrete mixes showed water absorption greater than 5%. The percentage increase in water absorption of control mixes is 8 to 13% at 400°C, 43 to 67% at 800°C and for Al+Ns mixes is 18 to 26% at 400°C, 80 to 118% at 800°C. The percentage increase in water absorption was greater for mixes M4AlNs, M5AlNs, & M6AlNs mixes at 800°C compared to M4, M5 & M6 mixes.

Increase in temperature leads to the formation of large number of air voids due to evaporation of free water, accompanied by capillary water, and then physically bound water [24]. Porosity of Al+Ns concrete mixes ranged from 8.6 to 9.5 %, 11.4 to 11.8 %, and 16.3 to 17.7 % at RT, 400°C, and 800°C, respectively, as shown in Fig. 11. And porosity of control mixes ranged from 10.1 to 11.4 %, 11.9 to 12.5 %, and 15.6 to 16.1 % at RT, 400°C, and 800°C, respectively. The percentage increase in porosity of control mixes is 9 to 18% at 400°C, 38 to 59% at 800°C and for Al+Ns mixes is 25 to 35% at 400°C, 73 to 102% at 800°C. The percentage increase in porosity was greater for Al+Ns concrete mixes M4AlNs, M5AlNs, & M6AlNs at 800°C compared to control mixes M4, M5 & M6. Because at high temperature as water evaporates, the internal pore pressure increases, which causes significant internal pressures upon on solid skeleton of concrete due to the compact structure and lower permeability of Al+Ns concrete mixes. And thereby increases no. of micro cracks leading to increase in no. of voids in concrete matrix [24].

The graph of water absorption versus porosity is plotted considering all concrete mix at all temperatures as shown in Fig.12. The porosity of concrete is linearly proportional to water absorption [25]. Therefore, increase in porosity increases water absorption due to increase in total pore volume of concrete. Similar results were reported by Karahan et al. [12] for concrete using slag with the porosity values varying between 9.3–11.0% at 20°C, 10.4–11.7% at 400°C, and 16.2–17.4%, at 800°C, and water absorption varied between 4–4.5% at 20°C, 4.5–5.5% at 400°C, and 7.5–8.5%, at 800°C, respectively.

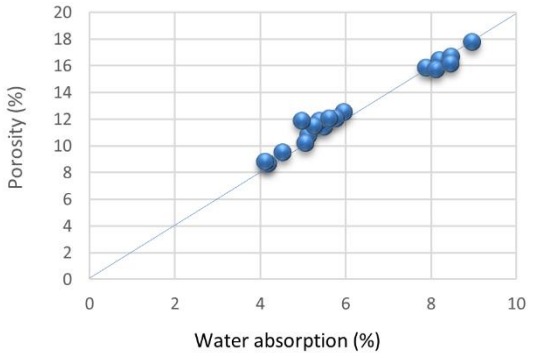

Fig. 12 Water absorption vs. Porosity

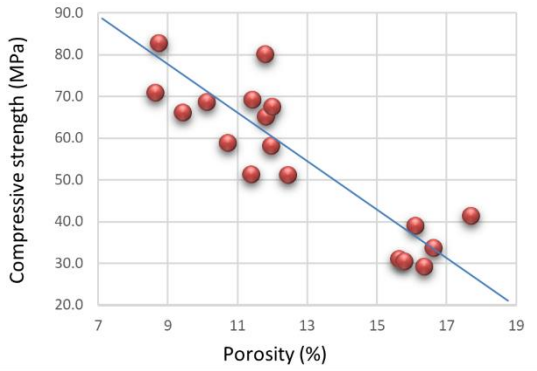

Fig. 13 Porosity vs. compressive strength

3.3. Rapid Chloride Permeability

The RCPT test, that is used to measure concrete's durability in terms of chloride-ion permeability, is easy to perform and can be completed in just 6 hours. Before exposing to high temperatures all the concrete mixes showed very low permeability s per ASTM 1202. As when the temperature was elevated, there was a substantial loss of permeability. If the charge moving through the concrete specimen is greater than 4000 C, then as per ASTM 1202 it is categorized as highly permeable [10, 25]. Since more current flows into a highly permeable concrete its chloride-ion resistance is an indirect indicator of its permeability and internal pore structure [7]. RCPT values of Al+Ns concrete mixes ranged from 700 to 940 C at RT, 1170 to 1590 C at 400°C, and 4920 to 6990 C at 800°C, respectively, as shown in Table 4.

The RCPT values of control mixes ranged from 1518 to 1740 C at RT, 2000 to 2420 C at 400°C, and 5380 to 6000 C at 800°C, respectively. At room temperature (RT), concretes mixes containing Al+Ns showed very low chloride ion penetrability compared to control mixes. Chloride ion penetration at 400°C was moderate for M4, M5 & M6 mixes and low for M4AlNs, M5AlNs, & M6AlNs mixes. The percentage of chloride ion entry into the concrete specimens largely depends on the structure of the internal pores and micro cracks. From Fig. 7, 8, & 9 it can be seen that with the increase in temperature the bond between aggregates and cement paste deteriorated and number of microcracks increased. The increase in rapid chloride permeability at elevated temperature is calculated by comparing it to the values at room temperature. The increase in rapid chloride permeability of control mixes is 1.3 to 1.4 times at 400℃, 3 to 4 times at 800℃ to that of rapid chloride permeability at room temperature. The increase in rapid chloride permeability of Al+Ns mixes is 1.6 to 1.7 times at 400℃, 5 to 10 times at 800℃ to that of rapid chloride permeability at room temperature. The relationship between porosity and RCPT is shown in Fig. 14, and it was observed that RCPT increases as porosity increases. Therefore, RCPT values of all the concrete mixes after subjected to high temperature of 800°C were greater than 4000 C due to excessive cracking and increased porosity from Fig 11, hence regarded as not durable [26]. As a reason, concrete using alccofine and nano-silica is considered as not durable, and also its utilization should be thoroughly considered for structures that are frequently subjected to heating and cooling cycles. Nadeem et al. [1] noticed an increase in rapid chloride permeability of concrete with fly ash and metakaolin by 3 to 15 times at 400℃ and 20 to 40 times at 800℃ when compared to rapid chloride permeability at room temperature. Poon et al. [7] noticed an increase in rapid chloride permeability of concrete with fly ash and silica fume by 5 to 20 times at 800℃ when compared to rapid chloride permeability at room temperature.

Table 4. RCPT Values at elevated temperatures

Admixtures	RT	400°C	800°C
M4	1732.5	2418.3	5639.4
M4AlNs	934.2	1584.9	4927.5
M5	1557	2035.8	5383.8
M5AlNs	758.7	1309.5	5647.5
M6	1518.3	2007	5996.7
M6AlNs	706.5	1170	6990.3

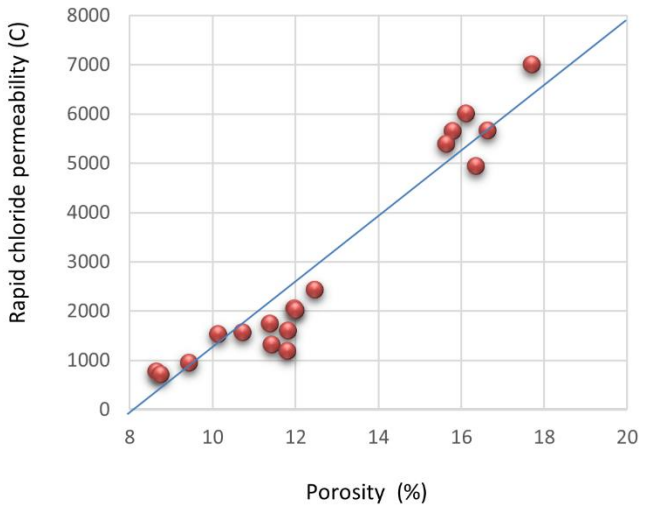

Fig. 14 Porosity vs. rapid chloride permeability

3.4. Microstructural Analysis

Microstructural analysis using SEM examinations of concrete specimens revealed distinct morphological changes as a result of exposure to high temperatures [27]. At 400°C, the concrete matrix appeared coarser and no ettringite was detected [28]. On concrete specimens heated to 400°C & 800°C, microcracks and voids are identified as shown in Table 5. The CH disintegrated at 800°C, resulting in a porous concrete matrix [28]. The microstructure seemed to be very porous in comparison to specimens heated to 400 °C, and porosity increased with concrete grade. Wide voids were noticeable in many areas of the M6AlNs mix concrete specimens as shown in Table 5. The number of voids in Al + NS mixes was higher than control mixes which is consistent with the strength characteristics and durability test results provided above. Due to voids, microcracks, and partially deteriorated CSH, concrete specimens subjected to 800°C showed substantial modifications in the micro - structural of the concrete [29]. As a result, the microstructure of the concrete deteriorated, affecting its strength and durability. Arioz et al. [29] and Handoo et al. [27] investigated the microstructures of concrete specimens exposed to 800°C and found similar results.

Table 5. SEM images of different concrete mixes

Concrete mixes	Temperature	
	400°C	800°C
M4	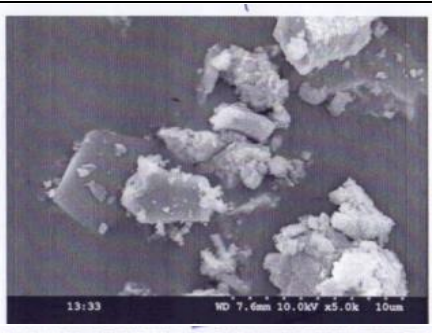	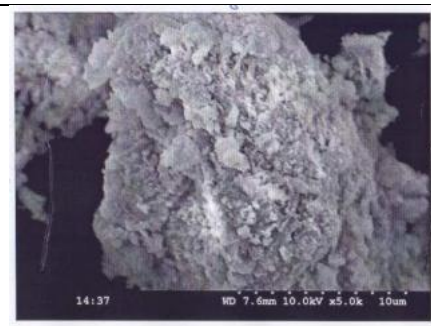
M4AlNs	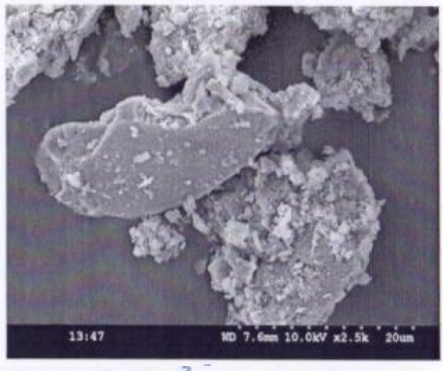	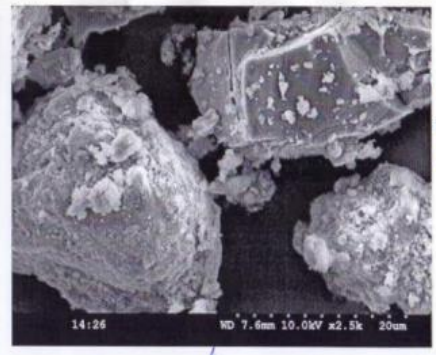
M5	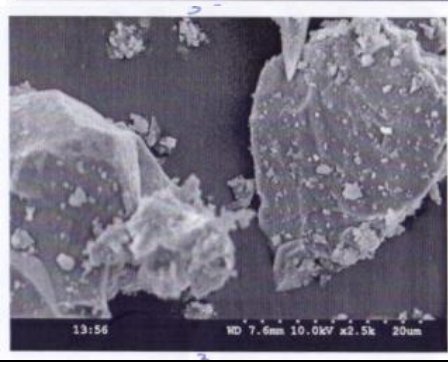	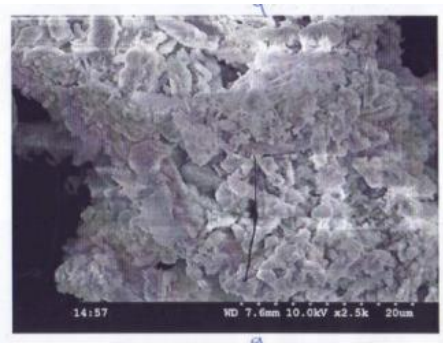

Table 5 (Con.). SEM images of different concrete mixes

Concrete mixes	Temperature	
	400°C	800°C
M5AlNs	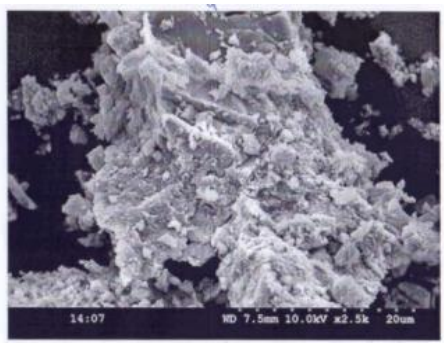	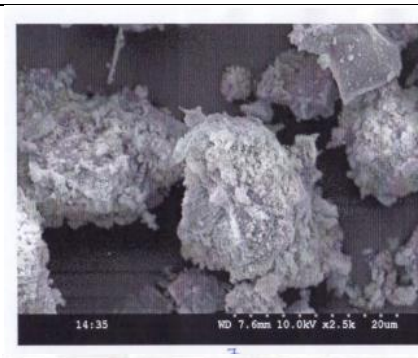
M6	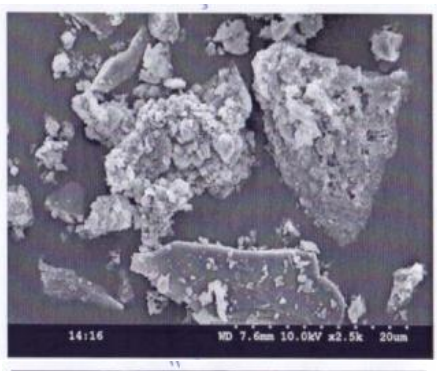	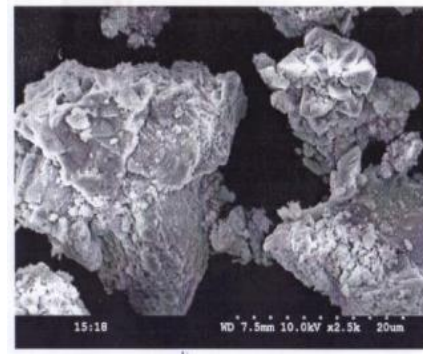
M6AlNs	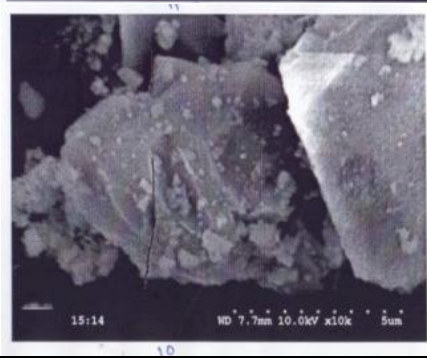	

4. Conclusions

The following conclusions can be drawn from the findings of this study:

- The compressive strength of all concrete mixes decreased with increase in temperature, a slight loss of strength was noticed between room temperature and 400 °C and the percentage reduction of Al+ Ns mixes was grater at 800°C. Compressive strength decreased by 0.3 to 1.7% at 400°C, 40 to 48% at 800°C for control mixes, and 1.5 to 3.3% at 400°C, 50 to 56% at 800°C for Al+Ns mixes.
- Cracks appeared in the aggregate & paste's interfacial transition zone (ITZ), as well as within the aggregate and also color of hardened concrete changed with temperature.

- The water absorption and porosity increased with increase in temperature. The percentage increase in water absorption and porosity was greater for Al+Ns concrete mixes M4AlNs, M5AlNs, & M6AlNs at 800°C compared to control mixes M4, M5 & M6.
- The percentage increase in water absorption of control mixes is 8 to 13% at 400°C, 43 to 67% at 800°C and for Al+Ns mixes is 18 to 26% at 400°C, 80 to 118% at 800°C.
- The percentage increase in porosity of control mixes is 9 to 18% at 400°C, 38 to 59% at 800°C and for Al+Ns mixes is 25 to 35% at 400°C, 73 to 102% at 800°C
- At room temperature and 400°C, Al and Ns reduced RCPT values compared to control mixes, but at 800°C, it increased due to increase in porosity.
- For control mixes, rapid chloride permeability increased by 1.3 to 1.4 times at 400°C, 3 to 4 times at 800°C, and for Al+Ns mixes 1.6 to 1.7 times at 400°C, 5 to 10 times at 800°C, compared to rapid chloride permeability at room temperature.
- According to microstructural analysis, the percentage of voids increased and became wider as the temperature rose. As a result, the microstructure of the concrete deteriorated, affecting its strength and durability.

Acknowledgement

The authors are grateful to the Jawaharlal Nehru Technological University Hyderabad (India) for providing the necessary laboratory facilities to carry out the research work discussed in the present paper.

References

[1] Nadeem A, Memon SA, Lo TY. The performance of Fly ash and Metakaolin concrete at elevated temperatures. Constr. Build. Mater, 2014; 62: 67–76. https://doi.org/10.1016/j.conbuildmat.2014.02.073

[2] Memon SA, Shah SFA, Khushnood RA, Baloch WL. Durability of sustainable concrete subjected to elevated temperature–A review. Construction and Building Materials, 2019; 199: 435-455. https://doi.org/10.1016/j.conbuildmat.2018.12.040

[3] Mohamedbhai GTG. Effect of Exposure Time and Rate of Heating and Cooling on Residual Strength of Heated Concrete. Magazine of Concrete Research, 1986; 38(136):151–158. https://doi.org/10.1680/macr.1986.38.136.151

[4] Horszczaruk E, Sikora P, Cendrowski K, Mijowska E. The effect of elevated temperature on the properties of cement mortars containing nanosilica and heavyweight aggregates. Construction and Building Materials, 2017; 137: 420–431. https://doi.org/10.1016/j.conbuildmat.2017.02.003

[5] Demirel B, Kelestemur O. Effect of elevated temperature on the mechanical properties of concrete produced with finely ground pumice and silica fume. Fire Safety Journal, 2010;45:385–391. https://doi.org/10.1016/j.firesaf.2010.08.002

[6] Poon CS, Azhar S, Anson M, Wong YL. Strength and durability recovery of fire-damaged concrete after post-fire-curing, Cem. Concr. Res., 2001;31:1307–1318. https://doi.org/10.1016/S0008-8846(01)00582-8

[7] Poon CS, Azhar S, Anson M, Wong YL. Performance of metakaolin concrete at elevated temperatures, Cem. Concr. Compos., 2003;25:83–89. https://doi.org/10.1016/S0958-9465(01)00061-0

[8] Dündar B, Çınar E, Çalışkan AN. An investigation of high temperature effect on pumice aggregate light mortars with brick flour. Res. Eng. Struct. Mat, 2020; 6(3): 241-255. http://dx.doi.org/10.17515/resm2019.163ma1121

[9] Fu YF, Wong YL, Tang CA, Poon CS. Thermal induced stress and associated cracking in cement-based composite at elevated temperatures - Part II: Thermal cracking around multiple inclusions, Cem. Concr. Compos., 2004;26(2):99-111. https://doi.org/10.1016/S0958-9465(03)00086-6
[10] Poon CS, Azhar S, Anson M, Wong YL. Comparison of the strength and durability performance of normal-and high-strength pozzolanic concretes at elevated temperatures. Cement and concrete research, 2001;31(9):1291-1300. https://doi.org/10.1016/S0008-8846(01)00580-4
[11] Khodja N, Hadjab H. Effects of Elevated Temperatures on Mechanical's concrete specimen behaviour. In MATEC Web of Conferences, 2018;165: 22010. https://doi.org/10.1051/matecconf/201816522010
[12] Karahan O. Transport properties of high-volume fly ash or slag concrete exposed to high temperature. Construction and Building Materials, 2017;152: 898-906. https://doi.org/10.1016/j.conbuildmat.2017.07.051
[13] Demez A, Karakoç MB. Mechanical properties of high strength concrete made with pyrophyllite aggregates exposed to high temperature. Structural Concrete, 2021;22: E769-E778. https://doi.org/10.1002/suco.201900381
[14] Ercolani G, Ortega NF, Priano C, Señas L. Physical–mechanical behavior of concretes exposed to high temperatures and different cooling systems. Structural Concrete, 2017;18(3): 487-495. https://doi.org/10.1002/suco.201500202
[15] Mousavimehr M, Nematzadeh M. Post-heating flexural behavior and durability of hybrid PET–Rubber aggregate concrete. Construction and Building Materials, 2020; 265:120359. https://doi.org/10.1016/j.conbuildmat.2020.120359
[16] Xiao J, Xie Q, Xie W. Study on high-performance concrete at high temperatures in China (2004–2016)-An updated overview. Fire safety journal, 2018; 95:11-24. https://doi.org/10.1016/j.firesaf.2017.10.007
[17] Ashwini K, Rao PS. Evaluation of correlation between compressive and splitting tensile strength of concrete using alccofine and nano silica. In IOP Conference Series: Materials Science and Engineering, 2021;1091(1): 012056.
[18] IS: 516–1959. (1979). Indian Standard Code of Practice-Methods of Test for Strength of Concrete.
[19] ASTM C642-06, Standard Test Method for Density, Absorption, and Voids in Hardened Concrete, ASTM International, West Conshohocken, PA, 2006, www.astm.org
[20] ASTM C1202-19, Standard Test Method for Electrical Indication of Concrete's Ability to Resist Chloride Ion Penetration, ASTM International, West Conshohocken, PA, 2019, www.astm.org
[21] Carvalho EFTD, Silva Neto JTD, Soares Junior PRR, Maciel PDS, Fransozo HL, Bezerra ACDS, Gouveia AMCD. Influence of cooling methods on the residual mechanical behavior of fire-exposed concrete: An experimental study. Materials, 2019;12(21): 3512. https://doi.org/10.3390/ma12213512
[22] Pan HH, Li JC, Hou TC, Liao KS. Effect of temperature to micro-displacement of interfacial transition zone in cementitious materials by espi measurement. In 35th Conference on our world in concrete & structures, 25-27.
[23] Kosmatka SH, Kerkhoff B, Panares'e WC, MacLeod NF, McGrath RJ. Design and Control of Concrete Mixtures, 7th ed. Cement Association of Canada, Ottawa, Ontario, Canada, 2002.
[24] Hager. Behavior of cement concrete at high temperature. Bulletin of the polish academy of sciences, Technical sciences, 2003; 61(1):1-10.
[25] Kearsley EP, Wainwright PJ. Porosity and permeability of foamed concrete. Cement and concrete research, 2001;31(5):805-812. https://doi.org/10.1016/S0008-8846(01)00490-2

[26] Hossain KMA. High strength blended cement concrete incorporating volcanic ash: Performance at high temperatures. Cement and Concrete Composites, 2006;28(6): 535-545. https://doi.org/10.1016/j.cemconcomp.2006.01.013
[27] Handoo SK, Agarwal S, Agarwal SK. Physicochemical, mineralogical, and morphological characteristics of concrete exposed to elevated temperatures. Cement and Concrete Research, 2002;32:1009–1018. https://doi.org/10.1016/S0008-8846(01)00736-0
[28] Annerel E, Taerwe L. Assessment of the Fire Damage of Concrete Members after Fire Exposure. In Innovative Materials and Techniques in Concrete Construction, 2012;283-290.
[29] Arioz, O. Retained properties of concrete exposed to high temperatures: Size effect. Fire and Materials: An International Journal, 2009;33(5):211-222. https://doi.org/10.1002/fam.996

Research on Engineering Structures & Materials
journal homepage: http://www.jresm.org
MIM Research Group

Research Article

Impact of controlled permeable formwork liner against chloride penetration on the concrete structures

Vishal Ambad*[a], Raju Narwade[b], Karthik Nagarajan[c]

Department of Civil Engineering, Pillai HOC College of Engineering and Technology, Rasayani, Mumbai, India

Article Info

Article history:
Received 05 May 2021
Revised 14 Oct 2021
Accepted 13 Nov 2021

Keywords:

Concrete;
Controlled Permeable formwork (CPF);
Chloride penetration;
RCPT;
Permeability;
Durability

Abstract

It has become a requirement to enhance the surface quality of concrete structures and their durability. A non-woven formwork called Controlled Permeable formwork (CPF) liner was developed. This CPF liner is permeable to air and water however prevents the getaway of cement and small particles. This paper investigates experimentally the impact of CPF liner on the concrete surface against chloride penetration. The concrete mix contained ordinary Portland cement (OPC) 53, pulverized fly ash (PFA), Micro silica, locally available aggregates, crushed sand, water and superplasticizer. The cylindrical and cubical concrete specimens were cast with impermeable steel formwork (SF) and CPF liner. The cubic and cylindrical specimens were tested at the age of 7 days and 28 days. Compressive strength and Rapid chloride penetration tests (RCPT) were conducted. The concrete cast with CPF liner gives excellent compressive strength 14% more than specimens cast with steel formwork and has acquired better resistance against Chloride penetration. The results show that the concrete sample cast with CPF liner shows 9.98% less charges passed than specimens cast with steel formwork.

1. Introduction

Reinforced concrete structures need to be durable. Their durability is a major subject on a global scale [1]. Corrosion of steel reinforcement depends upon the exposure conditions, ensuing in millions of expenses being spent on repair and maintenance. Durability of reinforced concrete structures depends on the quality of the cover zone. Cover region is a primary line of defence against either physical or chemical deterioration of the concrete structures [2]. Corrosion of the steel reinforcement in the concrete is due to chlorides and CO_2 from the surrounding environment [3]. Chloride diffusion coefficient of concrete relies upon the water/cement ratio and the cement type [4]. Impermeability of the surface of the concrete structures performs an essential role for attaining long term durability. And that can be achieved by increasing the cement content for the whole entire volume of concrete and decreasing the water/binder ratio [5]. And another method is to use Controlled Permeable formwork (CPF) liner.

CPF liner is a hydrophilic fiber texture, which removes excess quantities of water and decreases water/binder ratio and improves the concrete strength [6].

CPF liner consists of three different primary factors. 1) A filter that allows water and air from fresh concrete to pass through it and keeps cement and other small particles. 2) This water and air are transferred to outside the formwork through drainage system and creates denser and less porous concrete surface. 3) The filter and drainage system is supported by structural support that maintains formwork shape and concrete pressure. Figure -1 shows the overall factors of a CPF system.

*Corresponding author: vishalambad@gmail.com
[a] orcid.org/0000-0001-6998-005X; [b] orcid.org/0000-0003-2349-0172; [c] orcid.org/0000-0002-2306-0327
DOI: http://dx.doi.org/10.17515/resm2021.306st0605

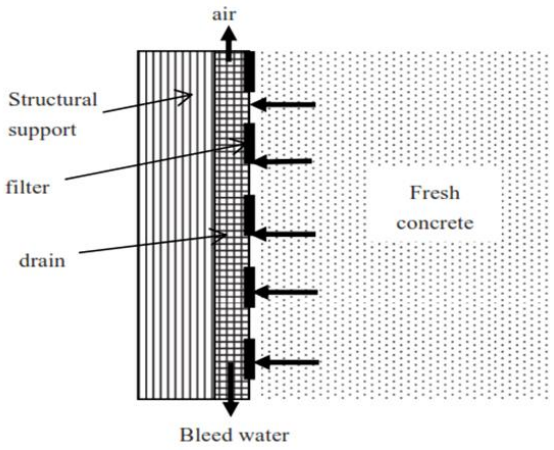

Fig. 1 Factors of a CPF System [8]

A range of research have shown the impact of CPF liner on concrete performance.

S Kothandarama et al. [2] have reported that CPF liner has extensively improved the tensile strength of concrete by almost 20% and abrasion resistance has been enhanced remarkably 50-80%.

S. Kumar et al. [4] have shown that the coefficient of chloride diffusion decreases as the strength of concrete increases, thus durability of the concrete structures increases.

Philip McKenna et al. [7] have reported that by using CPF liner, initial construction cost can be reduced, and improved surface strength, durability and overall appearance of the finished concrete can be achieved [7].

Suryawanshi AK et al. [8] have shown that improvement in impermeability can be achieved by using CPF liner. He used 350 kg/m3 cement as only cementitious material and kept cement/aggregate ratio 5.26.

Sahil Garg et al. [9] reported that CPF liners reduce w/c ratio and porosity of the concrete in the cover region and also found decreased chloride ion penetration depth. Sahil Garg et al. also found increased efficiency of permeable Formwork liner with increased water content in concrete mix.

L Basheer et. al. [10] used cement 450 kg/m^3 and water/cement ratio was kept 0.45. The author have shown that by the use of CPF liner that resistance to the ingress of Chlorides and CO2 was increased and impermeability of concrete also increased.

The use of mineral admixture gives improved quality to the concrete. The use of micro silica improves quality of hardened concrete like compressive strength, hence flexural and tensile strength. The use Micro silica reduces the rate of carbonation permeability; therefore, it helps in protecting reinforcement steel from corrosion. The use of fly ash can help in decreasing porosity and can make concrete highly dense as it has very small particles.

Therefore, it is proposed to have look into to analyze the effect of the CPF liner against chloride penetration on concrete surface cast with two different formworks, with lower W/C ratio and use of mineral admixtures.

2. Objectives

- To analyze the impact on compressive strength of concrete with decreased W/C ratio by the application of CPF liner.
- To achieve the better concrete surface performance against Chloride penetration by application of CPF liner using fly ash and micro silica as replacement to the cement.

3. Method

3.1. Materials

In this test O.P.C. 53 grade cement having specific gravity 3.08 was used. Aggregates of size 10 mm, 20 mm and crushed sand, having specific gravity 2.85, 2.87 and 2.71 respectively, were used. Pulverized Fly Ash (PFA) and Micro silica were used as replacement materials. Fly ash is an industrial by-product from combustion process of coal used in power stations. The specific gravity of fly ash was 2.15. Micro silica is also a mineral admixture found as by-product in the industrial manufacture of ferrosilicon and metallic silicon. Microsilica is grey in colour and specific gravity of microsilica was 2.24. Additionally, a Super plasticizer, named Fosroc Auracast 270M, based on polycarboxylic ether polymer was used. The water which was accessible to the lab was used. In this experiment Type II CPF liner was used. It has two sides, one side acts as a drain and another side as a filter. Its average pore size is 30 μm and thickness is 1.5-2.0 mm. This CPF liner has water retaining capability of about 1L/m2 and drainage capacity about >3L/m2.

3.2. Specimen Preparation

Concrete mix of M55 was used to cast the samples. The w/c ratio was kept low 0.26. The details of the concrete mix proportion is shown in table 1. The mix proportion shown in the table 1 is surface saturated dry (SSD) before moisture correction. It is shown that different mineral admixtures were used to replace cement. The concrete mix was identified as CMD-1. The mix of M55 grade is with 21% fly ash and 3% micro silica as a replacement to cement by weight. The superplasticizer replaced 30% water content. The codes IS 456, IS 383, IS 10262:2009 and IRC 112:2011 were followed to conduct the experiment.

Table 1. Concrete Mix Proportion (Kg/m^3)

Ingredients	CMD-1
Cement	424
Fly Ash	118
Micro silica	17
20 mm	614
10 mm	606
Crushed sand	573
Water	171
Admixture	8.4 kg
W/C ratio	0.26

Conventional Steel moulds were used to prepare the concrete specimens. Concrete specimens of size 150 x 150 x 150 mm^3 and small cylinders of 100 mm Dia. and 200 mm height were cast for this study. Steel moulds were oiled before placing the concrete. The casted specimens in steel formwork serve as a reference for comparison purpose. Commercially produced CPF liner is used to paste on the inner side of the other moulds where oil is not used, only glue is used.

Figure- 2 shows the steel mould with CPF liner pasted inside. The specimens cast with CPF liner were recognized as 'CPF' and those cast without CPF liner in the steel moulds were recognized as 'SF'. Further to this, specimens were categorized as FlyAsh SF and FlyAsh CPF etc. to compare the results.

Fig. 2 Steel Mould with CPF Liner Pasted Inside

Before concrete mix, the concrete mix proportion is corrected as per water absorption and moisture content of the aggregates. The water absoption for 20mm, 10mm and crushed sand was 1.4%, 1.6% and 2.65% respectively. And moisture content for crushed sand was 1.5%. The concrete mixes were mixed in a pan of 0.037 m3 capacity. The moulds were filled with the fresh concrete. Then these moulds with concrete were compacted using a tamping rod. 12 cubic specimens and 2 small cylinders were cast. Half number of specimens were cast with steel mould and half with CPF liner. After 24 hr the moulds were removed and specimens cured in a water tank for 7 and 28 days.

3.3 Test Methods

3.3.1 Compressive Strength

The specimens cast with CPF liner were easy to demould. The cast specimens were cured and kept in curing tank for 7 and 28 days. The cubic specimens were taken out from the curing tank and kept outside to open air to dry for some time. IS 516 (1969) was followed for testing the specimens. The demoulded cubic specimens were measured for size, weighed and tested in Compression Testing Machine (CTM) to determine the compressive strength. 3 cubic specimens for each category were tested at age of 7 and 28 days. The cubic specimens were crushed by applying load and load was automatically recorded on digital screen and noted down.

3.3.2 Rapid Chloride Penetration Test (RCPT)

The RCPT test was conducted as per ASTM C1202-07. This test required a specimen of 100 dia. The 50 mm samples were cut from the cylindrical specimen.

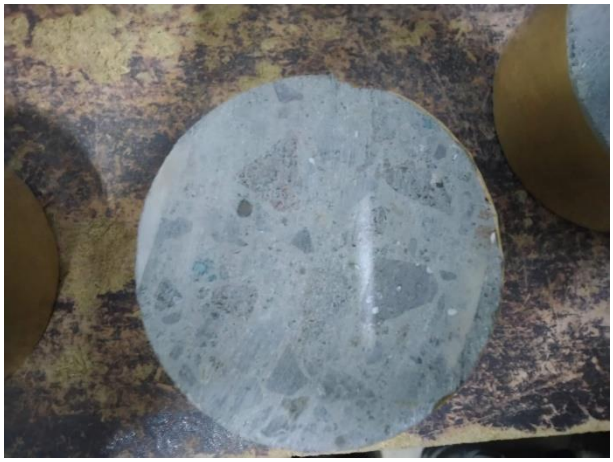

Fig. 3 Core Sample From Specimen for RCPT

The side of the specimens were coated with sealer allowing it to dry and then specimens were vacuum saturated. The specimens were fixed in test apparatus and edges were sealed with sealant.

Fig. 4 RCPT Apparatus with Specimens

These two reservoirs were filled with 3% NaCl solution in – ve and 0.3n NaOH solution in + ve terminals as shown in figure – 3. Then terminals were connected to the unit and current was set to 60 V. Initial reading (I_0) was noted and continued to take reading in SI unit Ampere for 6 hrs at the interval of every 30 mins ($I_{30}, I_{60}, I_{90}, \ldots\ldots, I_{360}$).

4. Results and Discussion

4.1 Visual Observations

The specimens demoulded are observed visually. The Figures 5 and 6 shows surfaces of the demoulded specimens. The specimens cast with steel formwork were found with small pin holes and air bubbles on the surface. Air bubbles and pin holes create due to accumulation of air and mix-water on the interface of concrete and surface of the

formwork. Specimens cast with CPF liner were found with clear texture and free from blow holes but with few pin holes.

Fig. 5 Surface of Demoulded Cubic Specimens

Fig. 6 Surface of Demoulded Cylindrical Specimens

Samples cast with CPF liner found dark in colour and the sample cast with steel form (SF) were lighter in colour. The dark colour of the samples can be due to CPF liner. The CPF liner has the capacity to hold the water, that provide humid environment for concrete curing before demoulding. So the samples cast with CPF liner were dark.

4.2 Compressive Strength Test Results

The Compressive strength test was conducted on cubic samples at the age of 7 and 28 days. The specimens cast with CPF liner were small in size with an average of 2 mm on each side due to thickness of CPF liner and accordingly test was conducted.

For concrete mix proportion CMD-I, it is observed that average compressive strength at 7 days for cubic specimens cast with steel formwork (SF) was 47.50 Mpa and 48.97 Mpa for specimens cast with CPF liner. And for 28 days it was 66.62 Mpa and 76.01 Mpa, respectively. The compressive strength test results are shown in Fig 7.

The cubic samples cast with CPF liner shows increased compressive strength than the specimens cast with steel formwork (SF), 3.09% and 14.09% at 7 and 28 days respectively.

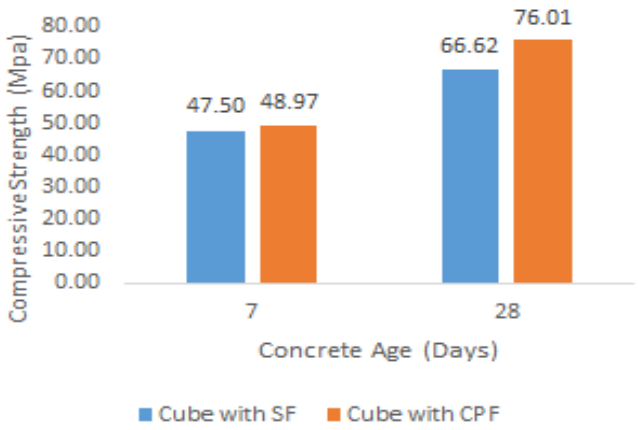

Fig. 7 Compressive Strength vs Age Test Results

It is found that the use of CPF liner contributed to increase the compressive strength of concrete mix CMD I with substitute of cement with fly ash and micro silica.

4.3 Rapid Chloride Penetration Test Results

RCPT was conducted after 28 days of curing. The table 2 shows that the lower is the charge passed, the greater is the resistance to the chloride penetration. The results are good for the concrete mix CMD I.

Table 2. Performance of Chloride Permeability Based Totally on Charge Passed. [8]

Chloride Permeability	Charges Passed (coulombs)
High	> 4000
Moderate	2000 - 4000
Low	1000 - 2000
Very low	100 - 1000
Negligible	< 100

For CMD-I, specimens cast with CPF liner shows 9.98% reduction in charge passed than specimens cast with steel formwork. That clearly shows the CPF liner is effective. That CPF liner reduces the permeability of the chlorides by creating strong, dense and impermeable structural surfaces. RCPT value of specimens was calculated using the formula;

$$R = 900 \times \{I_0 + 2 \times (I_{30} + I_{60} + I_{90} + I_{120} + \ldots\ldots\ldots + I_{330}) + I_{360}\} \quad (1)$$

where,

R = Charge passed (Coulombs)

I_0= Current (Amperes) immediately after voltage is applied

I_t= Current (Amperes) at t min after voltage is applied

I_0 is the initial reading taken from RCPT apparatus and I_{30} is reading taken at 30 minutes and so on for I_{60}, I_{90},...,I_{360}.

The RCPT test results are shown in Fig. 8 and 9.

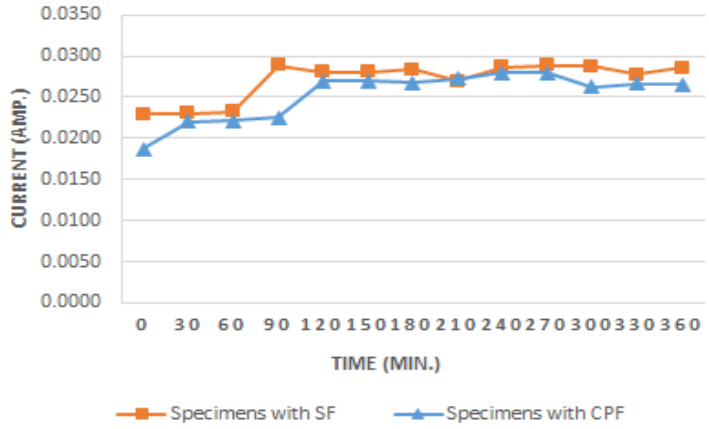

Fig. 8 Current Vs Time for RCPT Test

The concrete mix with micro silica and fly ash as a substitute to the cement is showing great reduction in chloride penetration with the use of CPF liner.

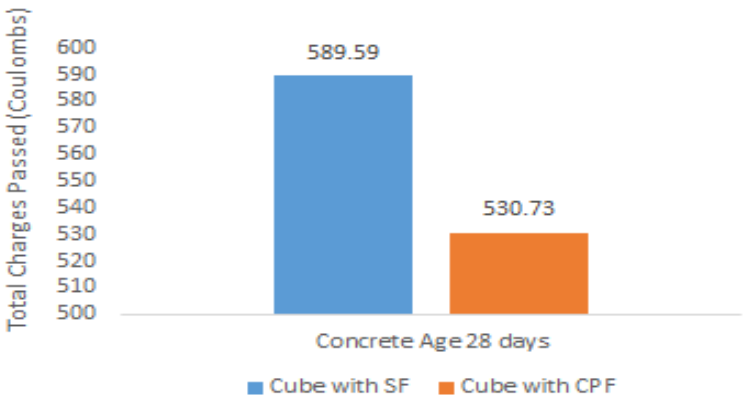

Fig. 9 RCPT Test Results - Coulombs Passed.

This shows that the CPF liner is helpful to reduce the chloride penetration.

5. Conclusions

The conventionally cast structures may result into opening of the pores and structure surface gets exposed to aggressive environments. This may lead to corrosion. This problem is addressed with applying surface treatments and coatings. This paper has demonstrated a different method. The experiment was carried out with replacement of cement with Fly Ash and micro silica and with lower W/C ratio in the concrete mix proportion. The steel moulds were used to cast the specimens. Half specimens were cast with steel mould formwork and half with Controlled Permeability Formwork liner pasted inside the steel

mould. Concrete mix was prepared and samples were cast for testing and samples were kept in water for curing. After curing period the specimens were demoulded. The specimens cast with Controlled Permeability Formwork liner were easy to demould than the samples cast with steel formwork.

The Controlled Permeability Formwork liner helped to modify the properties of freshly placed concrete. The surface of the specimens cast with Controlled Permeability Formwork liner appeared better with less defects and blowholes. The dark colour of the surfaces shows the reduction in water/binder ratio in the cover zone. The use of mineral admixture makes the concrete mix cohesive and dense. The cubic specimens cast with CPF liner showed increased compressive strength than the specimens cast with conventional steel formwork.

The specimens cast with Controlled Permeability Formwork liner showed reduction in charges passed in Rapid Chloride Penetration test (RCPT). This shows reduction in chloride penetration through the surface. This shows Controlled Permeability Formwork increased the strength of concrete in cover zone. The Controlled Permeability Formwork liner has improved the durability, strength and overall appearance of the finished concrete surfaces.

This experiment shows that the performance of the concrete structures surfaces can be improved using Controlled Permeability Formwork liner as it is helpful to increase strength and impermeability.

Acknowledgement

I would like to convey my deep appreciation to my teachers for their valuable suggestions and encouragement in completion of my project.

Special thanks to Mr. Rajshekhar sir for permitting access to the lab and materials. The support and help extended, in carrying out the experiment by the Engineers and laboratory staff of the concrete lab of JMM I P L, Navi Mumbai is gratefully acknowledged.

Finally, I would like to thank my parents and friends, without them this project would not have been completed

References

[1] Law D, Molyneaux T, Patnaikuni I, Adam A. The site exposure of concrete cast using controlled permeability formwork. Australian Journal of Civil Engineering.2012;10(2):163-176. https://doi.org/10.7158/C11-705.2012.10.2

[2] Kothandaraman S, Kandasamy S. The effect of controlled permeable formwork liner on the mechanical properties of concrete. Materials and Structures. 2016;49(11):4737-4747. https://doi.org/10.1617/s11527-016-0821-9

[3] Kothandaraman S, Kandasamy S. Influence of controlled permeable formwork liner on surface quality of self-compacting concrete. Construction and Building Materials. 2020;260:119756. https://doi.org/10.1016/j.conbuildmat.2020.119756

[4] Kumar S, Rao B, Misra S. Chloride penetration resistance of concrete containing blast furnace slag. Indian Concrete Journal. 2002;76(12):745-751.

[5] Liu J, Miao C, Chen C, Liu J, Cui G. Effect and mechanism of controlled permeable formwork on concrete water adsorption. Construction and Building Materials.2013;39:129-133. https://doi.org/10.1016/j.conbuildmat.2012.05.005

[6] Schubel P, Warrior N, Elliott K, Jones M. An investigation into factors affecting the performance of composite controlled permeable formwork liners: Part I - Filter

medium. Construction and building materials. 2008;22:1551-1559. https://doi.org/10.1016/j.conbuildmat.2007.03.030
[7] Philip M, Baxi C. The role of Controlled Permeability Formwork in life cycle design. Tailor Made Concrete Structures. 2008:81-85,ISBN 978-0-415-47535-8.
[8] Suryavanshi A, Swamy R. An evaluation of controlled permeability formwork for long-term durability of structural concrete elements. Cement and Concrete Research. 1997; 27(7):1047-1060. https://doi.org/10.1016/S0008-8846(97)00094-X
[9] Garg S, Singh K, Kunwar K. Bajpai, Misra S. Enhancement in the quality of near surface concrete using some formwork liners. Construction and Building Materials. 2019;207:722-733. https://doi.org/10.1016/j.conbuildmat.2019.02.124
[10] Basheer L, Nanukuttan S, Basheer P. The influence of reusing 'Formtex' controlled permeability formwork on strength and durability of concrete. Materials and Structures. 2008;41:1363-1375. https://doi.org/10.1617/s11527-007-9335-9
[11] Schubel P, Warrior N, Elliott K. An investigation into factors affecting the performance of composite controlled permeable formwork liners: Part II - Drainage medium. Construction and building materials. 2008;22:2235-2249. https://doi.org/10.1016/j.conbuildmat.2007.08.006
[12] Nolan E, Basheer P, Long A. Effects of three durability enhancing products on some physical properties of near surface concrete. Construction and building materials. 1995;9(5): 267-272. https://doi.org/10.1016/0950-0618(95)00020-G
[13] Schubel P, Warrior N, Elliott K. Evaluation of concrete mixes and mineral additions when used with controlled permeable formwork (CPF). Construction and building materials. 2008;22:1536-1542. https://doi.org/10.1016/j.conbuildmat.2007.03.029
[14] McCarthy M, Giannakou A. In-situ performance of CPF concrete in a coastal environment, Cement and concrete research. 2002;32:451-457. https://doi.org/10.1016/S0008-8846(01)00706-2
[15] McCarthy M, Giannakou A, Jones M. Specifying concrete for chloride environments using controlled permeability formwork. Materials and structures. 2001;34:566-576. https://doi.org/10.1007/BF02482183
[16] Jianxiong Ye, Linwen Yu, Yong Chen. Study on the mitigative effect of controlled permeable formwork (CPF) liner on early-age shrinkage of box-girder concrete. Advances in Material Science and Engineering. 2019;8:Article ID: 4150279. https://doi.org/10.1155/2019/4150279
[17] IS:456(2000) Plain and reinforced concrete-code of practice. Bureau of Indian Standards, New Delhi.
[18] IS:383(1987) Specification for coarse and fine aggregates from natural source for concrete. Bureau of Indian Standards, New Delhi.
[19] IS10262(2009) Concrete Mix Proportioning Guidelines. Bureau of Indian Standards, New Delhi.
[20] IRC:112(2011) Code of Practice for Concrete Road Bridges. Indian Roads Congress.
[21] IS:516(1969) Methods of tests for strength of concrete. Bureau of Indian Standards, New Delhi.
[22] ASTM C1202-07 Standard Test Method For Electrical Indication Of Concrete's Ability To Resist Chloride Ion Penetration. American Society for Testing and Materials.
[23] Alibaba.com. [Online]. Available from: www.gzhmpc.en.alibaba.com [Accessed October-December 2020].
[24] The Constructor. [Online]. Available from: www.theconstructor.org [Accessed October 2021]

Research on Engineering Structures & Materials
journal homepage: http://www.jresm.org
Research Group

Research Article

Influence due to interface in finite element modeling of soil-structure interaction system: a study considering modified interface element

Gaurav D. Dhadse*[,a], Gangadhar Ramtekkar[b], Govardhan Bhatt[c]

Department of Civil Engineering, National Institute of Technology, Raipur - 492010, C.G., India.

Article Info

Article history:
Received 02 July 2021
Revised 31 Aug 2021
Accepted 6 Oct 2021

Keywords:

Soil-Structure Interaction;
Interface Modeling;
Interface Non-Linearity;
De-bonding;
Finite Element Analysis;
Solid to Skeletal Contact

Abstract

The finite element (FE) modeling of interface in Soil-Structure Interaction (SSI) problem is most important aspect from early days of modeling i.e. during 1960. The overall performance of the structure is completely influenced due to behavior of interface. Such as realistic interface modeling of SSI system subjected to lateral loads leads to appropriate evaluation of lateral sway and base shear stress. During recent times, many modifications have been done in interface modeling such as incorporation of slip and bonding effects. Also the interface joining variable degrees of freedom system (interface for solid to skeletal contact) has come into existence. Still the de-bonding behavior, interface non-linearity as well as modification in solid to skeletal contact has been unexplored in literatures. Hence there is necessity to develop a FE-SSI model and to study the influence of interface in SSI system considering unexplored features. In this paper, an attempt has been made to show the influence due to interface (including de-bonding and non-linearity) in FE modeling of SSI system using modified 5 noded zero thickness interface element. The performance of modified interface element is a novel contribution in present paper. The present study is limited to static loading conditions only. The effect of interface has been studied by determining bending moment, lateral sway, base shear stress and footing settlement in structure. The inclusion of modified interface has improved the performance of structure by reducing the base shear stress and allowing the sway. Also, the true redistribution of bending moment has been observed after considering the modified interface.

1. Introduction

The modeling of soil-structure interface model considering slip, bonding and de-bonding at soil-structure junction including interface non-linearity is an active topic of research. During 1960's, the researchers started working on interfaces with finite element method. The performance of the structure is highly influenced by interface between soil and structure [1-2]. Hence modeling the interface considering realistic physical condition is an important task [3]. In early days of research, the interface between solid-solid contacts has been studied considering slip and bonding. Later stages the need of soil non-linearity has been investigated for interface performance. The solid-solid contacts don't suitable for representation of all physical cases. Hence the need of solid-skeletal interface has been arisen. As a results zero thickness solid-skeletal interface came into existences during 1990's. Later years, the thin layer interfaces have been invented as an alternative modeling consideration to zero thickness interface. The modification in solid-skeletal interface has been reported by few authors stating the suitability as per physical condition [4-5]. Thus by modeling the interface as per physical conditions, the realistic SSI modeling can be executed [5-7]. The appropriate modeling of interface is applicable to many SSI problems for evaluation of true settlement, lateral displacement, etc. [8-11].

*Corresponding author: gdhadse@yahoo.com
[a]orcid.org/0000-0002-8857-9509; [b]0000-0002-3063-4480; [c]orcid.org/0000-0002-8683-1918
DOI: http://dx.doi.org/10.17515/resm2021.322st0702

The inclusion of interface in SSI modeling alters the performance of structure. The interfaces allow the structure to slip, bond and de-bond with soil mass [12-15]. Frequently the researchers have been focused on slip and bonding analysis in interface [16-18]. De-bonding has been unexplored due to occurrence of numerical ill-conditioning [19-20]. Interfaces were also used as a geometric attachment to various dissimilar materials where relative motion is not of great importance [21-22].

As per Aivazzadeh and Verchery [23], the discontinuous deformations and stresses at the junction of two dissimilar materials are taken care by the interfaces. The presence of interface permits the slip, bonding and de-bonding between soil-structure contacts and redistributes the member forces in structure [15, 19, 24]. The consideration of bonding and de-bonding in addition to slip at interface has improved the performance of SSI analysis in this paper.

According to the literature available on interface modeling for two dissimilar materials, there are two types of zero thickness interfaces. The first type consists of solid-to-solid contact whereas the second type consists of solid to skeletal contact. As of now, various interface elements have been presented by researchers. The solid-to-solid contact element includes modified Goodman's element by Viladkar et al. [25], axisymmetric element by Rafael et al. [12] and Sharma et al. [26]. Whereas solid to skeletal contact element includes 3 noded isoparametric zero thickness interface element proposed by Viladkar et al. [19], Noorzaei et al. [27] and 5 noded thin layer isoparametric interface element by Dalili et al. [24]. These solid to skeletal elements are of special importance as they used to combine variable degree of freedom (DoF) system at interface. Few researchers commented on computational difficulties observed in zero thickness interface elements, such as meshing and ill-conditioning due to aspect ratio [26, 28-30]. Mayer and Gaul [31] suggested the zero thickness elements have been most compatible for Solid-to-Solid contact due to independency of contact stiffness on interface thickness. One more special interface for solid to beam element is suggested by Jang-Keun Lim et al. [21]. This element is used as a geometric arrangement for joining variable DoF system. The execution of zero thickness interfaces in many SSI problems has proved its feasibility. In this paper, the thin layer interface element proposed by Dalili et al. [24] has been modified to zero thickness interface with non-linearity for studying the influence of interface in SSI system.

In present scenario, the interfaces are used in almost all SSI problems. But the modeling of interface considering realistic physical condition is unexplored and needs to be address precisely. As a result, the de-bonding at soil-structure junction in addition to slip and bonding as well as interface non-linearity has been considered in this paper to get acquainted with field conditions. Also, the SSI analysis has been carried with modified interface element. Hence the obtained results are more appropriate because of the realistic modeling than that of earlier research. Presently the scope of study has been restricted to static loading only. The methodology presented in this study will definitely put foundation of future research such as dynamic SSI analysis with realistic interface modeling.

The primary objective of this study is to investigate the influence due to interface in FE modeling of SSI system. The study is essential to understand the bonding and de-bonding in addition to slip at interface. The investigation has been completed with modified 5 noded zero thickness interface element with non-linearity, which is a novel contribution.

2. Problem Definition

From the reviewed literatures, it has been observed that, the modeling of soil-structure interface needs to be explored in more details such as; realistic physical condition must be taken into considerations. As a result, the appropriate performance of structure and soil can be evaluated. Hence the realistic modeling of interface has been carried out by

modified 5 noded zero thickness interface elements, considering de-bonding in addition to slip and bonding as well including non-linearity. Therefore, considering all such modifications, the appropriate influence due to interface on SSI system has been studied.

In order to study the influence due to interface on SSI system, a frame structure with combined footing resting on soil subjected to vertical and lateral loads has been considered. In this problem, the interface is used to study slip, bonding and de-bonding at soil-structure junction. The FE model of SSI system with interface has been developed on MATLAB platform. The superstructure and footing have been modeled as 2 noded beam bending elements having 3 DoF per node and soil is modeled as 8 noded plane strain isoparametric elements with 2 DoF per node. The interface is modeled as 5 noded zero thickness isoparametric element. The soil and interface non-linearity have also been included in FE model. The elements used in FE model are shown in Fig. 1.

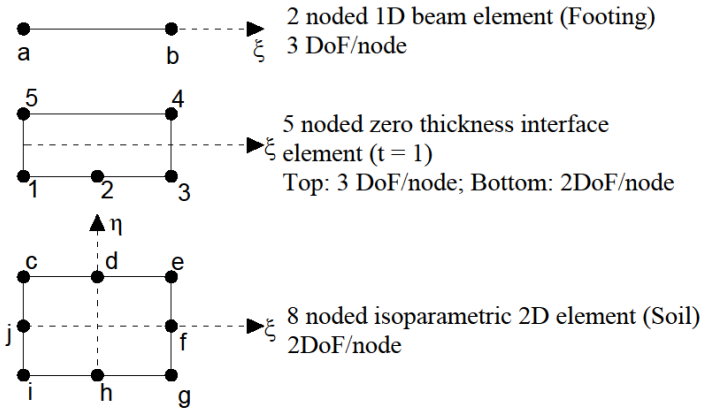

Fig. 1 Elements used in the FE Model of frame footing Soil Interaction System (t – thickness of interface)

3. Mathematical Formulation

3.1. Frame, Footing and Soil Element

For modeling the frame and combine footing, 2 noded isoparametric beam bending element has been used. The detailed formulation with the stiffness matrix is referred from Chandrupatla and Belegundu [32]. The geometry of the element is shown in Fig. 2.

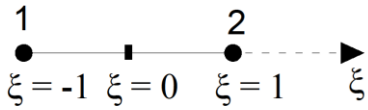

Fig. 2 Two noded isoparametric beam bending element

The idealization of the soil has been done by using quadrilateral 8 noded isoparametric plane strain element (Fig. 3). The selection of element is helpful in getting high-stress concentration near footing [19, 33]. Also, it is reported that the element is compatible with various soil constitutive models. The detailed mathematical formulation for this element is referred from Chandrupatla and Belegundu [32].

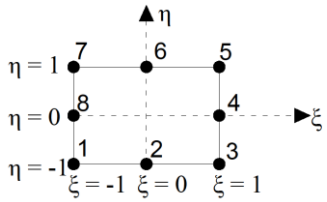

Fig. 3 8 noded isoparametric plane strain element

3.2. Interface Element

The soil-structure interface is an important component for modeling of SSI system. Interface connects soil and structure as well as allows structure to slip, bond and de-bond at soil-structure junction. In present study, the interface has been used to connect soil and beam element with consideration of slip, bond and de-bond as well as inclusion of non-linearity.

The thin layer interface element proposed by Dalili et al. [24] has been modified for zero thickness as given below. The element is compatible with 2 noded isoparametric beam bending element and 8 noded isoparametric plane strain soil element. The geometrical details of the element are shown in Fig. 4.

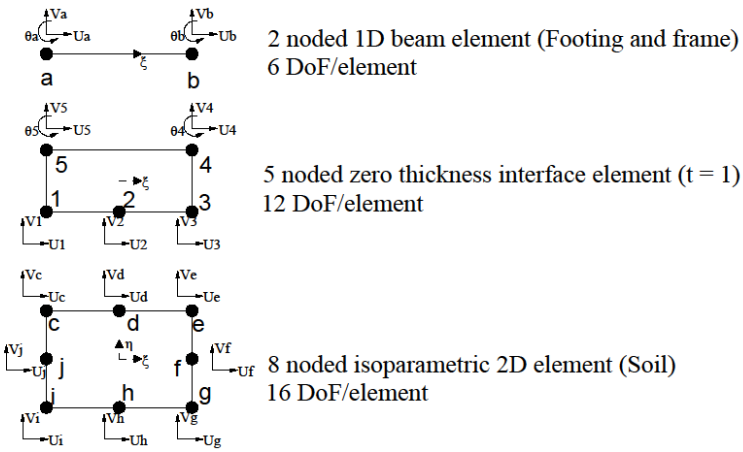

Fig. 4 Geometrical details of 5 noded zero thickness interface element with adjacent element

As per the geometrical details, the interface element is having 12 DoF. The upper part is having 3 DoF per node wherein the lower part is having 2 DoF per node. The element thickness is considered to be unit, though it is called zero thickness interface [19].

The formulation of 5 noded zero thickness interface element has been initialized with combining two one dimensional 3 noded isoparametric element separated by unit thickness as shown in Fig. 5. But the top layer of the interface element is attached to 2 noded beam elements hence incompatibility has been raised due to middle top node as shown in Fig.5. As a result, the middle node has been eliminated in Fig. 4. The corresponding displacement of the node is reported as an average displacement of adjacent upper nodes as given in equation 1. Thus, using equation 1, the transformation matrix has been developed (equation 2).

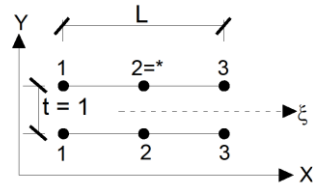

Fig. 5 Formation of 5 noded zero thickness element with two-three noded 1D element

According to Fig. 4, the displacement compatibilities are shown in Table 1.

Table 1. Displacements Compatibility with Soil and Beam element [24]

Node 1	U1 = Uc	V1 = Vc	
Node 2	U2 = Ud	V2 = Vd	
Node 3	U3 = Ue	V3 = Ve	
Node 4	U4 = Ub	V4 = Vb	θ4 = θb
Node 5	U5 = Ua	V5 = Va	θ5 = θa

$$U^{*} = \frac{U_a + U_b}{2}$$
$$V^{*} = \frac{V_a + V_b}{2} \quad (1)$$
$$\theta^{*} = \frac{\theta_a + \theta_b}{2}$$

where,

U = horizontal displacement, V = vertical displacement and θ = rotation

Therefore, considering Δ as a vector of interface element displacement and δ as a vector of adjacent element displacement, the relation between Δ and δ has been formed using transformation matrix [T] (equation 2 and 3) .

$$\begin{Bmatrix} U1 \\ V1 \\ U2 \\ V2 \\ U3 \\ V3 \\ U4 \\ V4 \\ \theta 4 \\ U^{*} \\ V^{*} \\ \theta^{*} \\ U5 \\ V5 \\ \theta 5 \end{Bmatrix}_{15x1} = \begin{bmatrix} 1 & 0 & 0 & 0 & 0 & 0 & 0 & 0 & 0 & 0 & 0 & 0 \\ 0 & 1 & 0 & 0 & 0 & 0 & 0 & 0 & 0 & 0 & 0 & 0 \\ 0 & 0 & 1 & 0 & 0 & 0 & 0 & 0 & 0 & 0 & 0 & 0 \\ 0 & 0 & 0 & 1 & 0 & 0 & 0 & 0 & 0 & 0 & 0 & 0 \\ 0 & 0 & 0 & 0 & 1 & 0 & 0 & 0 & 0 & 0 & 0 & 0 \\ 0 & 0 & 0 & 0 & 0 & 1 & 0 & 0 & 0 & 0 & 0 & 0 \\ 0 & 0 & 0 & 0 & 0 & 0 & 1 & 0 & 0 & 0 & 0 & 0 \\ 0 & 0 & 0 & 0 & 0 & 0 & 0 & 1 & 0 & 0 & 0 & 0 \\ 0 & 0 & 0 & 0 & 0 & 0 & 0 & 0 & 1 & 0 & 0 & 0 \\ 0 & 0 & 0 & 0 & 0 & 0 & 0.5 & 0 & 0 & 0.5 & 0 & 0 \\ 0 & 0 & 0 & 0 & 0 & 0 & 0 & 0.5 & 0 & 0 & 0.5 & 0 \\ 0 & 0 & 0 & 0 & 0 & 0 & 0 & 0 & 0.5 & 0 & 0 & 0.5 \\ 0 & 0 & 0 & 0 & 0 & 0 & 0 & 0 & 0 & 1 & 0 & 0 \\ 0 & 0 & 0 & 0 & 0 & 0 & 0 & 0 & 0 & 0 & 1 & 0 \\ 0 & 0 & 0 & 0 & 0 & 0 & 0 & 0 & 0 & 0 & 0 & 1 \end{bmatrix}_{15x12} \cdot \begin{Bmatrix} U_c \\ V_c \\ U_d \\ V_d \\ U_e \\ V_e \\ U_b \\ V_b \\ \theta_b \\ U_a \\ V_a \\ \theta_a \end{Bmatrix}_{12x1} \quad (2)$$

$$\Delta_{15x1} = [T]_{15x12} \cdot \delta_{12x1} \quad (3)$$

As the interface element is of isoparametric type, the displacements and rotations at any point in an element are expressed in terms of shape functions (equation 4).

$$\Delta U = \sum_{i=1}^{n} N_i U_i$$
$$\Delta V = \sum_{i=1}^{n} N_i V_i \quad (4)$$
$$\Delta \theta = \sum_{i=1}^{n} N_i \theta_i$$

Therefore from Fig. 5, the shape functions at node 1, 2 and 3 is written as, (equation 5)

$$N_1 = -\frac{1}{2}\xi(1-\xi),$$
$$N_2 = (1-\xi^2), \quad (5)$$
$$N_3 = \frac{1}{2}\xi(1+\xi),$$

The element is having a unit thickness; thus, the strain displacement relation has been written in terms of relative displacement of upper and lower nodes as shown in equation 6 [19, 24]. Also, it has been reported that the coordinates of upper beam nodes and lower soil top nodes along with interface element nodes are same; hence the element is called a zero-thickness interface element.

$$\varepsilon = \begin{Bmatrix} \varepsilon_{s1} \\ \varepsilon_n \\ \varepsilon_{s2} \end{Bmatrix} = \frac{1}{t}\begin{Bmatrix} \overline{\Delta U} \\ \overline{\Delta V} \\ \overline{\Delta \theta} \end{Bmatrix} = \frac{1}{t}\begin{Bmatrix} U_{top} - U_{bottom} \\ V_{top} - V_{bottom} \\ \theta \end{Bmatrix}$$

$\because t = 1$

$$\begin{Bmatrix} \varepsilon_{s1} \\ \varepsilon_n \\ \varepsilon_{s2} \end{Bmatrix} = [B]\{\Delta\} = [B][T]\{\delta\} = [B_J]\{\delta\} \quad (6)$$

ε_{s1}, ε_n and ε_{s2} are tangential, normal and rotational strain respectively corresponding to $\Delta U, \Delta V$, and $\Delta\theta$. Therefore, strain displacement matrix [B_J] as per Viladkar et al. [19] is given in equation 7.

$$[B_J] = \begin{bmatrix} -N_1 & 0 & -N_2 & 0 & -N_3 & 0 & N_1 & 0 & 0 & N_2 & 0 & 0 & N_3 & 0 & 0 \\ 0 & -N_1 & 0 & -N_2 & 0 & -N_3 & 0 & N_1 & 0 & 0 & N_2 & 0 & 0 & N_3 & 0 \\ 0 & 0 & 0 & 0 & 0 & 0 & 0 & 0 & N_1 & 0 & 0 & N_2 & 0 & 0 & N_3 \end{bmatrix}.[T] \quad (7)$$

The stresses at any point in interface element are related to corresponding strain by constitutive relation in equation 8 in local coordinates. It has been also noted that the parameters in stress-strain relation are in non-linear form, the details are elaborated in a further section.

$$\begin{Bmatrix} \tau_s \\ \sigma_n \\ M \end{Bmatrix} = \begin{bmatrix} K_{ss1} & 0 & 0 \\ 0 & K_{nn} & 0 \\ 0 & 0 & K_{ss2} \end{bmatrix} \begin{Bmatrix} \varepsilon_{s1} \\ \varepsilon_n \\ \varepsilon_{s2} \end{Bmatrix}$$

$$\{\sigma\} = [D]\{\varepsilon\} \tag{8}$$

Here τ_s, σ_n and M are known as tangential stress, normal stress and moment corresponding to $\varepsilon_{s1}, \varepsilon_n$, and ε_{s2}. Also K_{ss1}, K_{nn} and K_{ss2} are tangential, normal and rotational stiffness respectively.

The relation matrix [D] is written in a global form as,

$$[D_{global}] = [D_g] = [R]^T \begin{bmatrix} K_{ss1} & 0 & 0 \\ 0 & K_{nn} & 0 \\ 0 & 0 & K_{ss2} \end{bmatrix} [R]$$

where,

$$[R] = \begin{bmatrix} \frac{1}{J}\frac{dx}{d\xi} & \frac{1}{J}\frac{dy}{d\xi} & 0 \\ -\frac{1}{J}\frac{dy}{d\xi} & \frac{1}{J}\frac{dx}{d\xi} & 0 \\ 0 & 0 & 1 \end{bmatrix} \tag{9}$$

and

$$J = Jacobian = \left[\left(\frac{dx}{d\xi} \right)^2 + \left(\frac{dy}{d\xi} \right)^2 \right]^{\frac{1}{2}}$$

Therefore, the element stiffness matrix in global form for the interface is written as,

$$[K] = \int [B]_J^T [D_g] [B]_J \, dv$$

$$[K] = \sum_{gp=1}^{n} [B]_J^T [D_g] [B]_J |J| W_{gp} \tag{10}$$

$gp = gauss\ pt.$

$W_{gp} = weights$

The above formulation for structure, soil and interface has been used to develop a FE model using MATLAB for the analysis of frame-footing and soil interaction system.

4. Soil and Interface Non-Linearity

Soil is a non-linear material; as a result, many constitutive relations have been established to model its appropriate behavior. In present study, sand is used, hence amongst the well-established constitutive models, Duncan-Chang hyperbolic model has been used to represent the non-linear nature of soil [34-35]. This model is mainly based on the stress-strain curves of drained triaxial compression tests of sands and clays. Its failure criterion is based on the Mohr-Coulomb model. Also, the model has been worked on associated flow rule and non-linearity of stiffness parameters has also been included [36]. The model has some limitations such as neglecting volume change and unloading stiffness hence it is called a non-linear elastic model. Due to the versatile nature of the model, it is amongst the

commonly used model for SSI analysis [19]. This model calculates the tangent modulus (E_T) at any stress level using equation 11. The parameters 'K' and 'n' in equation 11 have been used to predict the in-situ condition from stress-strain relation. The parameters predominately depend on the stress-strain response of material as a result there is no specific range for 'K' and 'n'.

$$E_T = \left[1 - \frac{R_f(1-\sin\varphi)(\sigma_1 - \sigma_3)}{2(C\cos\varphi + \sigma_3 \sin\varphi)}\right]^2 K.P_a\left(\frac{\sigma_3}{P_a}\right)^n \tag{11}$$

where, 'K' is Modulus number, 'P_a' is atmospheric pressure, 'σ_1' and 'σ_3' are major and minor principal stresses, 'φ' is the angle of friction, 'R_f' is failure ratio, 'n' is an exponent. The incremental loading is used to calculate 'E_T' at any stress level. As 'E_T' is a stress-dependent parameter, its value is updated based on earlier stress level.

The variation of stress-strain at the interface has been considered as hyperbolic. In the present study, the hyperbolic relation given in equation 12 has been used for calculation of tangential stiffness and assumed an arbitrary high value for normal stiffness [19]. The reason of choosing high value of normal stiffness is that, the interface node should not intersect at soil-footing junction. These arbitrary normal stiffness values are chosen from the permissible range (i.e. 10^5–10^{10} kN/m^3) through trial and error basis [19]. In this research the normal stiffness of 10^8 kN/m^3 has been chosen by taking reference from Viladkar et al. [25]. The hyperbolic behavior of interface (tangential stiffness) is given as,

$$K_{ss1} = (1-\lambda_2)^2 K_i$$

$$K_i = k_j \gamma_w \left[\frac{\sigma_n}{P_a}\right]^n \tag{12}$$

$$\lambda_2 = \frac{R_f \tau}{(C_a + \sigma_n \tan\varphi)}$$

where, 'K_i' is initial stiffness, 'γ_w' is the unit weight of water, 'C_a' is adhesion at the interface, 'τ' is shear stress, 'φ' angle of friction, 'P_a' is atmospheric pressure, 'R_f' is failure ratio, 'σ_n' is normal stress, 'n' is the exponent and 'k_j' is modulus number. The value of tangential stiffness is obtained in incremental loading at every load step. Also, K_{ss1} is evaluated as a function of 'σ_n' and 'τ' at any stress level of non-linear analysis.

Few literatures have suggested the values for 'K_s' and 'K_n' at soil-structure interface. Thus, for full bond case it is in between 10^5–10^{10} kN/m^3, whereas for no bond case 'Ks' is zero and 'Kn' is in between 10^5–10^{10} kN/m^3 [25].

5. Methodology

In order to model the realistic SSI system with modified interface, it is necessary to write a FE program consisting of soil and interface non-linearity. Hence it is decided to develop the FE model in MATLAB. The developed model has been validated with literature and then it has been used for studying the influence due to interface on SSI system. Hence such methodology is useful in tackling present problem.

The FE model of SSI system was developed using MATLAB. This model is formed of the soil, footing and frame. It also considers the interface between the different modeled elements and it is capable of handling multiple DoF systems. The developed FE model includes soil and interface non-linearity with the incremental iterative process which is helpful in carrying out realistic SSI analysis.

The convergence in non-linear analysis has been achieved by residual forces. The tolerance of 1 % for residual forces has been chosen. The residual forces are checked against tolerance limit. If the solution does not converge, the residual forces are again calculated and applied on the structure so that the corresponding displacement is calculated and sum up to the total displacement. The process is continued till convergence is achieved. If convergence has not achieved till 15th iteration, then solution will stop. After convergence, the next load increment is applied and the same process is repeated.

In order to validate the FE model, the SSI example from Viladkar et al. [37] has been solved with the developed FE model. After validating the results, further analysis has been carried out for understanding the influence of interface in frame-footing-soil interaction system with modified interface element.

The methodology is versatile and it can be used to analyze realistic SSI system with interface.

6. Validation of the FE model

The developed FE model has validated with Viladkar et al. [37] model for Bending Moment and Settlement of the Footing. Viladkar et al. [37] has used finite-infinite elements for modeling soil as linear elastic and non-linear elastic. The frame structure with combined footing has modeled as 3 noded isoparametric beam bending element. In the present study, a similar model has been prepared in MATLAB with soil as finite element (8 noded isoparametric plain strain element) and other components are same as that of Viladkar et al [37]. The finite extent of soil mass has been modeled in such a way that, the deformations in x and y directions up to 0.5 m from the boundary is approximately null. Also, the finite extent of soil mass has been decided on the basis of pressure bulb. Thus, the boundaries were put beyond the pressure bulb limit as a result the boundaries are not reflecting wave towards the model. Hence it has been concluded that, 30.5 m x 30.5 m extent of soil mass is behaving like infinite soil for the frame considered by Viladkar et al. [37] (Fig. 6 (a)). The mesh sensitivity study has been carried out on extent of soil mass and mesh size of 1017 x 1017 mm (Total no. of soil elements = 900) has been fixed for developed model. The mesh convergence study has been carried out on the basis of settlement for each mesh configuration. The boundary condition for the developed model is shown in Fig. 6 (b) i.e. hinged at bottom boundary and roller at vertical boundaries. In other words, it is said that the displacements at bottom boundary is restricted in horizontal and vertical direction (constraining both DoF). Whereas at vertical boundaries, the vertical displacement is allowed and horizontal displacement is restricted.

The footing settlement and bending moment in frame as well as combined footing for finite extent of soil mass (30.5 m x 30.5 m) are in good agreement with Viladkar et al. [37] results.

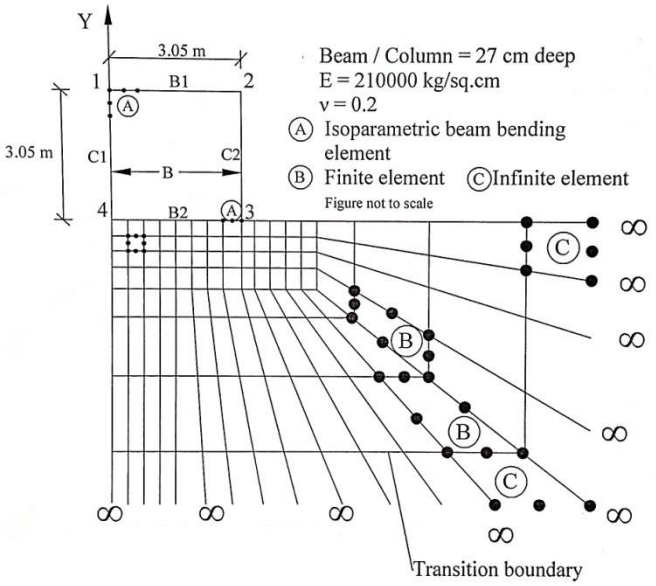

(a)

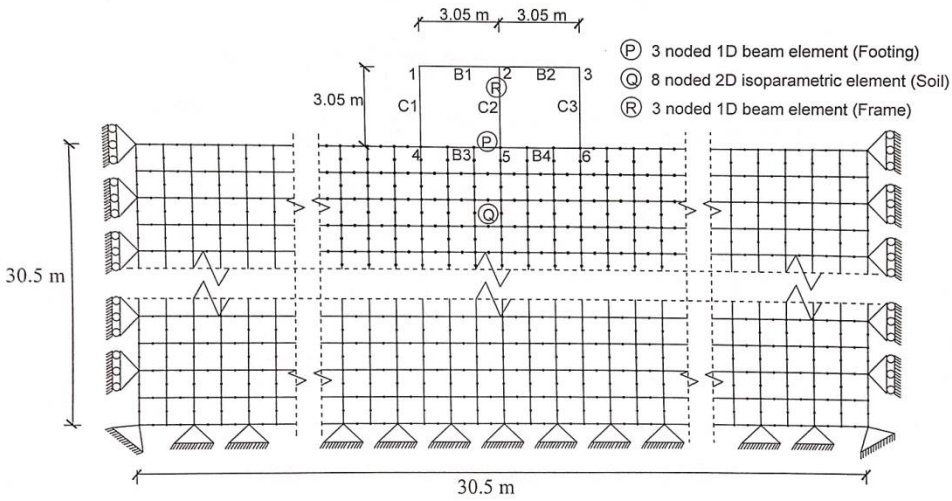

(b)

Fig. 6 (a) SSI Model by Viladkar et al. [37], (b) SSI FE Model used in Present Study

6.1. Detailed sensitivity analyses of soil boundary limits and mesh size

The detail sensitivity analysis for deciding the soil boundary limits and mesh sizes has been carried out as shown in Table 2. The soil boundary limits were decided from Boussinesq Method. To decide the soil boundary limits, 04 extent of soil mass were considered. For every soil mass the pressure on boundaries (i.e., bottom and vertical boundary) has been calculated from Boussinesq Method. The soil extent has been chosen in such a way that; the least soil pressure should act on the boundaries as well as the boundaries should not reflect wave back to the structure so that the true settlement will be observed.

Table 2. Sensitivity analyses of soil boundary limits and mesh size

Sr. No.	Extent of Soil Mass (m)	Pressure at boundaries calculated from Boussinesq Method (kPa)		Mesh Size (m)	No. of Elements	Δ/B Present Study	Δ/B Viladkar et al. [37]
		Bottom	Vertical				
1.	15.25 x 15.25 5B x 5B	0.0307	0.0054	3.05 x 3.05	25	0.0268	0.0300
				1.525 x 1.525	100	0.0275	
				1.017 x 1.017	225	0.0278	
				0.508 x 0.508	900	0.0278	
2.	21.35 x 21.35 7B x 7B	0.0156	0.0027	3.05 x 3.05	49	0.0275	0.0300
				1.525 x 1.525	196	0.0281	
				1.017 x 1.017	441	0.0285	
				0.508 x 0.508	1764	0.0285	
3.	27.45 x 27.45 9B x 9B	0.0094	0.0016	3.05 x 3.05	81	0.0278	0.0300
				1.525 x 1.525	324	0.0285	
				1.017 x 1.017	729	0.0291	
				0.508 x 0.508	2916	0.0291	
4.	30.5 x 30.5 10B x 10B	0.0076	0.0013	3.05 x 3.05	100	0.0291	0.0300
				1.525 x 1.525	400	0.0304	
				1.017 x 1.017	900	0.0310	
				0.508 x 0.508	3600	0.0310	

B is the width of footing and Δ is the footing settlement

From Table 2, it is observed that, for 15.25 x 15.25 m extent of soil mass, the pressure on the boundaries is about 1% that of the pressure applied on the structure. Due to such pressure on boundaries the confinement in soil mass increases and as a result the settlement is reduced for all mesh configurations with respect to Viladkar et al. [37] settlement (Linear elastic analysis). Thus, it is decided to increase the extent of soil, such that boundaries should not reflect the wave back to the structure. In other words, the boundaries are placed beyond the pressure bulb boundaries.

Thus, 7B x 7B, 9B x 9B and 10B x 10B soil masses were checked against boundary pressure and settlement criteria. The 9B x 9B soil extent shows good results for 1.017 x 1.017 m mesh but the boundary reflection is influencing the settlement. Hence the extent is further increased to 10B x 10B. The boundary pressure is showing approximately null value (around 0.1% of applied pressure) and settlement for 1.017 x 1.017 m mesh is also appropriately matching with Viladkar et al. [37]. Hence 10B x 10B extent of soil mass and 1.017 x 1.017 m mesh size has been considered in developed FE-SSI model.

6.2. Geometric, Material Properties and Loadings

Geometric and material properties are shown in Table 3, 4 and 5 as given by Viladkar et al. [37] for validation purpose.

Static - Uniformly Distributed Load = 0.24 N/mm for top and foundation beam (vertically downward)

Table 3. Geometrical Properties for Frame, Footing and soil

Sr. No.	Structure	Component	Size
1.	Frame	No. of Storey	01
		No. of Bays	02
		Storey height (mm)	3050
		Bay Width (mm)	3050
		Beam (mm)	270 x 270
		Column(mm)	270 x 270
2.	Foundation	Combined Footing Beam(mm)	270 x 270
3.	Soil	The extent of Soil Mass (m)	30.5 x 30.5

Table 4. Linear Elastic Material Properties for Structure and Soil

Sr. No.	Component	Elastic Modulus (N/mm^2)	Poisson's Ratio
1	Structural	21000	0.2
2	Soil Mass	3	0.3

Table 5. Non-Linear Material Properties for sand

Sr. No.	Description	Value
1	Relative Density	50%
2	Initial Tangent Mod. of sand 'Ei'	30 kg/cm^2
3	Modulus Number 'K'	305
4	Exponent 'n'	0.90
5	Failure Ratio 'Rf'	0.80
6	Cohesion 'C'	0
7	The angle of Internal Friction	39^0
8	Poisson's Ratio of sand	0.3

6.3. Results and Discussion

A plane strain linear and non-linear analysis has been carried out. The results in terms of footing settlement and bending moment in all members are represented in order to validate the present FE model. The results for Bending Moments in frame members and

combined footings are shown in Table 6, 7 & 8 and graphically represented in Fig. 7, 8 and 9. (For member numbers kindly refer Fig. 6 (a)).

Table 6. Bending Moments (N-mm) in Frame Members (Linear Elastic Analysis)

Member	End	Viladkar et al. x 10^2	Present Study x 10^2	% Difference with respect to present study	NIA*
B1	1 (Inner)	678.4	707.9	4.17	2213.60
	2 (outer)	-2073.7	-2095.4	1.04	-919.20
B2	4 (Inner)	-3190.98	-3210.5	0.61	NA
	3 (outer)	-983.41	-1026.5	4.20	
C1	1 Top	0	0	0.00	0.00
	4 Bottom	0	0	0.00	0.00
C2	2 Top	2073.7	2095.4	1.04	919.20
	3 Bottom	983.4	1026.5	4.20	452.10

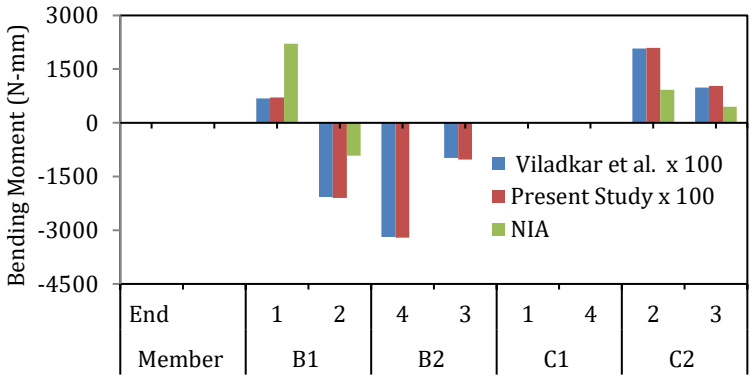

Fig. 7 Graphical representation of Bending Moments from Table 6

Table 7. Bending Moments (N-mm) in Frame Members (Non-Linear Elastic Analysis)

Member	End	Viladkar et al. x 10^2	Present Study x 10^2	% Difference with respect to present study	NIA*
B1	1 (Inner)	488.44	476.29	-2.55	2213.60
	2 (outer)	-2224.12	-2214.46	-0.44	-919.20
B2	4 (Inner)	-3310.00	-3336.42	0.79	NA
	3 (outer)	-1133.84	-1190.28	4.74	
C1	1 Top	0.00	0.00	0.00	0.00
	4 Bottom	0.00	0.00	0.00	0.00
C2	2 Top	2224.29	2214.46	-0.44	919.20
	3 Bottom	1134.07	1190.28	4.72	452.10

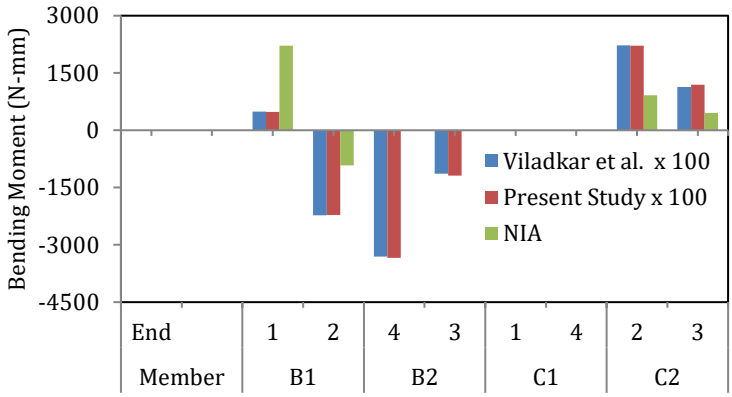

Fig. 8 Graphical representation of Bending Moments from Table 7

Table 8. Comparison of Bending Moments (N-mm) for LIA and NLIA in Present Study

Member	End	LIA**x 10^2	NLIA*** x 10^2	% Difference with respect to NLIA
B1	1 (Inner)	707.9	476.29	-48.62
	2 (outer)	-2095.4	-2214.46	5.37
B2	4 (Inner)	-3210.5	-3336.42	3.77
	3 (outer)	-1026.5	-1190.28	13.75
C1	1 Top	0	0.00	0.00
	4 Bottom	0	0.00	0.00
C2	2 Top	2095.4	2214.46	5.37
	3 Bottom	1026.5	1190.28	13.75

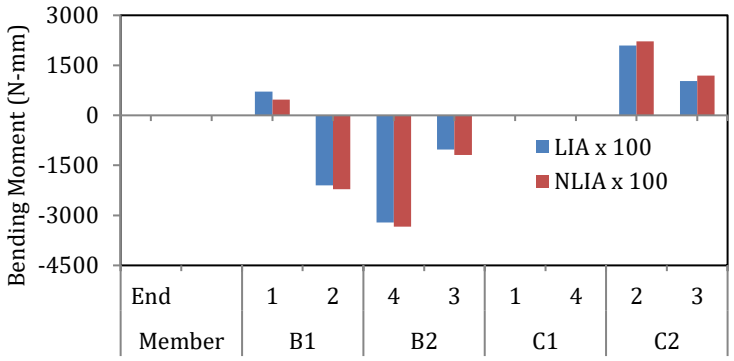

Fig. 9 Graphical representation of Bending Moments from Table 8

* NIA - Non-Interaction Analysis
**LIA - Linear Interaction Analysis
*** NLIA - Non-Linear Interaction Analysis

The variation of footing settlement in non-dimensional form along the width of footing from the center to end is plotted in Fig. 10. Where, 'x' denotes the distance from center to the edge of footing, B is the width of footing and Δ is footing settlement.

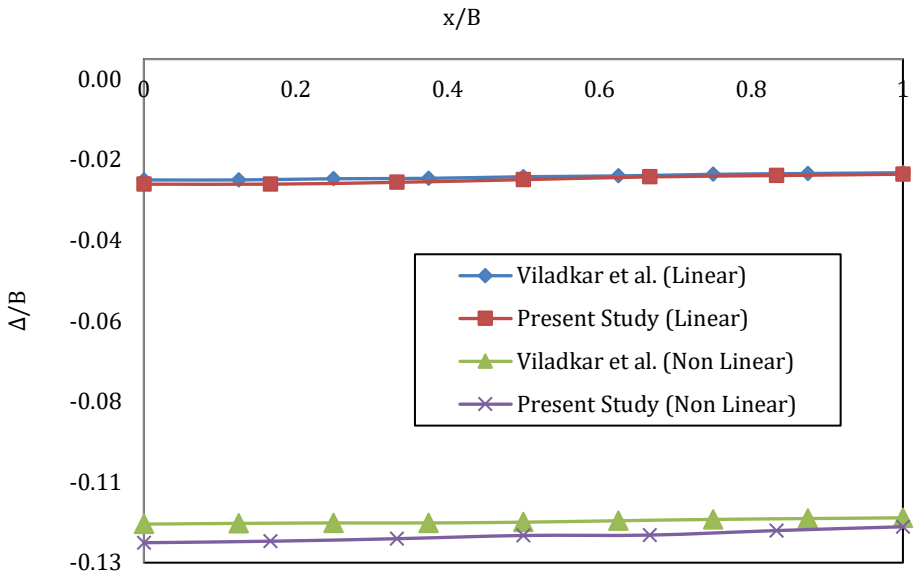

Fig. 10 Variation of Footing Settlement along Footing Width from the centre to end

The result in terms of bending moment and settlement from the present study shows good agreement with the available results of Viladkar et al. [37] model. Hence the developed FE-SSI model has been validated and further cases are considered to study the influence due to interface in FE modeling of SSI system.

7. Considered Cases

The developed FE model for SSI system has been validated in the section 6. In order to achieve the objectives of the present study, the following cases have been considered (Table 9).

The FE models used in all three cases are having the same geometrical properties as given in Table 3. The model with boundary conditions is shown in Fig. 6 (b). The structural part in all the cases have been modeled as linear elastic so the linear elastic material properties are used as shown in Table 4. Whereas, the soil (sand) [38] and interface has been modeled as linear as well as non-linear elastic. The non-linear material properties for sand and interface reported by Viladkar et al. [25] has been used for all the cases as given in Table 10 and 11 respectively.

Table 9. FE models considered for frame footing soil interaction system

Case No.	Component	Elements used (Ref: Section 3)	Constitutive Model (Ref: Section 4)	Loading	Interface Response
I	Structure	2 noded 1D isoparametric beam element	Linear Elastic	Vertical	Direct Contact (bonding)
	Soil	8 noded isoparametric plane strain element	Linear and Non-Linear		
II	Structure	2 noded 1D isoparametric beam element	Linear Elastic	Vertical and Lateral	Direct Contact (slip, bonding and de-bonding)
	Soil	8 noded isoparametric plane strain element	Linear and Non-Linear		
III	Structure	2 noded 1D isoparametric beam element	Linear Elastic	Vertical and Lateral	Modified interface (slip, bonding and de-bonding)
	Soil	8 noded isoparametric plane strain element	Linear and Non-Linear		
	Interface	5 noded isoparametric zero thickness element	Linear and Non-Linear		

Table 10. Non-Linear Material Properties for Sand

Sr. No.	Description	Value
1	Soil Type	SP
2	Unit weight	16.3 kN/m^3
3	Relative Density	84%
4	Modulus Number 'K'	700
5	Exponent 'n'	0.50
6	Failure Ratio 'Rf'	0.90
7	Cohesion 'C'	0
8	The angle of Internal Friction 'ϕ'	41^0
9	Poisson's Ratio of sand	0.3

Table 11. Non-Linear Material Properties for Interface

Sr. No.	Description	Value
1	Modulus Number 'k_j'	8625
2	Exponent 'n'	0.662
3	Failure Ratio 'Rf'	0.82
4	Adhesion 'C_a'	0
5	The angle of Internal Friction 'ϕ'	29.3^0
6	Unit weight of water γ_w	0.00001 N/mm^3
7	Atmospheric pressure 'P_a'	0.10132 N/mm^2
8	Normal Stiffness (K_{nn})	10^8 kN/m^3

The static loading and member identification for all the cases are shown in Fig. 11 (a), (b) and (c) whereas the boundary conditions are shown in Fig. 6 (b).

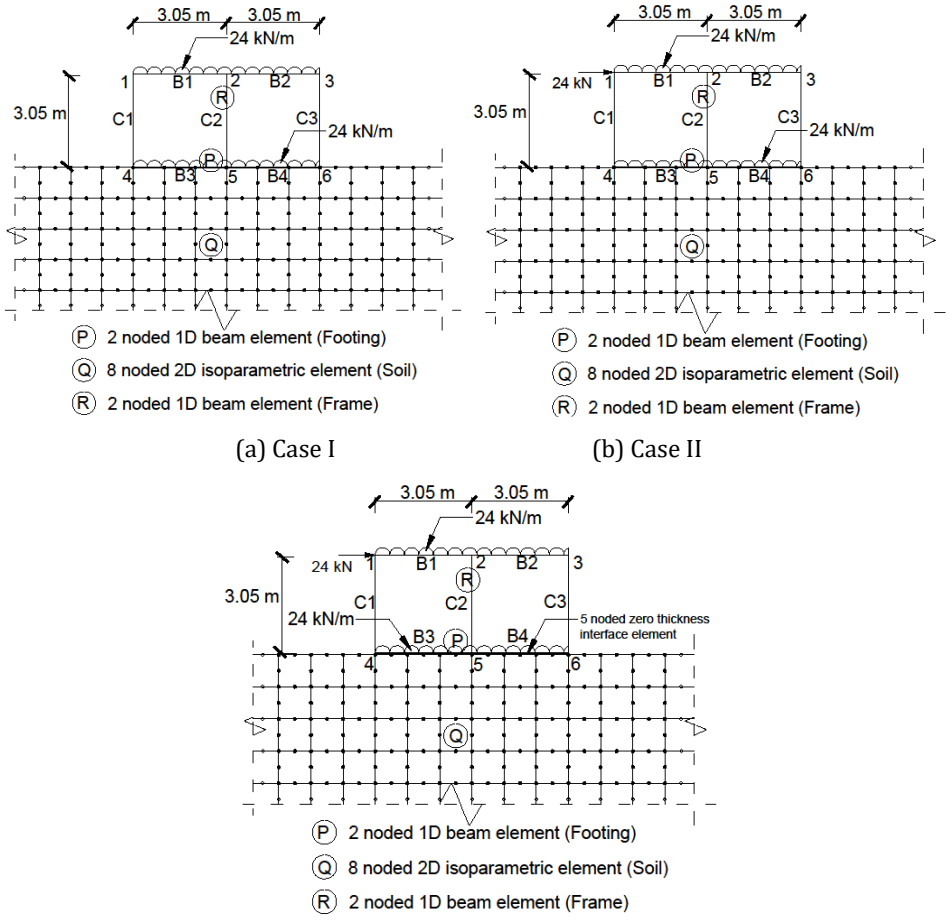

(a) Case I

(b) Case II

(c) Case III

Fig. 11 Representation of FE Models with Loading and member identification

7.1. Result and Discussion

The plane strain FE analysis has been carried out for all 3 cases. For non-linear analysis, the total load has been applied into 7 load increment such as 30%, 15%, 15%, 10%, 10%, 10% and10% of the total load on the basis of sensitivity analysis. The analysis result (linear and non-linear soil) in terms of bending moment, footing settlement, lateral sway and base shear stress has been presented to study the influence of interface in SSI analysis. The study includes modified interface element with consideration of slip, bonding and de-bonding at soil-structure junction.

7.1.1 Bending moment

a. for Case I

For Case I, the structure is loaded as UDL only (vertically downward). Also, there is direct contact between soil and structure i.e., soil and structure is tied at intersecting nodes. The variation of bending moments clearly shows the necessity of interaction analysis (Table 12 and Fig. 12). Whereas the performance of structure improves further after considering non-linear analysis (Table 12 and Fig. 12).

Table 12. Bending moment comparison for NIA, LIA and NLIA for Case I

Member	End	NIA (kNm)	LIA (kNm)	% difference (NIA and LIA)	NLIA (kNm)	% difference (LIA and NLIA)
B1	1	9.19	17.17	-86.83	19.36	-12.75
	2	-22.13	-9.64	56.44	-6.89	28.53
B2	2	22.13	9.64	56.44	6.89	28.53
	3	-9.19	-17.17	-86.83	-19.36	-12.75
B3	4	NA	6.79	NA	9.50	-39.91
	5	NA	26.79	NA	26.72	0.26
B4	5	NA	-26.79	NA	-26.72	0.26
	6	NA	-6.79	NA	-9.50	-39.91
C1	1	-9.19	-17.17	-86.83	-19.36	-12.75
	4	-4.52	-6.79	-50.22	-9.50	-39.91
C2	2	0	0	0.00	0.00	0.00
	5	0	0	0.00	0.00	0.00
C3	3	9.19	17.17	-86.83	19.36	-12.75
	6	4.52	6.79	-50.22	9.50	-39.91

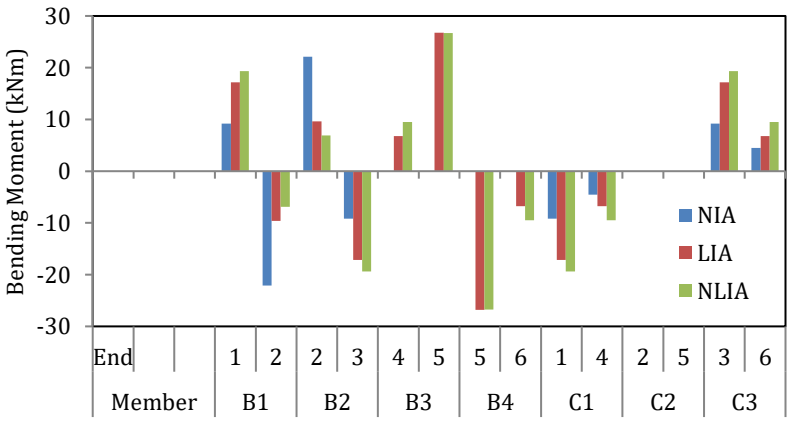

Fig. 12 Graphical representation of Bending Moments from Table 12

The bending moment (BM) comparison (Table 12 and Fig. 12) for Case I shows that there is redistribution of moments when compare LIA and NLIA with NIA. Also, it is observed that the center column is relieved from BM whereas edge columns are getting more moments. It is due to settlement of the footing. The results also find the importance of soil non-linearity on BM results, as the variation of -39% to 28% is observed. Such variation is due to the increased settlement in NLIA and continuous change of relative stiffness between soil and footing due to load increments. It is also observed that footing have the least pressure at center and maximum pressure at edges.

b. for Case II

In Case II, the static lateral load in addition to vertical load is acted on the structure. Also, the soil and structure are tied at intersection nodes (i.e., without interface as direct contact). The results of BM show the variation due to relative motion between structure and soil (Table 13 and Fig. 13). Again, the results show improvement in NLIA but reliability is getting affected due to tied contact at soil-structure junction.

Table 13. Bending moment comparison for NIA, LIA and NLIA for Case II

Member	End	NIA (kNm)	LIA (kNm)	% difference (NIA and LIA)	NLIA (kNm)	% difference (LIA and NLIA)
B1	1	0.151	7.33	-	9.56	-30.42
	2	-28.88	-18.13	37.22	-15.23	16.00
B2	2	15.442	0.98	93.65	-1.76	-
	3	-18.131	-27.1	-49.47	-29.36	-8.34
B3	4	NA	-1.3	NA	1.23	-
	5	NA	17.52	NA	17.60	-0.46
B4	5	NA	-36.35	NA	-36.04	0.85
	6	NA	-14.94	NA	-17.98	-20.35
C1	1	-0.151	-7.33	-	-9.56	-30.42
	4	8.359	1.3	84.45	-1.22	-
C2	2	13.438	17.15	-27.62	16.99	0.93
	5	14.978	18.83	-25.72	18.44	2.07
C3	3	18.131	27.1	-49.47	29.36	-8.34
	6	17.245	14.95	13.31	17.98	-20.27

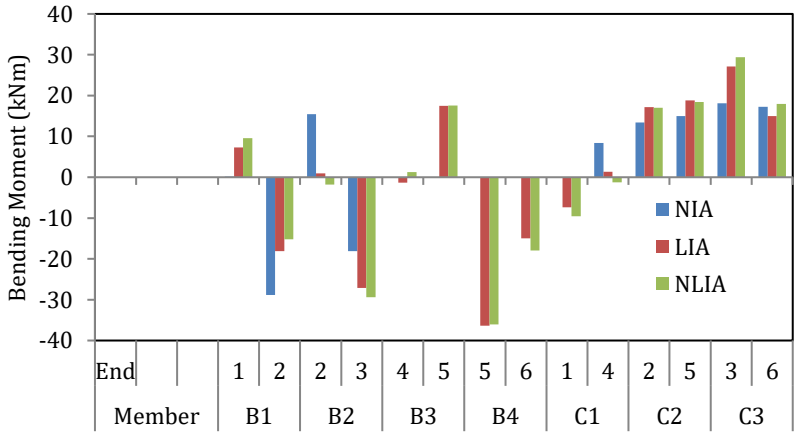

Fig. 13 Graphical representation of Bending Moments from Table 13

From Table 13 and Fig. 13, it is observed that the effect of lateral load in addition to vertical loads is dominant on column C2 and C3. As a result, a very high redistribution of BM in LIA is observed up to 93% and for some members, the reversible sign is also observed. As far as B1 and B2 are concerned (LIA), the edge 1 (where lateral load acts) is experiencing a very high increase in BM (indicated by '-'). In fact, due to the settlement of C1 as compare to fixed C1 in NIA, edge 1 is attracting very high moment with respect to NIA. Moreover, edge 2 is relieved from BM as corresponding edge 1 and 3 is getting higher values. In the case of LIA column members, the variation of -49 to 85% is observed. For NLIA, it is observed that the footing settlement and sway increases, as a result, the BM is increased up to 30%. In addition to this, foundation beam in NLIA shows reversible in the sign of BM at edge 4, whereas at edge 6, 21% BM is increased. It is happened due to lateral load, edge 4 is uplifted whereas edge 6 is sinking more (Fig. 16(a)).

c. for Case III

Case III is inclusive of interface. The interface is capable of slip, bonding and de-bonding at soil-structure contact. Also, the non-linear nature of interface has been considered to get acquainted with field conditions. As a result, Case III is more realistic as compare to earlier cases. The relative motion between structure and soil is taken care by interface hence; the performance of structure is improved and reliable as well. As a result, the true BM is observed from Table 14 and Fig. 14.

Table 14. Bending moment comparison for NIA, LIA and NLIA for Case III

Member	End	NIA (kNm)	LIA (kNm)	% difference (NIA and LIA)	NLIA (kNm)	% difference (LIA and NLIA)
B1	1	0.151	11.57	-	11.65	-0.69
	2	-28.88	-12.64	56.23	-12.52	0.95
B2	2	15.442	-4.08	-	-4.20	-2.94
	3	-18.131	-31.38	-73.07	-31.46	-0.25
B3	4	NA	3.53	NA	3.63	-2.83
	5	NA	16.85	NA	16.93	-0.47
B4	5	NA	-34.71	NA	-34.81	-0.29
	6	NA	-21.14	NA	-21.21	-0.33
C1	1	-0.151	-11.57	-	-11.65	-0.69
	4	8.359	-3.53	-	-3.63	-2.83
C2	2	13.438	16.71	-24.35	16.72	-0.06
	5	14.978	17.86	-19.24	17.87	-0.06
C3	3	18.131	31.38	-73.07	31.47	-0.29
	6	17.245	21.14	-22.59	21.22	-0.38

In Case 3, BM with the interface is given in Table 14 and graphically represented in Fig. 14. Due to incorporation of normal and tangential stiffness at footing soil interface, the resistance because of tied contact (without interface) between soil and footing is completely reduced. Hence the base shear stress is reduced and sway is allowed, as a result, true BM observed in LIA. Reversible BM sign is also observed at end 1 and 4, it is due to fact that, lateral load (at end 1) is lifting end 4 in LIA. It is also found that very less variation i.e. 3% is observed when soil and interface are considered as non-linear (NLIA). Thus the response of the structure is improved due to realistic numerical modeling of frame-footing-soil interaction system.

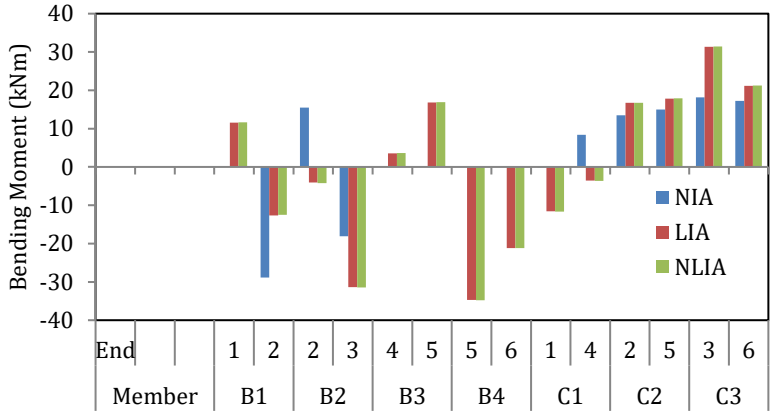

Fig. 14 Graphical representation of Bending Moments from Table 14

The comparison of BM for Case II and Case III is given in Table 15 and Fig. 15. The comparison is helpful in understanding the influence of interface on BM values.

Table 15. Bending moment comparison (with and without interface) for Case II and Case III

Member	End	LIA (without interface) (kNm)	LIA (with interface) (kNm)	% difference	NLIA (without interface) (kNm)	NLIA (with interface) (kNm)	% difference
B1	1	7.33	11.57	-57.84	9.56	11.65	-21.86
	2	-18.13	-12.64	30.28	-15.23	-12.52	17.79
B2	2	0.98	-4.08	-	-1.76	-4.20	-
	3	-27.1	-31.38	-15.79	-29.36	-31.46	-7.15
B3	4	-1.3	3.53	-	1.23	3.63	-
	5	17.52	16.85	3.82	17.60	16.93	3.81
B4	5	-36.35	-34.71	4.51	-36.04	-34.81	3.41
	6	-14.94	-21.14	-41.50	-17.98	-21.21	-17.96
C1	1	-7.33	-11.57	-57.84	-9.56	-11.65	-21.86
	4	1.3	-3.53	-	-1.22	-3.63	-
C2	2	17.15	16.71	2.57	16.99	16.72	1.59
	5	18.83	17.86	5.15	18.44	17.87	3.09
C3	3	27.1	31.38	-15.79	29.36	31.47	-7.19
	6	14.95	21.14	-41.40	17.98	21.22	-18.02

('-' indicates irreversible sign or very high difference)

The influence of interface on BM is found out from Table 15 and Fig. 15. The variation from -57 to 30 % and some irreversible sign in BM value of LIA (as compared to LIA without interface) is observed. Whereas the variation of -21 to 17% with some irreversible sign in BM value of NLIA (as compared to NLIA without interface) is observed. Thus the inclusion of interface has resulted increase in free sway and settlement as a realistic physical behavior. As a result, the BM values are giving better result considering interface stiffness values.

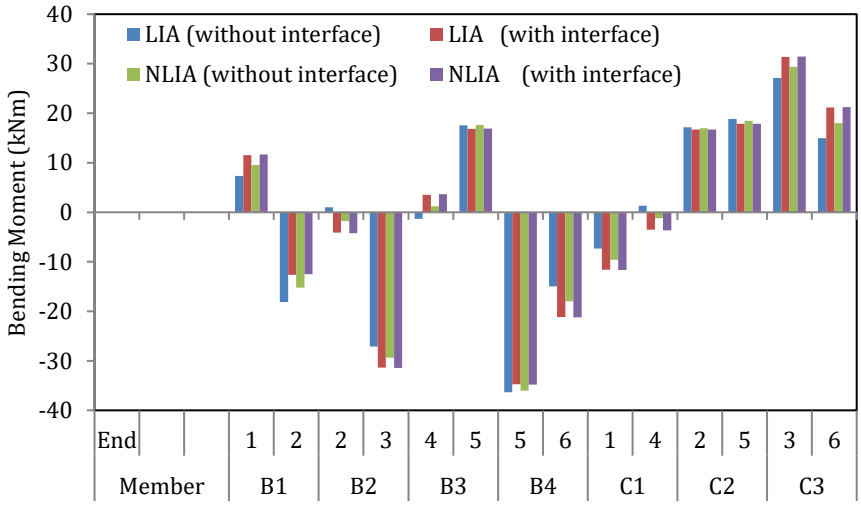

Fig. 15 Graphical representation of Bending Moments from Table 15

7.1.2 Footing Settlement

The variation in bonding and de-bonding at soil-structure contact is clearly observed from footing settlement results. Fig. 16 (a) shows the comparison of footing settlement for various cases. It is predominately observed that the values of settlement for non-linear analysis are 3.5 to 4 times that of linear analysis.

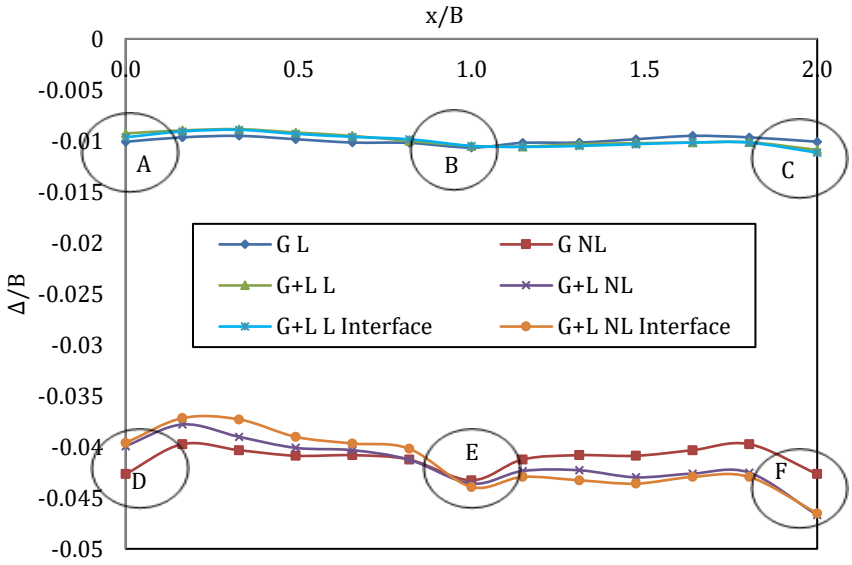

(a)

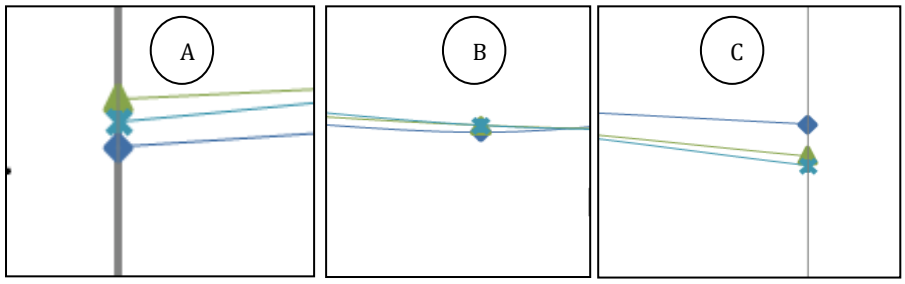

(b)

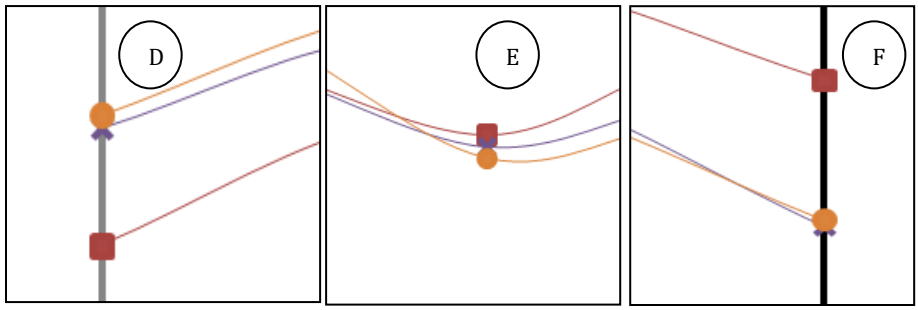

(c)

Fig. 16 (a) Non-dimensional representation of footing settlement for all the cases, (b) Close view of A, B and C, and (c) Close view of D, E and F

G L – Gravity load and linear analysis
G NL – Gravity load and Non-linear analysis
G+L L – Gravity + Lateral load and linear analysis
G+L NL – Gravity + Lateral load and Non-linear analysis
G+L L Interface – Gravity + Lateral load and linear analysis with linear Interface
G+L NL Interface – Gravity + Lateral load and Non-linear analysis with non-linear Interface
Δ – Footing settlement (mm)
B – Footing Width (mm)
x – Distance between end 4 and end 6 (mm)

The increase in settlement is due to lesser value of tangent modulus as compare to initial tangent modulus. As a result, stiffness of soil is reduced and settlement is increased.

It is also observed that, due to soil uplift pressure, the middle portion between two columns is looking like concave shape in all the cases. This is supposed to be a realistic response in SSI analysis. The similar kind of results has also depicted by Viladkar et al. [19].

The important consideration in interface element is to allow slip, bonding and de-bonding at soil footing interface. Thus, it is necessary to evaluate the behavior of 5 noded zero thickness interface element for such relative motions. From Fig. 16(a), Fig. 16(b) and 16(c), it is observed that (at end 4), there is de-bonding of 8% and 4.3% for 'G+L L' and 'G+L L Interface' cases respectively. Whereas, the de-bonding of 6.43% and 7.16% is observed for 'G+L NL' and 'G+L NL Interface' cases respectively. In addition to this, end 6 is found more sinking (bonding) as compare to 'G L' and 'G NL' cases. The extra sinking of 8% and 10.53% is found for 'G+L L' and 'G+L L Interface' cases respectively. Whereas sinking of 9.43 and 9% is found for 'G+L NL' and 'G+L NL Interface' cases respectively. Thus, it is noted that due to lateral loads the bonding and de-bonding has been observed in case II and case III. Moreover, the presence of interface has provided the appropriate values of bonding and

de-bonding at footing-soil junction. It is also found that the resistance to slip, bonding and de-bonding due to tied contact (without interface) is completely reduced due to inclusion of the interface. Hence the value of de-bonding is increased by 11.35 % than 'G+L NL' case and bonding is increased by 31.62% than 'G+L L' case.

It is also found that, the presence of interface is necessary for laterally loaded structure. Whereas for only vertical loads, the interface may be neglected as there is full bond between structure and soil.

7.1.3 Footing Base Shear stress and Sway of the frame

The performance of interface for de-bonding and bonding has discussed through settlement and BM results. But the slip occurs due to interface is not clearly visible. The performance of interface for slip is very well seen through graphical representation of footing base shear stress and sway of the frame.

To evaluate the realistic performance of the structure subjected to lateral loads, the realistic modeling consideration has been adopted with the interface element. The response in terms of footing base shear stress and sway of the frame has been compared for with and without interface cases as shown in Fig. 17 and 18 respectively.

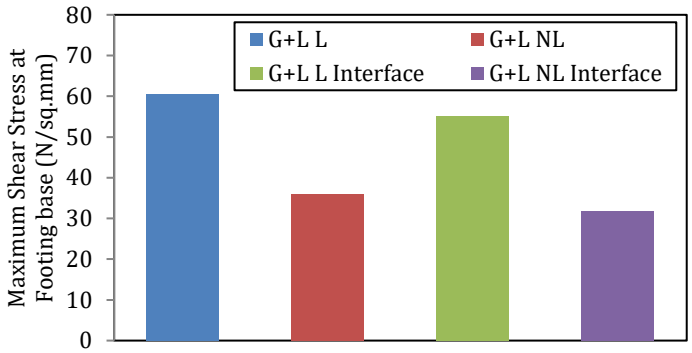

Fig. 17 Variation of maximum shear stress at the base of the footing

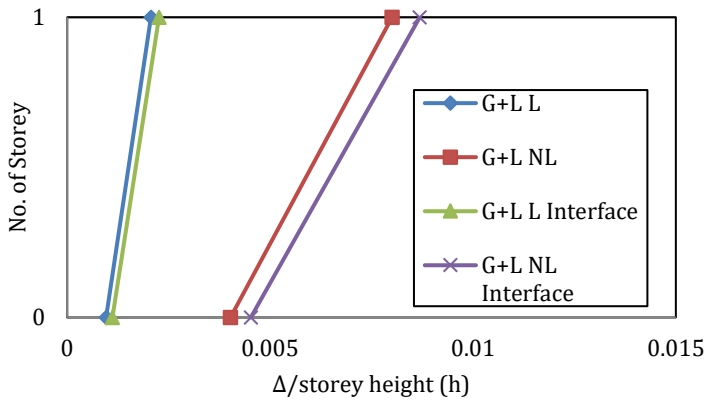

Fig. 18 Non-dimensional representation of Sway of the frame along the height

From Fig. 17, it is observed that the footing base shear stress is decreased after consideration of interface. It is also found that, the non-linearity of interface has further decreased the footing base shear stress as compare to linear results. It has happened due

to reduction of shear stiffness along the footing base which results in more tangential displacement. It is also shown in Fig. 17 that the consideration of interface improves the performance of structure by reducing the footing base shear stress.

As the footing base shear stress is decreasing after consideration of interface, the slip at footing level and sway of the structure has been increased (slip increased by 13.82% and 11.08% for LIA and NLIA respectively and sway increased by 8.80% and 7.84% for LIA and NLIA respectively) as shown in Fig. 18. The sway in structure for non-linear analysis has found approximately 4 times than that of the linear analysis. It has also happened due to reduction in shear stiffness at base of the footing during incremental loading which results in increasing slip and sway. As a result, the realistic performance of the structure has been observed. The non-linearity of soil and interface is necessary for analysis of SSI problems.

8. Conclusions

Influence due to interface in FE modeling of SSI system has been studied using modified interface element. The realistic modeling of interface has been done by including slip, bonding and de-bonding at soil-structure contact. The interface non-linearity has also been considered to get acquainted with the field conditions. Thus, the appropriate influence due to interface has been found out by comparing BM, settlement, footing base shear stress and sway of the frame. Based on the analysis and results obtained, following conclusions are made,

- The FE model for SSI system with realistic interface behavior has been developed and validated successfully with available literature.
- Modified 5 noded zero thickness interface element has been successfully implemented in this study. The element has showed good compatibility with 2 noded 1D beam and 8 noded 2D soil elements. The execution of such interface element in frame-footing-soil interaction system subjected to lateral load is a novel contribution.
- The proposed model, due to the inclusion of interface has improved the mathematical performance of structure by reducing the base shear stresses and allowing the sway. Thus it is giving more realistic behavior of SSI problems.
- The response such as slip, bonding and de-bonding at soil-footing contact has been successfully evaluated by the modified interface element. Hence the proposed methodology is suitable for appropriate modeling SSI problems.
- The redistribution of BM as well as a reversible sign for some frame members has made SSI analysis a necessary study with realistic modeling considerations.
- The non-linearity of soil as well as interface in modeling of SSI system is necessary, as the settlement and sway has increased (about 4 times of linear analysis) drastically for non-linear interaction analysis.

The present study is limited for static loading conditions only. The methodology suggested in this study is useful for future research such as dynamic SSI analysis considering realistic interface modeling.

Acknowledgement

The author is acknowledging to the Director NIT Raipur, Head of the Department and Faculty members, Department of Civil Engineering, NIT Raipur for their continuous motivation, support and guidance to carry out this work.

References

[1] Terfaya N, Berga A, Raous M, Abou-bekr N. A Contact Model Coupling Friction and Adhesion: Application to Pile/Soil Interface. International Review of Civil Engineering. 2018; 9(1):1-11. https://doi.org/10.15866/irece.v9i1.14034

[2] Nde NM, Fokwa D, Mbessa M, Tamo TT, Pettang C. Numerical Study of the Interaction between a Reinforced Concrete Pile and Soil. Open Journal of Civil Engineering. 2020; 10: 259-269. https://doi.org/10.4236/ojce.2020.103022

[3] Tahghighi H, Mohammadi A. Numerical Evaluation of Soil – Structure Interaction Effects on the Seismic Performance and Vulnerability of Reinforced Concrete Buildings. International Journal of Geomechanics. 2020; 20(6): 1-14. https://doi.org/10.1061/(ASCE)GM.1943-5622.0001651

[4] Rachamadugu R, Vikash G. Significance of Interface Modeling in the Analysis of Laterally Loaded Deep Foundations. Recent Advances in Computational Mechanics and Simulations, Lecture Notes in Civil Engineering, S. K. S. and M. Mukherjee, Ed. 2021: 199–209. https://doi.org/10.1007/978-981-15-8138-0_16

[5] Ichihara Y, Nakamura N, Moritani H, Choi B, Nishida A. 3D FEM Soil-Structure Interaction Analysis for Kashiwazaki – Kariwa Nuclear Power Plant Considering Soil Separation and Sliding. Frontiers in Built Environment. 2021; 7(June): 1-14. https://doi.org/10.3389/fbuil.2021.676408

[6] Qian XX, Yuan HN, Li QM, Zhang BY. Comparative study on interface elements, thin-layer elements, and contact analysis methods in the analysis of high concrete-faced rockfill dams. Journal of Applied Mathematics. 2013:1–11. https://doi.org/10.1155/2013/320890

[7] Ninic J, Meschke G. Beam – solid contact formulation for finite element analysis of pile – soil interaction with arbitrary discretization. International Journal of Numerical and Analytical Methods in Geomechanics. 2014; 38; 1453–1476. https://doi.org/10.1002/nag.2262

[8] Guo C, Lin P, Guo P, Wang F, Zhao L. A Weibull-based damage model for the shear softening behaviours of soil – structure interfaces. Geotechnical Research. 2021; 8(2): 54–63. https://doi.org/10.1680/jgere.20.00043

[9] Afrazi M, Yazdani M. Determination of the Effect of Soil Particle Size Distribution on the Shear Behavior of Sand. Journal of Advance Engineering and Computation. 2021; 5(2): 125–134. http://dx.doi.org/10.25073/jaec.202152.331

[10] Majedi MR, Afrazi M, Fakhimi A. A Micromechanical Model for Simulation of Rock Failure Under High Strain Rate Loading. International Journal of Civil Engineering, 2020. https://doi.org/10.1007/s40999-020-00551-2

[11] Majedi MR, Afrazi M, Fakhimi A. FEM-BPM simulation of SHPB testing for measurement of rock tensile strength. 54th US Rock Mechanics/Geomechanics Symposium, USA, 1-9, 2020.

[12] Barros RC, Vasconcelos LAC, Nogueira CL, Silveira RAM. Interface Elements In Geotechnical Engineering - Some Numerical Aspects and Applications. XXXVIII Iberian Latin-American Congress on Computational Methods in Engineering P.O. Brazil., 1–20, 2017.

[13] Dhadse GD, Ramtekkar GD, Bhatt G. Finite Element Modeling of Soil Structure Interaction System with Interface : A Review. Archives of Computational Methods Engineering. 2020. https://doi.org/10.1007/s11831-020-09505-2

[14] Beer G. An Isoparametric Joint/Interface Element for Finite Element Analysis. International Journal for Numerical Methods in Engineering . 1985; 21: 585-600. https://doi.org/10.1002/nme.1620210402

[15] Nowroozi V, Hashemolhosseini H, Afrazi M, Kasehchi E. Optimum Design for Soil Nailing to Stabilize Retaining Walls Using FLAC3D. Journal of Advance Engineering and Computation. 2021; 5(2): 108-124. http://dx.doi.org/10.25073/jaec.202152.329

[16] Maheshwari P, Viladkar M. Strip footings on a three layer soil system: theory of elasticity approach. International Journal of Geotechnical Engineering. 2007; 1: 47-59. https://doi.org/10.3328/IJGE.2007.01.01.47-59
[17] Liu KX, Lee FH, Yong KY. A New Finite Element Model for Pile-Soil interaction. GeoTrans, USA, 441–451, 2004.
[18]Rao S, R KV, Allam MM. Representation of Soil Support in Analysis of Open Plane Frames. Computers and Structures. 1995; 55(6): 917–925.. https://doi.org/10.1016/0045-7949(94)00579-R
[19] Viladkar MN, Godbole PN, Noorzaei J. Modelling of interface for soil-structure interaction studies. Computers and Structures. 1994; 52(4): 765–779. https://doi.org/10.1016/0045-7949(94)90358-1
[20] Ai-shamrani MA, Ai-mashary FA. A Simplified Computation of the Interactive Behavior between Soils and Framed Structures. Journal of King Saud University - Engineering Sciences. 2003; 16(1): 37–60. https://doi.org/10.1016/S1018-3639(18)30779-7
[21] Lim J, han Song T, Seog BH. Formulation Method for Solid-to-Beam Transition Finite Elements. KSME International Journal. 2001; 15(11) 1499–1506. https://doi.org/10.1007/BF03185739
[22] Mao J. A finite element approach to solve contact problems in geotechnical engineering. International Journal of Numerical and Analytical Methods in Geomechanics. 2005; 29: 525–550. https://doi.org/10.1002/nag.424
[23] Aivazzadeh S, Verchery G. Stress analysis at the interface in adhesive joints by special finite elements. International Journal of Adhesion and Adhesives. 1986; 6(4): 185–188. https://doi.org/10.1016/0143-7496(86)90004-7
[24] Dalili Shoaei M, Huat BBK, Jaafar MS, Alkarni A. Soil-framed structure interaction analysis – A new interface element. Latin American Journal of Solids Structures. 2015; 12(2): 226-249. https://doi.org/10.1590/1679-78251130
[25] Viladkar MN, Zedan AJ, Saran S. Nonlinear elastic analysis of shallow footings subjected to eccentric inclined loads. Geomechanics and Geoengineering : An International Journal. 2015; 10(1): 45-56. https://doi.org/10.1080/17486025.2014.902117
[26] Pande GN, Sharma KG. On Joint / Interface Elements and Associated Problems of Numerical Ill-Conditioning. International Journal of Numerical and Analytical Methods in Geomechanics. 1979; 3(3): 293-300. https://doi.org/10.1002/nag.1610030308
[27] Noorzaei J, Viladkar MN, Godbole PN. Nonlinear Soil-Structure Interaction In Plane Frames. Engineering Computations. 1994; 11: 303-316. https://doi.org/10.1108/02644409410799308
[28] Day RA, Potts DM. Zero Thickness Interface Elements-Numerical Stability and Applications. International Journal of Numerical and Analytical Methods in Geomechanics. 1994; 18: 689-708. https://doi.org/10.1002/nag.1610181003
[29] Potts DM, Zdravkovic L. Finite element analysis in geotechnical engineering Theory. Thomas Telford, London, 1999, ISBN 0-7277-2783-4.
[30] Kaliakin VN, Li J. Insight into Deficiencies Associated With Commonly Used Zero-Thickness Interface Elements. Computers and Geotechnics. 1995; 17: 225–252. https://doi.org/10.1016/0266-352X(95)93870-O
[31] Mayer MH, Gaul L. Segment-to-segment contact elements for modelling joint interfaces in finite element analysis. Mechanical Systems and Signal Processing. 2007; 21: 724–734. https://doi.org/10.1016/j.ymssp.2005.10.006
[32] Chandrupatla TR, Belegundu Ashok D. Introduction to Finite Elements in Engineering, Fourth edition, New York, Pearson Education Limited, 2012.
[33] Dhadse GD, Ramtekkar GD, Bhat G. Response of Single and Multilayered Flexible Base for Static and Earthquake Loading Under Framed RC Structure. S. Adhikari et al. (eds.), Advances in Structural Technologies, Lecture Notes in Civil Engineering, Springer Singapore. 169–183, 2020. https://doi.org/10.1007/978-981-15-5235-9_13

[34] Dong W, Hu L, Yu YZ, Lv H. Comparison between Duncan and Chang's EB Model and the Generalized Plasticity Model in the Analysis of a High Earth-Rockfill Dam. Journal of Applied Mathematics. 2013; 2013; 1-12. https://doi.org/10.1155/2013/709430
[35] Lade PV. Overview Of Constitutive Models For Soils. Geo-Frontiers Congress 2005, Austin, Texas, United States, 1–34, 2005.
[36] Brinkgreve RBJ. Selection of Soil Models and Parameters for Geotechnical Engineering Application. Geo-Frontiers Congress 2005, Austin, Texas, United States, 69–98, 2005. https://doi.org/10.1061/40771(169)4
[37] Viladkar MN, Godbole PN, Noorzaei J. Soil-Structure Interaction in Plane Frames Using Coupled Finite-Infinite Elements. Computers and Structures. 1991; 39(5): 535-546. https://doi.org/10.1016/0045-7949(91)90062-Q
[38] Rouhanifar S, Afrazi M, Fakhimi A, Yazdani M. Strength and deformation behaviour of sand- rubber mixture. International Journal of Geotechnical Engineering. 2021; 15(9): 1078-1092. https://doi.org/10.1080/19386362.2020.1812193

Research on Engineering Structures & Materials
journal homepage: http://www.jresm.org
Research Group

Research Article

Effect of position of steel bracing in L-shape reinforced concrete buildings under lateral loading

Birendra Kumar Bohara[1,a*], Kafeel Hussain Ganaie[1,b], Prasenjit Saha[2,c]

[1]*M.Tech in Structural Engineering Sharda University*
[2]*Department of Civil Engineering, Sharda University, India*

Article Info

Article history:
Received 19 May 2021
Revised 17 Aug 2021
Accepted 22 Aug 2021

Keywords:

Steel bracing;
L shape RC buildings;
Irregular buildings;
Inter-story drift;
Retrofitting, torsional;
Irregularity ratio

Abstract

The level of damage in irregular structures is more compared to regular structures. In this study, L shaped RC buildings are investigated with and without steel bracings in different positions in frames. The response spectrum analysis has been done by using ETABs software. The two cases considered, case I and case II for understanding the effect in inverted V bracing in L shape building. Case II shows the suitable seismic parameters when bracing is used properly. Inter-story drift, displacements, base shear, fundamental time period, torsional irregularity ratio and the capacity ratio of the columns are evaluated. It is also noticed that adding the steel bracing decreases the inter-story drift, displacements of the structure effectively. The torsional irregularity ratio of each 12 models are studied carefully. The capacity ratio of the selected columns is studied to understand the performance of the columns while using the steel bracing in the buildings. The steel bracings are effectively used as retrofitting in L shaped buildings if the position of bracings are considered in the frames appropriately. While designing irregular buildings with steel bracings, the torsional effect should be checked.

1. Introduction

The construction of irregular buildings in India is very common, and it has been observed that during the earthquake, irregular building failures are most common. Since India is also located at highly seismic region in the world and it is because of the historical interaction of the Indian plate underneath the Eurasian plate. The past earthquakes such as Nepal (2015), Sikkim (2011), Kashmir (2005) and Uttarkashi (1990) caused serious loss of life, economical losses as well as damage of structures and even some serious failures to the large number of structures. Even the low magnitude ground motion (earthquake) shows the serious effect on the structural element in the buildings. Sikkim is one of the examples which causes some serious damage during the earthquake [1]. The seismic performance of the building mainly depends upon the shape, size, and arrangement of beams, columns and configurations of the buildings. Irregular buildings may possess seismic vulnerability and failure of the structural member. Mass irregularity, stiffness irregularity, vertical irregularity, geometrical irregularity, and plan irregularity are the common irregularities observed in the structures. Overall, the irregularities of the buildings are divided into two types, vertical and horizontal irregularity. Sudden change in stiffness, geometry, irregularity in strength stiffness and mass along the height known as vertical irregularity. Discontinuities in the horizontal plan, like cut-outs, large opening, asymmetrical plan shape (T, E, F, H, L, etc.) are known as horizontally irregular structures. It is important to relate the relationship between the physical damage of the irregular building and earthquake ground motion which helps to understand the seismic risk assessment of the buildings. The presence of irregularity in the structures, induced stress in the beam,

*Corresponding author: bbohara2@gmail.com
[a] orcid.org/0000-0002-4654-3428; [b] orcid.org/0000-0002-2731-3248; [c] orcid.org/0000-0002-1238-5636;
DOI: http://dx.doi.org/10.17515/resm2021.295st0519

columns and slab, which makes the important to study the irregularity and its performance during ground motions. As compared to the regular structure the nonlinear and inelastic behaviors of the irregular structures is very complex. Retrofitting of irregular structures is the process of making a structure to resist the earthquake load.

Many researchers observed the seismic effect in the regular and irregular buildings with and without various earthquake resisting elements such as a shear wall, moment-resisting frame, and bracing. Mohammad et al. [2] studied the vertical irregularity in the structure and its effect during the earthquake was analyzed in the ETABs software. Mitesh Surana et al. [3] observed the seismic vulnerability of the hillside building in the Indian Himalayan region. Siva et al. [4] studied the different types of irregularity present in the structures. This research mainly focused on the vertical irregularity in the buildings. The irregular structures have more chances to fail during the earthquake than the regular structures that is the performance of regular structures have better than the irregular structure [5]. Chopra, A. K., & Goel, R. K. [6] studied the pushover analysis methodology for irregular structures and estimated the seismic demand for asymmetric buildings. In another paper, K.C. Anil and K. G. Rakesh [7] provided the model pushover analysis method and procedures to evaluate the seismic performance of the asymmetrical irregular in plan structures. Sachin G., P. S. Pajgade [8] studied the two cases, one with torsional effect and without torsional effect, and the result was compared based on the reinforced provided in the columns. Generally, the torsional effect in the structures is due to the eccentricity induced between the center of mass and the center of rigidity in the asymmetric plan buildings. A. Fredrick C. Dya and A. W. C. Oretaa [9] analyzed the existing structures to identify the seismic vulnerability of the irregular structures (mainly soft story) and observed the seismic effect by using pushover analysis and dynamic analysis. Marco Valente [10] investigated the plan irregular buildings for restrengthening purposes. The columns were retrofitted by using the RC jacketing and FRP to reduce the torsional component and analyzed with nonlinear time history analysis and pushover analysis. The displacement-based seismic design (DBSD) method was also used to analyze the irregular in plan shape structures. F. Mazza [11] and F. Mazza et al. [12] studied the DBSD method for the L shape irregular buildings for a retrofitting purpose. For the retrofitting, the researchers used the hysteretic damped braces.

L shape building possesses two types of problems. One of the problems associated with the opening and closing mode which cases the high-frequency oscillatory mode. It is due to the slender projection of the buildings. Which creates a high-stress concentration at the corners and causes the failure of structural members. Another problem is based on the torsional effect induced in the L shape buildings. Researchers have mainly focused on the seismic behaviors of the L shape building based on the displacements, drift, by using the response spectrum analysis (RSA) and static linear analysis. They focused on the observation of comparative study on the regular and L shape buildings and torsional irregularity ratio (B. Khanal and H. Chaulagain [13], Shehata E. Abdel Raheem et al. [14], Momen M. M. Ahmed et al. [15]). Some other researchers such as S.S. Tezcan, C. Alhan [16], Özmen et al. [17], Ali Koçak et al. [18] were focused on the study of the torsional effect of shear wall buildings. Researchers observed the torsional irregularity ratio of the different shear walls buildings. Prajwal T P [19] studied the regular and re-entrant L-shaped buildings and the analysis was based on the pushover analysis and nonlinear time history analysis to check the vulnerability of the irregular structures. Researchers also performed a comparative study between the pushover analysis and nonlinear time history analysis of the plan irregular buildings [20]. P. Giannakouras, C. Zeris [21] performed the pushover analysis and nonlinear time history analysis with the direct displacement-based seismic design (DDBD) method in the vertically irregular structure to study the performance of the structures. To understand the seismic performance of the irregular structure, the pushover

and nonlinear time history analysis help better than linear analysis and it also helps to prevent failure [22], [23].

Concentrically braced frames and eccentrically braced frames are normally used in both the new construction and retrofitting process. Concentrically braced frames such are V bracing, inverted V–type bracing, diagonal bracing, multi X bracing, X bracing, etc. are used in the structure to resist the earthquake and to improve the drift, displacement, and increases stiffness. Many researchers studied the use of steel bracing in RC frame buildings. Applying the steel bracing in the RC frame improves the seismic performance and ductility of the existing buildings [24]-[29]. A. Rahimi, M.R. Maheri [30], [31] studied the effect of X-type steel bracing in the 2D RC frame to understand the braced and unbraced performance of the structures. The result shows that adding the bracing in the RC frame reduces the inter-story drift and displacement. Steel bracing improves the seismic performance strength and stiffness of the RC building when the inverted V, X shape bracing is used [32]-[34]. A. Hemmati et al. [35] studied the experimental analysis of rehabilitation of RC frame by using concentric and eccentric bracings and observed that the absorbed energy capacity of rehabilitated frames with eccentric and concentric bracings increased about 1.98 and 1.63 times of concrete frame. The compression of regular and irregular buildings with different types of steel bracings were observed by a different researcher, to know the effectiveness of steel bracing [36], [37]. Some other types of bracing such as commonly used high-performance structural elements, the buckling restrained bracing, may be used for lateral force-resisting systems in the structures [38], [39]. Many other techniques are used to improve the seismic behavior of structures such as hysteretic bracing systems [40], high strength diagonal precast panels [41] and for eccentric steel bracings connection (shear links) [42], [43] and these studies to understand the effectiveness of the steel bracings in the structures.

In this study the seismic behavior of the L-shape RC buildings with and without concentrically inverted V bracing. There is a lack of study on L-shape RC buildings with different positioned inverted V-shaped steel bracings. Many studies only focused on either regular RC buildings or vertically irregular buildings with steel bracing. The study focused on the different positioned inverted V bracing used in the RC L shape irregular buildings where steel bracing is used for a retrofitting purpose. The comparative study is presented different positioned steel braced frames based on the seismic performance. The seismic performance such as displacement, drift, shear force, fundamental time period, stiffness, torsional irregularity ratio, the capacity ratio in columns, axial forces and moment in the base columns are studied and compared. Best performed braced configurations are identified in L-shape buildings. The outcomes results help to observe the significant effect of steel bracing in L shape RC frames and reduce vulnerability. After studying the various research it is essentially needed to understand the seismic behaviors for inverted V braced RC structures in different configurations.

2. Proposed Problem

To study the effectiveness of the steel bracing in the existing L-shape RC building, the hypothetical L-shape of 6-story buildings is assumed. The 6-story buildings are designed as a moment-resisting frame. The 6 story building is irregular in plan shape like L shape (see in Table 3 and Fig.13) the 6-story L-shape building having 3.2m height each except the first story which is assumed as 4 m story height normally adopted in India. The overall height of the building is 20m. Each bay width is considered as 6m that is a column to columns span is 6m as shown in Fig 13 in both x and y-direction. The material and final selected cross-sectional property are shown in Table1 and 2 respectively. The columns section is changed every 3 stories of the building.

The L shaped moment resisting building is designed initially and it is assumed that, the column cross-section for all columns are the same (see table 2). The columns (including C1, C2, C3 and C4) consist of almost 3.8% of steel reinforcement for up to 3 stories from ground level and above 3 story and the reinforcement used as 3.08% of its cross-section. Beams and columns are designed according to the Indian standard [44]. The depth of the slab is considered as 120mm and its compressive strength 25MPa. The reinforcement used in the RC members is considered as a grade of 415MPa. For inverted V bracings, a hollow box section (square section) is used for retrofitting process (see table 2). The hollow section with a limited slenderness ratio (KL/r = 65) and compact section is selected to avoid the local buckling failure during lateral loading. The bracing is selected such that, it should be the weakest member of all other members (beam and columns) [32], [33]. The joint between steel and RC member are considered as a pin joint and hence the lateral load transfer through the bracings as an axial loading only (compression and tension).

The inverted V-bracing is used in different bays as shown in Table 3 (bold thick bays represents where the steel bracing is used). Table 3 shows the L shape building with inverted V-bracing (thick bold bays) and a 3D view of the respective model. Almost 12 models are observed and each model is named as L1 to L12 in which the L1 is the original without a braced RC frame. The models from L2 to L12 which are of the different steel braced configurations are shown in the Table 3. The models are further grouped in two categories, L2 to L8 known as the case I and L9 to L12 as case II. The building is designed by using Indian standard codes like for concrete design IS 456:2000 [44] and for seismic design IS 1893:2016 [45] ductile design code [47] used. The building is designed for 5 KN/m^2 as a live load and for the top floor, the live load is considered as 2 KN/m^2. The seismic weight of the structure is taken as 100% of dead load, 50% for live load when the live load is greater than 3KN/m^2 and 25% of live load when the live load is less than 3KN/m^2 [44].

The ETABs finite element software is used to study the seismic behaviors of the L-shape building with and without steel bracings. For a seismic design, the building is assumed in India, and the Indian seismic design code is used in this study. The seismic zone factors (z) of the building is 0.36 and 5% damping factor is considered [45]. The soil is medium soil (type ii) and the importance factor is considered as 1. The response reduction factor for the structure is considered as a 5 for the SMRF (Special moment-resisting frame) system of the buildings [45]. For the seismic design of the structure, some assumption is made such as P-Δ effect is considered for each model for both RSA. Soil-structure interaction is not considered in the model and base are restraints in all three X, Y and Z directions. For the RSA, SSRS (square root of the sum of square) and CQC (Complete quadratic Combination) are considered. A sufficient number of modes are considered in the analysis such that to get the sum of the all model mass for all modes assumed 90% of the total seismic mass, according to the IS 1893: 2016 part1 [45].

Table 1. Material properties of the concrete and steel materials

Concrete	Grade	Modulus of elasticity	Poisson's ratio		Density	Stress-strain diagram
	M25	25000 MPa	0.2		7850 Kg/m^3	(Fig 1 (b))
Steel bracing	Grade	Modulus of elasticity	Minimum yield stress	Minimum tensile stress	Density	Stress-strain diagram
	FE250	210 GPa	250 MPa	410MPa	7850 Kg/m^3	(Fig. 1 (a))

Table 2. Specifications of beams, columns and bracing used in the 6 story L-shape study buildings

RC section		Steel section
Columns(mm)	Beam (mm)	Bracing (hollow section in mm)
400X400 (1-3 story) 350X350 (4-6 story)	300X400	200X200X12

3. Methodology

To study the seismic behaviors of concentric steel braced RC frames and without steel braced RC frames, ETABs software is used for the analysis and design of each model. Linear dynamic analysis (RSA) is used for understanding and analyzing the torsional effect, story drift and story displacements of each model. The RSA is the linear dynamic analysis and is used to find the seismic response based on the vibrational mode shape. The method provides all almost realistic profile of the lateral forces. The comparative analysis is made before and after the steel bracing is used. The beams and columns are analyzed and designed. After the design, the concentric steel bracing is used for a retrofitting purpose. The study is mainly focused on the effect of bracing after applying in the RC building as retrofitting.

In this study, the soft story is presented in the first story which is the common practice in India [9]. According to the Indian standard [45], the soft story is defined as the story have lateral stiffness that is less than the stiffness of the above story. The height of the first story is taken 4m whereas the rest of the story has 3.2m in height. The stiffness equation ($K=12EI/L^3$) in which it is clear that the height of the story reduced the stiffness. Hence the soft story ratio is defined as the cube of the ratio of first story height and second story height. And the soft story ratio is calculated as 1.95.

If the projection is greater than 15 % of the overall plan dimension in that direction, it is said to be a Re-entrant corner [45]. In the study, the projection is 66% along the x-direction and 57% along y-direction greater than the overall dimension of the plan in each direction. Hence the re-entrant corner is present in the plan configuration. Torsional irregularity is calculated with the help of drift at each corner of the 3D model. Almost every seismic code (IS 1893:2016, UBC 97, ASCE 7–10) has a similar provision for the calculation of the torsional irregularity of the L shape building. For understanding, the accidental torsional effect torsional amplification factor (A_x) [46] shall be observed. The Δ_{max}, Δ_{min} and Δ_{avg} are the maximum, minimum and average drift and calculated when earthquake load is applied from x-direction as shown in Figure 2 respectively. The torsional irregularity coefficient is defined as the ratio of the drift maximum and average drift ($\eta_t = \Delta_{max}/\Delta_{avg}$). Three conditions are described i) when η_t is less than or equal to the 1.2 then no torsional irregularity exists and A_x is equal to the 1, ii) when η_t is between 1.2 to 2.083 the torsional irregularity exists and A_x is calculated as given formula, iii) When the η_t is greater than 2.083 then η_t=2.083 and A_x equal to 3 [46].

$$A_x = \left(\frac{\Delta_{max}}{1.2\Delta_{avg}}\right)^2$$

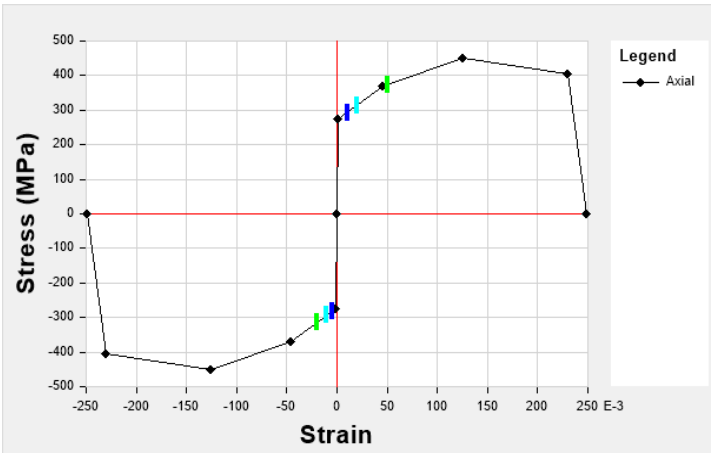

(a) Steel (Fe 250)

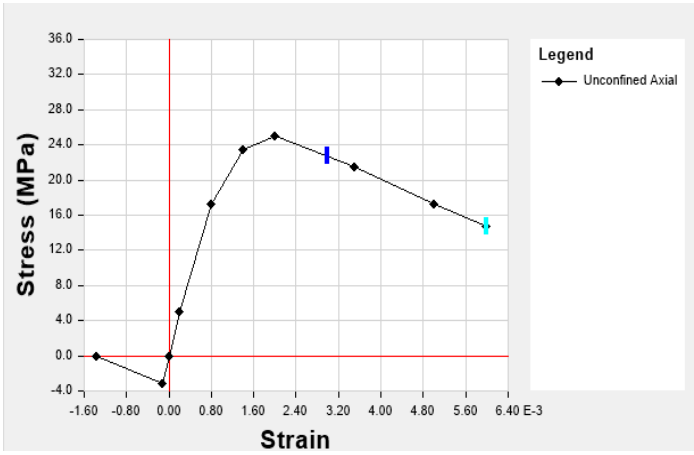

(b) Concrete (M25)

Fig. 1 Stress-strain diagram for a) steel and b) concrete.

Table 3. Plans and 3D views of proposed buildings

Models	Plan View	3D view	Remarks
L1	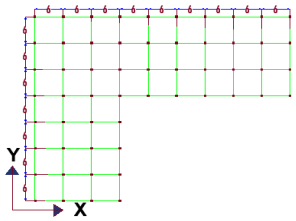	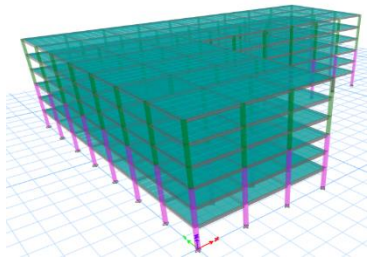	#Without braced moment-resisting frame. # Dimension in meter (m) # Inverted V bracing are applied only left portion side as shown in Fig L2. # Bracings are used in four bays # Bracings are applied in the left portion side (same as L2) and right portion side (2 bays) shown in plan view. # Bracings are applied upper portion (5 bays) of the plan view only.
L2	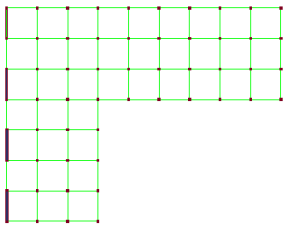	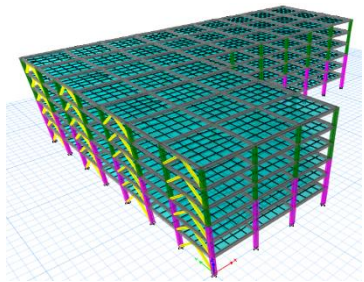	
L3	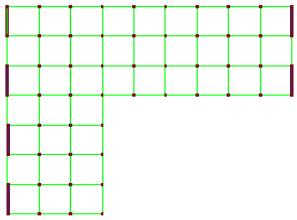	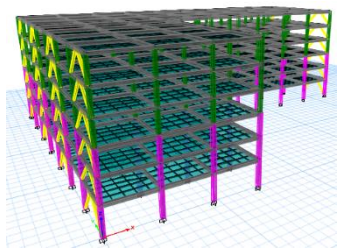	
L4	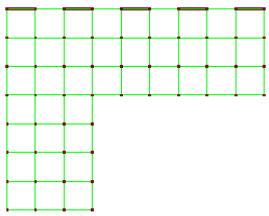	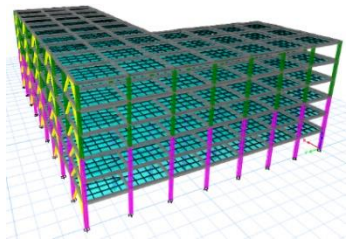	

L5	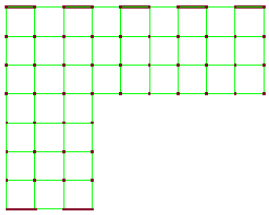	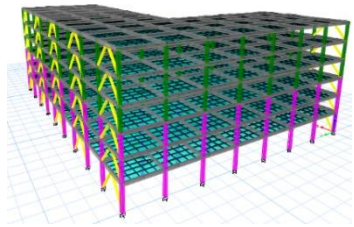	# Same as L4 but additional 2 bottom bays are braced.
L6	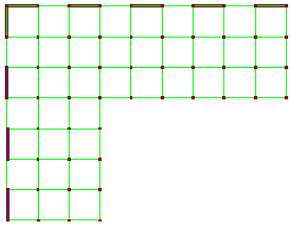	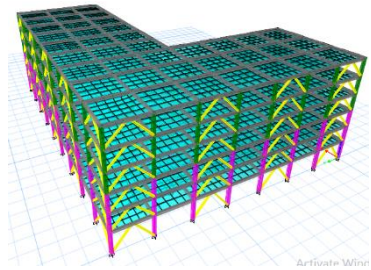	# Bracings are used left and an upper portion only. # It is the Combination of L2 and L4 configurations of bracings.
L7	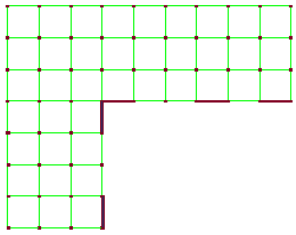	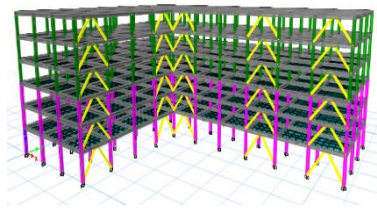	# Bracings are applied as shown in Fig L7.
L8	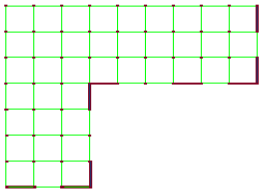	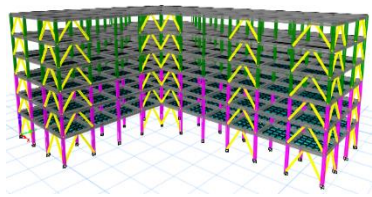	# Bracings are applied right and bottom portion of L shape buildings.
L9	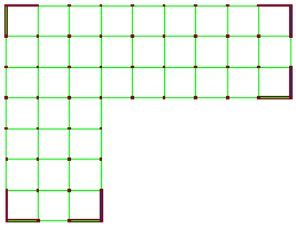	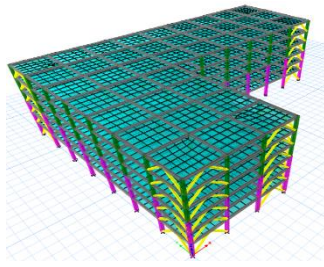	# Bracings are applied only outer corner portion of L shape buildings.

L10	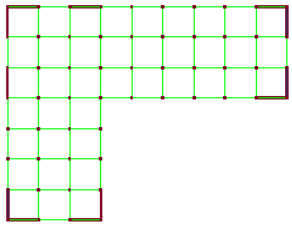	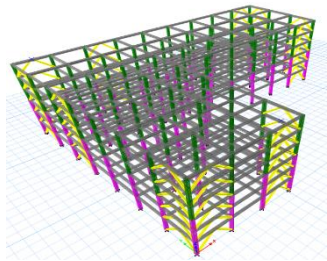	# Same as L9 and additional 2 bays (see fig L10 plan views) are braced. # Slabs are hidden.
L11	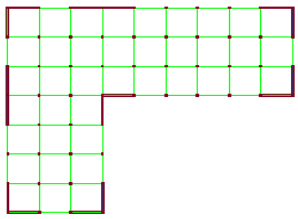	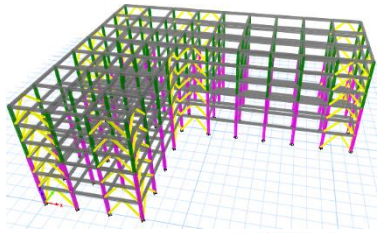	# Bracings are used symmetrically and a total of 16 bays are braced.
L12	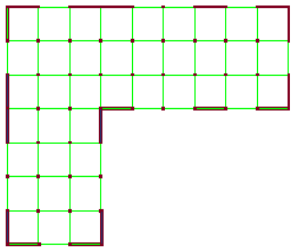	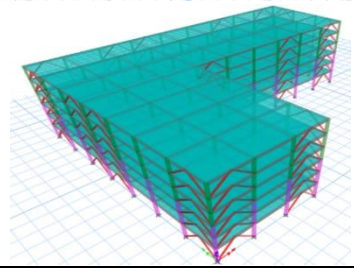	# Same as L11 and additional 2 bays are braced. # Total 18 bays are braced.

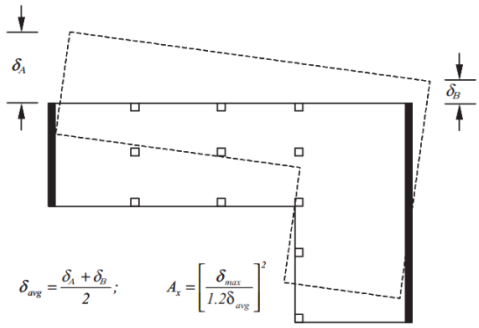

Fig. 2 Torsional irregularity calculation of the L shape buildings [46].

4. Result and Discussion

The L shape buildings are analyzed with different braced configurations by using the ETABs software. The various seismic parameters are observed such as Fundamental time periods, base shear, inter-story drifts, and torsional irregularity, stiffness and column forces to understand the effect of inverted V bracings in L shape RC buildings.

4.1. Design Base Shear Variations

The base shear is the lateral total force at the base of the structures induced due to the earthquake ground motions and it depends upon the plan shape of the structures, fundamental time periods and soil types of the sites. It also depends upon the seismic weight of the structures. in the study, the two cases are analyzed where the in case I, the inverted V bracings are used such a that it only applied in the incomplete ways or only added the bracings in a single axis of the structures and in case II the bracings are applied in both the directions as shown in Table 3. In both cases, the design base shear is observed in both directions as shown in Fig 3. It is observed that adding the steel bracings increases the base shear values of the structure and similar results also observed in [28], [31]. In model L3, the bracings are added in such a way that it resist the lateral load along the y-axis. So the in the L3 models the base shear values are more along the y-axis as compared to the x-axis. In models L4 and L5, bracings are added to resist the lateral load along the x-axis only so that only along the x-axis, the base shear values are more as compared to the y-axis. However in the model L1, which is represented without braced frame L shape buildings. In the L1 model, almost the same design shear forces are observed. In the models, L9 to L12 (case II) almost similar base shear values are observed in both the x and y-axis.

4.2. Fundamental Time Periods (FTP)

The seismic behaviors of the structures depend upon the FTP of the structures and the base shear of the structures also depends upon the natural time period of the buildings. Normally to calculate the FTP of the buildings, the code provided the empirical formula is used but in this study program based natural period of building is considered. However the formula is only for regular structures, the code-provided formula does not give accurate FTP for structures when the buildings are irregular and braced [13], [15]. Fig 4 shows the variation of the fundamental time period of the structures on both the x and y-axis. Fig 4 it is clear that where the steel bracings are used to resist the lateral load, the fundamental time period at that axis is decreased however the base shear at that axis increases. When the steel bracings are provided in both axis, in models L9 to L12, the fundamental time period of the structures is decreased and observed minimum in the L12 model.

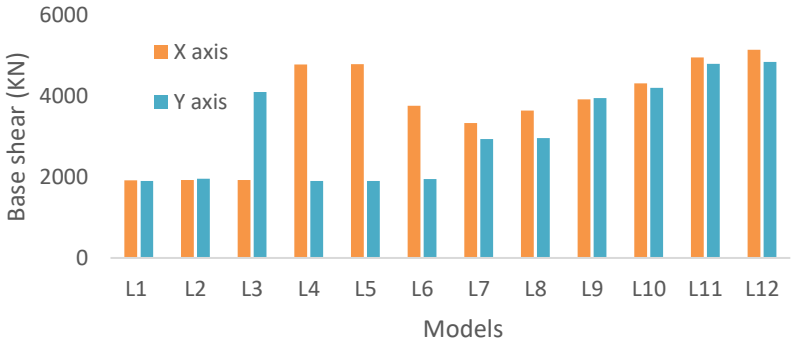

Fig. 3 Base shear variations along the x and y-axis in different models.

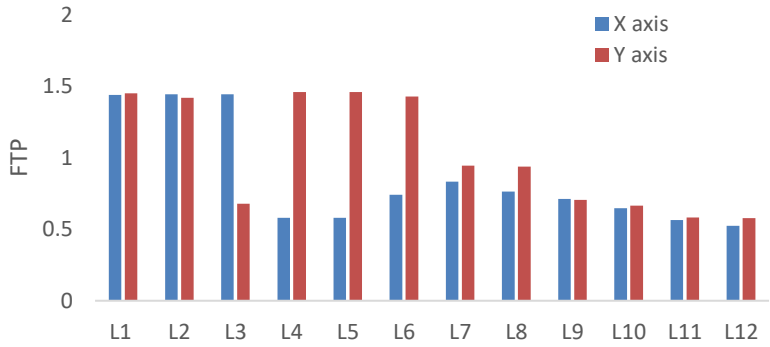

Fig. 4 Fundamental time periods of the different models

4.3. Maximum Displacements Response

The story displacements of the irregular structures subjected to lateral loadings are a significant parameter for buildings design. The top story displacements response of the structures helps to understand the damage level of the structures [31]. While designing the structures, the lateral deformation and drift of the structures should be considered carefully, avoiding excessive deformation in the structures. In irregular structures, excessive deformations damage the structural and nonstructural members in the buildings. Fig. 5 and Fig. 6 show the maximum displacements in the L shape buildings.

Fig.5 shows that the maximum displacements in the different models in both x and y directions. It is noticed that adding steel bracings in different positions, affected the maximum displacements of the structures. In case I (L2-L8) adding the steel bracing in the model L1, does not show as much effective control in the maximum displacements. Even due to the torsional effect, in the model L4 along with the x directions, the maximum displacements increase as compared to the L1 references model. In the L4 models as shown in Fig. 1, the bracings are added that to resist lateral load along the x-axis, however, due to the torsional effect, it amplified the displacements which is not good. The re-entrant corner behavior amplified the displacement along the x-axis [17]. It is noticed that in the case II (L9-L12) models, the steel bracings effectively reduced the maximum displacements [31] as shown in Fig. 5 and 6. In the models L9, L10, L11 and L12, it can be noticed that the maximum lateral displacements are decreased by 40%, 47%, 51% and 54% along the x-axis and 42 50 46, and 46 along the y-axis after adding (retrofitting) the steel bracing in L1 models respectively. The steel bracings are added along the x and y-axis properly shows good seismic behaviors and reduced displacements effectively. In case I the maximum displacements are observed as 43mm along with x directions due to the lateral-torsional vibration coupled behavior in the L shape of soft-story buildings. In case II the displacement gets its maximum value of 15.5mm for the L9 model, and the minimum value of 12 mm for the L12 model along the x-axis. And the similar response is observed in y directions as shown in Fig 5 and 6. By comparing the maximum displacements of 6 story L shape soft-story buildings with different braced configurations (see Table 3), it is observed that inverted V bracings used properly in the L shape RC buildings reduce the maximum lateral story displacements in the models.

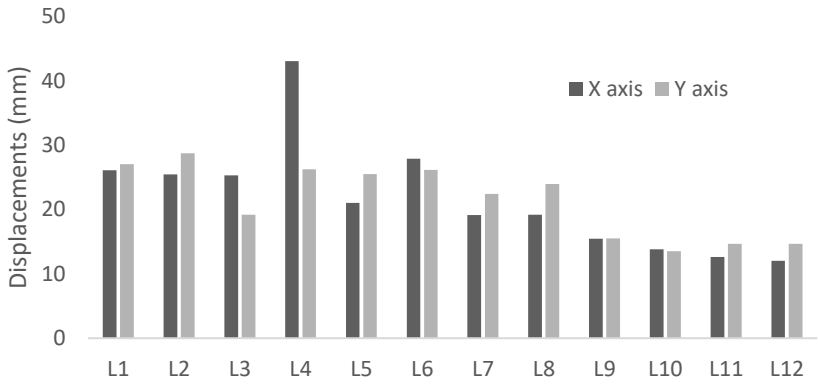

Fig. 5 Maximum top story displacements along the x and y-axis.

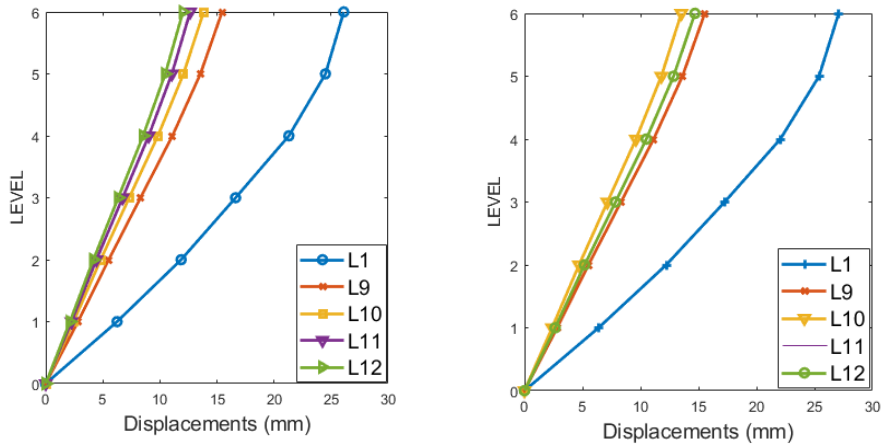

a) Case II (x axis) b) Case II (y axis)

Fig. 6 Maximum story displacements in case II along both axis.

4.4. Inter Story Drift Ratio

Inter story drift is another important significant parameter for examining the structural behaviors effectively. The inter-story drift (ISD) is the more reliable parameter to observe the structural and nonstructural damage as compared to the displacements [31].

The story drift of the L shape 6 story irregular buildings is observed with steel bracing in different configurations. The graph is plotted for both case I and case II as shown in Fig. 7 and 8. It is observed that the ISD of all models are under the drift limits 0.004 as the Indian code [45] suggested. In all cases, the maximum drift is observed in the second floor or third-floor level and it is due to the soft story in base level. It is also noticed down the uniform drift is observed where the steel bracings are used for resisting the lateral load. Without steel braced frames L1 and braced frames L2 to L12, RC L shape buildings are compared. The inter-story response decreased in case II when the steel bracings are used. It is observed that in the L shape buildings in case II the maximum ISD of 0.000888, 0.00079, 0.000724 and 0.000688 along the x-axis and 0.000887, 0.00077, 0.000845 and

0.000846 along the y-axis for models L9, L10, L11 and L12 respectively. As increased numbers of bays with steel bracings in the frames in both directions, the ISD of the models decreases more. Similar to the maximum displacements in case I, model L4 show a maximum ISD of 0.0026 along with the x directions as shown in Fig 7(a). Which is greater than the drift limit of 0.002 for inverted V bracings in RC buildings [32], [34]. Overall in case II Fig 7(b) and 8(b) shows that adding the steel bracings properly in the RC buildings decreased the ISD of the structures effectively. However the case I should be shows unpredictable ISD of the structures due to the torsional behaviors in these models.

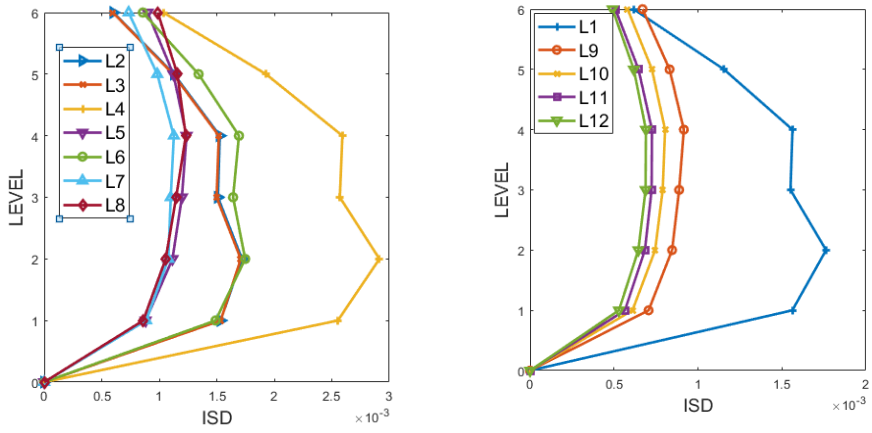

a) Case I b) Case II

Fig. 7 Inter story drift of the L shape buildings along x axis in both cases

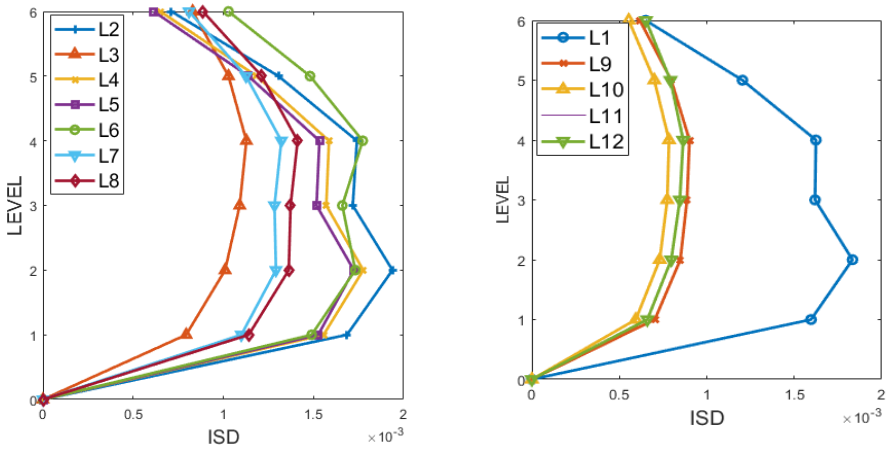

a) Case I b) Case II

Fig. 8 Inter story drift of the L shape buildings along the y-axis in both cases.

4.5. Story Stiffness Response

Story stiffness of the buildings depends upon the size, shape and length of the columns or bracings. Fig.9 represents the variation of story stiffness of each model. The maximum x-direction story stiffness demands almost the same for L1, L2 and L3 models. The maximum story stiffness of the model L4 is increased by 2.18 times of L1. Similarly for L5 to L12 story stiffness increased by 5, 2.8, 3, 4, 4.9, 5.6, 7 and 8.25 times of L1 respectively along x-direction (see Fig. 9). Along the y-direction, the story stiffness observed in L1, L4 and L5 are almost equal. The maximum story stiffness along the y-axis of models L2 and L3 are increased by 1.5 and 5.12 times of L1. And similarly, for models L6 to L12, the maximum story stiffness are increased by 1.6, 2.4, 2.9, 5, 5.7, 6.7 and 6.8 times of L1 respectively along y-direction (see Fig. 9). It is noticed that adding the steel bracings in the models to resist the lateral loadings, increases the story stiffness of the buildings. In case II, the increasing the stiffness of the story in each direction, noticed more uniform. The minimum story stiffness is observed in the model L1 and maximum in L12, which is retrofitting by steel inverted V bracings.

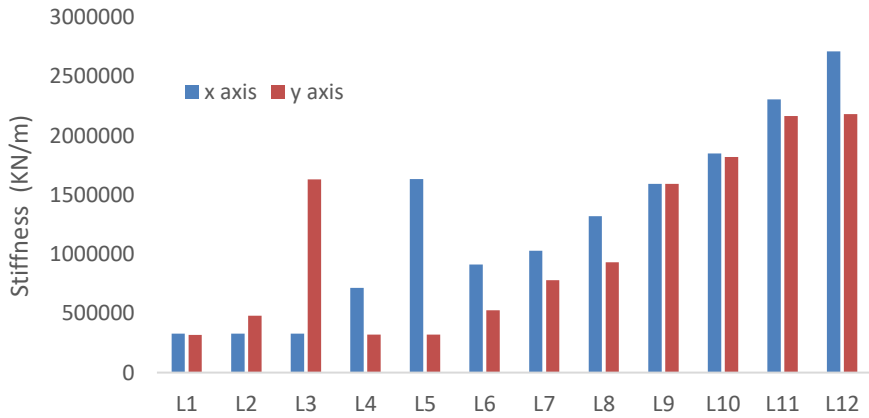

Fig. 9 story stiffness of the models

4.6. Torsional Irregularity Ratio

The torsional irregularity ratio of the structures gives the most important information about buildings' damages levels during earthquake loading. It is an analytical index, created based on the structural response, multidirectional response of the asymmetry structure. The different studies studied the limit of torsional irregularity ratio which is 1.2 [13], [14] and [17]. It means when the torsional irregularity ratio limits exceed such structures is affected by differential displacements in the plan. It affects the seismic behaviors of the structure. When the torsional irregularity ratio is less than 1.2, there is no torsional irregularity exist in the buildings [46].

Figure 10 shows the first mode and second mode of vibration for the selected models L1, L4, L8 and L12. The models are selected every fourth model and also these models possess a considerable torsional irregularity ratio. This mode shape shows the analytical fundamental time period for the first and second mode of vibration. These 3D views also show the torsional behaviors of the structures. Fig 11a and 12a show the torsional irregularity ratio for L shape braced and without braced frames along with the story of the buildings. The torsional irregularity ratio changed over the building story height. In some models lower story shows a more torsional irregularity ratio than the upper story. It may be due to the L shape projection of the buildings and the lower story is created as a soft

story. The maximum torsional irregularity ratio when unidirectional spectrum used along the x-axis for the case I are 1.01, 1, 1.53, 1.43, 1.44, 1.11 and 1.25 for models L2-L8 respectively. It is observed that model L4 shows the maximum torsional irregularity ratio in case I. However for models L1 show the safe torsional irregularity ratio (less than 1.2). In case I, L5, L6 and L8 have torsional irregularity ratios are greater than 1.2 along the x-axis and along the y axis L2, L3, L6 and L8 have torsional irregularity ratios that are more than 1.2 (see Fig 11 and 12). In case I, these models represent the incomplete braced frame configurations, hence shows torsional irregularity in the structures. The model L4, along the x-axis, further studied the torsional amplification factors because the model L4 has a greater torsional irregularity ratio (>1.2). Table 4 shows the amplification factors for L4 models and the torsional amplification factors are greater than 1 and less than 3. Similarly for model L3 in Table 5 shows the torsional amplification factors.

In case II, only the L12 model shows the Torsional irregularity ratio greater than 1.2 and its torsional amplification factors are given in Tables 6 and 7, which are within the limits. Fig 11b and 12b show the L12 buildings have maximum torsional irregularity ratios are 1.33 and 1.51 for the x and y-axis respectively. Other models L9, L10 and L11 show better torsional behavior within limits. Models L9-L11 have provided suitable bracing along the x and y-axis. It is observed if carefully bracings are applied in the L shape RC buildings shows good seismic behaviors. The buildings shows torsionally safe and have minimum displacements and drifts. The steel bracings improve the stiffness and torsionally safe (if properly applied) have also better to use for a retrofitting purpose in irregular buildings.

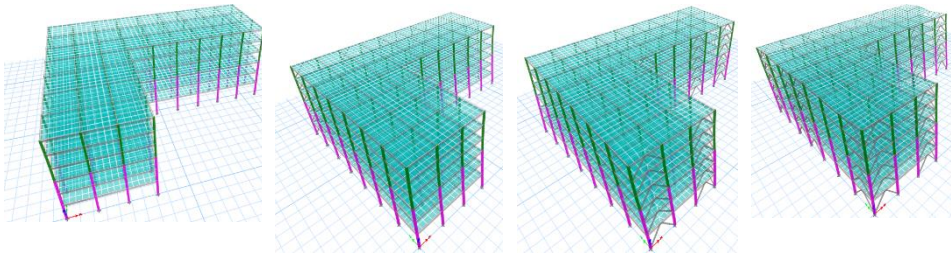

L1, T= 1.457 Sec L4, T=1.46 L8, T=0.939 L12, T=0.578

a) first mode shape

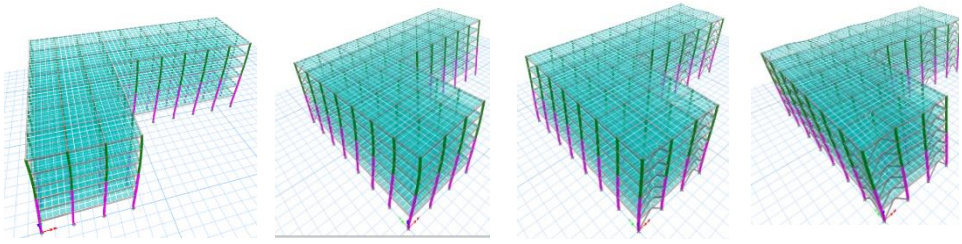

L1, T=1.441 sec L4, T=1.39 sec L8, T=0.764 sec L12, T=0.523 sec

b) Second mode shape

Fig. 10 View of mode shape of the studied buildings.

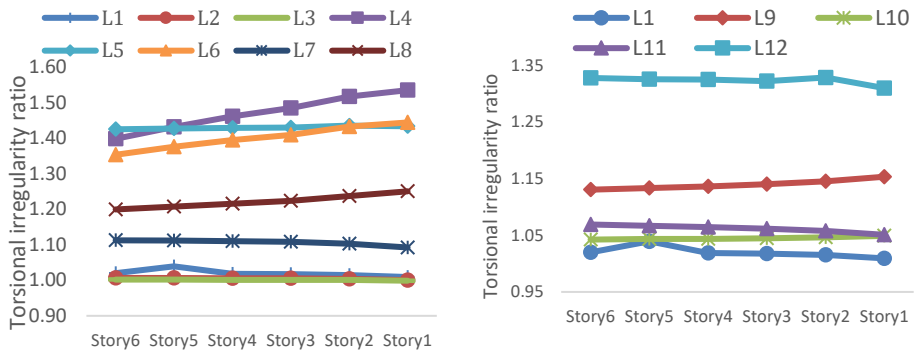

a) Case I b) Case II

Fig. 11 Torsional irregularity ratio along the x-axis

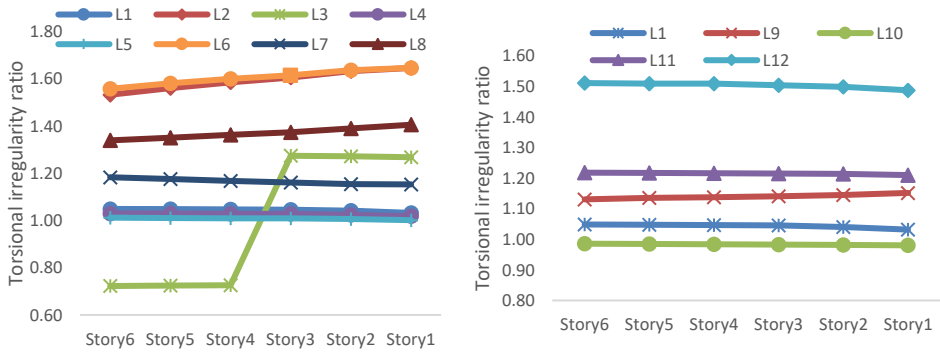

a) Case I b) Case II

Fig. 12 Torsional irregularity ratio along the y-axis

Table 4. Calculation of torsional irregularity and torsional amplification factors for L4 along x axis.

Δ_{max}(mm)	Δ_{min} (mm)	Δ_{avg}(mm)	$\eta_t = \Delta_{max}/\Delta_{avg}$)	A_x
43.1	18.5	30.8	1.40	1.36
40.4	16.0	28.2	1.43	1.42
35.1	13.0	24.0	1.46	1.48
27.5	9.5	18.5	1.48	1.53
19.5	6.2	12.8	1.52	1.60
10.2	3.1	6.7	1.53	1.64

Table 5. Calculation of torsional irregularity and torsional amplification factors for L3 along y axis.

Δ_{max}(mm)	Δ_{min} (mm)	Δ_{avg}(mm)	$\eta_t = \Delta_{max}/\Delta_{avg}$)	A_x
10.9	19.2	15.0	0.72	0.36
9.4	16.6	13.0	0.72	0.36
7.6	13.4	10.5	0.73	0.37
9.8	5.6	7.7	1.27	1.13
6.4	3.7	5.0	1.27	1.12
3.2	1.8	2.5	1.27	1.12

Table 6. Calculation of torsional irregularity and torsional amplification factors for L12 along x axis.

Δ_{max}(mm)	Δ_{min} (mm)	Δ_{avg}(mm)	$\eta_t = \Delta_{max}/\Delta_{avg}$)	A_x
12.0	9.1	10.5	1.33	0.90
10.5	7.9	9.2	1.33	0.90
8.5	6.4	7.5	1.32	0.90
6.4	4.8	5.6	1.32	0.90
4.2	3.1	3.7	1.33	0.90
2.1	1.6	1.9	1.31	0.89

Table 7. Calculation of torsional irregularity and torsional amplification factors for L12 along y axis.

Δ_{max}(mm)	Δ_{min} (mm)	Δ_{avg}(mm)	$\eta_t = \Delta_{max}/\Delta_{avg}$)	A_x
14.7	9.7	12.2	1.51	1.01
12.8	8.5	10.7	1.51	1.00
10.5	7.0	8.7	1.51	1.00
7.8	5.2	6.5	1.50	1.00
5.2	3.5	4.3	1.50	1.00
2.6	1.8	2.2	1.49	0.99

4.7. Columns Design Property

The reference model L1 and other braced models L2-L12, the columns, beams slabs and imposed loads are the same. The rebar in the columns is also fixed for all models all base columns have 3.8%. The columns are designed and sized properly in the L1 model. After adding the steel bracings in model L1 in a different way and named these models as L2 to L12. It is essential to study the columns for their safety based on capacity ratio, design moments and design axial loads [30]. The effect of steel inverted V bracing in the column is observed by investigating the capacity ratio, axial load and moment in the selected columns (corner columns may or may not be directly connected to the bracings) as shown in Fig 13. C1, C2, C3 and C4 are the corner base column and their design parameter variation are observed in models L1 to L12 to compare each other.

Table 8 shows the design axial load, design moment and capacity ratio in each selected column in models L1 to L12. It is observed that when the columns are connected to the bracings, the axial load in the columns increase. The axial load in model L1 is 1778 KN and model, L12 has 2200 KN for C1 columns, which shows the bracing increases the axial load in the columns. When the columns are near the bracing configurations, the design moment in the column decreased. In table 8, observed that in the columns directly connected to the bracing, the design moment in the columns decreases and it also decreases the main rebar demand in columns. The capacity ratio of the columns indicates the stress condition. The capacity ratio of the model L1 is 0.738, 0.52, 0.51 and 0.51 for C1, C2, C3 and C4 respectively. Maximum stress is induced in the C1 columns, it is due to the re-entrant effect in corner columns. It is noticed that model L4 is overstressed. However for case II, properly braced models, the capacity ratio of the columns slightly decreased in columns and increases in C2, C3 and C4 columns. To reduce the torsional hazard level in the L shape buildings, the steel bracings should be used symmetrically to balance the torsional effect. If only one direction, the bracing has used some columns may be overstressed and fail. To design the L shape braced RC buildings the torsional effect should be considered carefully.

Table 8. selected columns for study and design parameter

Columns	Columns design parameters	L1	L2	L3	L4	L5	L6	L7	L8	L9	L10	L11	L12
C1	Axial force (KN)	1778	1778	1778	1785	1778	2194	2667	2696	2194	2194	2241	2200
	Moment (KN-m)	122	121	121	146	121	45	81	62	45	45	46	45
	Capacity ratio	0.74	0.74	0.74	0.80	0.74	0.69	0.88	0.86	0.69	0.69	0.71	0.69
C2	Axial force (KN)	649	645	1387	335	1955	987	622	1050	1797	1804	1721	1739
	Moment (KN-m)	137	170	59	206	62	150	120	72	51	46	47	46
	Capacity ratio	0.52	0.637	0.822	1.02	0.66	0.938	0.467	0.723	0.59	0.581	0.559	0.565
C3	Axial force (KN)	644	752	1972	1300	1964	1392	604	593	1980	1887	1782	1738
	Moment (KN-m)	135	132	40	115	46	42	94	96	53	46	36	35
	Capacity ratio	0.51	0.53	0.62	0.97	0.633	0.789	0.419	0.499	0.643	0.605	0.56	0.547
C4	Axial force (KN)	643	1409	1975	509	1534	831	576	1580	1861	1803	1649	1685
	Moment (KN-m)	135	73	40	305	66	121	94	97	53	44	42	34
	Capacity ratio	0.51	0.53	0.62	1.28	0.916	0.79	0.434	0.629	0.61	0.577	0.53	0.529

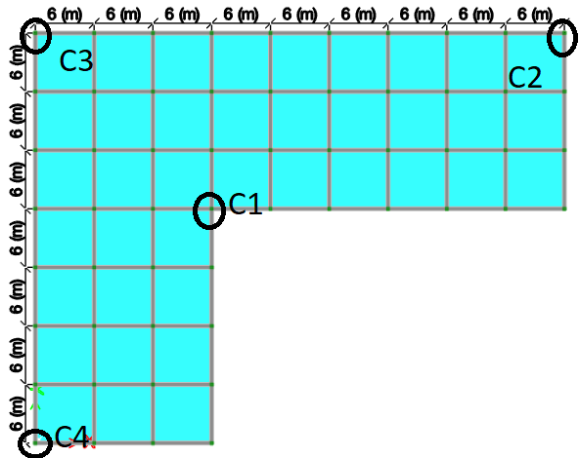

Fig. 13 Plan view with selected columns for study

5. Conclusions

The L shaped six-story building with the soft story in base level buildings are considered with and without inverted V steel braced RC buildings. A total of 12 models are considered which have been categorized into two cases, case I and case II. This study aims to understand the effect of steel bracings in irregular plan shape RC buildings. The modelling of the building is done in the ETABs software to determine the seismic parameter such as base shear, fundamental time period, maximum displacements, inter-story drift, stiffness, torsional irregularity ratio and columns forces (axial forces, moment and capacity ratio). The RSA is used in every 12 models and results are compared to each other in order to understand the effect of bracing in L shaped buildings. The followings conclusions are noticed in this study:

- As studying the effect of inverted V bracing in RC buildings the lateral base shear value is increased in the L shape buildings when the steel bracing is used. Especially in case II, the base shear value increases as increases the number of braced bays along the both directions. The fundamental time period of the structures decreased when the steel bracing used in the L shape buildings are effective.
- Providing the steel bracings in the L shaped RC buildings, reduced the maximum displacements in the buildings. The case II models shows the effective reduction of maximum displacements in the models. It is noticed that nearly 50% reductions in maximum displacements are observed as compared to the L1 model. If the bracings are provided symmetrically, it reduces the maximum displacements properly with a minimum torsional effect.
- As expected, adding the steel bracing as a retrofitting in the L shaped RC buildings, it decreased the ISD of the structures effectively if bracing is used properly. The maximum ISD of the structures is under the permissible limit (0.004 as IS suggested) is noticed. In case II, models show the minimum ISD of the structures. The maximum ISD is observed in the middle story of the structures.
- The steel bracings in the L shape buildings increase the story stiffness of the structures effectively. When the number of bays are braced, it also increased the stiffness of the buildings.

- The torsional irregularity ratios are studied in both case I and case II and it is found that case I shows an unexpected torsional effect. However, case II shows good seismic behaviors except for L12 models. As providing the steel bracing in L shape buildings (case II) shows the accepted torsional irregularity ratio. While using the steel bracings in the irregular building, the torsional irregularity ratio should check carefully.
- Column C1 shows the maximum axial forces and capacity ratio in the RC L shape structures. It is observed that incomplete adding bracing in the RC buildings affected that capacity ratio in the columns which is directly attached with bracings. In the C1 column adding steel, bracings reduced the capacity ratio in case II models. However, in C2, C3 and C4 columns, the capacity ratio of the columns increases slightly. It is also observed that adding the steel bracings in the models, increases the axial load and decreases the moment.
- As a general conclusion, it can be stated that retrofitting of 6 story L shape RC frame structures with inverted V bracing is beneficial to the structure if the position of steel bracing (L9-L12) is effectively used.
- The steel bracing is effectively used as retrofitting in L shape buildings if bracings are applied in the models appropriately. While designing irregular buildings with steel bracings, the torsional effect should be checked by the designer.

This research focuses on the effect of inverted V bracing in L shape RC structure with linear seismic response only. Therefore, the result from this study are limited to this case. However, further study is needed with nonlinear dynamic and static analysis methods. Also, it is necessary to study the interaction of columns and steel bracing connections and their effect in the overall structures. Indeed, future study is needed to ensure the ductility design of L shape RC buildings with inverted V bracing.

References

[1] Dutta SC, Mukhopadhyay PS, Saha R, Sanket N. 2011 Sikkim Earthquake at Eastern Himalayas: Lessons learnt from performance of structures. Soil Dynamics and Earthquake Engineering, 2015; 75: 121-129. https://doi.org/10.1016/j.soildyn.2015.03.020

[2] Mohammad Z, Baqi A, Arif M. Seismic Response of RC Framed Buildings Resting on Hill Slopes. Procedia Engineering, 2017; 173:1792-1799. https://doi.org/10.1016/j.proeng.2016.12.221

[3] Surana M, Meslem A, Singh Y, Lang DH, Analytical evaluation of damage probability matrices for hill-side RC buildings using different seismic intensity measures. Engineering Structures, 2020; 207: 110254. https://doi.org/10.1016/j.engstruct.2020.110254

[4] Siva Naveen E, Abraham NM, Anitha Kumar SD. Analysis of Irregular Structure under Earthquake Loads. Procedia Structural Integrity, 2019; 14: 806-819. https://doi.org/10.1016/j.prostr.2019.07.059

[5] Haque M, Ray S, Chakraborty A, Elias M, Alam I. Seismic performance analysis of RC multi-storied buildings with Plan irregularity. Am J of Civil Eng. 2016; 4(3):68-73. https://doi.org/10.11648/j.ajce.20160403.11

[6] Chopra AK, Goel RK. A modal pushover analysis procedure to estimate seismic demands for unsymmetric-plan buildings. Earthquake engineering & structural dynamics, 2004; 33(8): 903-927. https://doi.org/10.1002/eqe.380

[7] Moghadam AS, Tso WK. Pushover analysis for asymmetric and set-back multi-story buildings. In Proceedings of the 12th world conference on earthquake engineering, 2000; Vol. 1093.

[8] Sachin Maske G, Pajgade PS. Torsional behaviour of asymmetrical buildings. Int J Modern Eng Res. 2013; 3(2): 1146-9.

[9] Dya AFC, Oretaa AWC. Seismic vulnerability assessment of soft story irregular buildings using pushover analysis. Procedia Engineering, 2015; 125: 925-932. https://doi.org/10.1016/j.proeng.2015.11.103
[10] Valente M. Seismic upgrading strategies for non-ductile plan-wise irregular R/C structures. Procedia Engineering, 2013; 54: 539-553. https://doi.org/10.1016/j.proeng.2013.03.049
[11] Mazza F. Displacement-based seismic design of hysteretic damped braces for retrofitting in-plan irregular rc framed structures. Soil Dynamics and Earthquake Engineering, 2014;66:231-240. https://doi.org/10.1016/j.soildyn.2014.07.001
[12] Mazza F, Mazza M, Vulcano A. Displacement-based seismic design of hysteretic damped braces for retrofitting in-elevation irregular rc framed structures. Soil Dynamics and Earthquake Engineering, 2015; 69: 115-124. https://doi.org/10.1016/j.soildyn.2014.10.029
[13] Khanal B, Chaulagain H. Seismic elastic performance of L-shaped building frames through plan irregularities. Structures, 2020; 27: 22-36. https://doi.org/10.1016/j.istruc.2020.05.017
[14]Raheem SEA, Ahmed MMM, Ahmed MM, Abdel-shafy AGA. Evaluation of plan configuration irregularity effects on seismic response demands of L-shaped MRF buildings. Bull Earthquake Eng. 2018; 16: 3845-3869. https://doi.org/10.1007/s10518-018-0319-7
[15] Ahmed MM, Raheem SEA, Ahmed MM, Abdel-Shafy, AG. Irregularity effects on the seismic performance of L-shaped multi-story buildings. Journal of Engineering Sciences Assiut University Faculty of Engineering, 2016; 44(5): 513-536. https://doi.org/10.21608/jesaun.2016.111440
[16] Tezcan SS, Alhan C. Parametric analysis of irregular structures under seismic loading according to the new Turkish Earthquake Code. Engineering structures, 2001; 23(6): 600-609. https://doi.org/10.1016/S0141-0296(00)00084-5
[17] Özmen G, Girgin K, Durgun Y. Torsional irregularity in multi-story structures. International Journal of Advanced Structural Engineering (IJASE), 2014; 6(4): 121-131. https://doi.org/10.1007/s40091-014-0070-5
[18] Koçak A, Zengin B, Kadioğlu F. Performance assessment of irregular RC buildings with shear walls after Earthquake. Engineering Failure Analysis, 2015; 55: 157-168. https://doi.org/10.1016/j.engfailanal.2015.05.016
[19] Prajwal TP, Parvez IA, Kamath K. Nonlinear Analysis of Irregular Buildings Considering the Direction of Seismic Waves. Materials Today: Proceedings, 2017; 4(9): 9828-9832. https://doi.org/10.1016/j.matpr.2017.06.275
[20] Mahdi T, Gharaie VS. Plan Irregular Rc Frames: Comparison Of Pushover With Nonlinear Dynamic Analysis. Asian Journal Of Civil Engineering (Building And Housing), 2011; 12(6): 679-690.
[21] Giannakouras P, Zeris C. Seismic performance of irregular RC frames designed according to the DDBD approach. Engineering Structures, 2019; 182: 427-445. https://doi.org/10.1016/j.engstruct.2018.12.058
[22] Krishnan PA, Thasleen N. Seismic analysis of plan irregular RC building frames. In IOP Conference Series: Earth and Environmental Science, 2020; 491(1): 012021. https://doi.org/10.1088/1755-1315/491/1/012021
[23] Bhasker R, Menon A. Characterization of ground motion intensity for the seismic fragility assessment of plan-irregular RC buildings. Structures, 2020; 27: 1763-1776. https://doi.org/10.1016/j.istruc.2020.08.019
[24] Formisano A, Massimilla A, Di Lorenzo G, Landolfo R. Seismic retrofit of gravity load designed RC buildings using external steel concentric bracing systems. Engineering Failure Analysis, 2020; 111: 104485. https://doi.org/10.1016/j.engfailanal.2020.104485

[25] Youssef MA, Ghaffarzadeh H, Nehdi M. Seismic performance of RC frames with concentric internal steel bracing. Engineering Structures, 2007; 29: 1561-1568. https://doi.org/10.1016/j.engstruct.2006.08.027
[26] Safarizki HA, Kristiawan SA, Basuki A. Evaluation of the Use of Steel Bracing to Improve Seismic Performance of Reinforced Concrete Building. Procedia Engineering, 2013; 54: 447-456. https://doi.org/10.1016/j.proeng.2013.03.040
[27] Liu F, Wang L, Lu X. Experimental Investigations on the Seismic Performance of Un-Retrofitted and Retrofitted RC Frames. Proceedings, 15th World Conference on Earthquake Engineering, Lisbon, Portugal, 2012.
[28] Bohara BK. Seismic Response of Hill Side Step-back RC Framed Buildings with Shear Wall and Bracing System. International Journal of Structural and Construction Engineering, 2021; 15(4): 204-210.
[29] Almeida A, Ferreira R, Proença JM, Gago AS. Seismic Retrofit of RC Building Structures with Buckling Restrained Braces, Engineering Structures, 2017; 130(1): 14-22. https://doi.org/10.1016/j.engstruct.2016.09.036
[30] Rahimi A, Maheri MR. The effects of retrofitting RC frames by X-bracing on the seismic performance of columns. Engineering Structures, 2018; 73:813-830. https://doi.org/10.1016/j.engstruct.2018.07.003
[31] Rahimi A, Maheri MR. The effects of steel X-brace retrofitting of RC frames on the seismic performance of frames and their elements. Engineering Structures, 2020; 206: 110149. https://doi.org/10.1016/j.engstruct.2019.110149
[32] Godínez-Domínguez EA, Tena-Colunga A. Nonlinear Behavior of Code-Designed Reinforced Concrete Concentric Braced Frames under Lateral Loading. Engineering Structures, 2010; 32(4): 944-963. https://doi.org/10.1016/j.engstruct.2009.12.020
[33] Godínez-Domínguez EA, Arturo Tena-Colunga A. Behavior of ductile steel X-braced RC frames in seismic zones. Earthq Eng & Eng Vib. 2019; 18:845-869. https://doi.org/10.1007/s11803-019-0539-0
[34] Ganaie KH, Bohara BK, Saha P. Effects Of Inverted V Bracing In Four-Story Irregular Rc Structures. International Research Journal of Modernization in Engineering Technology and Science, 2021; 03(04): 2346-2351.
[35] Hemmati A, Kheyroddin A, Farzad M. Experimental Study of Reinforced Concrete Frame Rehabilitated by Concentric and Eccentric Bracing. *Journal of Rehabilitation in Civil Engineering*, 2020; 8(1): 97-108 https://doi.org/10.22075/JRCE.2019.16055.1301
[36] Khade RB, Kulkarni PM. Effect of Wind Load on Structural Performance of Dimensionally Regular and Irregular High rise Buildings with different Outrigger Systems. International Journal of Engineering and Management Research, 2019; 9(4): 25-29. https://doi.org/10.31033/ijemr.9.4.5
[37] Saji SM, Sreedevi L. Comparison of Seismic Analysis of Chevron Bracings in Regular and Irregular Buildings. International Journal of Engineering Research And Technology, 2017; (06): 562-565. https://doi.org/10.17577/IJERTV6IS060269
[38] Özkılıç YO. The Effects of Steel Core Imperfection, Gap Size and Friction Coefficient on the Behavior of All-Steel Buckling Restrained Braces. Düzce Üniversitesi Bilim ve Teknoloji Dergisi, 2021. Inpress. https://doi.org/10.29130/dubited.843214
[39] Di Sarno L, Manfredi G. Experimental tests on full-scale RC un-retrofitted frame and retrofitted with buckling-restrained braces, Earthquake Engineering & Structural Dynamics, 2012; 41(2):315-333. https://doi.org/10.1002/eqe.1131
[40] Di Cesare A, Ponzo FC. Seismic Retrofit of Reinforced Concrete Frame Buildings with Hysteretic Bracing Systems: Design Procedure and Behaviour Factor. Shock and Vibration, 2017. https://doi.org/10.1155/2017/2639361
[41] Aksoylu C, Sezer R. Investigation of precast new diagonal concrete panels in strengthened the infilled reinforced concrete frames. KSCE Journal of Civil Engineering, 2018; 22(1):236-246. https://doi.org/10.1007/s12205-017-1290-6

[42] Özkılıç YO, Bozkurt MB, Topkaya C. Mid-spliced end-plated replaceable links for eccentrically braced frames. Engineering Structures, 2021; 237:112225. https://doi.org/10.1016/j.engstruct.2021.112225
[43] Özkılıç YO, Topkaya C. Extended end-plate connections for replaceable shear links. Engineering Structures, 2021; 240: 112385. https://doi.org/10.1016/j.engstruct.2021.112385
[44] IS 456:2000, Indian Standard Plain and Reinforce Concrete- Code of Practice. New Delhi, bureau of Indian standard, 2000
[45] Code IS 1893 (part 1), criteria for earthquake resistant design of structures. Bureau of Indian Standards, 2016; New Delhi, India.
[46] American Society of Civil Engineers ASCE 7-10, minimum design loads for buildings and other structures, 2010; p 658.
[47] IS 13920: 2016. Ductile design and detailing of reinforced concrete structures subjected seismic forces-code of practice. 2016; New Delhi, India.

Research on Engineering Structures & Materials
journal homepage: http://www.jresm.org
Research Group

Research Article

Analysis of various flow field designs for PEM fuel cells used in vehicular systems through 3D modelling

Muhammed Mücahid Toprak[*1,a], Ceyda Kök[2,b], Suha Orçun Mert[3,c],

[1]*Yuzuncu Yıl University, Department of Chemical Engineering 65080, Kampus, Van, Turkey*
[2]*Iskenderun Technical University- ISTE, Institute of Graduate Studies, 31200 Iskenderun, Hatay, Turkey*
[3]*Iskenderun Technical University- ISTE, Department of Petroleum and Natural Gas Engineering, 31200 Iskenderun, Hatay, Turkey*

Article Info

Article history:
Received 05 Aug 2021
Revised 04 Oct 2021
Accepted 14 Oct 2021

Keywords:

Proton Exchange Membrane;
Fuel Cell;
Electric vehicles;
Modeling and Simulation;
Flow Channels;
CFD

Abstract

The importance of green energy has increased in recent years. Vehicles that don't run on fossil fuels and have zero CO_2 emissions are on the agenda of many developed countries. Battery-based vehicles have long charge times and low range problems, making hydrogen-based fuel cell vehicles a good alternative candidate as a solution. Fuel cell system designs used in these vehicles is one of the most important subjects in the dawn of the renewable energy age. The present study compares different flow channel pattern designs for PEM fuel cells used in vehicles, all of which were designed and modeled as part of the study. Simulations were run on the three-dimensional flow channel designs to determine the most efficient patterns. Efficiency analyses were extended to include the membrane surfaces, where different properties of fuel flow channels, overall energy efficiency, and certain other parameters used in the PEM fuel cell systems were investigated. The study also includes comparison of the designed systems with fuel cell designs currently in commercial use. Finally, the effects of H_2 and O_2 concentrations used in the system were also investigated.

1. Introduction

Energy is a factor that affects the transportation, economy and infrastructure of all developed and developing countries, which in turn greatly influence the living standards of their citizens. The amount of energy required to sustain our civilization is gradually increasing, hand to hand with the technological developments. This energy, however, is mostly supplied through consumption of fossil fuels, which are not sustainable energy sources. Moreover, the rapid depletion of non-renewable energy sources seems to be unstoppable. For this reason, the issue of energy production from renewable energy sources is discussed at international scales by both industrial and scientific communities.

Almost the all of transportation sector uses fossil fuels. Energy Information Administration (EIA) 2014 report shows that 55% of total energy consumption in the world and 30.9% of carbon dioxide gas emissions are in the transportation sector [1]. Figure 1 seems that the CO_2 emissions of the transportation sector in 1990-2015. CO_2 emissions increased from 3.3 gigatonnes (Gt) to 6 Gt for twenty-five years and increased almost 68%.

[*]Corresponding author: orcun.mert@iste.edu.tr
[a] orcid.org/0000-0002-2409-7260; [b] orcid.org/0000-0002-5536-3488; [c] orcid.org/0000-0002-7721-1629
DOI: http://dx.doi.org/10.17515/resm2021.328en0805

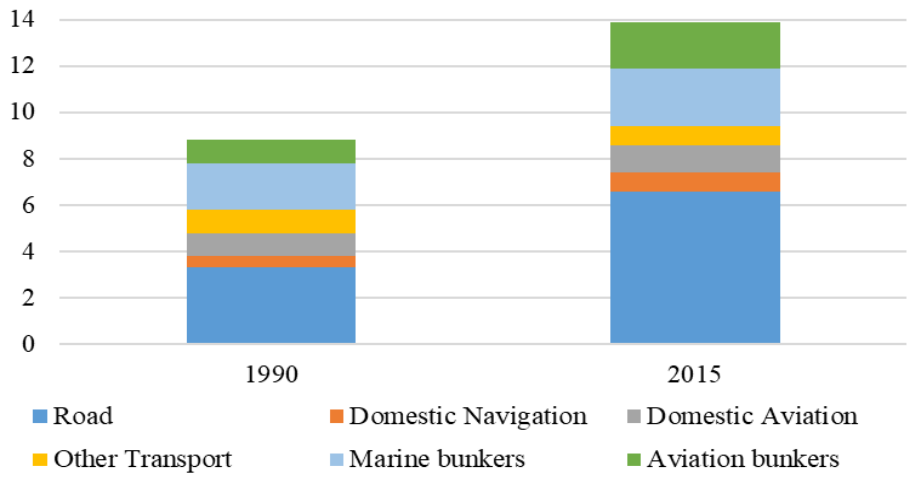

Fig. 1 CO_2 emissions of the transportation sector in 1990-2015 [2]

Interest in new, innovative and green energy sources has increased further in recent years due to the decrease in the amount of non-renewable energy resources. The living standards of developed and developing countries are on a steady increase, which usually is reflected as increased energy demands. There are also environmental concerns with the use of non-renewable energy sources. These developments have placed environmentally-friendly vehicles that do not run on fossil fuels on the agenda of many countries. Scientists have developed and proposed Electric and Hybrid Electric Vehicles (EV's and HEV's, respectively) to alleviate these problems. Lithium Ion (Li-ion) batteries which are used in these vehicles have many advantages such as long shelf life, wide working range, high power and energy density. Yet they also have certain disadvantages such as long charging times and low average ranges. As an alternative to these vehicles, fuel cell vehicles that can store energy in shorter times and offer have a longer range compared to other vehicles have been proposed. It is envisaged that hydrogen can overcome the disadvantages of other vehicles and is a prime candidate as the transportation fuel of the future [3].

There are many reasons to use hydrogen in fuel cell vehicles. The primary advantage of hydrogen lies in its molecular structure, as hydrogen has the simplest form of all molecules. While its energy content per unit volume is relatively low, its energy content per unit weight is the highest amongst all molecules. Unlike fossil fuels, it creates zero emissions when used [4]. Due to these features it has been used in different types of fuel cells and to fuel different types of rockets.

A fuel cell can convert the chemical energy stored in the fuel into electrical energy with a very efficient process that can reach efficiency values as high as 80%. In addition, fuel cells do not emit CO_2 during this process and instead release only water as a by-product. Fuel cells that do not use fossil fuels and do not create emissions are considered environmentally friendly.

Numerous studies have been performed on fuel cells, which lead to improvements in hydrogen applications in the transportation sector. Leading car manufacturers in the industry are now producing fuel cell vehicles, which are mainly available in North America, Asia and Europe. As of June 2018, more than 6500 fuel cell vehicles are reportedly sold. California has the world's largest hydrogen fuel station network, and is a leader in

hydrogen based vehicles where the country delivers 3000 of the 5233 vehicles produced worldwide [5].

Both electric vehicles and fuel cell vehicles have zero CO_2 emissions, and both types of vehicles are environmentally friendly as they use renewable and sustainable energy sources as fuel. The main difference between the two, however, is in refueling and driving distance aspects. Fuel cell vehicles can refuel in less than 10 minutes and offer a driving range of 300 miles on average. It is believed that these vehicles will begin compete in these aspects with conventional fossil fuel vehicles after 2030 [4]. The long-term powertrain scenario is given in Figure 2. According to the figure, International Energy Agency (IEA) estimates that by 2050, the market share of fuel cell vehicles will be 17% with an annual sales of 35 million.

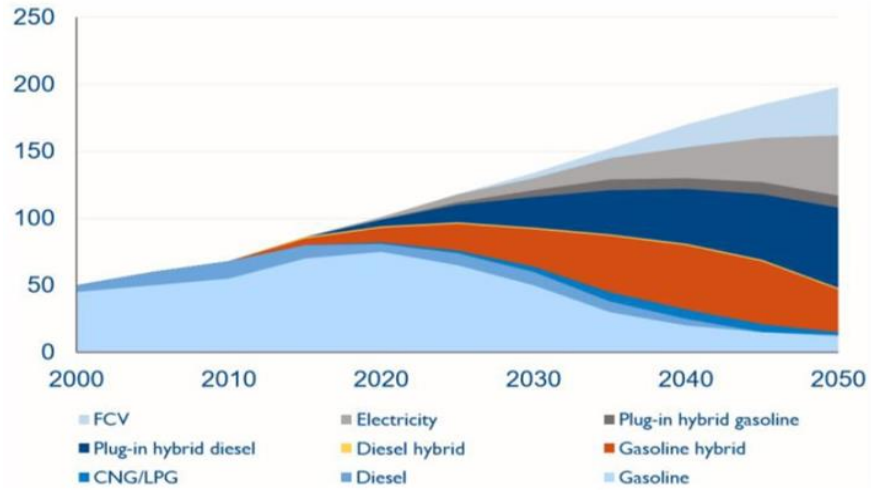

Fig. 2 The long-term scenario of sales [6]

Proton Exchange Membrane (PEM) fuel cell is preferred in fuel cell vehicles that are considered as vehicles of the future. A PEM fuel cell consists of electrodes, flow plates and current collectors. Increasing the fuel cell efficiency and reducing the production costs will make vehicles that use PEM cells preferable. That being said, increasing the efficiency and ensuring a homogeneous reaction rate on the entirety of the catalyst area can only be achieved with the optimum distribution of temperature, concentration, and humidity. This, in turn, can only be achieved by ensuring a homogeneous distribution in the flow plates.

The effect of the flow-field design on PEM fuel battery performance is in the literature. Manso et al. have studied parameters of the types of flow fields, such as width, depth, height, and so on. They also observed the effect of the non-uniform distribution of gases and water on performance. [7]. In flow-field designs, the performance impact of the non-uniform distribution of pressure drop and current density was examined by Fahim et al. [8]. The effects of conventional, serpentine and pin type channel configuration on cell performance were investigated by Pal et al. [9]. Vijay examined the design of serpantin and parallel Z-type flow channel geometry on PEM fuel battery cell performance using CFD modeling simulation [10]. Using the CFD program, the PEM fuel cell with single, double and triple serpentine flow channels and a round-angle active area was designed by Velisela et al. [11]. Shen et al. investigated the performance in the PEM fuel cell by designing parallel, single serpentine and pressurized parallel flow fields to provide a more uniform gas and water distribution [12]. Optimized 3D flow channels have been developed to provide

better flow and mass transfer in the channels [13]. To examine the performance effect of flow channels in a PEM fuel cell, the lung and leaf branches were designed by Badduri et al. [14]. Liao et al. have designed zigzag and straight flow channels for uniform distribution in the PEM fuel cell and examined in terms of their performance [15].

In the present study, six different three-dimensional flow channels were designed with the Comsol multiphysics program, which uses the finite element method for PEM fuel cell. The efficiency analysis of the designed flow channels on the membrane surfaces was made. Energy efficiency of existing designs and proposed designs were compared. This study brings a detailed and comprehensive inner look to the various fuel cell flow field designs that are either currently being used or have the potential to be used in the future for transportation applications. The verified model [16] and simulation covers the concentrations for both of the hydrogen and oxygen inputs, as well as the water content that would flow through the channels and fuel cell, resulting in specific designs. Investigation of the "current density" in different slices was also performed, providing an important perspective for the researchers interested in this property.

2. Fuel Cell

Fuel cells are in essence systems where an electrochemical reaction taking place between an oxidant and a suitable fuel produces electrical energy. These are, therefore, systems that convert the stored chemical energy inside the fuel into electrical energy. This conversion is a result of an reaction that can best be described as the opposite of an electrolysis reaction, and a fuel cell system produces Direct Current (DC) as a result of it. In that regard fuel cells are quite similar to ordinary batteries and accumulators, as they also produce electricity out of an electrochemical process through an electrochemical reaction. The difference, however, lies in the fact that batteries and accumulators are limited with the initial energy stored in them [17], [18], while fuel cells can perform the reaction continuously and infinitely on the condition that they are supplied further fuel and air [19].

Fuel cells are divided into 6 different groups based on their operating temperatures and chemical properties. These are: the Proton Exchange Membrane / Polymer Electrolyte Membrane Fuel Cell (PEMFC), Alkaline Fuel Cell (AFC), Phosphoric Acid Fuel Cell (PAFC), Molten Carbonate Fuel Cell (MCFC), Solid Oxide Fuel Cell (SOFC), and Direct Methanol Fuel Cell (DMFC). Figure 3 shows the areas where these fuel cells are used according to their operating temperatures and power characteristics.

Based on their operating temperatures and power levels, DMFC, AFC, PAFC and PEMFC are considered "low temperature fuel cells", and are generally used in mobile phones, electronic tablets, and transportation. SOFC and MCFC are used in constant power generation and Combined Heat and Power (CHP) applications, as they are high temperature fuel cells and with high power levels.

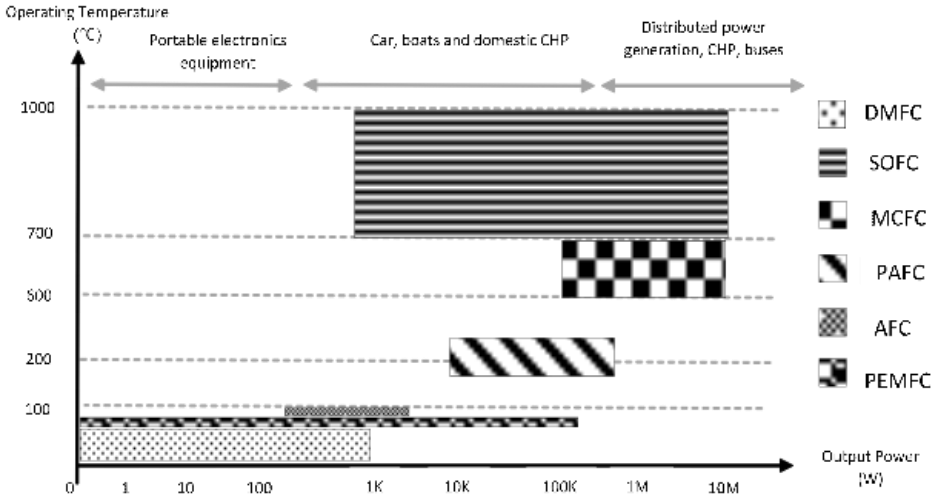

Fig. 3 Fuel cell types according to the operating temperature and power range (adapted) [20].

2.1. Proton Exchange Membrane Fuel Cell

A "Proton Exchange Membrane Fuel Cell" (PEM) is one of the most well thought-out fuel cell designs in terms operational variables. PEM fuel cells have a solid polymer electrolyte membrane which is placed between platinum-catalyzed electrolytes that are porous in structure. This setup provides it with more power density compared to other fuel cells, while reducing its physical volume and weight. The proton-permeable polymer membrane used in PEM cells as the electrolyte is also thinner in structure, where the thickness is measured in micron levels.

PEM cells have quite approachable operational temperatures that are almost always below 100 °C, generally at a ballpark between 60 °C and 80 °C. These cells also use a noble metal –often platinum- as the catalyst, which is quite an advantage in terms of operational properties but increases the production cost. Another disadvantage is the requirement of separation of carbon dioxide from the fuel input, as the platinum catalyst is quite sensitive to it. The separation process also increases the production and operational costs associated with the PEM cells. Different designs suggest the use of platinum/ruthenium catalysts to overcome these shortcomings as this combination is much more durable against carbon monoxide.

The equations provided below show the PEM fuel cell reactions taking place during each cycle: [21]

- Anode Reaction: $2H_2 \rightarrow 4H^+ + 4e^-$
- Cathode Reaction: $4H^+ + 4e^- + ½\ O_2 \rightarrow 2H_2O$
- Total Reaction: $2H_2 + O_2 \rightarrow 2H_2O$ + Electric energy

The working principle of PEMFC fuel cell is given in Figure 4.

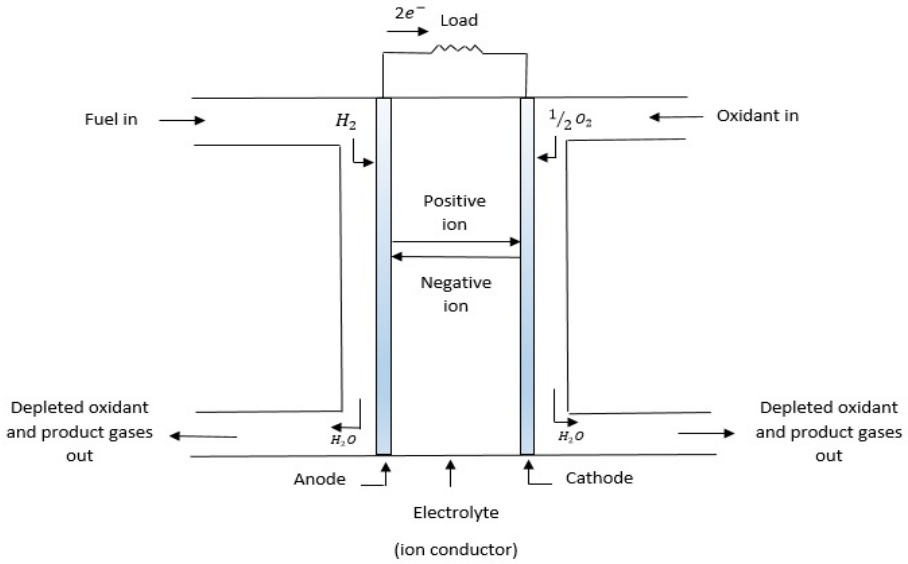

Fig. 4 The working principle of PEMFC fuel cell (adapted) [22]

As can be seen in Figure 4 this fuel cell consists of an anode, a cathode and the electrode. In this design pure hydrogen is used as the fuel, which is fed into the anode. Air (or based on the design, pure oxygen) on the other hand, is fed through the cathode. As the gas passes through the electrolyte membrane on the anode, it decomposes into its electrons. The membrane acts as a filter that separate electrons and hydrogen ions in this process, allowing only the hydrogen ions to pass. The hydrogen ions then combine with oxygen in the cathode compartment to form water molecules (H_2O), through which the reaction heat is released. While in internal combustion engines air and fuel get mixed, in the fuel cell the fuel and the oxidant are separated from each other. Due to this simple difference of operation, fuel cells produce no harmful emissions as internal combustion engines do [23]. This is one of the main reasons why they are preferred in environmentally friendly vehicle designs.

Although there are various types of fuel cells, PEMFC is the most type suitable for vehicles according to scientific works. The fuel cells used an electric vehicle replace the internal combustion engines. Hybrid vehicles that can compete with both electric and conventional vehicles are designed through using PEMFCs with rechargeable batteries. Figure 5 shows the basic design of a fuel-cell electric vehicle.

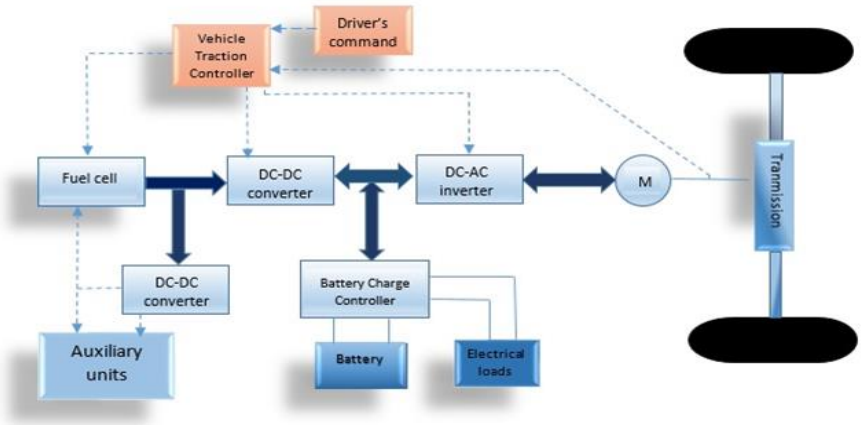

Fig. 5 The basic structure of fuel cell electric vehicles (adapted) [24]

2.2. Performance of the Fuel Cell

The performance of a given fuel cell is based on the performances the performance of the systems that make it up. The performance is primarily tied to the reaction that takes place on the catalyst. The collection of electrons that create the current, the transfer of the hydrogen ions through membrane, and the production of the water as a final product of the combustion reaction all factor into the performance. Finally, the electrical resistances of the components used within the fuel cell also contribute to the performance.

The system of a PEM cell is rather complex and consists of the interactions between numerous chemical and thermodynamic processes. This results in a final performance of the fuel cell that is closely tied to the operating conditions. The most influential operating conditions that influence the fuel cell performance are listed below:

- Temperature
- Pressure
- Membrane thickness
- Humidity
- Current Density

It is important to ensure that the reaction taking place on the catalyst surface is uniform to reach the optimum performance levels. This uniformity is dependent on numerous different parameters the temperature, humidity, and reactant concentration throughout the flow plates. Considering this, 3D models of the investigated flow plate charts were created, and the reactions were simulated to search for the more effective distribution patterns. The results of these simulations were then interpreted to measure the expected performance of different fuel cell designs under different environmental parameters like temperature, concentrations, and humidity.

3. Materials and Methods

3.1. Comsol Multiphysics Simulations

Multiphysics software, which includes a multi-physics infrastructure to run different simulations on the modeled equipment for engineering purposes [25]. The software runs simulations that provide relatively quick results due to having different physical interfaces

being already pre-modeled in it, which cover fluid-flow, electromagnetism, and structural mechanics equations [26]. These pre-defined interfaces that come with the software make it a functional tool to use in solution of different mainstream problems.

The software also has a series of modules that can run near real-like simulations with finite element method simulations. Comsol Multiphysics can model any geometry using different types of materials that can be selected from a built-in library that contains different parameters required to simulate systems that use them. The users can also model their own materials in terms of relative functions. It is possible to work on a single physical geometry, or to simulate numerous geometries that interact with each other in one or more problem steps. Once the system is meticulously modeled using these existing libraries or user entries, simulations can be run to reach multiple potential results or solutions when needed [27].

3.2. Models for the Thermodynamics and Electrochemical Properties of Fuel Cells

Evaluation of the fuel cell performance and analysis of factors that influence it are based on the laws of thermodynamics [28]. Accordingly, it is possible to define the physical volume control limit as the physical area of the investigated system (the fuel cell in this case), and the corresponding equation for energy analysis can simply be defined as the following (Equation 1):

$$Q - W = \Delta H \tag{1}$$

Where; (ΔH) represents enthalpy change, Q is heat and W is work. If there are no irreversible reactions taking place inside a system, the maximum amount of voltage that can be reached with a fuel cell equals the performance and efficiency of the reversible processes in the system, which can be expressed with a Nernst equation. Specifically designed Nernst equations are provided below considering the use cases for the designed cells as part of this study (Eqn. 2).

$$V_{rev} = 1.229 - 8.5 \cdot 10^{-4}(T_{FC} - 298.25) + 4.3085 \cdot 10^{-5} \cdot T_{FC}\left[\ln\left(p_{H_2}\right) + \frac{1}{2}\ln\left(p_{O_2}\right)\right] \tag{2}$$

Where; V_{rev} is the reversible cell voltage and T_{FC} is the cell reaction temperature. In the above equation, hydrogen and oxygen pressures can be determined using the following:

$$p_{H_2} = \frac{1 - x_{H_2O,A}}{1 + (x_A / 2)(1 + \xi_A /(\xi_A - 1))} \cdot P_A \tag{3}$$

$$p_{O_2} = \frac{1 - x_{H_2O,C}}{1 + (x_C / 2)(1 + \xi_C /(\xi_C - 1))} \cdot P_C \tag{4}$$

For equations (3) and (4), p_{H_2} and p_{O_2} hydrogen and oxygen partial pressures, x_{H_2O}, x_A, and x_C denote mole fraction of water, mole fraction of the anode, and for the cathode dry gas, respectively. Anode and cathode stoichiometric constants are denoted by ξ_A ,$\xi_C \xi_C \xi_C$. P_A,P_C are the anode andcathode pressures in atm, respectively.

Actual operational voltages of a given fuel cell can be determined by determining the amount of "irreversibility" first, which are based on the inefficiencies identified in the

system. This amount is then deduced from the total reversible system voltage, as provided in equation 5 below.

$$V_{opr} = V_{rev} - V_{irrev} \tag{5}$$

The irreversibilities of a fuel cell system can be categorized in three main groups as "activation", "ohmic", and "concentration" irreversibilities [29]–[31]. These are represented in the equation below (Equation 6).

$$V_{Irrev} = V_{act} + V_{ohm} + V_{con} \tag{6}$$

"Activation losses" occur in low reaction rates, which are teoretically expressed and determined using equations 7 and 8 provided below:

$$vact, Anode = \frac{RT_{FC}}{\alpha_A nF} ln\ ln\ \left(\frac{i}{i_0}\right) \tag{7}$$

$$vact, Cathode = \frac{RT_{FC}}{\alpha_C nF} ln\ ln\ \left(\frac{i}{i_0}\right) \tag{8}$$

Where i is current density (A cm^{-2}); i_0 is exchange current density (A cm^{-2}); R is the universal gas constant (J $(kmol\ K)^{-1}$); n is the number electrons involved; F is the Faraday's constant (C $mole^{-1}$); n is number of electron involved α_A and α_C are the empirically determined electron transfer coefficient of the reaction at the electrodes at the anode and cathode.

Certain amount of voltage is expected to be lost, resulting in further inefficiency, due to the electrical resistances of the elements used in the production of the fuel cell. The amount of the voltage lost increases as the density of the current drawn from the system increases. According to the literature [16], [32], this loss can be accounted for using the following equations (eqn. 9-13):

$$v_{ohm} = i\, R_{ohm} \tag{9}$$

$$R_{ohm} = \frac{t_{mem}}{\sigma_{mem}} \tag{10}$$

$$\sigma_{mem} = \left(0.005139\, \lambda_{mem} - 0.00326\right) \times \exp\left[1268\, \frac{1}{303} - \frac{1}{T_{FC}}\right] \tag{11}$$

Membrane humidity is determined from the membrane water activity, a, from the following equation;

$$\lambda_{mem} = \begin{Bmatrix} 0.043 + 17.81a - 39.85a^2 + 39.85a^3\ , \\ 0 < a \le 1 \\ 14 + 1.4(a-1) \\ 1 < a \le 3 \end{Bmatrix} \tag{12}$$

$$a = \frac{x_{H_2O} P}{P_{sat}} \tag{13}$$

Where; σ_{mem} corresponds to the conductivity of the membrane ($1\Omega^{-1}cm^{-1}$), while λ_{mem} corresponds to the amount of water inside the membrane. t_{mem} is membrane thickness, x_{H_2O} denotes the mole fraction of the water. P_{sat} is saturation pressure.

Concentration over-potential is caused by a high rate of reaction due to the fact that the concentration tends to drop sharply, which particularly true for higher current densities. Homogenous distribution of the gas flow is important to reduce or prevent any such potential concentrations drops.

$$v_{conc} = i\left(\beta_1 \frac{i}{i_{max}}\right)^{\beta_2} \tag{14}$$

$$\beta_1 = \begin{cases} if \ \frac{p_{O_2}}{0.1173} + P_{sat} < 2 \\ (7.16 \cdot 10^{-4} T_{FC} - 0.622)(\frac{p_{O_2}}{0.1173} + P_{sat}) + \\ (-1.45 \cdot 10^{-3} T_{FC} + 1.68) \\ else \\ (8.66 \cdot 10^{-5} T_{FC} - 0.068)(\frac{p_{O_2}}{0.1173} + P_{sat}) + \\ (-1.6 \cdot 10^{-4} + 0.54) \end{cases} \tag{15}$$

Equations 14 and 15 have contain constants such as β_1, β_2 and i_{max}, all of which are well-defined by the literature and are resolved using empirical equations. The conditions and assumptions stated in the models are taken from the doctoral thesis [33].

4. Results and Discussion

The present study provides the designs for a total of six different fuel cells and their respective analyzes, all of which were performed with COMSOL Multiphysics software. The following section contains information regarding the results of these analyses and their graphical interpretations.

During the modeling, the total area of active membranes was arranged to be the same for all models, and the channels within the plates were roughly set to be the same size. The primary aim during the design of the plates was the homogeneously fuel distribution over the surface. The models are generated depending on the formations already used in the literature and the formations that seems to be potential.

Voltage levels applied on the designed fuel cells were also kept constant (0.5V-0.9V). Channel widths and heights were kept constant as well to ensure a consistent comparison of parameters at an equal setting. This also had the benefit of resulting in same pressure drops and flow rates for the fuel cells.

The verification of the findings of the study was performed by comparing the results of the simulations with the previous studies, especially Mert et al, 2007-2011 [16], [31] and found that the simulation model is in a good harmony with the model that already verified by experimental studies.

Figure 6 displays 3D models of the designed flow plates. Detailed configuration and properties for each design is provided in detail in its own section below.

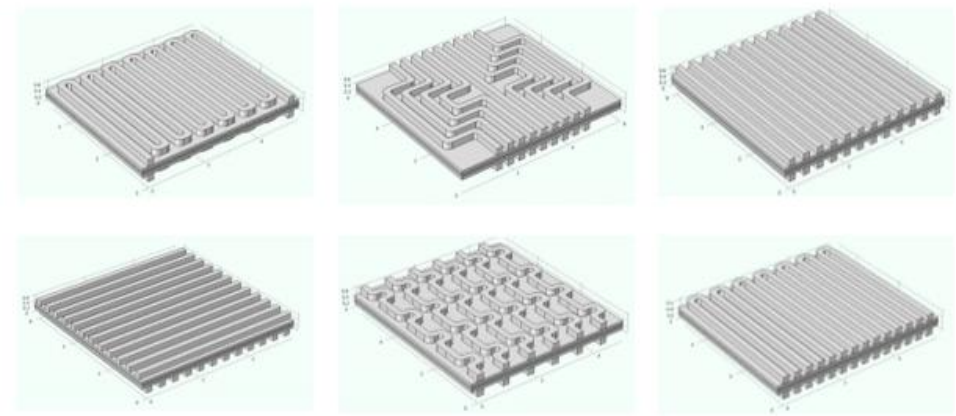

Fig. 6 3D models of the 6 different designs

4.1. Design 1

In the design 1, a model spread over the 13-curve area with a single entrance and exit in the classical S form was selected and examined. Channels with a surface area of 52.98 cm^2 and a volume of 2.661 cm^3 have been completed on anode and cathode plates with a total surface area of 59.62 cm^2 and a total volume of 2.175 cm^3.

The parameters necessary to simulate the fuel cell operation were then configured into the system, and the "3D Mesh" property of the software was used to perform the further studies on the design. The 3D mesh of the model can be seen in Figure 7.. This mesh was the basis for the future analysis.

Fig. 7 3D mesh view of 13 Curve Fuel Cell

The network structure of the designed fuel cell is given in 3D as shown in Figure 7. In the solution network a total of 1.510.434 four-surfaces (Tetrahedral), 53.919 pyramids, 474.059 prisms, 296.911 triangle elements were used, enhanced with corner refinement and boundary layers auxiliary elements. The smallest element size was 0,0034 cm, while the average element size was 0,63 cm.

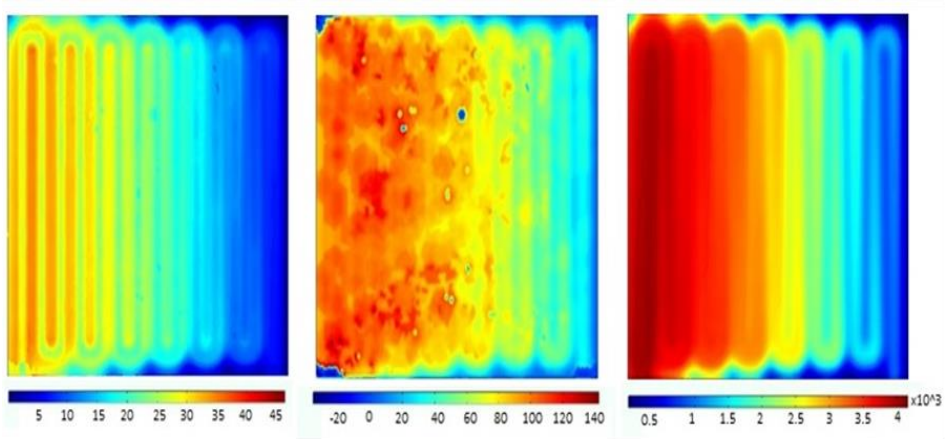

(a) (b) (c)

Fig. 8 2D Membrane Current Density (a) 0,2975 cm (b) 0,3175 cm (c) 0,3375 cm

Depending on the thickness of the membrane in the fuel cell, the current density distribution in the constant working voltage range (0.5 V) is shown in Figure 8. The red color represents high current density, while the blue color represents low current density. The effect of current density on the membrane is shown graphically in the region where the membrane shown in the Figure 8 (a) is 0,2975 cm in the y-axis. In this relatively close formation channel, the effect of the channel on the current density is strikingly visible. As expected, the current density is high in the input zone due to its high reaction rate and decreases gradually towards the output area. In all images of Figure 8, due to the increasing consumption of reactants, the current density decreases gradually along the gas flow direction. Therefore, it is observed that the current density increases as the membrane thickness increases, but it is far from the desired homogeneity.

The effect of the current density on the membrane is shown graphically at the mid-point where the thickness of the membrane shown in the Figure 8 (b) is determined as 0,3175 cm. Depending on the duct design, the distribution of the inlet region is somewhat spread, but an uneven current density and reaction rate are still observed.

The current density distribution is shown in Figure 8 (c). The y axis of the membrane shown in the figure is determined as 0,33375 cm and the effect of current density on the membrane is shown graphically. As seen in the graphs, current density values vary depending on the thickness of the membrane used in the fuel cell.

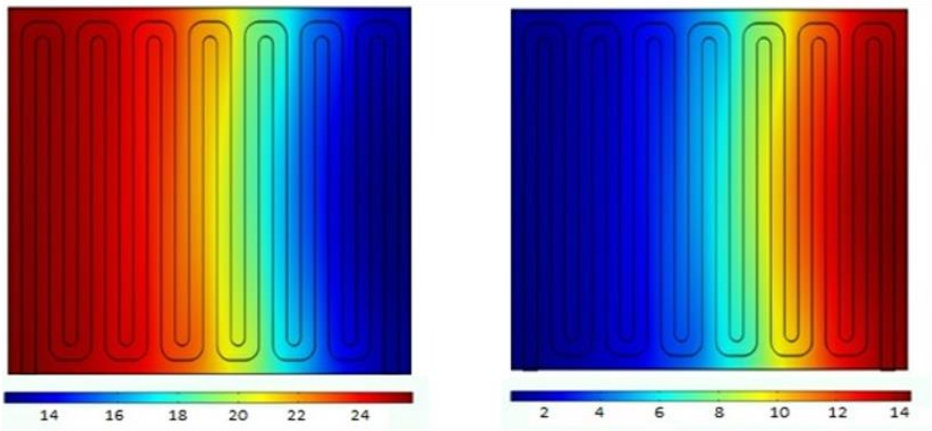

Fig. 9 Distribution of the (a) hydrogen concentration (b) water concentration in the x-y plane of the anode side

The anode reaction that takes place at the system, and the changes on the hydrogen concentration, can be observed in Figure 9 (a). As can be seen, H_2 concentration declines in the +x direction, while the formation of water increases. While hydrogen density is 24 mol/m^3 at the inlet, it decreases to 14 mol/m^3 towards the outlet.

Figure 9 (b) displays the anode reaction and the change in water concentration parameter over the course of the flow channels. The water concentration evidently rises in the + x axis. Considering this information in line with the information from the previous figure, it can be seen that the water formation is almost in parallel with H_2 formation in terms of actual amounts produced. In that regard this system can be considered quite efficient. Concentration graph also shows that the water content increased from 2 mol/m^3 to 14 mol/m^3 during the course of the plate.

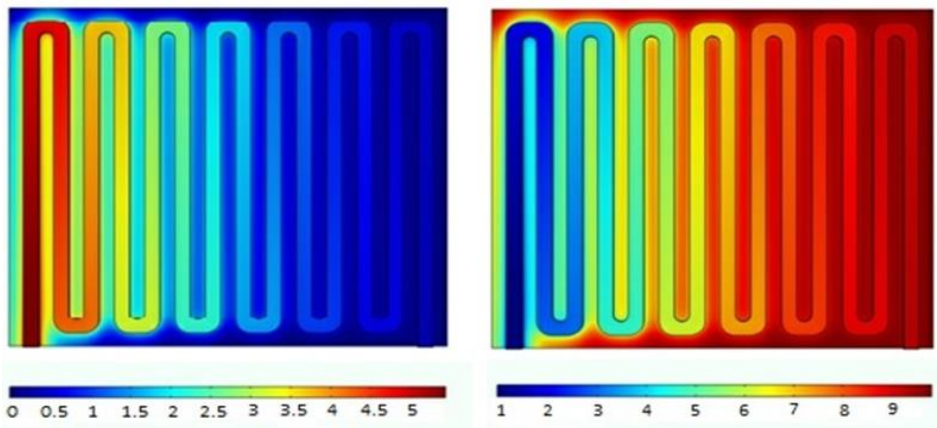

Fig. 10 (a) oxygen concentration and (b) water concentration graphs for the cathode side

Figure 10 (a) displays the change in the oxygen concentration over the course of the plate during the cathode reaction. As is evident, oxygen concentration decreases as the gas flows further, which happens due to the consumption of reactants by electrochemical reactions.

While the oxygen concentration was 5 mol/m^3 at the inlet, it decreased to 0.5 mol/m^3 at the outlet.

Figure 10 (b), on the other hand, displays the change in water concentration over the course of the plate during the cathode reaction. It can be seen here that the water concentration increases towards the later stages of the flow, and the amount of water generated is roughly equal to the amount of O_2 consumed. This is evidence for an efficient system. When looking at the concentration change graph of water, it was observed that it increased from 1 mol/m^3 to 9 mol/m^3.

For the following section, the results will similarly be evaluated for 2D membrane current density and the distribution of the anode and cathode side water concentrations in the x-y plane.

4.2. Design 2

Design 2 is formed as 9 input-output diamond-shaped channel formation. The channels with a surface area of 61.12 cm^2 and a volume of 2.863 cm^3 are designed on anode and cathode plates with a surface area of 69.08 cm^2 and 2.173 volume of cm^3. In the network structure of the flow plate designed by Tetrahedral prisms, 304.527 triangular elements, corner refinement and boundary layers auxiliary elements were also used in the solution using 66.732 pyramids, 587.451. The smallest element size is 0,0039 cm, and the average element size is 0,52 cm.

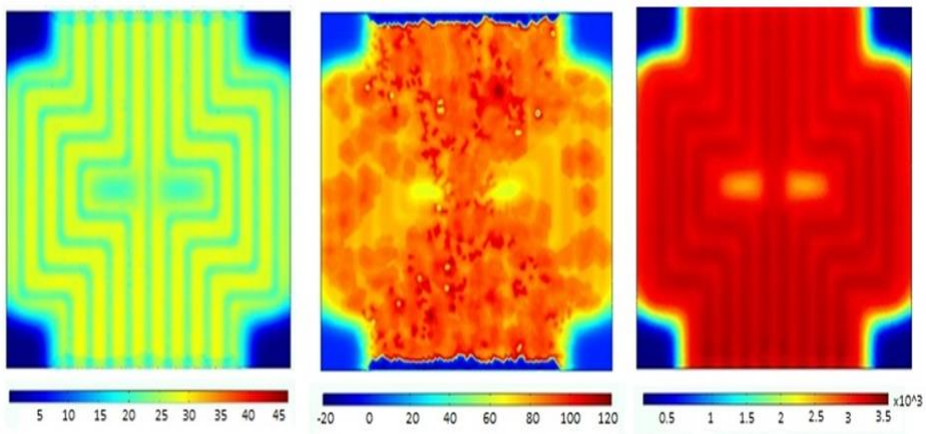

(a) (b) (c)

Fig. 11 2D Membrane Current Density (a) 0,2975 cm (b) 0,3175 cm (c) 0,3375 cm

The current density distribution of the membrane in the fuel cell depending on the y dimension is provided in Figure 11. It is visible that an accumulation occurs in the +Y axis, particularly towards the middle sections. Compared to the first design, this flow plate can be said to have a lower efficiency, mostly caused by the dead zones located at the four corners. The remianing section of the fuel cell system, however, remains at higher rates when compared to the other designs due to the dense channel formation it has. Although it is more homogeneous than Design 1, it shows lower performance due to inefficient areas in the corners.

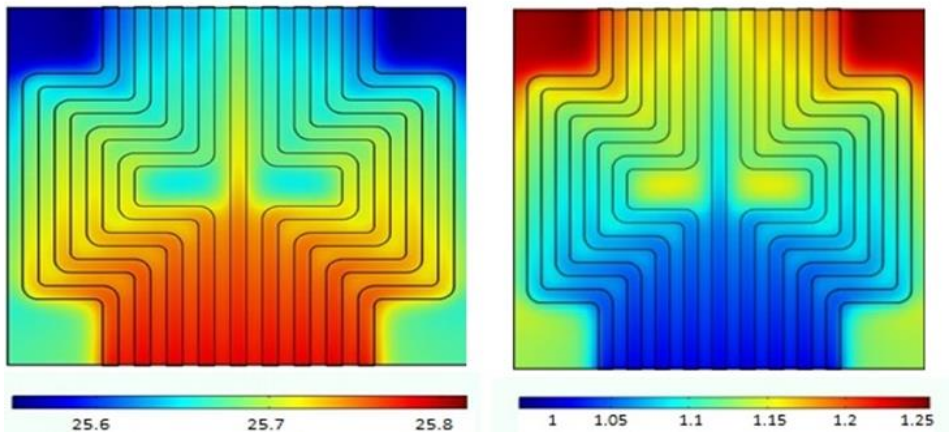

(a) (b)

Fig. 12 Distribution of the (a) hydrogen concentration (b) water concentration in the x-y plane of the anode side.

Figure 12 (a) shows the change of hydrogen concentration in the reaction taking place at constant working voltage (0.55 V) on the anode side. Since hydrogen is consumed during the reaction, it is seen that the hydrogen gradually decreases towards the gas flow direction. While hydrogen density was 25.8 mol/m^3 at the inlet, it decreased to 25.65 mol/m^3 towards the outlet. According to Design 1, it can be said that it is an inefficient design since the use of hydrogen is very low.

Figure 12 (b) shows the change of water concentration in the reaction taking place at constant working voltage (0.55 V) on the anode side. According to the water concentration change graph, it was observed that it increased from 1 mol/m^3 to 1.23 mol/m^3. The water concentration change was very low. So, this design may generally considered to be inefficient.

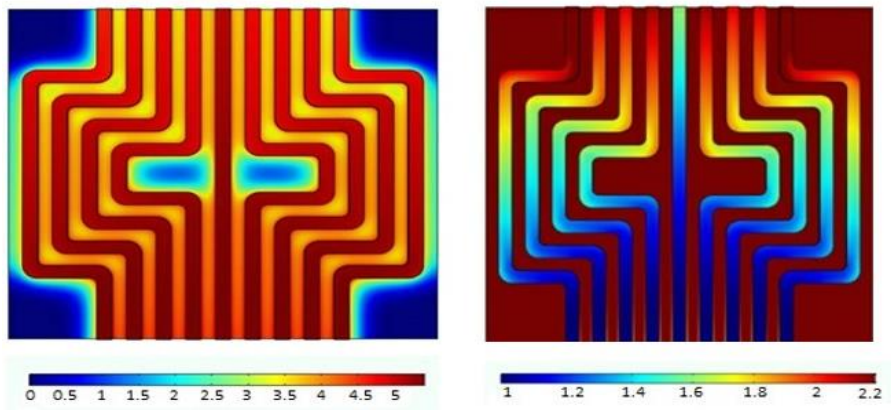

(a) (b)

Fig. 13 Distribution of the (a) oxygen concentration (b) water concentration in the x-y plane of the cathode side

The concentration change of the reaction that took place in the cathode half reaction is shown in Figure 13(a). As with the anode half reaction, it was observed that the concentration change was low in the cathode half reaction. It can be said that the geometry of the flow plate is not suitable for efficiency. Oxygen was 5 mol/m^3 at the inlet but decreased to 4.5 mol/m^3 at the outlet. Similar to the anode side, small changes have also occurred on the cathode side. Thus, it was seen that design 2 was quite inefficient compared to Design 1.

Figure 13 (b) shows the amount of water generation in relation with the O_2 amount on the cathode side. While water is also generated in the cathode side of the fuel cell, the amount of generated is comparatively small. According to the water concentration change graph, it was observed that it increased from 1 mol/m^3 to 2.2 mol/m^3, which amounts to a minor amount of change. This small amount is indicative of adverse effects in action on the plate, as further evidenced by formation of the undesired water. This particular flow plate design, therefore, can be said to have a low overall efficiency.

4.3. Design 3

With 12 straight inputs and outputs Design 3 has Channels with a surface area of 58.56 cm^2 and a volume of 2.88 cm^3 are designed on anode and cathode plates with a surface area of 73.8 cm^2 and 2.7 volume of cm^3.

In the network structure of the flow plate there are 1.221.031 four-surface (Tetrahedral), 49.813 pyramids, 447.719 prisms, 284.545 triangle elements, corner refinement and boundary layers auxiliary elements are also used for different flow channels. The smallest element size is 0,0023 cm, while the average element size is selected as 0,50 cm.

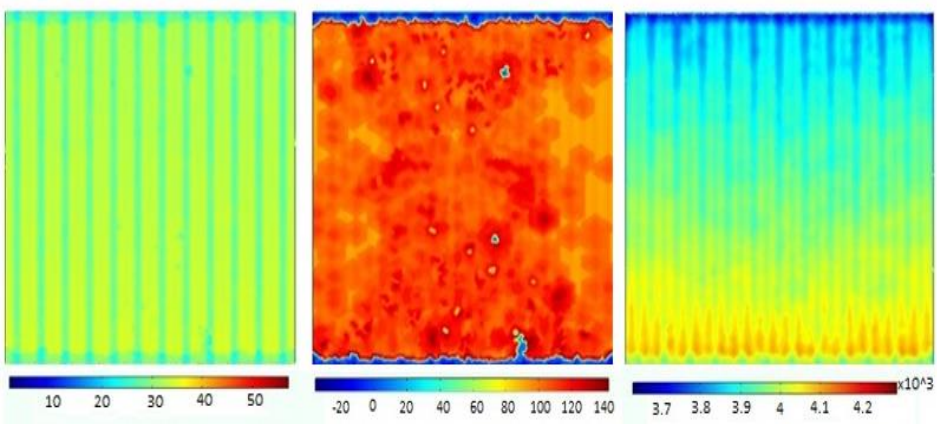

(a) (b) (c)

Fig. 14 2D Membrane Current Density (a) 0,2975 cm (b) 0,3175 cm (c) 0,3375 cm

The current density for the membrane of third design is provided Figure 14 . While the membrane thickness increased, the current density was found to stay homogeneous on all surfaces. Design 3 shows a more homogeneous distribution than Design 1. Since there are no inefficient regions in this design, the design is more positive than the Design 2. It can be said that it is more efficient Designs 1 and 2.

Figure 15 (a) shows the change of hydrogen concentration in the reaction taking place at constant working voltage (0.5 V) on the anode side. While hydrogen density was 25.8 mol/m^3 at the inlet, it decreased to 25.65 mol/m^3 towards the outlet. Although the use of

hydrogen is lower in this design, it can be said that the Design 2 is more efficient because of its wider activity area. Figure 15 (b) shows that water generation increased from 1 mol/m^3 to 1.25 mol/m^3, as can be seen in the water concentration change graph. The water concentration change is very low, but the design can still be considered "efficient" since it's active on all surfaces.

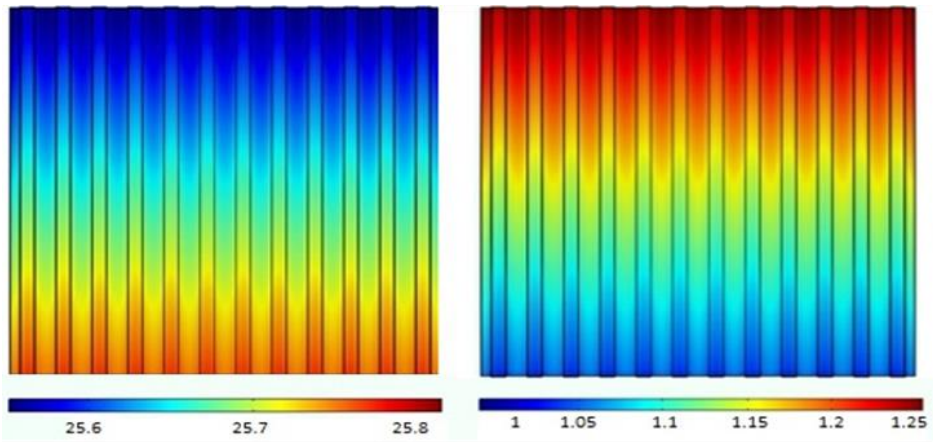

(a) (b)

Fig. 15 Distribution of the (a) hydrogen concentration (b) water concentration in the x-y plane of the anode side.

Oxygen concentration was 3.5 mol/m^3 at the inlet (Figure 16(a)), but decreased to 2.5 mol/m^3 at the outlet. Small changes were found to occur on the cathode side as well as on the anode side. As can be seen in Figure 16 (b), however, the water concentration changes from 3.5 mol/m^3 to 5.5 mol/m^3.

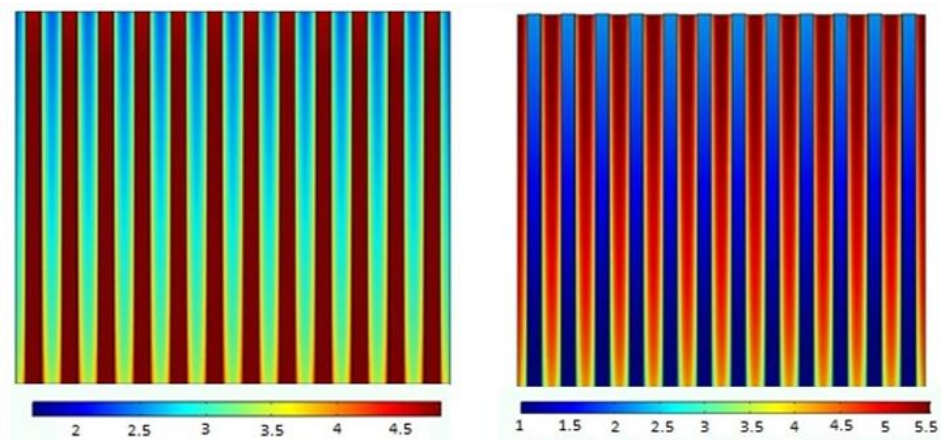

(a) (b)

Fig. 16 Distribution of the (a) oxygen concentration (b) water concentration in the x-y plane of the cathode side.

When the anode and cathode reactant concentrations are examined, the positive effect of multiple inputs can be observed as evidenced in Figure 15 and 16. The reaction is

monitored over a wider active area and at high concentrations. Fuel cell water management is also considered to be more easily applicable in this design.

4.4. Design 4

Design 4 composed of 12 reverse-straight inputs and outputs. Channels with a surface area of 58.56 cm^2 and a volume of 2.88 cm^3 are designed on anode and cathode plates with a surface area of 73.8 cm^2 and 2.7 volume of cm^3. The solution network used 1.187.049 four-surfaces (Tetrahedral), 48.659 pyramids, 429.385 prisms, 276.247 triangular elements, enhanced with corner development and corner layers (Boundary Layers) auxiliary elements for different flow channels. The smallest element size is 0,0023 cm, while the average element size is selected as 0,50 cm.

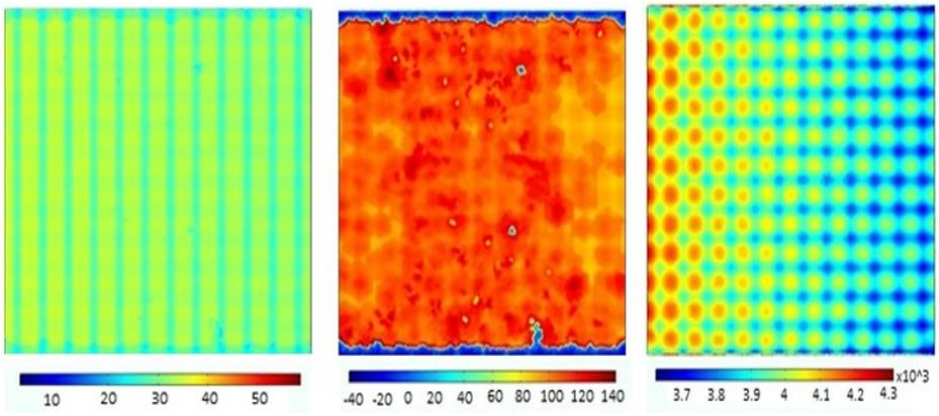

(a) (b) (c)

Fig. 17 2D Membrane Current Density (a) 0,2975 cm (b) 0,3175 cm (c) 0,3375 cm

Examination of the current density in different y-axis sections is shown in Figure 17. The effect of reverse current is clearly seen when compared with Design 3, which is a linear flat design. The current density is scattered across the channels and an interfering distribution is observed. The positive effect of flat channels is still seen in the middle section.

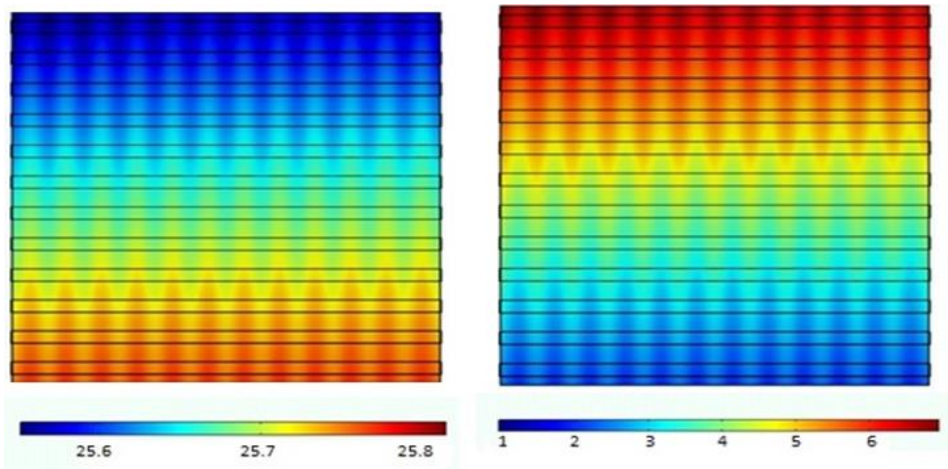

(a) (b)

Fig. 18 Distribution of the (a) hydrogen concentration (b) water concentration in the x-y plane of the anode side.

While hydrogen density was 25.8 mol/m^3 at the inlet, it decreased to 25.6 mol/m^3 towards the outlet. A small amount of change is occurred as seen in Figure 18 (a). Figure 19 (b) shows the distribution of water concentration in the reaction at the cathode interface at constant cell voltage (0.5V). According to the water concentration change graph, the water presence increases from 3 mol/m^3 to 5.5 mol/m^3.

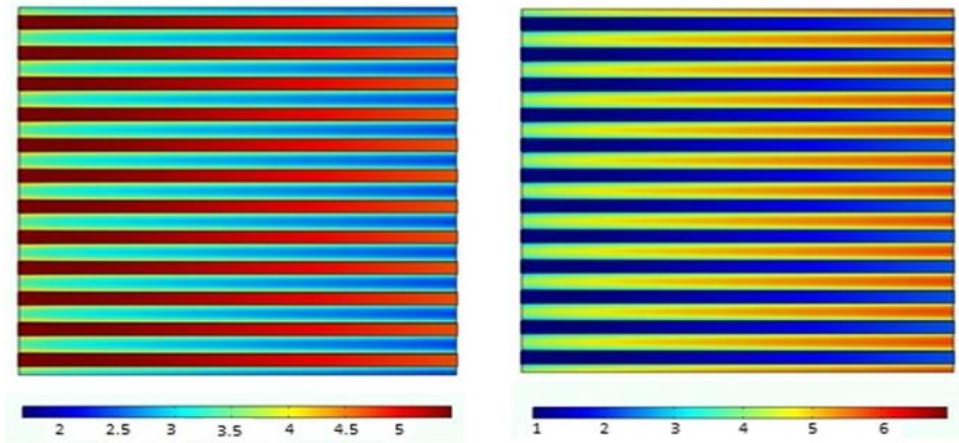

(a) (b)

Fig.19 Distribution of the (a) oxygen concentration (b) water concentration in the x-y plane of the cathode side

Concentration changes along the canals are considered positive with their wide distribution in terms of water management, but changes in oxygen and hydrogen concentrations are considered to be low on the individual canals. Detailed concentration distributions can be examined in Figure 18 and Figure 19. This low drop on concentration

confronts decreases in efficiency and lack of reaction. As the retention time becomes limited the high rate of voltage gradually will increase the efficiency drop.

4.5. Design 5

For sustaining a broader coverage on the cell area a wavy formation is used as presented in some applications on the literature. The wavy fuel cell with 6 inputs and outputs is designed on channels with a surface area of 70.44 cm^2 and a volume of 3.588 cm^3 and anode and cathode plates with a surface area of 100.1 cm^2 and a volume of 3.675 cm^3. There are 3.055.986 four-surface (Tetrahedral), 87.143 pyramids, 1.027193 prisms, 575.956 triangle elements are used, corner refinement and boundary layers auxiliary elements are also used for different flow channels. The smallest element size is 0,0018 cm, while the average element size is 0,51 cm.

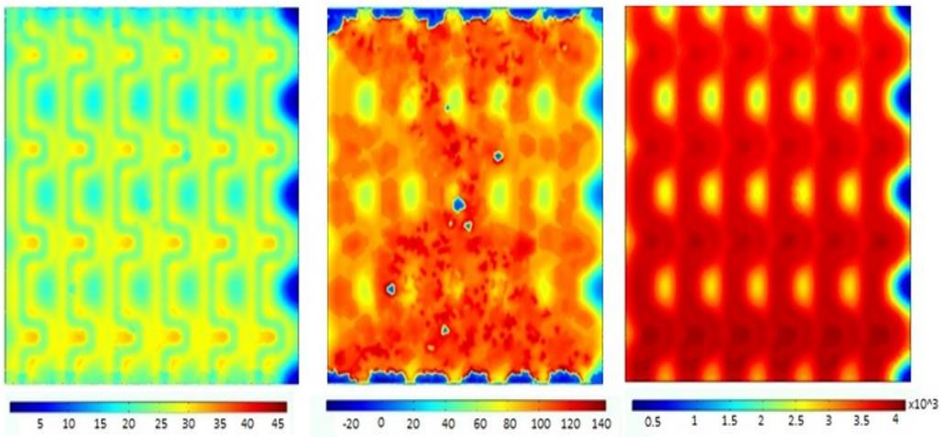

(a) (b) (c)

Fig. 20 2D Membrane Current Density (a) 0,2975 cm (b) 0,3175 cm (c) 0,3375 cm

The effect of the wavy channels used in Design 5 on the current density is shown in Figure 20. The positive effect of multiple inputs and the negative effect of the wavy design on the homogeneous distribution can be observed here. As expected, the current density decreases along the channels and goes down even further in the middle gaps and edges. Inefficient regions arising from the design can also be observed. This design is therefore less homogeneous compared to other designs. That being said, it is also concluded that with a denser structure the distribution can be further optimized in terms of homogeneity. The increased retention time will be another advantage in a denser structure as well.

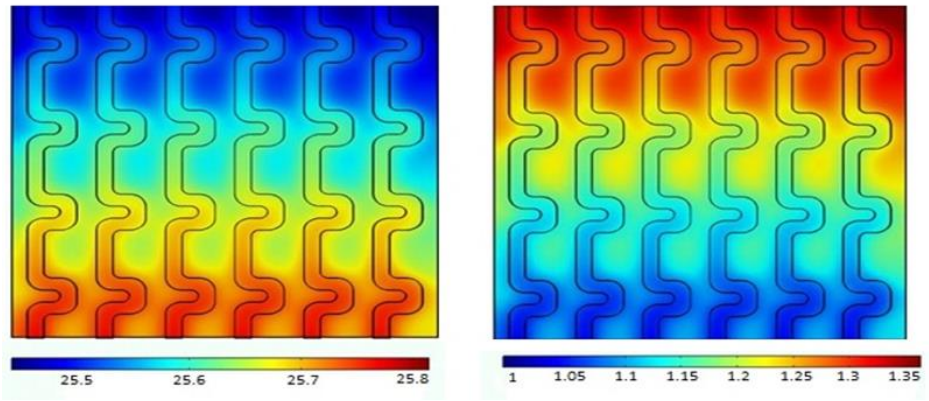

(a) (b)

Figure 21. Distribution of the (a) hydrogen concentration (b) water concentration in the x-y plane of the anode side.

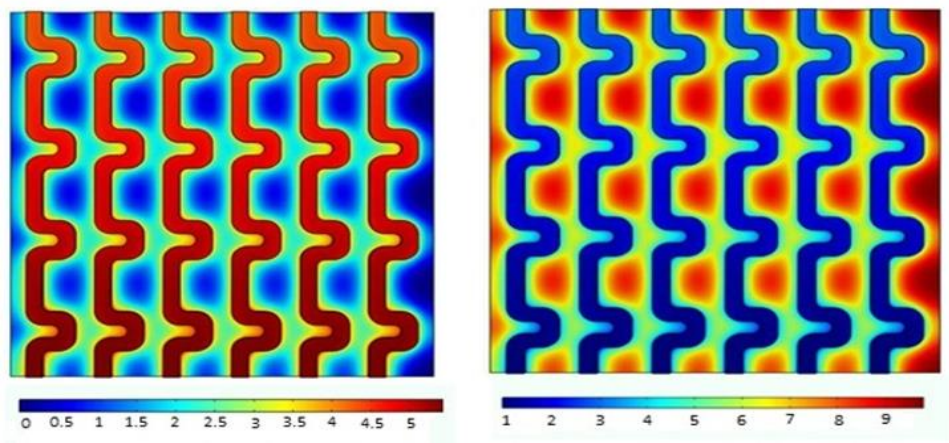

(a) (b)

Fig. 22 Distribution of the (a) oxygen concentration (b) water concentration in the x-y plane of the cathode side.

For Design 5, the concentrations of the components are shown Figures 21 and 22. Hydrogen density was 25.8 mol/m^3 at the inlet, whereas it decreased to 25.5 mol/m^3 towards the outlet. According to the water concentration change graph, it was observed that it increased from 1 mol/m^3 to 1.35 mol/m^3. It is evident that there is a higher reactant distribution than linear channels, and the rapid concentration drops are seen in the entry regions as a result of these. The increase in the retention time of the reactants in the system also enhances the efficiency. The formation, however, still needs to be smoother and denser for the sake of homogeneity and increasing high rates in reaction.

4.6. Design 6

U-shaped fuel cell with 7 inputs and outputs, the channels with a surface area of 61.22 cm^2 and a volume of 3.064 cm^3 are designed on anode and cathode plates with a surface area

of 63.68 cm^2 and a volume of 2.325 cm^3. In the solution network using 1.748.034 four-surface (Tetrahedral), 62.533 pyramids, 553.700 prisms, 345.402 triangle elements, corner refinement and boundary layers auxiliary elements are also used for different flow channels. The smallest element size is 0,0018 cm, while the average element size is 0,52 cm.

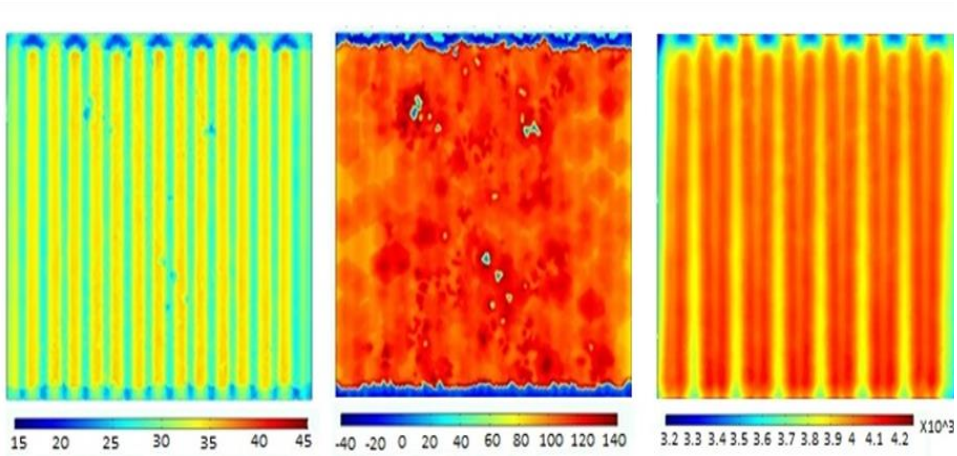

(a) (b) (c)

Fig. 23 2D Membrane Current Density (a) 0,2975 cm (b) 0,3175 cm (c) 0,3375 cm

The current densities of this design, with multiple inlets and outlets which extend the length of the channel with its spiral structure and cover the active area to the maximum, are shown in Figure 23. As a result, a dominant homogeneous structure appears where the majority of the active area is used. Since the canal design covers the entire surface area, it has a lower amount of inefficient zones.

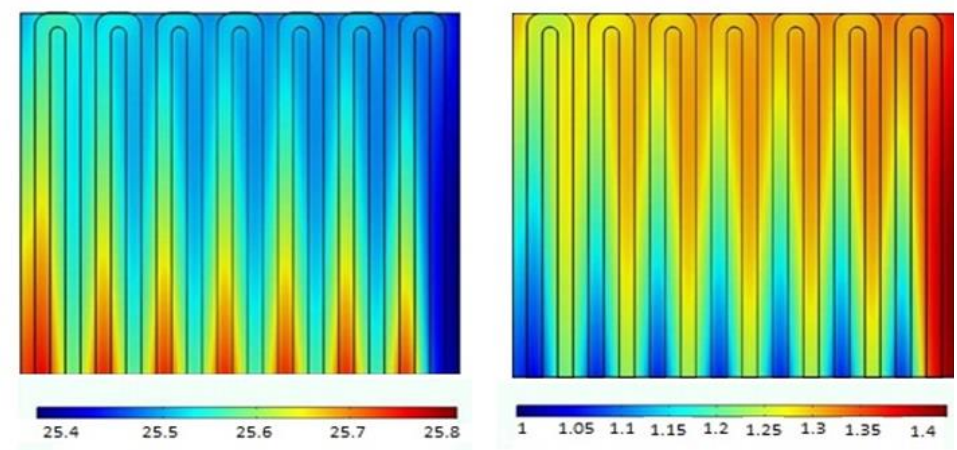

(a) (b)

Fig. 24 Distribution of the (a) hydrogen concentration (b) water concentration in the x-y plane of the anode side

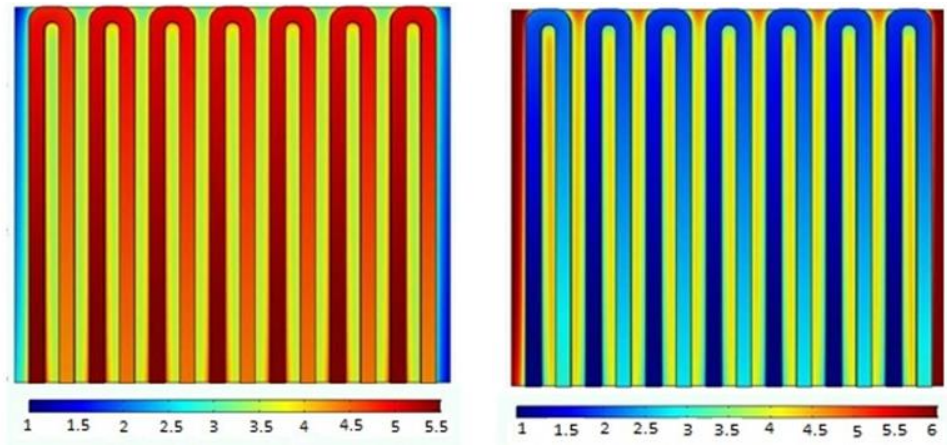

(a) (b)

Fig. 25 Distribution of the (a) oxygen concentration (b) water concentration in the x-y plane of the cathode side

One of the positive features of Design 6 is that it facilitates water management for the fuel cell system. According to Figure 24 and Figure 25, the multi-inlet-outlet channel design prevents excessive drop in concentrations. Accordingly, the hydrogen concentration was 25.8 mol/m^3 at the inlet, but it decreased to 25.4 mol/m^3, due to the relatively long channels providing adequate distribution of the reactants. Oxygen content was 5.5 mol/m^3 at the inlet, but decreased to 4.3 mol/m^3 at the outlet. From water concentration point of view, it was observed that it increased from 1 mol/m^3 to 1.35 mol/m^3 in the anode, whereas it increased from 1 mol/m^3 to 3 mol/m^3 in cathode side (Figure 25-b)

5. Conclusions

Today, due to the increase in environmental pollution, scientists have turned to clean energy. It has been scientifically proven that environmental pollution is mostly caused by vehicles using fossil fuels. For this reason, fuel cell vehicles have come to the fore instead of internal combustion engine vehicles. Fuel cells are highly preferred in vehicles due to their low fuel supply and long driving distance, as well as being environmentally friendly. However, optimum temperature and sufficient humidity must be provided for adequate efficiency from fuel cells. Therefore fuel cells must be well designed.

The present study investigated different flow channel layouts modeled using COMSOL Multiphysics program. A series of performance analyses were performed on these flow plates to determine their current densities, changes in hydrogen and oxygen contents, and overall efficiencies.

When the surface area of a given flow plate is used homogenously, the potential damage due to focal degenerations or breakdowns will be minimized. These focal degenerations occur as a result of high reaction rates in particular locations and the homogeneity of the reaction over the course of the reactant flow helps prevent them from taking place, making it very important in terms of overall efficiency and performance. From this perspective, multiple input fuel cell designs were found to help disperse the fuel on the membrane more equally, which in turn help achieve higher efficiencies. Similarly, cross-flow channels were with relatively shorter lengths were found to lead to more positive results compared to

their longer or parallel flow counterparts. As the cross-flow channels get longer, however, they begin to have negative effects.

We are hopeful that the findings of this study will present a useful source for those who are interested in fuel cell designs, particularly for those with vehicular use in mind. The modeling and simulation method used in the study reduces the time needed for the design stage and can reduce the number of experimental tests in search for the optimal flow plate design.

Acknowledgement

The authors would like to acknowledge the financial support of the Scientific Research Projects Fund of Yüzüncü Yıl University (YYÜ-BAP- 2015-MİM-B120) for the study, along with the Scientific and Technological Research Council of Turkey (TÜBİTAK-MAG-115M741). Also, author Ceyda KÖK is sponsored via a fellowship from the YOK 100/2000 Electric and Hybrid Vehicles Doctorate Program.

References

[1] Hilton Holloway. Japan pushes hydrogen infrastructure | Autocar, Autocar, 2011.
[2] IEA. CO2 EMISSIONS FROM FUEL COMBUSTION Highlights, Iea, 2015.
[3] Giorgi L. Fuel Cells: Technologies and Applications. Open Fuel Cells J, 2013. https://doi.org/10.2174/1875932720130719001
[4] Offer G, James G. Comparative analysis of battery electric, hydrogen fuel cell and hybrid vehicles in a future sustainable road transport system. Energy policy, 2010, 38.1: 24-29 https://doi.org/10.1016/j.enpol.2009.08.040
[5] Choi H, Shin J, Woo JR. Effect of electricity generation mix on battery electric vehicle adoption and its environmental impact, Energy Policy, 2018. https://doi.org/10.1016/j.enpol.2018.06.013
[6] IEA. World Energy Outlook, Iea, 2014.
[7] Kopp M, Coleman D, Stiller C, Scheffer K, Aichinger J, Scheppat B. Energiepark Mainz: Technical and economic analysis of the worldwide largest Power-to-Gas plant with PEM electrolysis. International Journal of Hydrogen Energy, 2017; 42(19), 13311-13320. https://doi.org/10.1016/j.ijhydene.2016.12.145
[8] Fahim KH, MAlfayydh EA. Effect of Geometric Design of the Flow Fields Plat on the Performance of A PEM Fuel Cell: A Review. Int. J. Sci. Eng. Res., 2017.
[9] Pal V, Karthikeyan P, Anand R. Performance Enhancement of the Proton Exchange Membrane Fuel Cell Using Pin Type Flow Channel with Porous Inserts. J. Power Energy Eng., 2015. https://doi.org/10.4236/jpee.2015.35001
[10] Edupuganti V. An Investigation of the Impact of the Proton Exchange Membrane Fuel Cell Flow Field Plate Geometry and Design Using Computational Fluid Dynamic Modeling and Simulation. 2012; 27.
[11] Velisala V, Srinivasulu GN. Computational fluid dynamics study of 3-pass serpentine flow field configuration on proton exchange membrane fuel cell performance. Int. J. Ambient Energy, 2020.
[12] Shen J, Tu Z, Chan SH. Evaluation criterion of different flow field patterns in a proton exchange membrane fuel cell. Energy Conversion and Management, 2020; 213, 112841. https://doi.org/10.1016/j.enconman.2020.112841
[13] Shen J, Tu Z, Chan SH. Performance enhancement in a proton exchange membrane fuel cell with a novel 3D flow field. Applied Thermal Engineering, 2020;164, 114464. https://doi.org/10.1016/j.applthermaleng.2019.114464
[14] Badduri SR, Srinivasulu GN, Rao SS. Influence of bio-inspired flow channel designs on the performance of a PEM fuel cell. Chinese Journal of Chemical Engineering, 2020; 28(3), 824-831. https://doi.org/10.1016/j.cjche.2019.07.010

[15] Liao Z, Wei L, Dafalla AM, Guo J, Jiang F. Analysis of the impact of flow field arrangement on the performance of PEMFC with zigzag-shaped channels. International Journal of Heat and Mass Transfer, 2021;181, 121900.
[16] Mert SO, Özçelik Z, Özçelik Y, Dinçer I. Multi-objective optimization of a vehicular PEM fuel cell system. Applied Thermal Engineering, 2011; 31(13), 2171-2176. https://doi.org/10.1016/j.applthermaleng.2011.04.031
[17] EG&G Technical Services, I. EG&G Technical Services. Fuel Cell Technology-Handbook, 7th Edition. U.S. Department of Energy, 2004.
[18] Hoogers G. Fuel Cell Technology - Handbook. CRC Press, 2003. https://doi.org/10.1201/9781420041552
[19] Andújar JM, Segura F. Fuel cells: History and updating. A walk along two centuries. Renewable and sustainable energy reviews, 2009; 13(9), 2309-2322. https://doi.org/10.1016/j.rser.2009.03.015
[20] Larminie J, Dicks A, Mcdonald M. Fuel cell systems explained. Chichester, UK: J. Wiley, 2003. https://doi.org/10.1002/9781118878330
[21] Barbir F. PEM Fuel Cells-Theory and Practice. Elsevier Academic Press, 2005.
[22] Kirubakaran, Jain S, Nema RK. The PEM Fuel Cell System with DC/DC Boost Converter: Design, Modeling and Simulation. Int. J. Recent Trends Eng., 2009.
[23] O'Hayre R, Colella W, Prinz FB. Fuel Cell Fundamentals. 2016. https://doi.org/10.1002/9781119191766
[24] Emadi A, Williamson SS. Fuel cell vehicles: opportunities and challenges. IEEE Power Engineering Society General Meeting, 2004; 1640-1645
[25] Dickinson EJ, Ekström H, Fontes E. COMSOL Multiphysics®: Finite element software for electrochemical analysis. A mini-review. Electrochemistry communications, 2014;40, 71-74. https://doi.org/10.1016/j.elecom.2013.12.020
[26] Comsol A. Comsol Multiphysics User's Guide. 2010.
[27] Vick JA. Multiphysics Simulation. IEEE Spectr., 2013.
[28] Wang L, Husar A, Zhou T, Liu H. A parametric study of PEM fuel cell performances. International journal of hydrogen energy, 2003; 28(11), 1263-1272. https://doi.org/10.1016/S0360-3199(02)00284-7
[29] Hussain MM, Baschuk JJ, Li X, Dincer I. Thermodynamic analysis of a PEM fuel cell power system. International journal of thermal sciences, 2005; 44(9), 903-911. https://doi.org/10.1016/j.ijthermalsci.2005.02.009
[30] Kazim A. Exergy analysis of a PEM fuel cell at variable operating conditions. Energy conversion and management, 2004; 45(11-12), 1949-1961. https://doi.org/10.1016/j.enconman.2003.09.030
[31] Mert SO, Dincer I, Ozcelik Z. Exergoeconomic analysis of a vehicular PEM fuel cell system. Journal of Power Sources, 2007; 165(1), 244-252. https://doi.org/10.1016/j.jpowsour.2006.12.002
[32] Midilli A, Dincer I. Exergetic performance analysis of a PEM fuel cell. Int. J. Energy, 2006; 307-321. https://doi.org/10.1002/er.1150
[33] Mert SO. (2012). Exergetıc based multı-objectıve optımızatıon of selected fuel cell systems. Ph.D. Dissertation, Ege University, Turkey.

Research on Engineering Structures Materials

R M E S

Content

Research Group